October 1996 • NREL/CP-430-21968 - Vol. 2

CONF-9605195-- Vol. 2

Proceedings of the 1996 U.S. DOE Hydrogen Program Review

Volume II

May 1–2, 1996 Miami, Florida

RECEIVED NOV 2 6 1996 OSTI

Sponsored by the Office of Solar Thermal, Biomass Power and Hydrogen Technologies U.S. Department of Energy

DISTRIBUTION OF THIS DOCUMENT IS UNLIMITED

MASTER



National Renewable Energy Laboratory 1617 Cole Boulevard Golden, Colorado 80401-3393 A national laboratory of the U.S. Department of Energy Managed by Midwest Research Institute for the U.S. Department of Energy under Contract No. DE-AC36-83CH10093

Proceedings of the 1996 U.S. DOE Hydrogen Program Review

Volume II

May 1-2, 1996 Miami, Florida

Sponsored by the Office of Solar Thermal, Biomass Power and Hydrogen Technologies U.S. Department of Energy



National Renewable Energy Laboratory 1617 Cole Boulevard Golden, Colorado 80401-3393 A national laboratory of the U.S. Department of Energy Managed by Midwest Research Institute for the U.S. Department of Energy under Contract No. DE-AC36-83CH10093

Prepared under Task No. HY611010

October 1996

DISCLAIMER

Portions of this document may be illegible in electronic image products. Images are produced from the best available original document.

NOTICE: This report was prepared as an account of work sponsored by an agency of the United States government. Neither the United States government nor any agency thereof, nor any of their employees, makes any warranty, express or implied, or assumes any legal liability or responsibility for the accuracy, completeness, or usefulness of any information, apparatus, product, or process disclosed, or represents that its use would not infringe privately owned rights. Reference herein to any specific commercial product, process, or service by trade name, trademark, manufacturer, or otherwise does not necessarily constitute or imply its endorsement, recommendation, or favoring by the United States government or any agency thereof. The views and opinions of authors expressed herein do not necessarily state or reflect those of the United States government or any agency thereof.



TABLE OF CONTENTS

Volume I

Systems	Analysis
----------------	-----------------

Supporting Analysis and Assessments Quality Metrics: Utility Market Sector, J. Ohi, National Renewable Energy Laboratory
H Scan/AHP Advanced Technology Proposal Evaluation Process, S. Mack, Energetics, Inc., M.R. Szoka deValladares, National Renewable Energy Laboratory
Systems Analysis - Independent Analysis and Verification, J.P. DiPietro, E. Skolnik, J. Badin, Energetics, Inc
System Comparison of Hydrogen with Other Alternative Fuels in Terms of EPAct Requirements, F. Barbir, K Özay, T.N. Veziroglu, University of Miami
Integrated Analysis of Transportation Demand Pathway Options for Hydrogen Production, Storage, and Distribution, C.E.Thomas, Directed Technologies, Inc
Comparative Costs and Benefits of Hydrogen Vehicles, G. Berry, Lawrence Livermore National Laboratory
Hydrogen Energy Systems Studies, J. Ogden, T. Kreutz, A. Cox, J. White, Princeton University
Coupling Renewables Via Hydrogen Into Utilities: Temporal and Spatial Issues, and Technology Opportunities, J. Iannucci, S. Horgan, J. Eyer, Distributed Utility Associates, S. Schoenung, Longitude 122 West, Inc
Modeling of Hydrogen Production Methods: Single Particle Model and Kinetics Assessment, R. Miller, J. Bellan, Jet Propulsion Laboratory
Technicoeconomic Analysis of Renewable Hydrogen Production, Storage, and Detection Systems, M. Mann, P. Spath, K. Kadam, National Renewable Energy Laboratory 249
Hydrogen Storage and Delivery System Development: Analysis, J. Handrock, Sandia National Laboratory
Production
Development of an Efficient Algal H ₂ -Producing System, M. Ghirardi, S. Markov, M. Seibert, National Renewable Energy Laboratory

Hydrogen Production By Photosynthetic Water Splitting, E. Greenbaum, J. Lee, C. Tevault, Oak Ridge National Laboratory
In Vitro Hydrogen Production by Glucose Dehydrogenase and Hydrogenase, J. Woodward, Oak Ridge National Laboratory
Biological H ₂ from Syngas and from H ₂ O, P. Weaver, PC. Maness, S. Markov, S. Martin, National Renewable Energy Laboratory
Photoelectrochemical Based Direct Conversion Systems for Hydrogen Production, S. Kocha, M. Peterson, D. Arent, H. Scott, A. Frank, J. Turner, National Renewable Energy Laboratory
Photoelectrochemical Hydrogen Production, R. Rocheleau, E. Miller, A. Misra, University of Hawaii
Photovoltaic Hydrogen Production, H. Hiser, S. Memory, T.N. Veziroglu, J. Padin University of Miami
Solar Photocatalytic H, Production from Water Using a Dual Bed Photosystem, C. Linkous, Florida Solar Energy Center
International Marine Biotechnology Culture Collection (IMBCC), O. Zaborsky, K. Baker, University of Hawaii
Biological Hydrogen Photoproduction, L. Brand, YH. Luo, T. Tszuki, University of Miami
Development of Solid Electrolytes for Water Electrolysis at Higher Temperature, C. Linkous, University of Central Florida
Solar Photochemical Production of HBr for Off-Peak Electrolytic Hydrogen Production, H. Heaton, Solar Reactor Technologies, Inc
Biomass-to-Hydrogen via Fast Pyrolysis and Catalytic Steam Reforming, E. Chornet, D. Wang, S. Czernik, D. Montané, M. Mann, National Renewable Energy Laboratory 457
Hydrogen Production from Municipal Solid Waste, P. Wallman, J. Richardson, C. Thorsness, Lawrence Livermore National Laboratory, T. Leininger, J. Klein, J. Winter, A. Robin, Montebello Technology Center, Texaco, Inc
Hydrogen Production from High-Moisture Content Biomass in Supercritical Water, M. Antal, T. Adschiri, T. Ekbom, A. Garcia, Y. Matsumura, T. Minowa, F. Nuessle, M. Sakurai, X. Xu, University of Hawaii

Production of Hydrogen by Thermocatalytic Cracking of Natural Gas, N. Muradov, Florida Solar Energy Center		
Sorption Enhanced Reaction Process (SERP) for Production of Hydrogen, M. Anand, J. Hufton, S. Mayorga, S. Nataraj, S. Sircar, Air Products and Chemicals, Inc		
Hydrogen Manufacturing Using Plasma Reformers, L. Bromberg, Massachusetts Institute of Technology		
Volume II		
Utilization		
Hydrogen Safety Analysis, M. Swain, B. Sievert, University of Miami, M. Swain, Analytical Technologies, Inc		
Design and Development of a Low-Cost Fiber-Optic Sensor for Hydrogen Detector, D. Benson, C. Tracy, C. Bechinger, National Renewable Energy Laboratory 605		
Chemical Kinetic Modeling of H ₂ Applications, C. Westbrook, N. Marinov, W. Pitz, H. Curran, Lawrence Livermore National Laboratory		
Hydrogen Engine Development: Experimental Program, P. Van Blarigan, Sandia National Laboratory		
Numerical Modeling of Hydrogen-fueled Internal Combustion Engines, N. Johnson, A. Amsden, T. Butler, Los Alamos National Laboratory		
Analysis of Experimental Hydrogen Engine Data and Hydrogen Vehicle Performance and Emissions Simulation, S. Aceves, Lawrence Livermore National Laboratory 691		
Development of a Lean Premixed Burner for Hydrogen Utilization, J. Keller, Sandia National Laboratory		
City of Chula Vista, Hydrogen Fuel Cell Bus Demonstration Project, B. Gustafen, B. Bamberger, City of Chula Vista		
A Polymer Electrolyte Fuel Cell Stack for Stationary Power Generation from Hydrogen Fuel, C. Zawodzinski, M. Wilson, S. Gottesfeld, Los Alamos National Laboratory		
The Palm Desert Renewable Hydrogen Transportation System, P. Lehman, Humboldt State University		

Storage

Carbon Nanotube Materials for Hydrogen Storage, A. Dillon, K. Jones, M. Heben, National Renewable Energy Laboratory	. 747
Hydrogen Transport and Storage in Engineered Glass Microspheres, G. Rambach, Lawrence Livermore National Laboratory, C. Hendricks, W. J. Schafer Associates	. 765
Hydrogen Storage and Delivery System Development: Fabrication, J. Handrock, M. Malinowski, K. Wally, Sandia National Laboratories	. 773
Hydrogen Storage via Polyhydride Complexes, C. Jensen, University of Hawaii	. 787
Thermodynamic Characterization of Polyhydride Complexes, R. Zidan, R. Rocheleau, C. Jensen, University of Hawaii	. 795
Hydride Development for Hydrogen Storage, G. Thomas, S. Guthrie, W. Bauer, N. Yang, Sandia National Laboratories, G. Sandrock, SunaTech, Inc.	. 807
Thermal Management Technology for Hydrogen Storage: Fullerene Option, J. Wang, F. Chen, R. Murphy, Oak Ridge National Laboratory	. 819

Task D: Hydrogen Safety Analysis

Michael R. Swain Brad G. Sievert University of Miami Coral Gables, FL 33124

Matthew N. Swain Analytical Technologies, Inc. Miami, FL 33186

Abstract

This report covers two topics. The first is a review of codes, standards, regulations, recommendations, certifications, and pamphlets which address safety of gaseous fuels. The second is an experimental investigation of hydrogen flame impingement. Four areas of concern in the conversion of natural gas safety publications to hydrogen safety publications are delineated. Two suggested design criteria for hydrogen vehicle fuel systems are proposed. It is concluded from the experimental work that light weight, low cost, firewalls to resist hydrogen flame impingement are feasible.

Introduction

The following report covers two subjects: a review of safety publications and an experimental investigation of hydrogen flame impingement. In the context of this report, safety publications include codes, standards, regulations, recommendations, certifications, and pamphlets which address safety and are published by the following organizations.

A.G.A. American Gas Association

A.N.S.I. American National Standard Institute, Inc.

A.P.I. American Petroleum Institute

A.S.T.M.	American Society for Testing and Materials
C.F.R.	Code of Federal Regulations
C.G.A.	Compressed Gas Association, Inc.
N.F.P.A.	National Fire Protection Association
S.A.E.	Society of Automotive Engineers
U.L.	Underwriters Laboratories

There are presently no safety publications for the use of hydrogen as a vehicle fuel. There are safety publications dealing with the transportation of hydrogen, and the use of compressed natural gas and liquid petroleum gas as vehicle fuels. These existing safety publications are being reviewed because they formulate guidelines for new safety publications governing the use of hydrogen as a vehicle fuel.

Terminology

When the various codes and standards are considered as a single body of work, terminology conflicts can cause confusion. It is important to recognize, when reviewing the various codes and standards, that the publications have been written by various committees over many years. For this reason the terminology is specific to each publication. A specific term may be defined somewhat differently in different publications. By way of example, the terminology used to describe pressurized storage of fuel gases is reviewed in the following section.

NFPA 52 refers to "containers" for all storage of compressed natural gas. Containers take the form of either "cylinders" or "pressure vessels". Cylinders are containers that meet DOT or TC regulations, ANSI/AGA NGV2, or CSAB51 standards. Pressure vessels are containers which meet ASME codes.

NFPA 50A refers to "containers" for storage of compressed hydrogen gas. Containers take the form of either "containers" or "pressure vessels". Containers meet DOT or ASME requirements. Pressure vessels are containers which meet ASME requirements.

NFPA 55 refers to "containers" or "cylinders" for storage of compressed gases. Containers and cylinders are used interchangeably and must be fabricated to or authorized for use by DOT, TC, or ASME.

NFPA 50B refers to "containers" for all storage of liquified hydrogen. Containers must meet DOT or ASME requirements.

NFPA 51 refers to "containers" or "cylinders" for all storage of compressed gases. Containers and cylinders are used interchangeably.

CGA P1-1991 refers to "containers" for all storage of compressed gases. Containers are either compressed gas cylinders or liquid containers. Containers are described as vessels that meet DOT, TC, or ASME requirements. Cylinders are compressed gas containers of less than 120 gallon capacity.

NGV2-1992 refers to "containers" or "vessels" for storage of compressed natural gas on vehicles. Containers and vessels are used interchangeably.

Differences in terminology have not produced significant problems in implementation, but must be recognized when comparisons are made between various safety publications.

Development of Hydrogen Standards

ISO/TC 197 (International Standards Organization Technical Committee) is presently developing standards, codes, and guidelines to assist in the implementation of hydrogen energy systems. The goal of ISO/TC 197 is to eliminate barriers to international trade, establish safe handling practices, facilitate the standardization of interfaces, and to harmonize testing methods and quality criteria. There are presently three working groups pursuing this goal. They are:

Working Group 1 Liquid Hydrogen Fueling Systems for Land Vehicles

Working Group 2 Liquid Hydrogen Tank Containers

Working Group 3 Product Specification for Hydrogen Used as a Fuel

They have produced the following working documents:

WD-13984 Liquid Hydrogen: Land Vehicle Fueling Interface: storage vessels, piping, valves, transfer hose, interface with vehicle fuel tank, interlocks, and safety.

WD-13985 Liquid Hydrogen: Land Vehicle Fuel Tanks: fuel container, piping, valves, interface, location, safety.

WD-13986 Tank Containers for multimodal transportation of liquid hydrogen: hydrogen container, piping, valves, transportation factors, interface, interlocks, safety.

Fuel Specifications

Fuel specifications are presently under development by ISO/TC 197. The allocated project number for "Hydrogen Fuel-Product Specification" is ISO/NP 14687. The project has participation from Canada, Egypt, Japan, Republic of Korea, Turkey, and the United States. Belgium, France, Germany, and Switzerland supported the addition of the project as a new work item. The convener for the project is Addison Bain.

The fuel specifications for natural gas are an example of the requirements for an existing gaseous fuel. Hydrogen fuel specifications share common needs with natural gas specifications. Three publications describe accepted fuel specifications for natural gas. They are SAE J 1616, NFPA 52, and ANSI/AGA NGV2-1992. Five chemical compounds are restricted in those specifications, referenced in the following gas quality statements: Water concentration, sulfide concentration, methanol concentration, oxygen concentration, and carbon dioxide concentration.

Water concentration restrictions differ slightly in the three publications. SAE J 1616 requires a water concentration below the dew point at -20 °C (-4 °F). NFPA 52 requires a water concentration below 7.0 lb/mmCF. NGV2 requires a concentration below the dew point 5.5 °C (10 °F) less than the 99% winter design temperature. The 99% winter design temperature is listed under Chapter 24, Table 1, Climatic Conditions for the United States, in the American Society of Heating, Refrigerating and Air Conditioning Engineering (ASHRAE) Handbook, 1989 Fundamentals Volume.

Hydrogen sulfide plus soluble sulfide restrictions are practically identical for the three publications. SAE J 1616 requires sulfide concentrations below 1.0 gm/100 CF (8 to 30 ppm mass). Though hydrogen sulfide can be corrosive in the presence of condensed water this restriction is primarily to avoid excessive exhaust catalyst poisoning. Both NFPA 52 and NGV2 limit sulfide concentration to 0.05 psi partial pressure. This would be typically 20 ppm, similar to the SAE J 1616 requirement.

Methanol concentration restrictions are identical for SAE J 1616 and NGV2. They both prohibit the addition of methanol to natural gas. Methanol addition is not needed if water condensation is prevented by remaining below the required maximum concentration of water vapor. NFPA 52 does not include a gas quality statement for methanol.

Oxygen concentration restrictions are identical for SAE J 1616 and NGV2. They both require the oxygen concentration to be below the flammability limit of the mixture. Corrosion is avoided by limiting the water vapor content of the fuel gas, making flammability the principal concern of the restriction. The restrictions of NFPA 52 are more stringent. NFPA 52 limits oxygen concentration to 0.5%, considerably below the flammability limit.

Carbon dioxide concentration restrictions are treated differently by each publication. SAE J 1616 restricts carbon dioxide concentrations to 3.0% (30,000 ppm) this done to maintain a relatively constant relationship between volumetric fuel flow rate and stoichiometry. NFPA 52 restricts carbon dioxide concentration to 7 psi partial pressure (approx. 2800 ppm). NGV2 does not address carbon dioxide as a natural gas constituent.

Gaseous Fuels in Safety Publications

In the following discussion comparisons are made of the hydrogen and natural gas transport and handling guidelines in the Codes of Federal Regulations and pamphlets by the Compressed Gas Association. These highlight the relative treatment of hydrogen and natural gas. Additionally, SAE makes statements concerning the future use of hydrogen.

The Codes of Federal Regulations (49 CFR 172 Hazardous Materials Table, Special Provisions, Hazardous Materials Communications, Emergency Response Information, and Training Requirements) compares compressed hydrogen with compressed methane and liquid hydrogen as hazardous materials for the purpose of transportation of those materials. In particular, the fuels are rated by hazard class, quantity allowed in passenger aircraft or rail car, and quantity allowed in cargo aircraft.

The hazard class is an indicator of how the fuel should be treated during transport. Compressed hydrogen, compressed methane, and liquid hydrogen are all classed as Division 2.1 (flammable gases). These are defined in 49 CFR 173.115. All three fuels have the same hazard class (Division 2.1) and are treated the same during transport.

49 CFR 172.101 addresses the quantity of compressed hydrogen, compressed methane, or liquified hydrogen allowed in passenger aircraft or rail car. All three are forbidden for transport in passenger aircraft or rail car.

49 CFR 172.101 addresses the quantity of these materials allowed in cargo aircraft. Liquid hydrogen is forbidden. Compressed hydrogen and methane are limited to 150 kilogram per package. Compressed hydrogen and methane are treated identically as are mixtures of the two gases.

The Compressed Gas Association pamphlet CGA P-1-1991 entitled "Safe Handling of Compressed Gases in Containers" classifies gases by hazard class. Classification is based on the chemical and physical hazards of the gas. Three of the gases grouped together by their principal hazards are acetylene, hydrogen, and methane. The limiting capacity for gas containers (2500 ft³) stored inside industrial buildings at consumer sites is the same for all three gases. Though compressed hydrogen is specified as combining high pressure with flammable hazard, methane also combines the same two hazards.

SAE has addressed the subject of hydrogen usage as a vehicle fuel. This was done in SAE J 1297 entitled "Alternative Automotive Fuels". SAE's positions was clearly stated "Safety and methods for storage of hydrogen fuel will require additional investigation". The references cited in the publication were all from the 1970's.

Four Areas of Potential Concern

The following four areas of potential concern were identified. This is not intended to be a comprehensive list as further investigation will likely identify additional areas for this list.

- 1. Odorants
- 2. Static Electricity
- 3. Leakage rate safety criteria
- 4. Tank permeability

Odorants

Odorants are required by all fuel gas specifications. Hydrogen fuel gas specifications will likely also require the use of odorants. The requirements are for odorant concentrations to be high enough to allow detection fuel gas concentrations of 1/5 the lean limit of combustion. These requirements exist for both natural gas and liquid petroleum gas.

SAE J 1616 "Recommended Practice for Compressed Natural Gas Vehicle Fuel" states "Natural gas introduced into any CNG fueling station or vehicle shall have a distinctive odor potent enough of its presence to be detected down to a concentration in air not over 1/5 of the lower limit of flammability.

NFPA 52 - 1992 edition "Standard for Compressed Natural Gas (CNG) Vehicular Fuel Systems" states "Natural gas introduced into any system covered by this standard shall have a distinctive odor potent enough for its presence to be detected down to a concentration in air of not over 1/5 of the lower limit of flammability".

NFPA 58 - 1989 edition "Standard for the Storage and Handling of Liquified Petroleum Gases" states "All LP-gases shall be odorized prior to delivery to a distributing plant by the addition of a warning agent of such character that they are detectable, by a distinct odor, down to a concentration in air of not over one-fifth the lower limit of flammability".

The implementation of a similar requirement for hydrogen poses questions that will impact the cost of hydrogen as a vehicular fuel source. Odorants in current use (mercaptans, disulfides, and commercial odorants) contain sulfur. Internal combustion engines have been shown to be tolerant of the concentrations necessary for gas detection. Fuel cells are, on the other hand, sulfur intolerant. Technology to remove odorants, or new non-sulfur containing odorants will need to be used. Removal of odorants is usually accomplished with a zinc oxide sulfur polisher. The zinc oxide polisher is able to remove the mercaptans and disulfides. However, some commercial odorants contain THT (tetrahydrothiophene), more commonly known as thiophane, and require the addition of a hydrodesulfurizer before the zinc oxide catalyst bed. The hydrodesulfurizer uses hydrogen to convert the thiophane into H₂S which is easily removed by the zinc oxide polisher (Internet Web Page). The cost of sulfur removal is a function of the concentration of sulfur in the hydrogen.

The concentration of odorant in hydrogen gas is not well defined by the term "1/5 the lean limit of flammability". All fuel gases have two lean limits of flammability (see Table 1) (Lewis, 1987):

	Upward propagating lean limit of combustion	Downward propagating lean limit of combustion
Propane	2.1% by volume	2.2% by volume
Methane	5.3% by volume	5.9% by volume

4.1% by volume

Table 1 - Lean Flammability Limits

Flames propagate upward with greater ease than they propagate downward. This is primarily due to natural convection of the hot burned gases in an upward direction. To propagate downward the flame speed must be high enough to overcome the upward gas motion due to natural convection. Note that for propane and methane the upward and downward propagating lean limit of combustion are approximately the same. They differ by a factor of 2.5 for hydrogen. The amount of odorant needed for use with hydrogen differs by the same factor depending on which lean limit is used as the basis for the requirement. As an example, if upward propagating lean limit is used, the odorant concentration in hydrogen would be 51% of that used for propane but 129% of that used for methane. If downward propagating lean limit is used, the odorant concentration in hydrogen would be 22% of that for propane and 59% of that for methane. Therefore, the proper odorant concentration for hydrogen needs to be determined.

10.0% by volume

Static Electricity

Hydrogen

The second potential area of concern is the generation of static electricity. Hydrogen's ignition energy is as low as 0.017 millipule for near stoichiometric mixtures, so the possibility of ignition by static electricity exists. This may well be the explanation for "spontaneous ignition" of hydrogen. Spontaneous ignition of hydrogen has been reported when venting at pressures higher than 2000 psi (1995 Proceedings). The source of this ignition may be traceable to the accumulation of static charge on the walls of the conduit through which the hydrogen is passing.

Static charge is an accumulation of electrons on a surface. Pure hydrogen will not carry electrons and cannot generate static charges by flowing through a conduit. However, if the hydrogen contains particles such as oxide flakes from the walls of pipes or containers to carry electrons, flowing hydrogen can generate static charges which may cause ignition if the hydrogen is mixed with air. For a vehicle, the installation of drag chains (drag straps) to bleed the static charge back to the road is not adequate to solve the problem (NFPA 77). The use of a filter to trap particles can increase the problem and produce from 10 to 200 times more charge than a system with no filter (API 2003). Filters have a large surface area due to the numerous small pores needed in their design. The large surface area allows static charge to accumulate more readily.

The potential for generation of static electricity is greatest for metal hydride systems where small particles of the hydride can be suspended in the hydrogen while it is flowing. It is anticipated that a safety publication will be needed to address the issue.

Leakage Rate Safety Criteria

The safety publications dealing with natural gas usage utilize volumetric leakage rates as performance criteria to assess the suitability of various devices (check valves, joints, connectors, etc.). Writing hydrogen standards based on the natural gas standards will require conversion of the natural gas leakage rate criteria values to values suitable for hydrogen.

How the conversion is made will determine whether or not existing hardware designed for natural gas will be suitable for hydrogen vehicles. If the conversion is made based on equivalent energy leakage rate for hydrogen compared to natural gas; hardware designed for natural gas will, in general, be suitable for usage with hydrogen systems without redesign. If, on the other hand, the conversion is made based on equivalent volumetric leakage rate it is probable that the hardware designed for natural gas will need to redesigned for usage with hydrogen. Table 2 presents the reasons for this conclusion.

Table 2 - Hydrogen to Methane Leakage Ratios

Ratio of Hydrogen to Methane Leakage Flow Rate	Energy Flow Rate	Volumetric Flow Rate
Laminar	0.39	1.29
Turbulent	0.85	2.83
Sonic Throttled	0.88	2.93

Shown in Table 2 are the ratios of hydrogen flow rate divided by methane flow rate for the three types of leaks. They are calculated for the same pressure drop across the leak for both hydrogen and methane. The three types of leaks are characterized by the type flow within the leak. A laminar leak is normally a small leak that, by virtue of the small passageway, is characterized by laminar flow. Laminar flow is predominately viscous flow. Though hydrogen molecules are small, the dynamic viscosity of hydrogen is only slightly smaller than methane. Consequently the volumetric flow rate of hydrogen is only 29% larger than methane in a laminar leak. These relative flow rates were verified experimentally with test sections of natural gas lines removed from service due to leakage by People's Gas Company of Miami, FL. A turbulent leak occurs through a larger passageway when the leak flow is predominately turbulent.

Turbulent flow has a relatively thin viscous boundary layer and the flow rate is inversely proportional to the square root of gas density. Hydrogen's low density causes a much higher volumetric flow rate relative to methane. A sonic throttled leak occurs for large relatively unobstructed passageways and pressure ratios greater than two across the leak. The flow rates for turbulent and sonic throttled leaks are similar.

As can be see in Table 2, performance criteria based on energy flow rate for hydrogen could be easily met with existing hardware. Hydrogen has inherently lower energy leakage rates than methane in a given leak at the same pressure. On the other hand, hydrogen performance criteria based on volumetric leakage flow rate will be difficult to meet with existing hardware. Hydrogen has inherently higher volumetric leakage rates than methane for all types of leaks.

Tank Permeability

ANSI/AGA NGV2-1992 "Basic Requirements for Compressed Natural Gas Vehicle (NGV) Fuel Containers" divides compressed natural gas containers of under 1000 liter capacity into four groups. They are as follows:

NGV2-1	All metal containers	
NGV2-2	Metal liner "hoop wrapped"	
NGV2-3	Metal liner "full wrapped"	
NGV2-4	Non-metal liner "full wrapped"	

In general, the standards could be applied to both natural gas and hydrogen. One area of concern does exist for NGV2-4. NGV2-4 states "The liner material and thickness shall be chosen such that the permeation of compressed natural gas through the wall of the finished container at service pressure is less than 0.25 normal cc per hour per liter water capacity of the container". Experience with polyethylene pipes (Swain, 1992) has shown that hydrogen's small molecular size does make permeability performance criteria difficult to meet. For polyethylene pipes the hydrogen volumetric permeation flow rate was on the order of 5.4 times that of methane at the same pipeline pressure. The ratio of hydrogen to methane energy flow rate, due to permeation, was on the order of 1.6. If the permeability of polyethylene pipe is an indicator of the permeability of non-metallic liners, then it may not be possible to meet the permeability performance criteria for hydrogen using existing containers with non-metallic liners. It will be more difficult to meet the permeability performance criteria if the conversion of NGV2 for natural gas to hydrogen is based on volumetric flow rate than if it is based in energy flow rate.

Hydrogen Fuel Delivery System

Figure 1 is a schematic of a hydrogen vehicle fuel delivery system. The components have been chosen to satisfy safety publications written for natural gas. The areas of concern when rewriting the safety publications for hydrogen usage were addressed in the previous section.

The relevant safety publications for natural gas are listed below with each of the fuel system components.

Fuel Container

ANSI/AGA NGV2-1992 AGA requirements No. 1-85 NFPA 52 ASME Boiler and Pressure Vessel Code Section VIII
Code of Federal Regulations, 49 CFR Parts 100 to 179 (US Department of Transportation)
Transportation of Dangerous Goods Regulations of Transport Canada

Pressure Gauge

UL 404

NFPA 52

Pressure Relief Device

CGA S1.1

CGA P-1-1991

ANSI/CGA standard V-9 1991

AGA requirements No. 1-85

49 CFR 173.34

NFPA 50A

NFPA 50B

NFPA 52

NFPA 58

Container Shut-off

ANSI/UL 429-1983

Pressure Regulator

UL 252

NFPA 52

Filler Connection

NFPA 52

ANSI/NFPA 30-A

Manual Shut-off

CGA P-1-1991

AGA requirements No. 1-85

NFPA 52

NFPA 58

Automatic Shut-off

NFPA 52

Hose, fuel line, connectors, adapters

SAE J 512

SAE J 1231

49 CFR 393 Subpart E

NFPA 52

ANSI/AGA NGV1-1994

CGA NGV1-1994

ASTM materials standards

Suggested Design Criteria

The following are two additional design criteria suggested for hydrogen fuelled vehicles. They are suggested for review and discussion by interested parties.

The first suggested design criteria is "vent upward". The intent of "vent upward" is to facilitate hydrogen's natural tendency to rise due to it's low density. "Vent upward" would require pressure relief devices and other venting hardware to have an unimpeded path out of the top of the vehicle. "Vent upward" would include hydrogen vented or released due to an accident or damage to the fuel system. An unimpeded pathway should be provided such that hydrogen released can leave the accident scene in an upward direction due to natural buoyancy without being trapped by vehicle geometry. "Vent upward" would reduce the likelihood that leaking hydrogen, if ignited, would impinge on vehicle parts or occupants. The general concept of avoiding impingement is addressed in NFPA 50B and NFPA 58. It is also addressed in NFPA 30A for service stations and NFPA 59 for utility plants.

"Vent upward" also implies the use of a rain cap or cover over the upward facing vents to provide protection from the elements. NFPA 58 and NFPA 59 allude to the use of such devices. The rain cap or cover may function as a vent door for hydrogen combustion and should be sized as such. NFPA 68 and NFPA 52 provide some guidelines for this sizing. If the rain cap/cover is located in the rear of the vehicle the effect on rear visibility (SAE J 985) during deployment must also be addressed.

The second suggested design criteria concerns fuel container location. Safety publications addressing fuel container location in natural gas fuelled vehicles (49 CFR 393 Subpart E, and NFPA 52) restrict fuel container location in three ways. The container or associated equipment cannot extend beyond the vehicle, be located in front of the front axle or behind the rear bumper. It is suggested that these restrictions be tightened, to provide additional protection to the fuel system by the body of the vehicle. By analyzing the most frequent impact points (Fig.2) and crush (SAE J 1555) that occur during an accident, fuel system location and minimum crush distances around the fuel system can be specified to afford additional protection to the fuel system.

An Example Vehicle Configuration

The following is a potential vehicle configuration that would meet the design criteria previously discussed. The system includes a bank of compressed hydrogen fuel tanks surrounded by a fuel system compartment. The location of the fuel system, in the forward part of the trunk area, is consistent with both the desire to "vent upward" and provide adequate crush distances for protection during an accident. Placing the compressed gas cylinders in the forward part of the trunk still allows the tops of the containers to be located behind the rear window. This would allow upward venting to be accomplished by providing a panel above the containers that can be released if hydrogen is detected in the fuel compartment. The location at the front of the trunk provides a large crush distance between the fuel compartment and the rear bumper in case of an accident.

Applying these criteria to a 1992 Toyota Tercel, a storage system of 32; 4.35 inch OD compressed gas containers could be incorporated (Figure 3 and 4). The tank length is limited to 35 inches. The trunk would need to be lengthened 6.7 inches (Figure 5 and 6). The resulting vehicle would have an estimated range of 150 miles using 3000 psi storage pressure and 225 miles at 5000 psi storage pressure, assuming

0-60 MPH times of 11.2 seconds. The estimates are made from engine performance measured from operating hydrogen fueled engines in the IC Engines Lab at the University of Miami.

Sheet Metal Impingement

The vehicle configuration discussed above requires a fuel compartment to house the hydrogen fuel storage system (Figure 4). The compartment must be able to survive hydrogen flame impingement if hydrogen leaks and is ignited. An experimental study was conducted to investigate hydrogen flame impingement on vehicle body panels.

The testing began with an investigation of hydrogen flame impingement on a standard automobile fender (Photo 1). Hydrogen flow rate was initially 250 CFM. At the end of the test the vehicle fender was glowing visibly (Photo 2). Investigation after the fender returned to ambient temperature showed the paint at the center of the impingement area was barely oxidized but had a powdery consistency (Photo 3). The hydrogen jet contained a very rich mixture at the center of the impingement area and excluded oxygen from reaching the hot surface of the fender.

Testing continued with 4ft by 3ft sheets of cold rolled steel and higher flow rates of hydrogen. The tests with flat steel sheets showed that the peak temperature reached at the center of the sheet metal, during the burn, was a function of three parameters. They were hydrogen flow rate, distance between hydrogen source and the sheet steel, and the thickness of the sheet steel. The hydrogen flow rate during the test was a function of time. The flow rate decayed exponentially from an initial value of 1000 CFM to essentially 0 CFM. This is the behavior exhibited by a high pressure storage system breach. The volume of gas released in each test was 328 SCF of hydrogen.

Each test consisted of venting and igniting 328 SCF of hydrogen on a 3 ft by 4 ft sheet of cold rolled steel. Since the flow rate of hydrogen decreases throughout the test, the location of maximum flame temperature moves closer to the source with time. The rate of heat production also decreases throughout the test as hydrogen flow rate drops. Starting with a steel sheet test location far from the source, the peak surface temperature reached during the test initially increases as the test location is moved closer to the source. At locations far away from the source, the surface is far away from the location of maximum flame temperature for much of the burn and a lower peak temperature is reached. Moving closer, at some point the test location for highest peak surface temperature is reached. At locations closer to the source, than the location for highest peak temperature, the surface is shielded by the extremely rich core of the hydrogen jet. The rich mixture does not burn near the sheet but, after striking the sheet, is blown away from the surface by the rather high gas velocities from the hydrogen jet and burns at a point several inches away from the surface.

Figure 7 shows the temperature versus time plot for three tests, using 0.027 inch thick cold rolled steel, at 1.5, 2.0, and 3.0 feet from the hydrogen source. As can be seen the test location for maximum peak surface temperature is approximately 2.0 feet. These tests were all run by venting 328 SCF of hydrogen at an initial flow rate of 1000 CFM. The temperature measurements shown in figure 7 were made at the center of the flame impingement. For the sheets at a distance of 2 or 3 feet from the hydrogen source a much larger area of the sheet was heated during the early, high flow rate portion of the burn. This allowed a continuing temperature rise later in the burn that was not displayed in the data for 1.5 feet away from the hydrogen source. The continuing temperature late in the burn occurred as heat was transferred from the hottest portion of the sheet which was a ring around the center of impingement.

Figure 8 shows the temperature versus time plot for two steel sheet tests at 2.0 feet, with material thicknesses of 0.027 inch and 0.037 inch. The temperature profiles vary only slightly with material thickness. The 328 SCF of hydrogen vented during a test released 88,250 BTU's, calculated using the lower heating value of hydrogen. Since the entire sheet of 4ft by 3ft by 0.027 inch cold rolled steel could be heated to 1500 °F with 2,062 BTU's, it is apparent that the heat capacity represents a small portion of the total heat liberated by the burning hydrogen. The temperature rise in the steel sheet is principally the difference between the heat transfer into the impingement surface and the heat transfer out of the non-impingement surface. The heat transfer in and out of the steel sheet is virtually identical for both sheets and a small function of sheet thickness.

Photo 4 shows the initiation of the type of test just discussed. The hydrogen flow rate is 1000 CFM, the steel sheet is 0.027 inches thick, 4 ft by 3 ft, and at a distance of 2.0 feet from the hydrogen source. Photo 5 shows the sheet when the surface temperature in the center has reached 1500 °F. Photo 6 shows the sheet with the hydrogen flow interrupted in the middle of the test. The sheet is glowing, but it was not possible to "burn through" the sheet metal during these tests. The over rich portion of the hydrogen prevented large scale oxidation of the material and the peak temperatures were not high enough to simply melt the steel sheet. Radiation from the glowing 1500 °F surface was, however, sufficient to ignite some materials used in the interior of automobiles and potentially harm vehicle occupants.

In an effort to reduce the likelihood of occupant injury, a series of tests were conducted to investigate the feasibility of using a double layer of cold rolled steel sheet to prevent heat transfer through the firewall. Firewalls constructed from two layers of 0.027 inch thick sheet steel were tested. The first sheet withstood the hydrogen flame impingement and the second sheet acted as a radiation shield. The surface temperature of the second plate was significantly lower than the first unless the sheets came in contact with one another. Unfortunately, the first sheet tended to warp when the hydrogen flame impinged on it and it expanded. The sheet bowed away from the flame and therefore moved closer to the second sheet. The two sheets very often did come in contact and this negated the effectiveness of the second sheet as a radiation shield. Preventing contact, particularly in an vehicle accident scenario, involved a relatively complicated array of stand-offs and was deemed impractical.

Firewall Material Impingement

In an attempt to find a light weight, inexpensive material for lining and insulating the fuel compartment, a polypropylene fiber reinforced cement foam was tested. This material was tested under the same conditions as the steel sheet; 328 SCF of hydrogen vented and ignited with an initial 1000 CFM flow rate. Tests were run with 2 ft by 3 ft sheets of the cement foam with 1 ft by 3 ft steel sheets on either side to complete the standard 4 ft by 3 ft test section. Data for the test is shown in Table 3. The values for temperature rise during burn are measured on the non-impingement side of the cement foam during the hydrogen burn. The peak temperature rise was measured on the non-impingement side 15 to 20 minutes after the test when the cement foam sheet had reached equilibrium. The temperature rise measured was very small. An investigation of the material after the test showed that the polypropylene fibers had been melted to only a depth of 0.075 inch.

Table 3 - Temperature Rise versus Material Thickness

Material Thickness	Temperature Rise During Burn	Peak Temperature Rise
2.0 inch	4.2 ⊕F (2.6 ⊕C)	24.6 #F (13.7 #C)
1.5 inch	4.6 #F (2.6 #C)	30.6 ⊕ F (17.0 ⊕ C)
1.0 inch	5.3 ⊕F (2.9 ⊕C)	35.8 ⊕ F (19.9 ⊕ C)

Vehicle Test

The full-scale fuel system leak test consisted of releasing and igniting the contents of a compressed hydrogen fuel system. This experiment was a simulation of a fuel system breach that released hydrogen at the bottom of the fuel system compartment. 984 SCF of hydrogen was released at an initial flow rate of approximately 3000 CFM (Photo 7). A 1986 Mercury Cougar was chosen for the experiment. The choice of vehicle was not critical. The 1986 Cougar had, however, a vertical rear window which presents an approximate worst case for heat transfer into the passenger area. The hydrogen was released inside a prototype fuel system container mounted in the trunk area of the test vehicle (Photo 8). The fuel system container was designed to include a fire wall on all sides of the compressed hydrogen gas fuel tanks. The fuel system container was constructed of 0.027 inch thick steel sheet and lined with 0.5 inch thick polypropylene fiber reinforced cement foam to provide an effective fire wall. Figure 9 shows the placement of the fuel system container in the test vehicle. Thermocouples were placed inside the passenger area and in the trunk area. The temperature at each thermocouple location was recorded with a National Instruments DACPad data acquisition system. The highest temperature (145 °F) was reached on the sheet metal which forms the trunk lid just behind the fuel compartment (Figure 10). The temperature at the top of the rear window (Figure 10) almost reached 145 °F. The heating at the top of the rear window occurred late in the burn when the hydrogen flow rate had diminished to the point that wind (from the rear of the vehicle) was able to redirect the flame toward the rear window (Photo 9).

Weight and cost of the fuel compartment are critical design criteria. The weight of the fuel compartment for the previously discussed 1992 Toyota Tercel would be 31.6 pounds for the sheet metal for the fuel compartment and 42.0 pounds for the polypropylene fiber reinforced cement foam. This assumes the foam is 0.5 inches thick as it was during the testing for this work. Investigation of cross sections of the foam after testing have led to the conclusion that the foam thickness could probably be reduced 70%. This would mean a foam thickness of 0.15 inch. The weight of the foam would be reduced from 42.0 pounds to 12.6 pounds and the cost would be reduced from \$4.80 to \$1.44.

Conclusions

- I. The same terminology may take on different meaning in different safety publications. Care needs to be taken when comparisons are made between various safety publications.
- II. Minor differences exist in the fuel specifications for natural gas in existing publications.

- III. Safety publications presently deal with natural gas and hydrogen in the same manner.
- IV. Four areas of potential concern exist in the conversion of natural gas safety publications to hydrogen safety publications. They are:
 - 1. The use of odorants
 - 2. Ignition by static electricity
 - 3. Conversion of natural gas leakage rates to hydrogen leakage rates
 - 4. Conversion of natural gas permeation rates to hydrogen permeation rates
- V. Fuel delivery systems used for natural gas can be used as guidelines for hydrogen fuel delivery systems.
- VI. Two additional design criteria are suggested for hydrogen. They are:
 - 1. Vent upward
 - 2. Restrict hydrogen container vehicle location.
- VII. Light weight, low cost firewalls to resist hydrogen flame impingement can be designed.

Acknowledgements

The authors would like to thank the Department of Energy without whose support this work could not have been conducted.

References

Lewis, B., and von Elbe, G., 1987, Combustion, Flames and Explosions of Gases, Harcourt Brace Jovanovich, Publishers, Academic Press, Inc., Orlando FL.

Swain, M.N., and Swain, M.R., "Fuel Gas Permeability of Non-Metallic Pipes", ASME Paper for ASME Winter Annual Meeting, Anaheim, California, November 8-13, 1992.

Summary Proceedings: Hydrogen Safety, Codes and Standards, A Workshop Presented by the National Hydrogen Association, June 26-28, 1995, Hilton Head, South Carolina

Internet Web Page: http://www.metc.doe.gov/research/power/fc syste.html

Safety Publications

AGA requirements No. 1-85 "Natural Gas Vehicle (CNG) Conversion Kits"

ANSI/AGA NGV1-1994 "Compressed Natural Gas Vehicle (NGV) Fueling Connection Devices"

ANSI/AGA NGV2-1992 "Basic Requirements for Compressed Natural Gas Vehicle (NGV) Fuel Containers"

ANSI/CGA standard V-9, 1991 "Standard for Compressed Gas Cylinder Valves"

ANSI/NFPA 30A "Automotive and Marine Service Station Code" 1990 Edition

ANSI/UL 429-1983 "Standard for Electrically Operated Valves"

API 2003-Fifth Edition, Dec 1991 "Protection Against Ignitions Arising Out of Static, Lightning, and Stray Currents"

ASME Boiler and Pressure Vessel Code Section VIII

ASTM A213/A213M-92 "Standard Specifications for Seamless Ferritic and Austenitic Alloy-Steel Boiler, Superheater, and Heat-Exchanger Tubes"

ASTM A47-90 "Standard Specification for Ferritic Malleable Iron Castings"

ASTM A105/A105M-92 "Standard Specifications for Forgings, Carbon Steel, for Piping Components"

ASTM A106-91 "Standard Specifications for Seamless Carbon Steel Pipe for High-Temperature Service"

ASTM A182/A 182M-92a "Standard Specifications for Forged or Rolled Alloy-Steel Pipe Flanges, Forged Fittings, and Valves and Parts for High-Temperature Service"

ASTM A216/A216M-89 "Standard Specifications for Steel Castings, Carbon, Suitable for Fusion Welding, for High-Temperature Service"

49 CFR 171.8 "Definitions and Abbreviations"

49 CFR 172 "Hazardous Materials Table, Special Provisions, Hazardous Materials Communications, Emergency Response Information, and Training Requirements"

49 CFR 172.101 "Purpose and Use of Hazardous Materials Table"

49 CFR 173.34 "Qualification, Maintenance, and Use of Cylinders"

49 CFR 173.115 "Class 2, Divisions 2.1, 2.2, and 2.3 - Definitions"

49 CFR 393 Subpart E "Fuel Systems"

CGA NGV1-1994 "Compressed Natural Gas Vehicle (NGV) Fueling Connection Devices"

CGA P1-1991 "Safe Handling of Compressed Gases in Containers"

CGA S1.1-1989 "Pressure Relief Device Standards Part 1 - Cylinders for Compressed Gases"

NFPA 50A "Gaseous Hydrogen Systems at Consumer Sites" 1989 Edition

NFPA 50B "Liquified Hydrogen Systems at Consumer Sites" 1985

NFPA 51 "Oxygen-Fuel Gas Systems for Welding, Cutting, and Allied Processes" 1992 Edition

NFPA 52 "Compressed Natural Gas (CNG) Vehicular Fuel Systems" 1992 Edition

NFPA 55 "Compressed and Liquified Gases in Portable Cylinders" 1993 Edition

NFPA 58 "Standard for the Storage and Handling of Liquified Petroleum Gases" 1989 Edition

NFPA 59 "LP-Gases at Utility Gas Plants" 1992 Edition

NFPA 68 "Guide for Venting of Deflagrations" 1994 Edition

NFPA 77 "Recommended Practice on Static Electricity" 1988 Edition

SAE J 512 June 94 2:22.06 "Automotive Tube Fittings"

SAE J 985 Oct 88 3:34.113 "Vision Factors Considerations in Rear View Mirror Design"

SAE J 1231 June 93 2:22.170 "Beaded Tube Hose Fittings"

SAE J 1297 March 93 1:12.77 "Alternative Automotive Fuels"

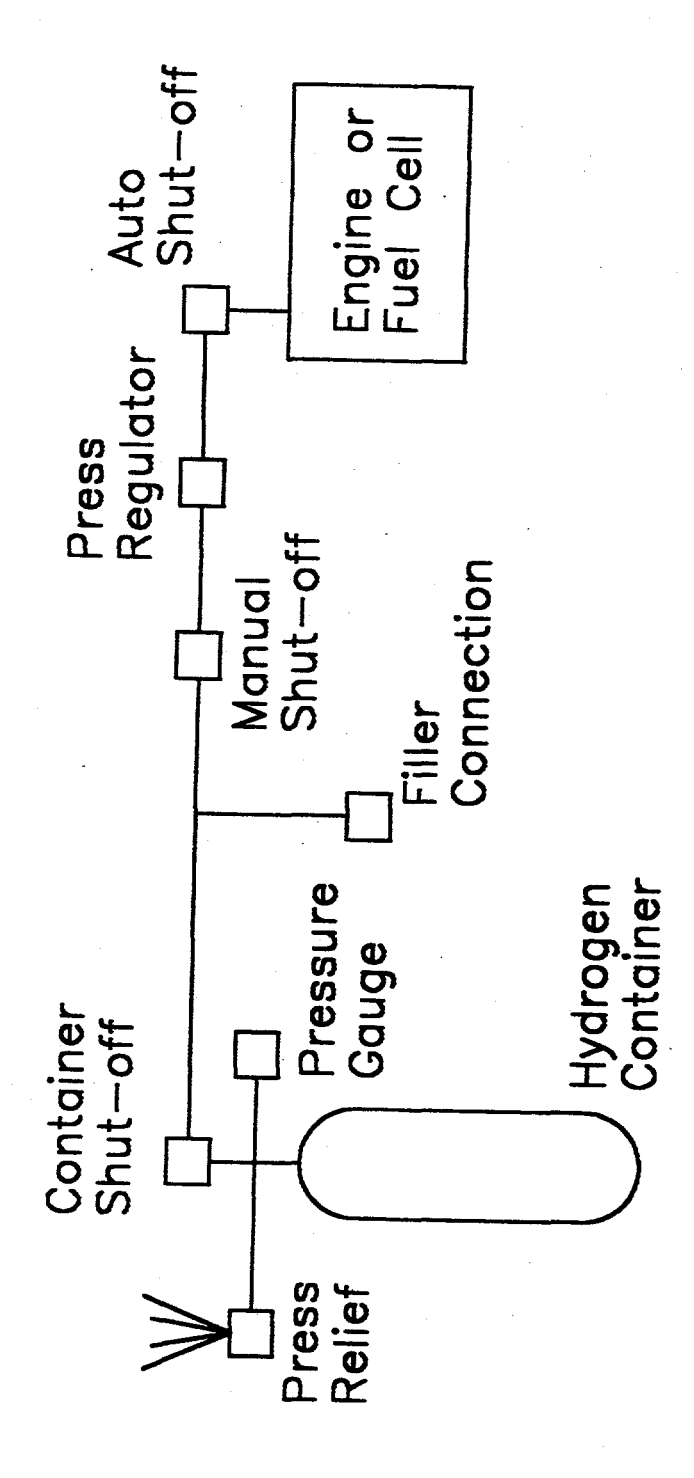
SAE J 1555 Oct 93 3:42.16 "Recommended Practice for Optimizing Automobile Damageability"

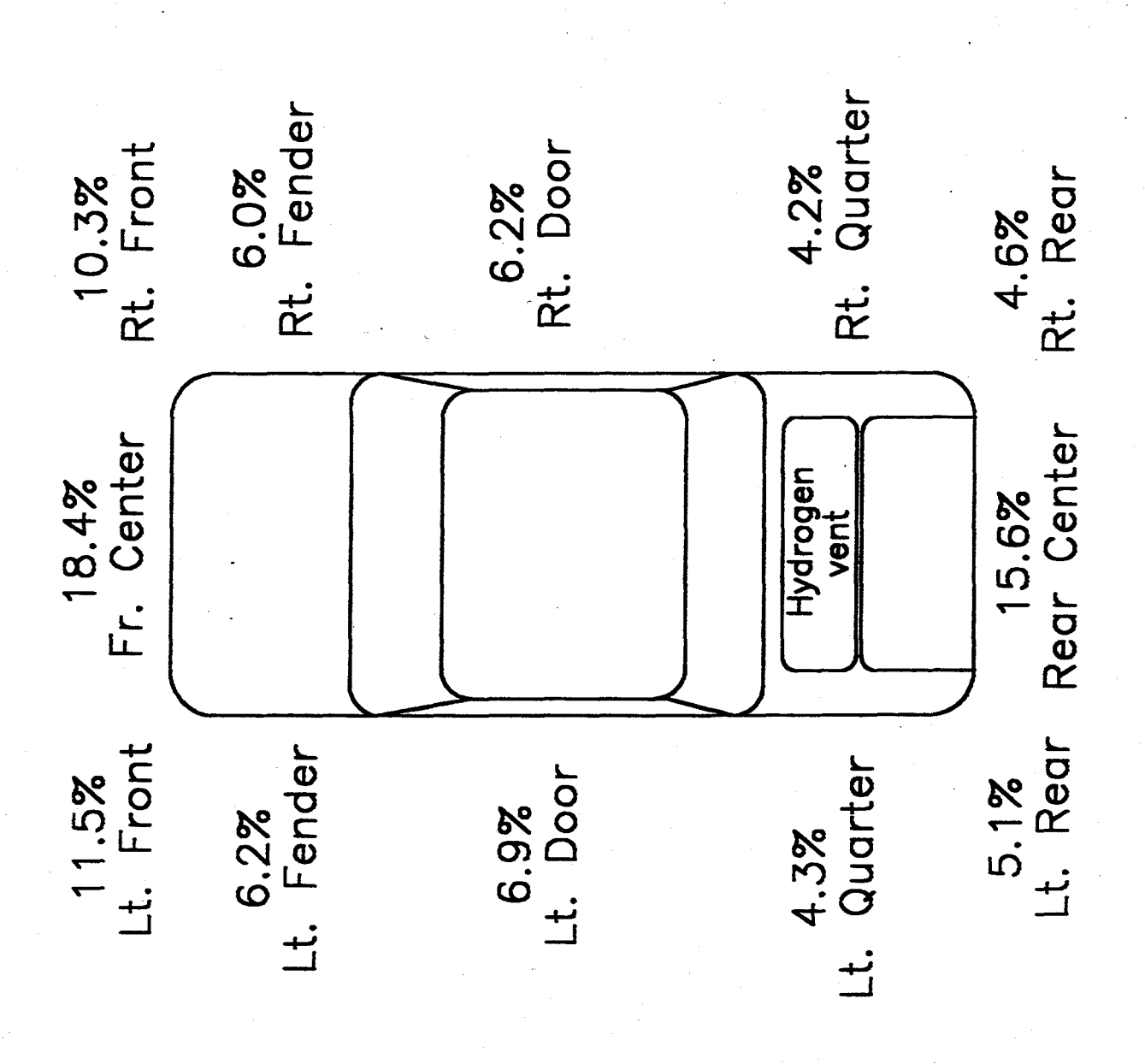
SAE J 1616 Feb 94 1:12.83 "Recommended Practice for Compressed Natural Gas Vehicle Fuel"

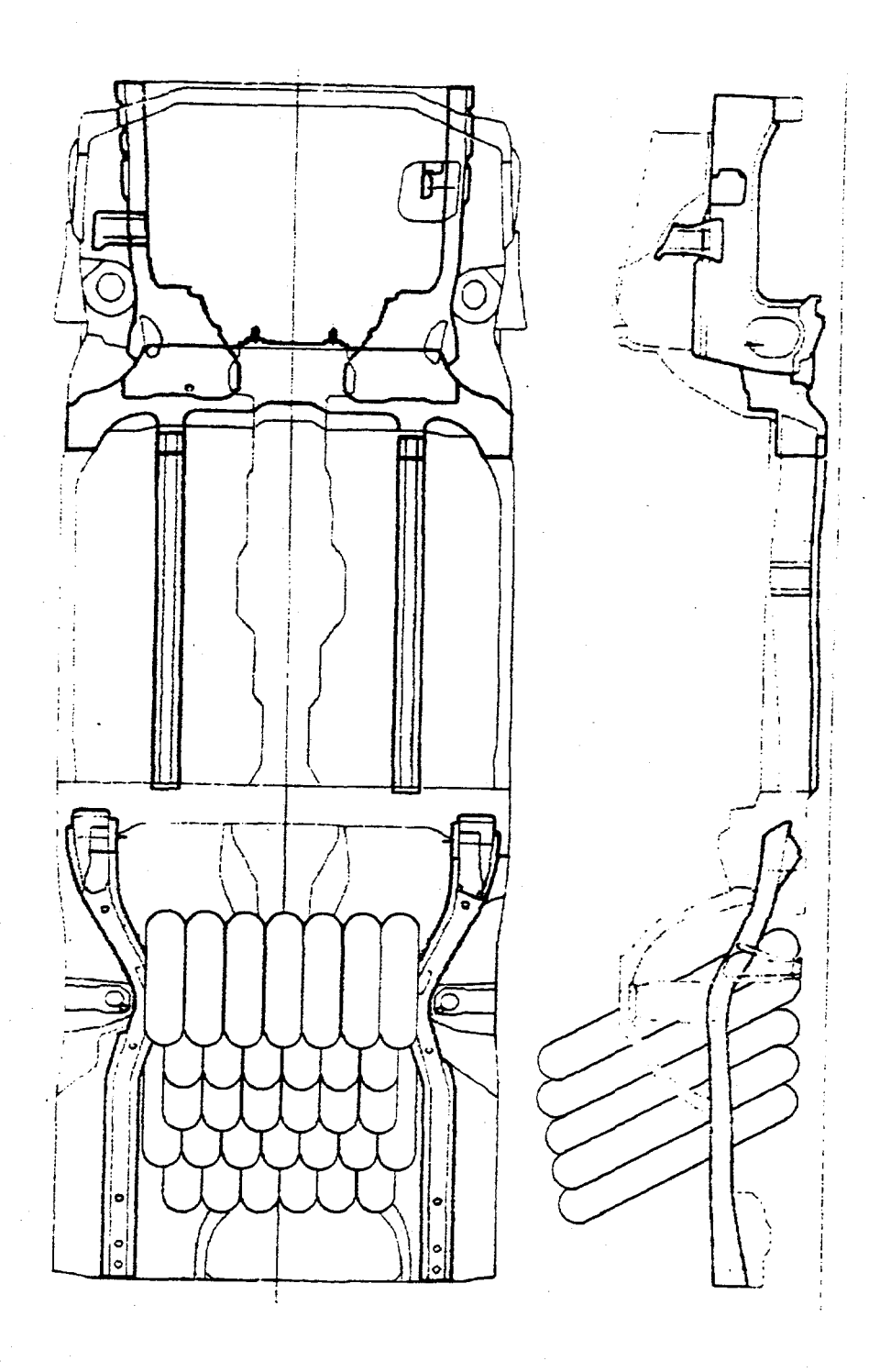
UL 252 "Compressed Gas Regulators"

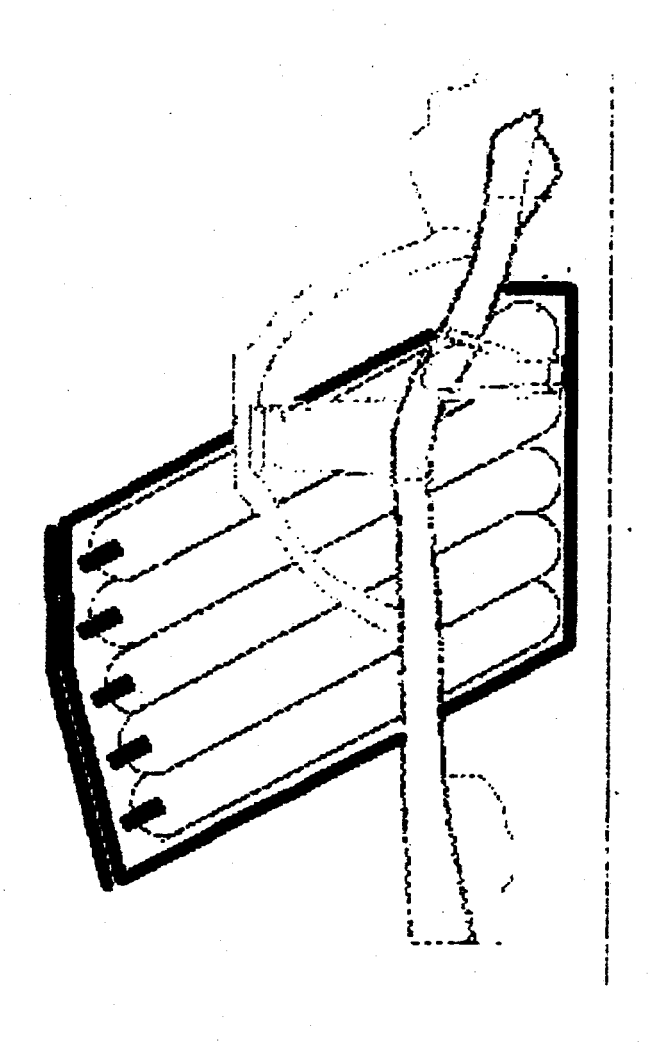
UL 404 "Gauges, Indicating Pressure, for Compressed Gas Service"

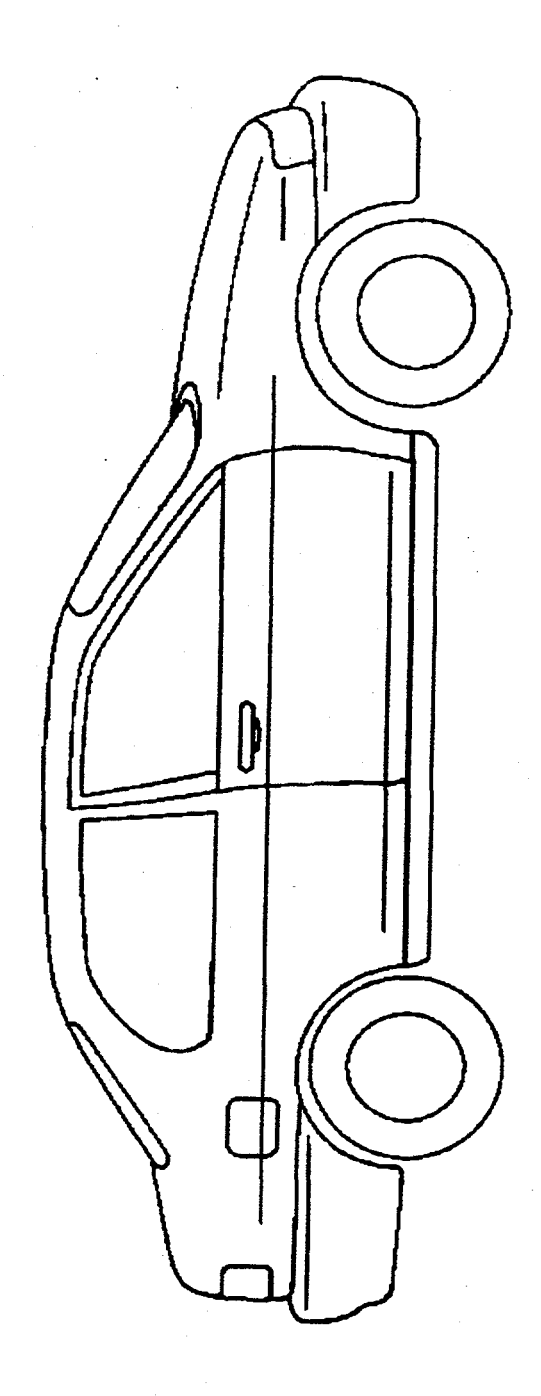
- Figure 1 Schematic of Fuel System
- Figure 2 Distribution of Collision Impact Point Locations
- Figure 3 Cut Away of Hydrogen Vehicle
- Figure 4 Hydrogen Fuel Compartment
- Figure 5 Unconverted Gasoline Vehicle
- Figure 6 Hydrogen Powered Vehicle
- Photo 1 250 CFM Hydrogen Impingement on Fender
- Photo 2 Fender Partially Glowing
- Photo 3 Fender After Returning to Ambient Temperature
- Figure 7 Temperature as a Function of Distance to Hydrogen Source
- Figure 8 Temperature as a Function of Sheet Steel Thickness
- Photo 4 1000 CFM Hydrogen Impingement on Sheet Steel
- Photo 5 Sheet Steel at 1500 °F
- Photo 6 Sheet Steel with Hydrogen Flow Interrupted
- Photo 7 3000 CFM Hydrogen Leak from Bottom of Fuel Compartment
- Photo 8 Fuel Compartment after Testing
- Figure 9 Location of Fuel Compartment in Test Vehicle
- Figure 10 Temperature at Two Locations on Test Vehicle
- Photo 9 Hydrogen Flame Near End of Testing

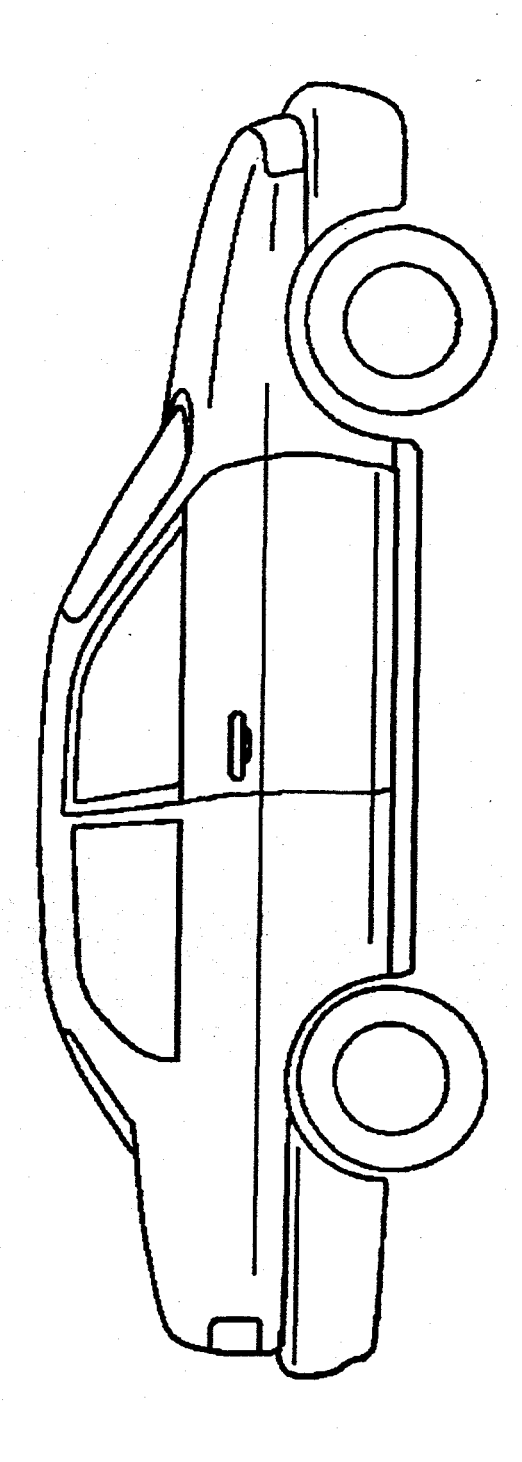






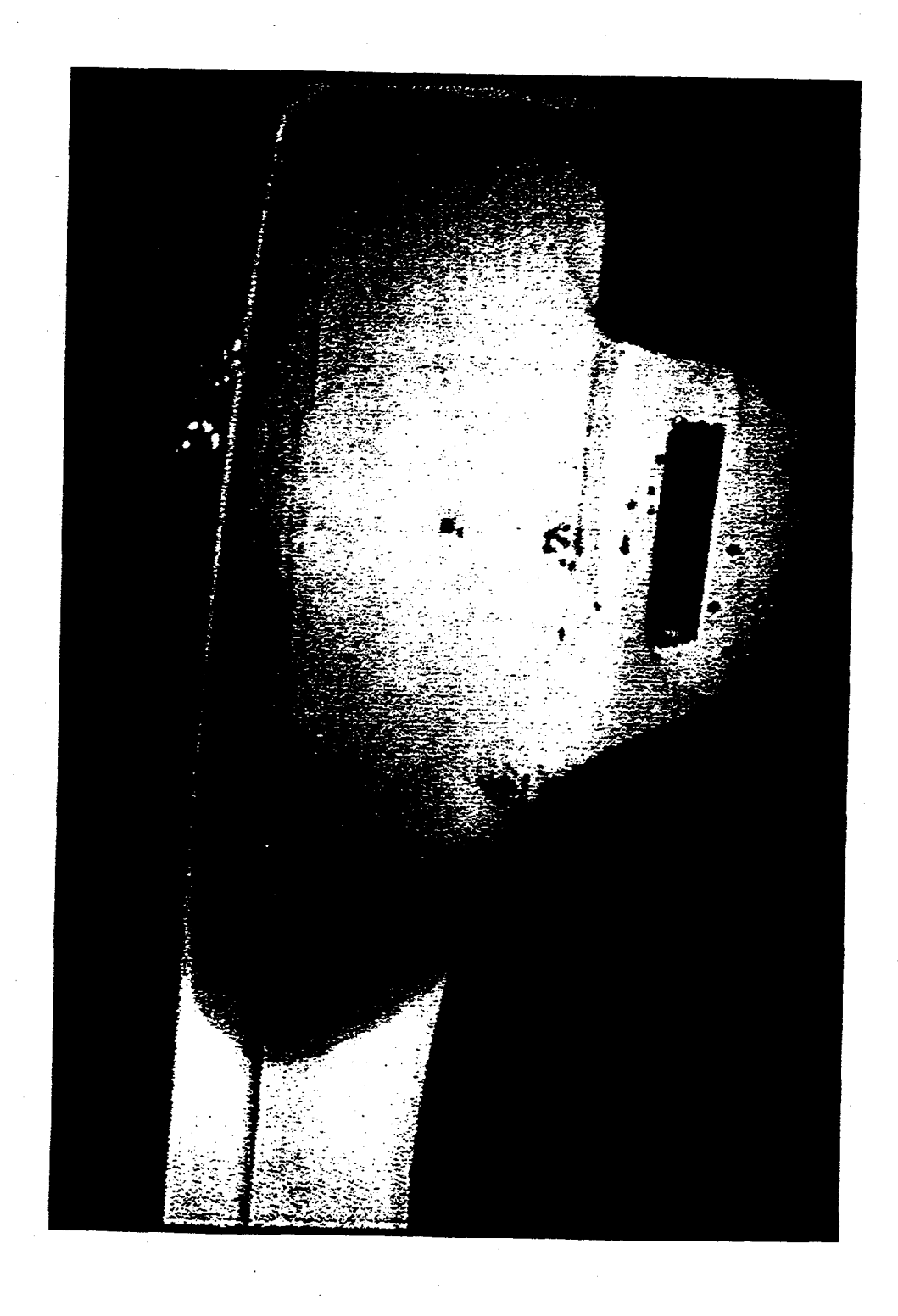


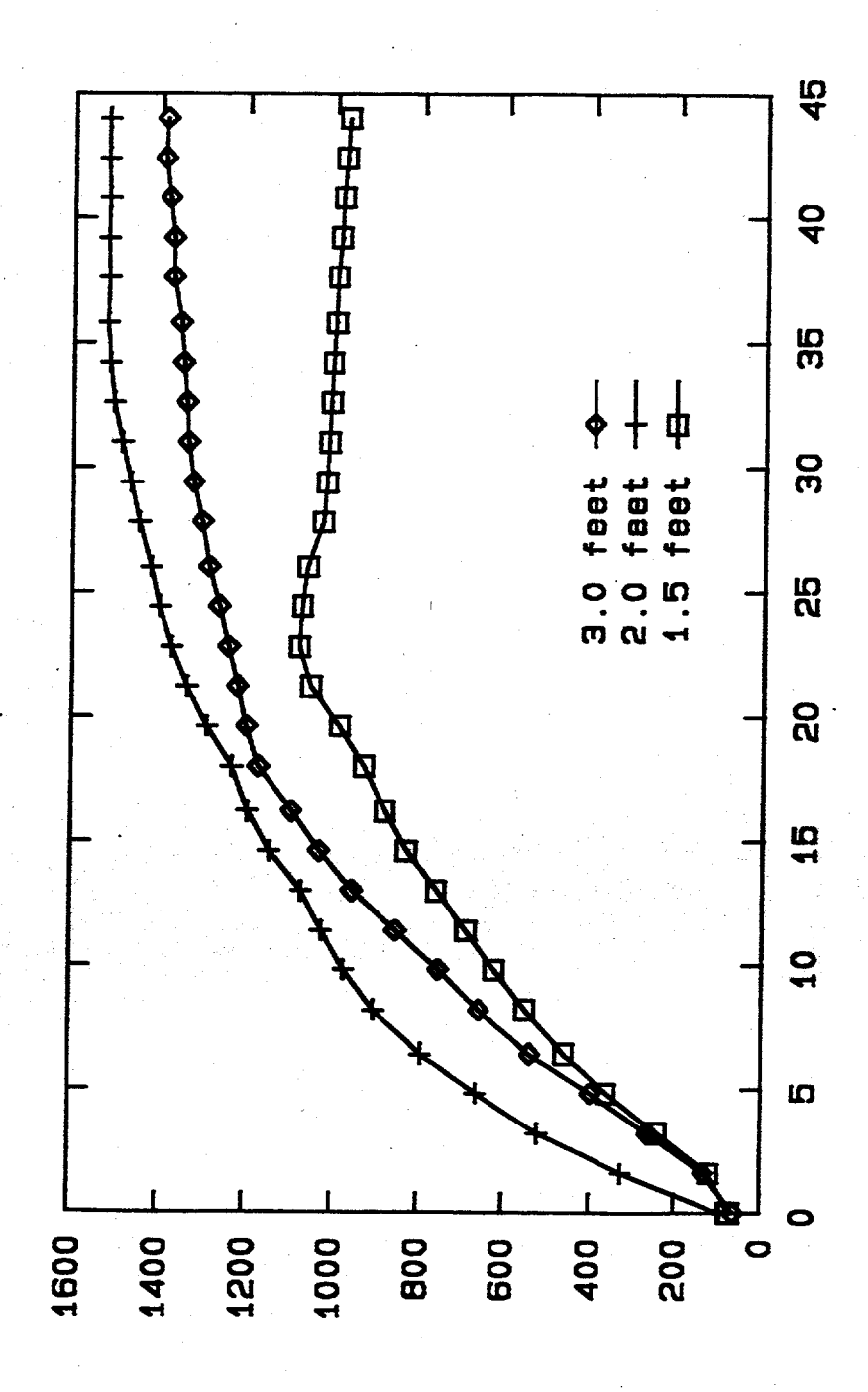


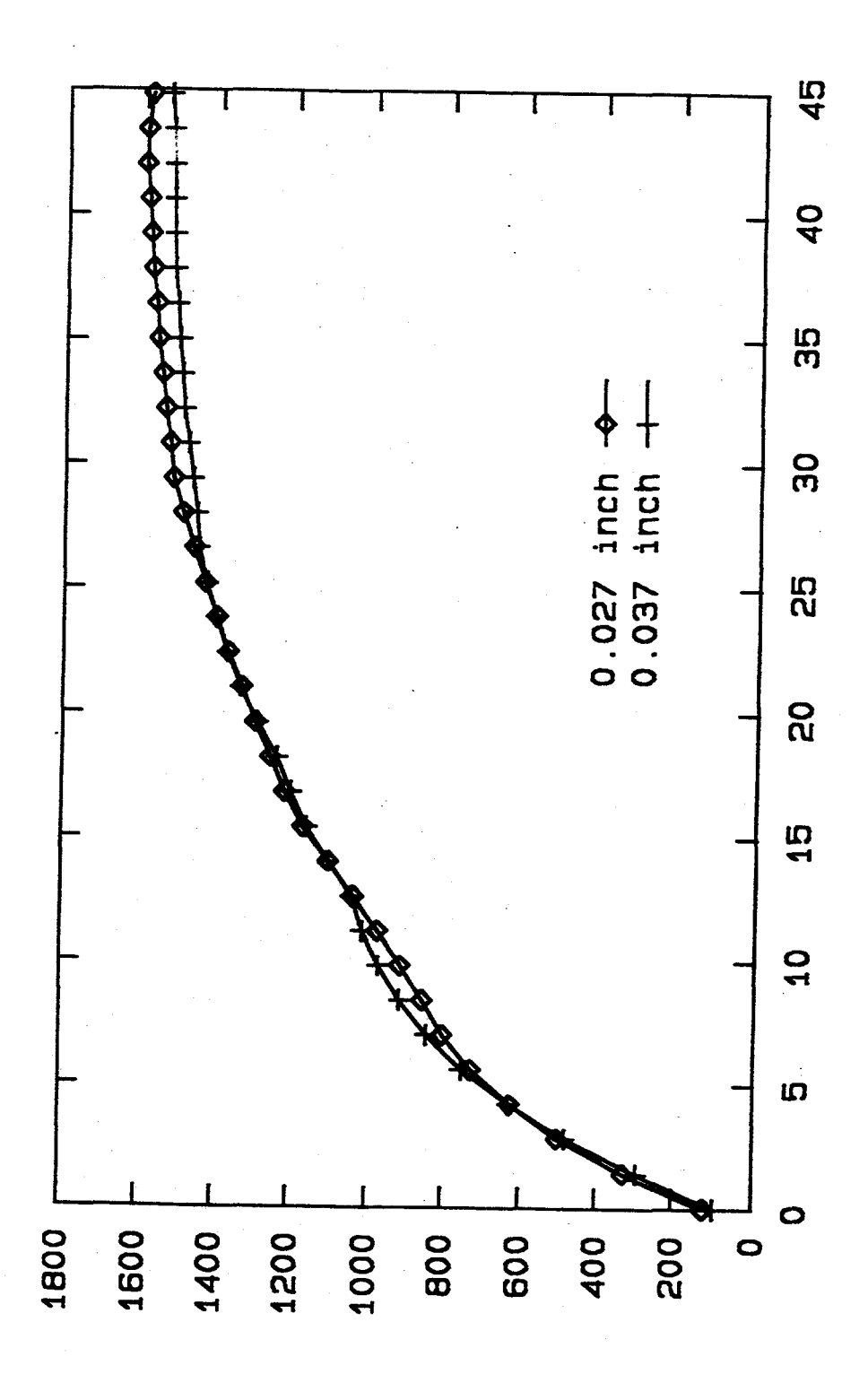


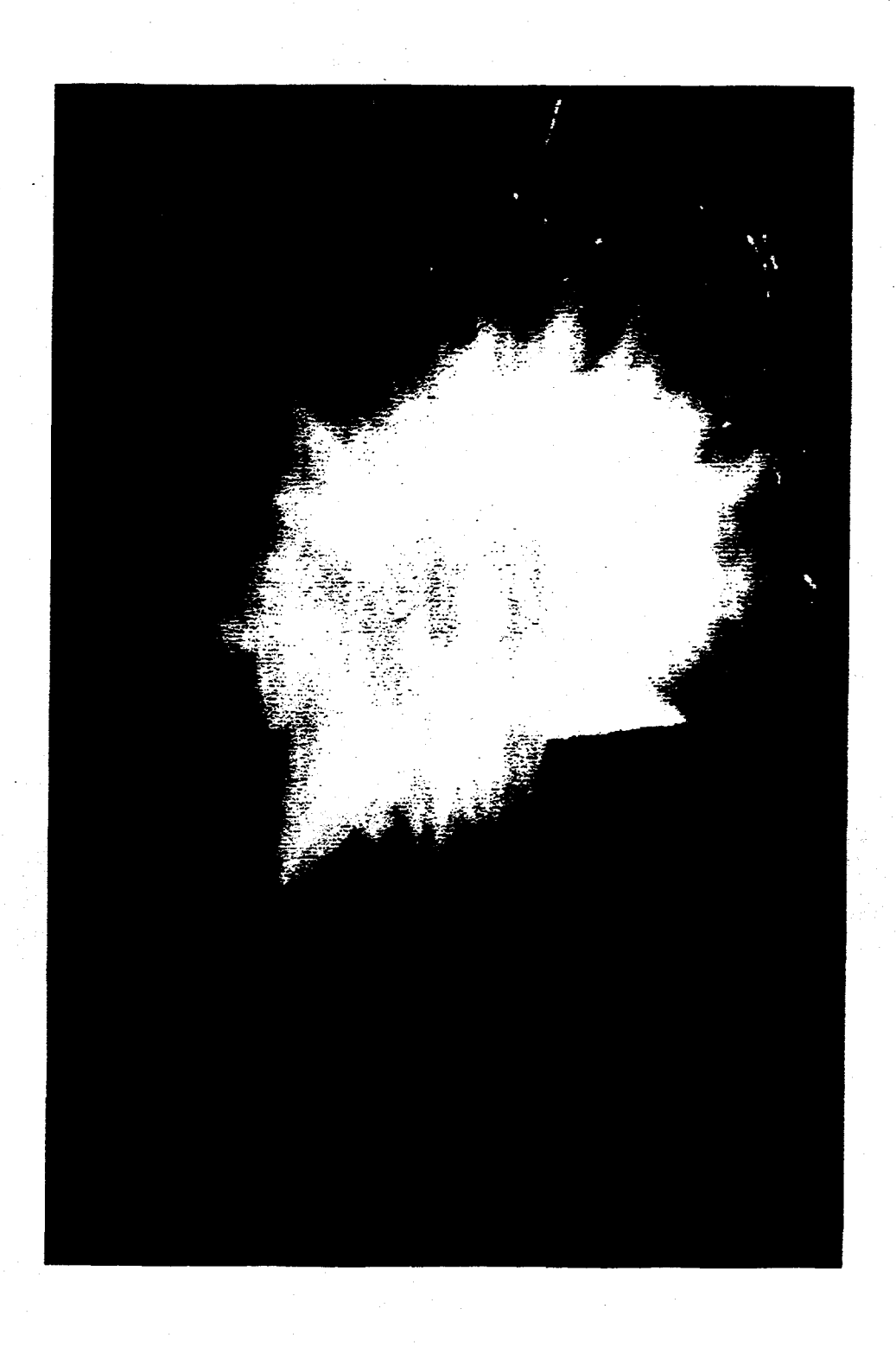


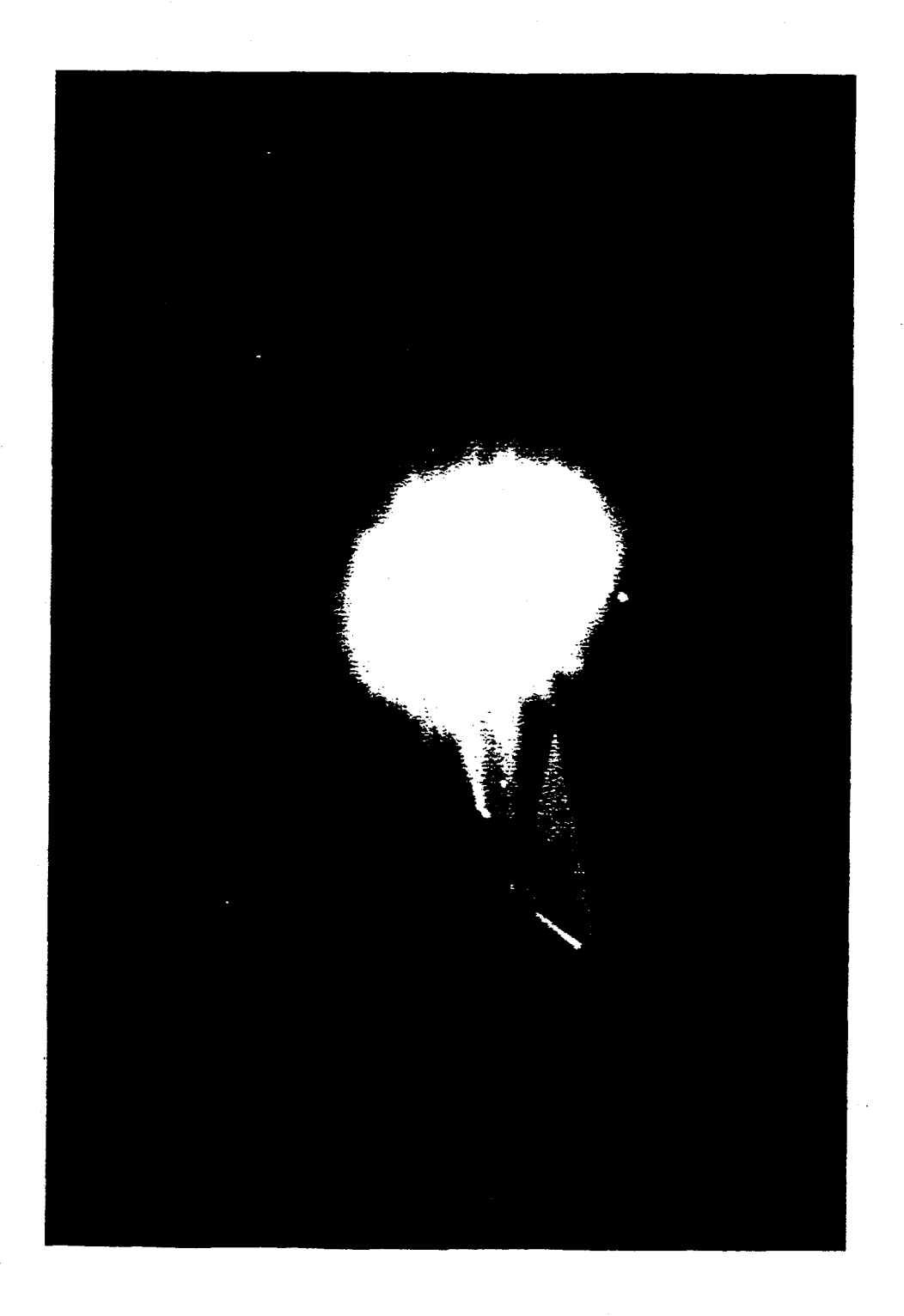


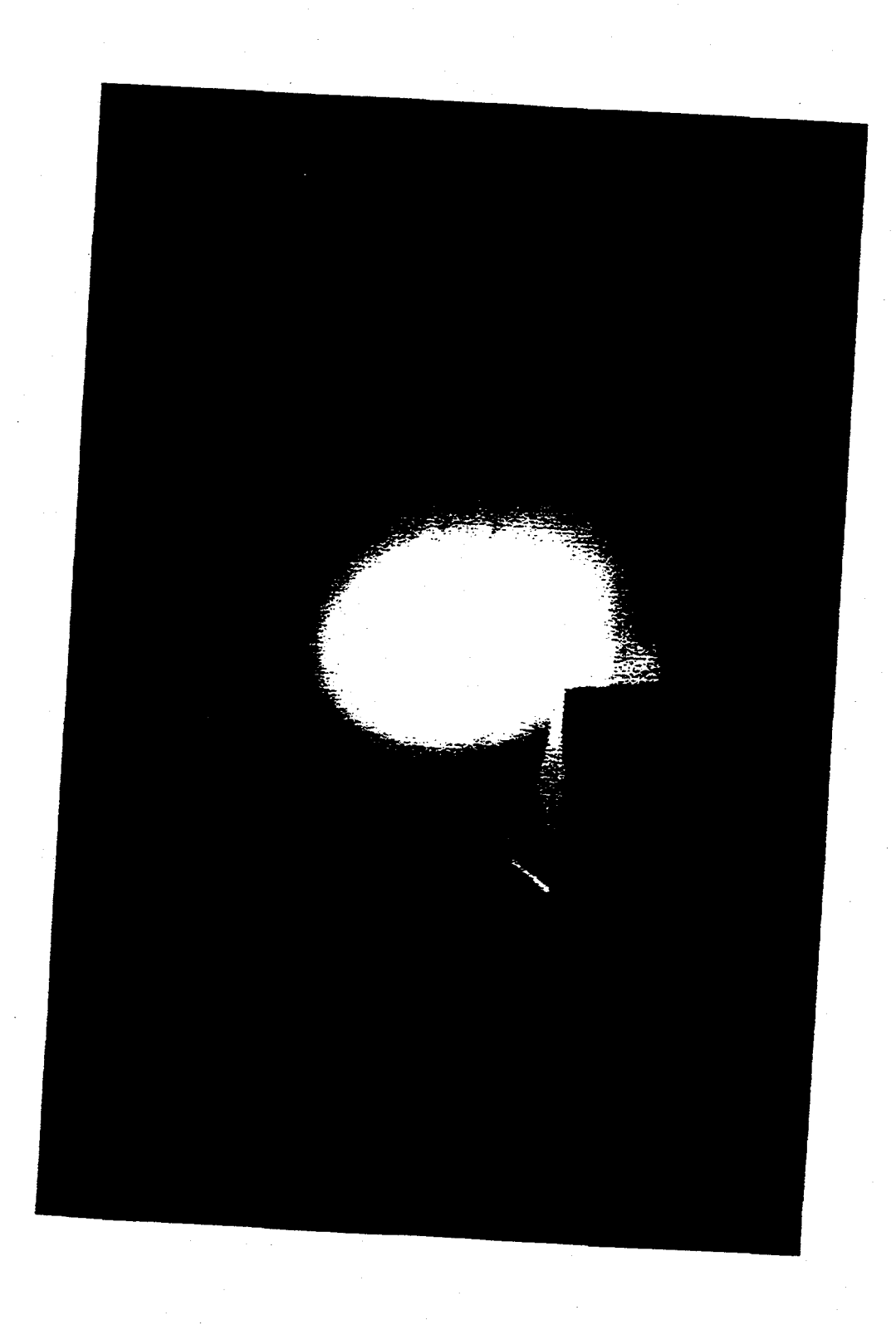


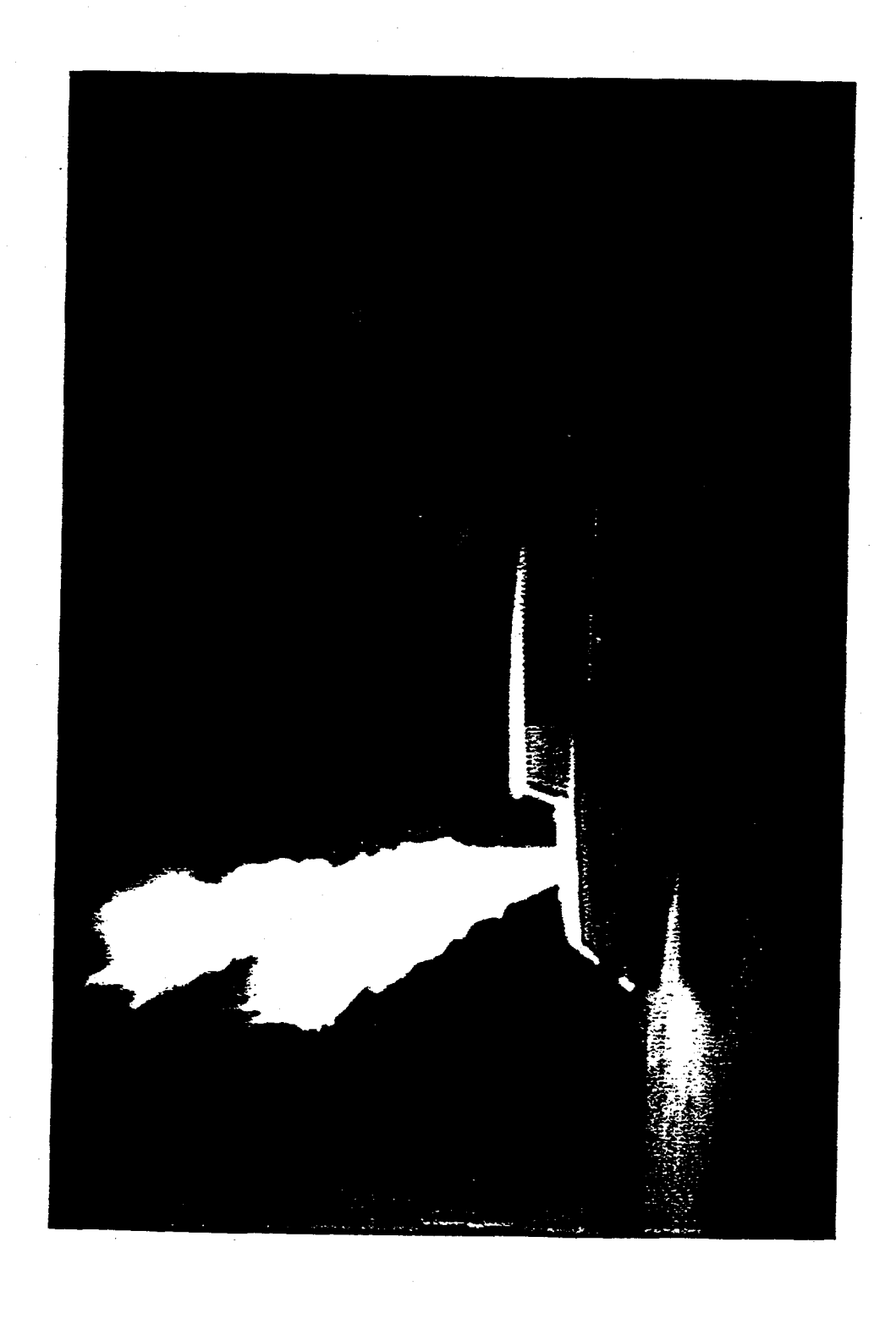




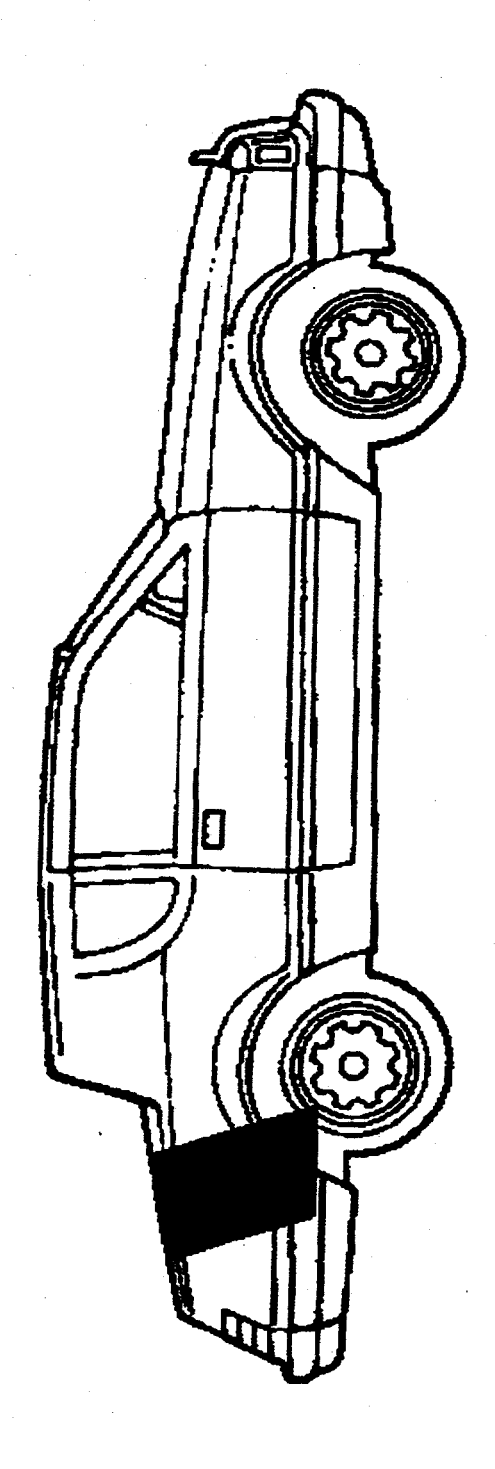


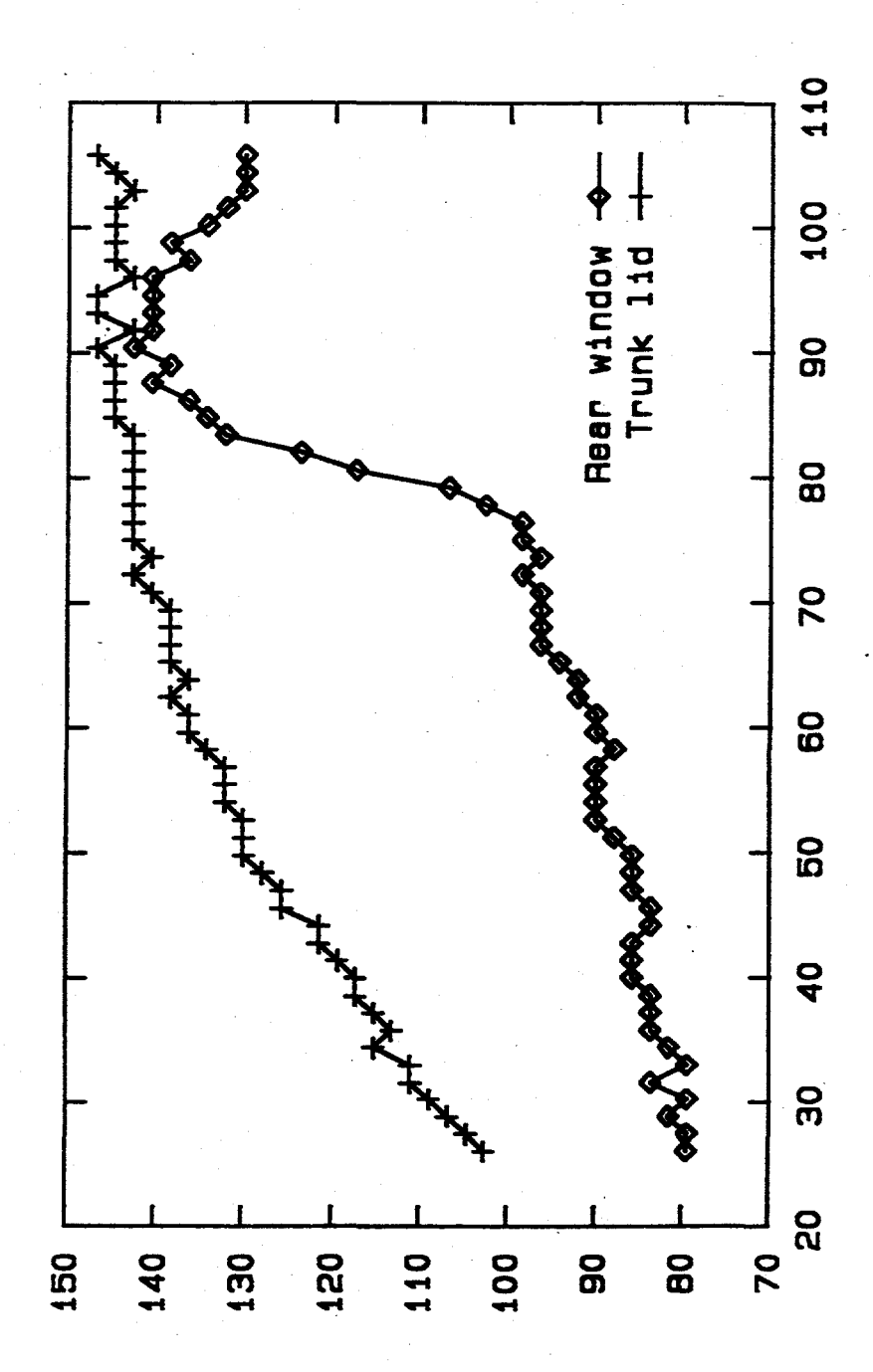














DESIGN AND DEVELOPMENT OF A LOW-COST FIBER-OPTIC HYDROGEN DETECTOR

David K. Benson, C. E. Tracy and Clemens Bechinger National Renewable Energy Laboratory Golden, Colorado 80401

Abstract

A cost-effective detector for hydrogen gas leaks will be needed in many hydrogen-fueled technologies of the future. In particular, the hydrogen-fueled automobile may require hydrogen leak sensors in several locations and their cost could be prohibitive if conventional sensor technology is used. This project is directed at the development of low-cost fiber-optic (FO) hydrogen gas detectors that could provide adequate sensitivity, response speeds and reliability in an automobile application. The FO sensor relies upon a reversible chemical reaction between gaseous hydrogen in air and a thin film of tungsten oxide. The initial sensor design consists of a thin tungsten oxide film coating on the flat end of a polymer or glass optical fiber. A very thin overcoating of palladium catalyzes the reaction between the hydrogen and the tungsten oxide and reflects a light beam back along the optical fiber to a light intensity monitor. When the hydrogen reacts with the coating, the tungsten oxide becomes optically absorptive and attenuates the reflected light. The sensitivity and response speed of this sensor were studied over a range of temperatures and found to be too slow for the intended application. A new, faster sensor design was invented that relies upon the resonant absorption of light at a beveled facet on the end of the optical fiber. The resonance occurs when the incident light strikes the metal coated facet at an angle just above the critical angle for total internal reflection. The evanescent wave stimulates resonant absorption by free electrons in the metal to produce a so-called surface-plasmon (SP). An overcoat of thin tungsten oxide on top of the metal film is designed to provide an optical wave-guide for light at the surface plasmon resonance. The two layer coating produces a coupled resonance at the SP wavelength that is very sensitive to the optical constants of the tungsten oxide. When hydrogen reacts with the tungsten oxide the resonance frequency shifts and this shift is detected in the spectrum of the reflected light beam. The facets are angled at 45 degrees to the fiber axis so as to reflect the light back along the fiber with a doubling of the SP absorption from the double reflection. A facet perpendicular to the fiber axis produces a reflected signal that is

not affected by hydrogen that is used as to produce an internal reference signal for comparison to the resonance, hydrogen-sensitive signal. The ratio of these two signals cancels out noise due to variation in the transmittance of the optical fiber. A patent application has been filed for this new design and a small business partner has formed a CRADA with NREL to develop a commercial detector based upon it.

The Concept

A cost-effective hydrogen gas detector is needed wherever a hydrogen leak can pose a safety hazard. Since hydrogen is not toxic, the purpose of the detector is to provide warning before a hydrogen concentration approaches the lower deflagration limit, about 4% in air. A high sensitivity is probably not needed.

A fiber-optic (FO) hydrogen gas detector has some potential advantages over conventional detectors that use hydrogen sensitive semiconductor and metal film resistors. The FO detector can be deployed over distances without electrical wiring. Since the hydrogen sensor signal is communicated optically, it is not susceptible to electromagnetic interference and does not extend an electrical energy source to the site of the potential hydrogen leak where an electrical fault could cause ignition. In cost-sensitive applications such as hydrogen-fueled automobiles, the lower costs of a FO hydrogen detector may be important. The initial cost of optical fibers may be less than copper wires and the cost burden during recycling of the vehicle may be less with optical fibers than with copper wires. This last feature is of growing importance as the automobile industry becomes financially responsible for the vehicle from "cradle to grave". Removing copper wiring from a vehicle chassis before remelting the steel scrap is a significant cost, partially avoided if glass or polymer optical fiber is used instead of copper wiring. If the copper is not removed, the quality and value of the scrap steel is compromised.

The FO sensors we have studied consist of a thin film coating on the end of the fiber. This coating reacts reversibly with hydrogen gas in air and undergoes a change in its optical properties. A light beam from a central source reflects from the coating and returns to a centrally located light detector. Changes in the character of the reflected optical beam signal the presence of hydrogen gas at the sensor end of the optical fiber. An electrical signal from the light detector is processed and used to activate appropriate safety measures. A central light source may be used for several FO sensors, but each individual sensor requires a dedicated light detector to monitor its response.

Approach

Three different designs for a FO sensor were explored and a new, improved design was invented. Initially, we evaluated the design of Ito (Ito 1984). This sensor consists of a thin film of amorphous tungsten oxide applied to the polished, flat end of the fiber plus a thin reflective overlay of palladium (Fig.1). When the coating is exposed to hydrogen gas, some of the hydrogen adsorbs and reacts with the palladium to form a solid solution of hydrogen in palladium (or a palladium hydride at higher concentrations), some of the atomic hydrogen diffuses through the palladium and reacts with the

tungsten oxide. An insertion compound, nominally H_xWO_{3-y} , is formed with x varying up to about 4, depending upon the concentration of the hydrogen in the air. The hydrogen insertion is accompanied by the introduction of reduced valence states, W^{+5} and W^{+4} in the H_xWO_{3-y} . Optical excitation of electrons between these reduced valence state tungsten ions causes a broad absorption band between about 400 and 1300 nm. Consequently, light in this wavelength range is attenuated when reflected from the coating if the sensor is exposed to hydrogen gas. When hydrogen gas is removed, the inserted hydrogen leaves the H_xWO_{3-y} spontaneously through the palladium film and is oxidized to water in the air. The intensity of the reflected light beam is the signal used to monitor the hydrogen sensor. This sensor design was studied for its sensitivity and kinetics over a range of temperatures as described in the Results section below. We discovered that this design had too slow a response time to be useful in critical safety applications.

A potentially faster, simpler detector design was also examined briefly. This design makes use of the thin palladium film alone as the hydrogen sensor coating (Butler 1991). The reaction with the hydrogen changes the optical reflectance of the palladium film enough to make a suitably sensitive sensor. However, much of the change in reflectance is due to expansion of the palladium as it forms a hydride. This expansion distorts the film into an "orange peal" texture that is not very reproducible and eventually causes the film to flake off the optical fiber.

Another configuration using a palladium film was also considered. This design is more sensitive and uses a thinner film that is less susceptible to flaking. In this design the palladium is placed on the face of a glass prism and the light beam is directed through the prism so as to reflect internally back into the prism from the palladium film (Sadowski 1994). At any wavelength there is a certain angle (somewhat larger than the critical angle for total internal reflection at the glass-air interface) at which the electric field of the incident light wave excites a resonance response in the free-electron cloud of the metal. This is called a surface plasmon (SP) resonance (Sambles 1991). At this resonance condition, the energy of the p-polarized portion of the light beam is transferred to the metal and dissipated as heat or re-radiated into the air. Whenever the electrical characteristics of the metal are changed, as for example by absorption of hydrogen, the conditions for this resonance change. The shift in the resonance condition can be detected quite sensitively in a number of ways. Unfortunately, this configuration is not very selective and detects any adsorbed gas including carbon dioxide and even helium about as well as hydrogen.

A new detector design was invented that also uses a SP resonance effect, but with a configuration that is less sensitive to adsorbed gases. In this new configuration, the resonance condition is affected by the bulk optical property changes in a tungsten oxide film overlying a thin metal film. The thin metal film is chosen to create the coupling condition between the light beam and the dielectric tungsten oxide film. The tungsten oxide film thickness is chosen so that a so-called "guided wave" is produced at the critical SP resonance wavelength of the light (Raether 1988). The guided wave propagates along the film, reflecting many times from both surfaces before being dissipated. In its many traverses of the tungsten oxide film, it interacts with the full thickness of the film many times. Consequently, the resonance condition of this sensor design is dominated by the bulk of the tungsten oxide and is most strongly affected by changes in the film as, for example, when it reacts with hydrogen gas.

A generic problem with the FO sensors was also discovered. Whenever the optical fiber is bent or subjected to a significant temperature gradient, its light transmission decreases. Whenever the connectors connecting the optical fiber to the light source or to the sensor head are shocked, their light transmission may change. These spurious changes in light transmission could superimpose a severe noise background upon the hydrogen detector, particularly in a moving vehicle.

In our new sensor design, we have introduced a way to create a reference beam that reflects from the sensor back along the optical fiber to a separate light detector. This reference beam is not significantly affected by the presence of hydrogen, but it is affected by any changes in the transmission of the optical fiber and connectors in exactly the same way as is the reflected light beam that carries the hydrogen signal to its separate, second light detector. By taking the ratio of the two light detector signals, we cancel out the noisy, changing fiber transmission and preserve a signal that changes only in response to the presence of hydrogen.

The combination of the guided wave SP and the reference beam into a detector was novel enough that we were encouraged to file a patent application for the new design.

Experiments

Measurements of the sensitivity and speed of sensors were made in an ultra-high vacuum system used to provide precise pressures of mixed gases (Fig. 2). This apparatus was adapted from an unrelated earlier project. The gas pressure is measured with cold-cathode ion-gages and capacitance manometers that are calibrated against a built-in spinning-rotor gage. A differentially pumped residual gas analyzer with controllable pressure-drop orifice allows mass-spectrometric analysis of gases over a very wide range of pressures. Hydrogen is provided on demand from an electrolytic hydrogen generator. Other gases are supplied from compressed cylinders. Gases are mixed in a separate chamber before admission to the sample.

The sample chamber (Fig. 3) is a stainless-steel vacuum cross with small sapphire windows through which light from a fiber-optic source is coupled. In all of the experiments with the Ito sensor design, monochromatic light from a laser diode (850 nm) was passed through a polymer optical fiber and through the sapphire window into the vacuum chamber where it interacted with the sensor coating and then reflected back through the same window, along the same fiber to a splitter where it was directed to a photodiode light detector. The intensity of the reflected light (typically tens of microwatts) was recorded by a PC through an RS232 connection. Sensor coatings were usually applied to microscope slide glass and monitored optically through the glass. Samples were placed with the glass substrate in contact with the sapphire window. The leg of the cross containing the sample was equipped with an external cooling coil and electrical heater with which the temperature of the sample could be controlled at any set temperature between about 0 and 100 C.

Experiments with the new SP resonance sensor coatings were initially conducted with an optical benchtop setup shown schematically in Fig. 4. The coatings were applied to one face of a right angle glass prism. A helium-neon laser provided the light source and the resonance was scanned by rotating the prism or the incident light beam to sweep through the critical incidence angle at the internal

surface of the coating.

Results

The Ito sensor design consists of a thermally evaporated thin film of tungsten oxide with a very thin overlay of palladium. Detailed measurements were made on this sensor design over a range of temperatures. The sensor was exposed to different pressures of hydrogen alone and hydrogen mixed in oxygen or air and the decrease in optical reflectance of the coating was recorded as a function of time using a HeNe laser light source. The recovery of the reflectance after the hydrogen was removed by evacuation or by replacement with oxygen or air was also recorded. Figure 5 shows a typical recording at 52 C.

Both the decrease in reflectance upon exposure to hydrogen and the recovery of the reflectance after removal of the hydrogen followed an approximately exponential function. Detailed analysis of the elevated temperature data showed a good fit to a double exponential curve where the change in reflectance over time could be accurately described as a sum of two exponentials, one with a relative fast time constant and another with a much slower time constant. This is shown in Figure 6 where a typical response curve is compared with the double exponential curve fit having time constants of 144 and 1283 seconds.

Measurements over a range of hydrogen pressures show the sensitivity and detection time constants to be only weakly dependent on temperature and to be virtually independent of the hydrogen pressures at temperatures above 25 C. Typical response time constants are shown in Table 1 for elevated temperatures. Room temperature response is slower but not easily analyzed in terms of time constants because of a small anomolous fast change in reflectance at the beginning of the response curve.

Table 1. Typical Hydrogen Response Time-constants for the Ito Sensor Design

Hydrogen Pressure (torr) ^a	7.6	15.2	30.4
Temperature			
52 C	140s ^b	190s	210s
	1300s	1700s	1500s
82 C	15s	8s	10s
	130s	100s	100s

a hydrogen test pressures correspond to the partial pressures of hydrogen at 1%, 2% and 4% concentration in air (one atmosphere = 760 torr)

b fast component and slow component time constants obtained from curve fit to recorded data

This kind of kinetics is consistent with a two-step reaction (sequential, first-order reactions) in which the hydrogen activity at the palladium/tungsten oxide interface is nearly constant. Such a condition may be explained by the formation of a palladium hydride from the alpha-palladium solid solution. This transformation is reported to occur at pressures above about 7.6 torr at 25 C (Fukai 1993). For most of the measurements, the results appear to be consistent with the assumption that the rate-controlling reaction is a hydrogen exchange between the tungsten oxide and palladium hydride.

At 25 C and hydrogen pressure above 15 torr, a small, anomolously fast response is superimposed upon the double exponential response (Fig. 7). This may be an additional optical reflectance change in the palladium film itself as it undergoes a transformation from solid-solution to hydride phase.

A separate, detailed technical publication of these results will be prepared for publication later this year.

The new sensor design is shown schematically in Figure 8. The sensor coating is applied to a faceted end of an optical fiber. Angled facets are at 45 degrees to the fiber axis so that a double reflection from these facets returns the light down the fiber. A flat portion of the fiber end also reflects a portion of the light back down the fiber. The coating consists of a thin reflective metal layer covered by a thin layer of amorphous tungsten oxide. The metal and its thickness are chosen to produce a surface plasmon (SP) resonance at a 45 degree incidence angle for a suitable wavelength of light. In order to get a sharp resonance, the metal must be highly conductive and silver or gold are preferred. The thickness of the tungsten oxide is selected to create a "waveguide" effect for this wavelength of light. This is a resonance condition itself in which the light is multiply reflected within the tungsten oxide film. In effect, this two-layer coating acts as a pair of coupled resonators at the SP resonance wavelength. No resonance occurs at the facet which is normal to the light beam.

Figure 9 shows schematically how the reflected light from the two kinds of facets are affected by the presence of hydrogen. A white light source is used to illuminate the sensor. The reflected beam is split and detected by two separate light detectors. One detector, S1, is unfiltered. It monitors the intensity of the entire reflected light spectrum and serves as a reference beam detector. On the other detector, S2, a narrow bandpass filter admits only the SP resonance portion of the spectrum. The S2 detector signal increases whenever the wavelength of the SP resonance shifts because of hydrogen reaction with the tungsten oxide. It provides the hydrogen signal.

If the transmittance of the optical fiber or its connectors change over time, both signals S1 and S2 will be affected in the same way. The ratio of the two signals, S2/S1, has the changes in the fiber transmittance "canceled out," but preserves the hydrogen signal.

Figure 10 shows the expected shift in SP guided-wave resonance for a typical sensor coating assuming that the real part of the optical dielectric constant of the tungsten oxide is increased by 1 % upon reaction with hydrogen. In this case the coating consists of 52 nm of gold plus 229.5 nm of tungsten oxide on a glass substrate. The angle of incidence is 45 degrees. The resonance shown here is the s-polarized portion of the beam which participates only because of the guided wave geometry. A p-polarized resonance also occurs at 660 nm. The calculation was made with the thin film optical modeling code from the Thin Film Center, Inc. (Macleod 1995).

A small company, Amerisen, Inc. of Brookfield, Wisconsin has entered into a CRADA with NREL to develop a commercial fiber-optic hydrogen leak detector using the new design concepts.

Conclusions

The Ito sensor design has been studied over a range of temperatures to determine its sensitivity and speed. While it is more than adequately sensitive for detecting hydrogen gas leaks in air, it is slow. With a detection time constant of more than 30 seconds at room temperature and a recovery time constant of more than 30 minutes, the Ito sensor design would probably not qualify as a critical safety device.

Fluctuations in the FO transmittance due to optical fiber bending, temperature changes and connector movement was found to present a background noise problem with the FO detectors. Such noise could be expected to be particularly serious in a moving vehicle.

A new sensor design was invented that has faster response and potentially reduced susceptibility to background noise. The new sensor uses a surface-plasmon guided wave resonance in a thin coating of tungsten oxide on a thin silver or gold underlayer. The design has not yet been fully developed, but preliminary measurements show it to have greater response speed with a detection time constant of about 0.2 seconds and a recovery time constant of about 1 second at room temperature (Fig. 11). The new design also incorporates a reference beam signal that can be used to cancel out the variations in transmittance through the FO light path. A patent application has been filed for the new design.

Plans

The new sensor design will be optimized and characterized in detail. Measurements will include sensitivity and speed over a range of temperatures and measurements of its susceptibility to interferences from other gases such as hydrocarbons, carbon oxides, water vapor, nitrogen oxides and sulfur compounds. Temperature changes at the sensor will cause changes in the SP resonance that must not be mistaken for a hydrogen signal. A method to compensate for such changes must be developed.

We will work closely with our CRADA partner to develop a cost-effective, manufacturable hydrogen gas leak detector based on our new design.

We will analyze the performance requirements for a hydrogen gas leak detector in a hydrogen-fueled automobile with help from industry consultants.

We will publish the results from our measurements of the Ito sensor in a suitable technical journal.

Acknowledgments

The authors gratefully acknowledge the assistance of Mr. Matthew Keyser in developing computer controls and data acquisition programs for our measurements and Mr. James Dombos for fabrication of much of our special optical and vacuum equipment. This work was funded by the U.S. Department of Energy's Hydrogen Program under contract No. DE-AC36-83CH10093.

References

Butler, M. A. 1991. "Fiber Optic Sensor for Hydrogen Concentrations near the Explosive Limit", *J. Electrochem. Soc.*, 138:L46-47.

Fukai, Y. 1993. The Metal-Hydrogen System, Berlin, Springer-Verlag.

Ito, K. and T. Kubo 1984. "Gas detection by hydrochromism." In *Proceedings of the 4th Sensor Symposium*, 1984, 153-156.

Macleod, A. 1995. The Essential Macleod Thin-film Design Software User Manual, Tucson, AZ, The Thin Film Center, Inc.

Raether, H. 1988. Surface Plasmons, Berlin, Springer-Verlag, p 21.

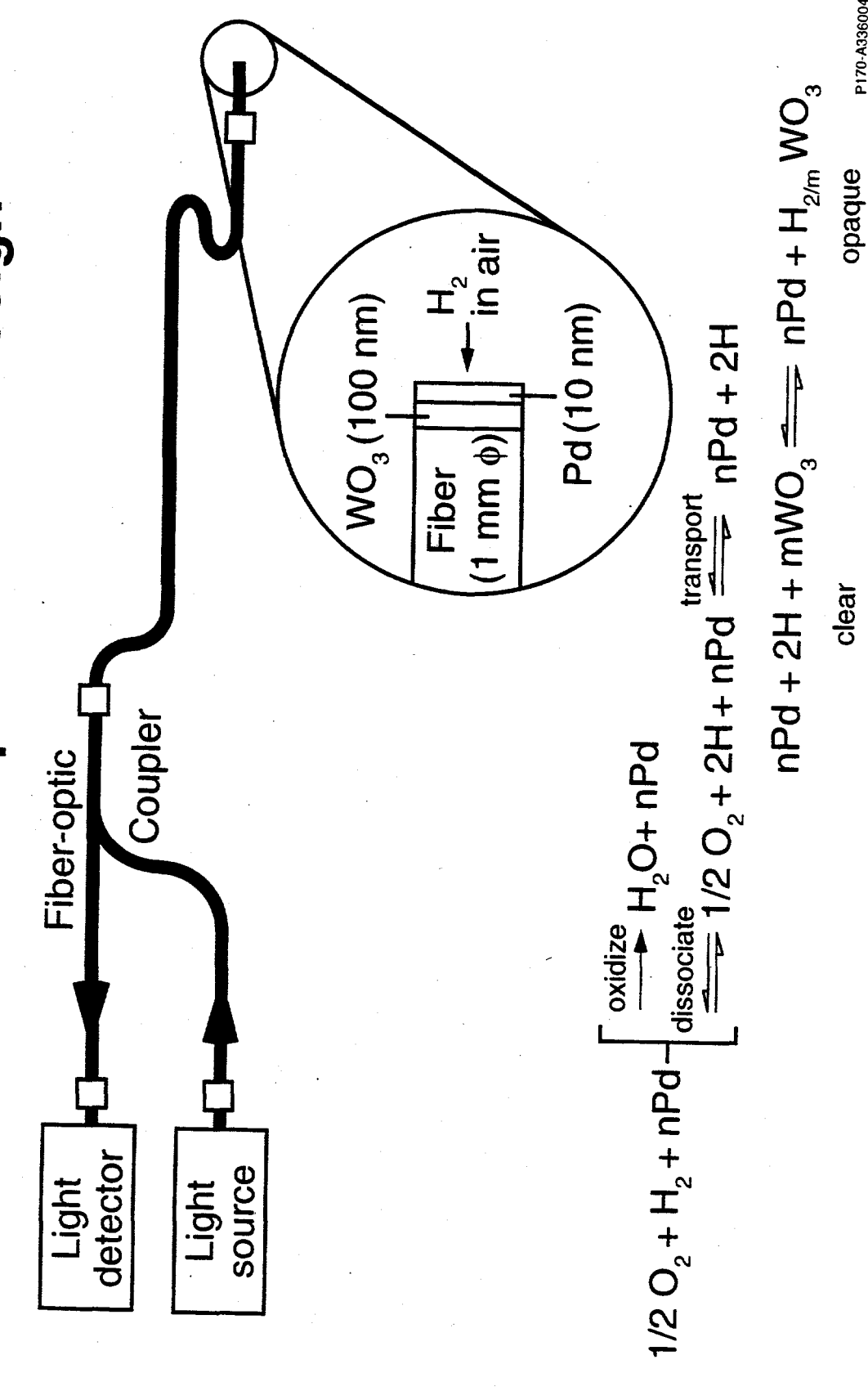
Sadowski, J. W. 1994. "Method for carrying out surface plasmon resonance measurement and sensor for use in method", U. S. Patent No. 5,322,798, June 21, 1994.

Sambles, J. R., G. W. Bradbery and F. Yang 1991. "Optical excitation of surface plasmons: an introduction.", *Contemporary Physics*, 32:173-183.

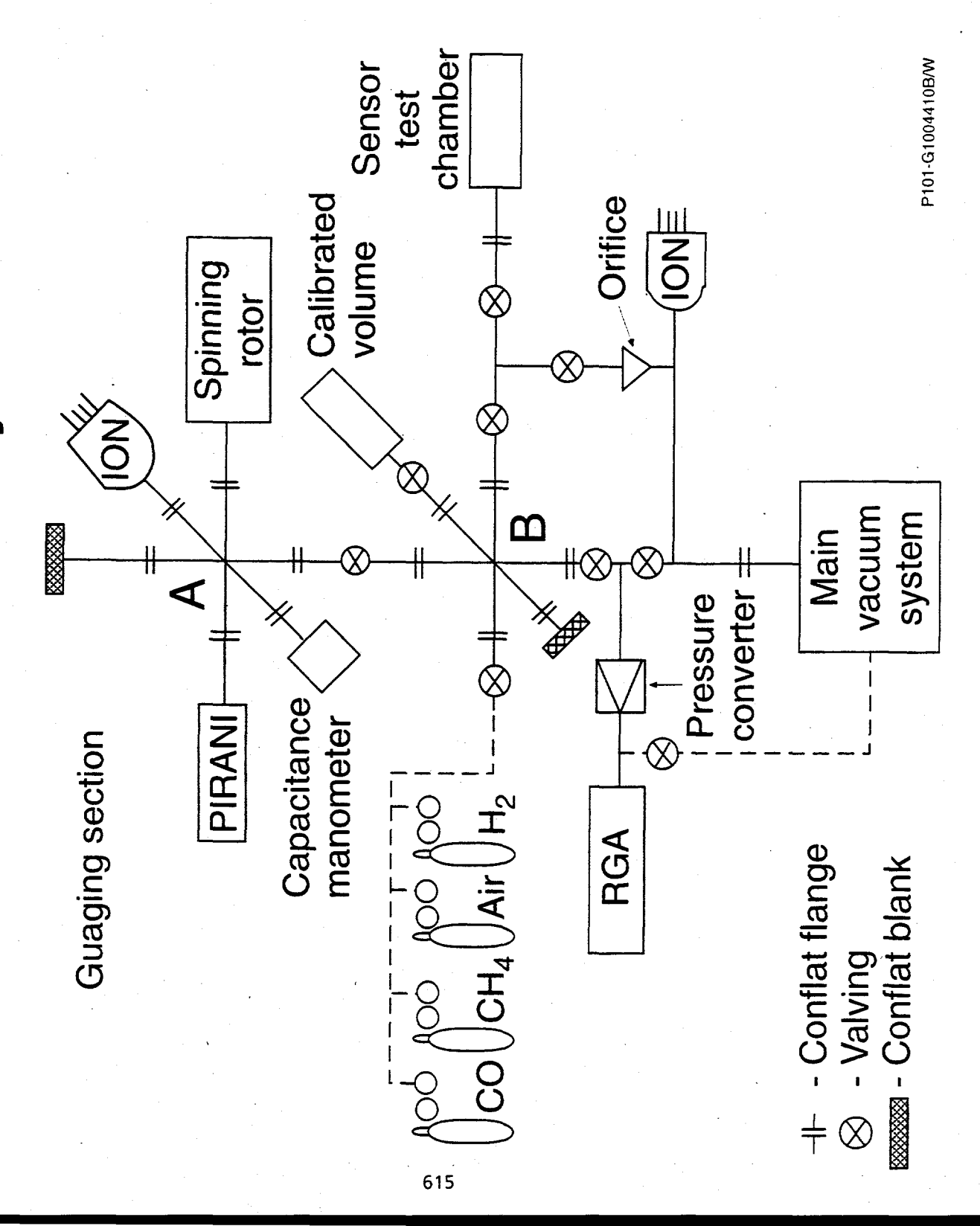
Figures

- 1. Schematic diagram of the initial fiber-optic sensor design.
- 2. Diagram of the ultra-high vacuum apparatus used to measure sensor response.
- 3. Schematic diagram of the sensor test chamber attached to the ultra-high vacuum apparatus.
- 4. Schematic diagram of the apparatus used to make initial measurements on surface-plasmon resonance sensors.
- 5. Typical response of an Ito sensor to hydrogen.
- 6. Double exponential decay curve fit to the response recording of Fig. 5.
- 7. A response curve showing an anomolously fast initial drop in reflectance at 25 C.
- 8. Schematic diagram of the guided wave surface-plasmon sensor design.
- 9. Schematic diagram of the optical response of the guided-wave surface-plasmon detector.
- 10. Theoretical calculation of the shift in resonance caused by exposure to hydrogen.
- 11. Comparison of the measured response of the Ito sensor and the new guided-wave surface-plasmon sensor.

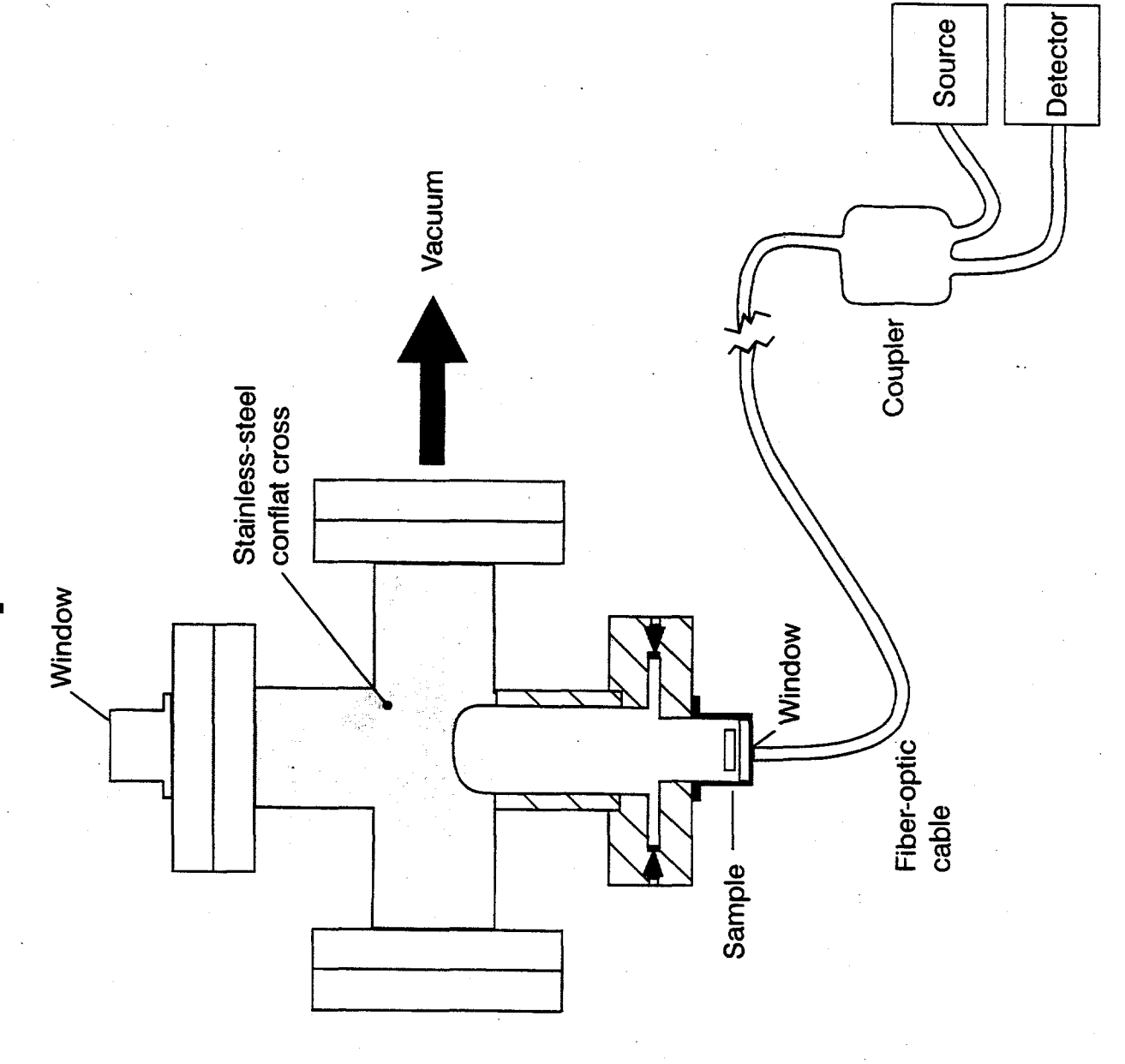
Initial Fiber-Optic Detector Design



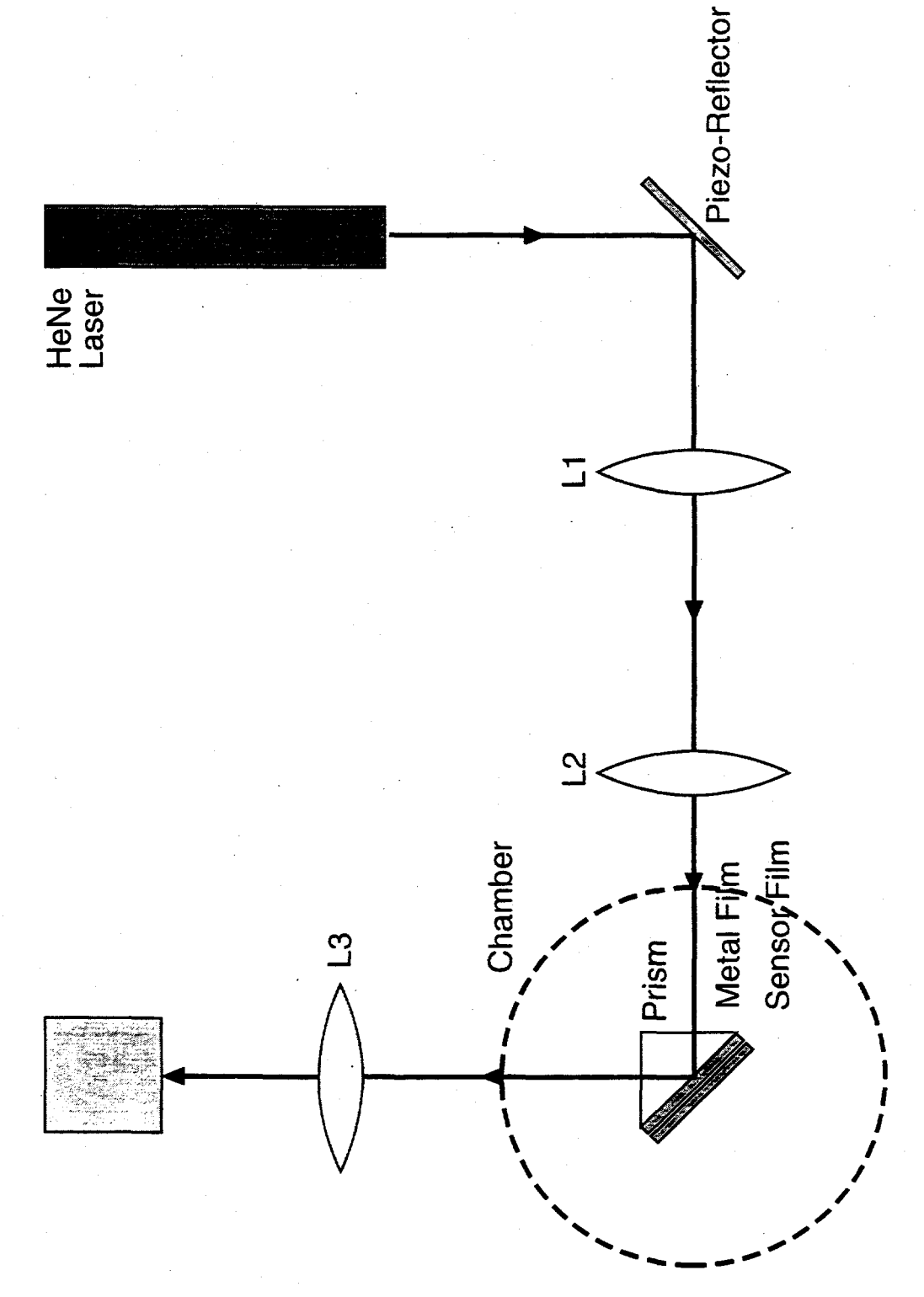
Instrument System



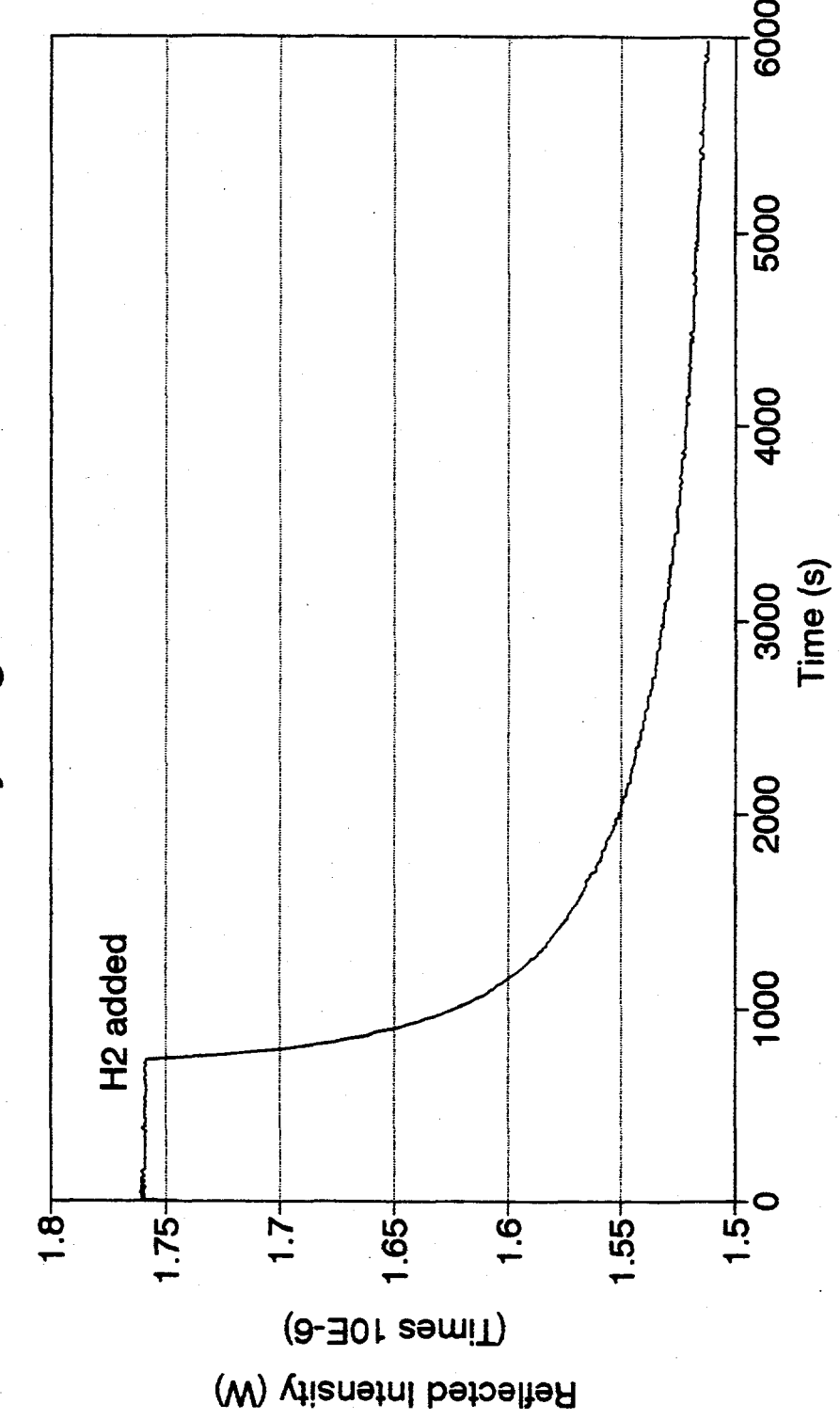
Sample Holder

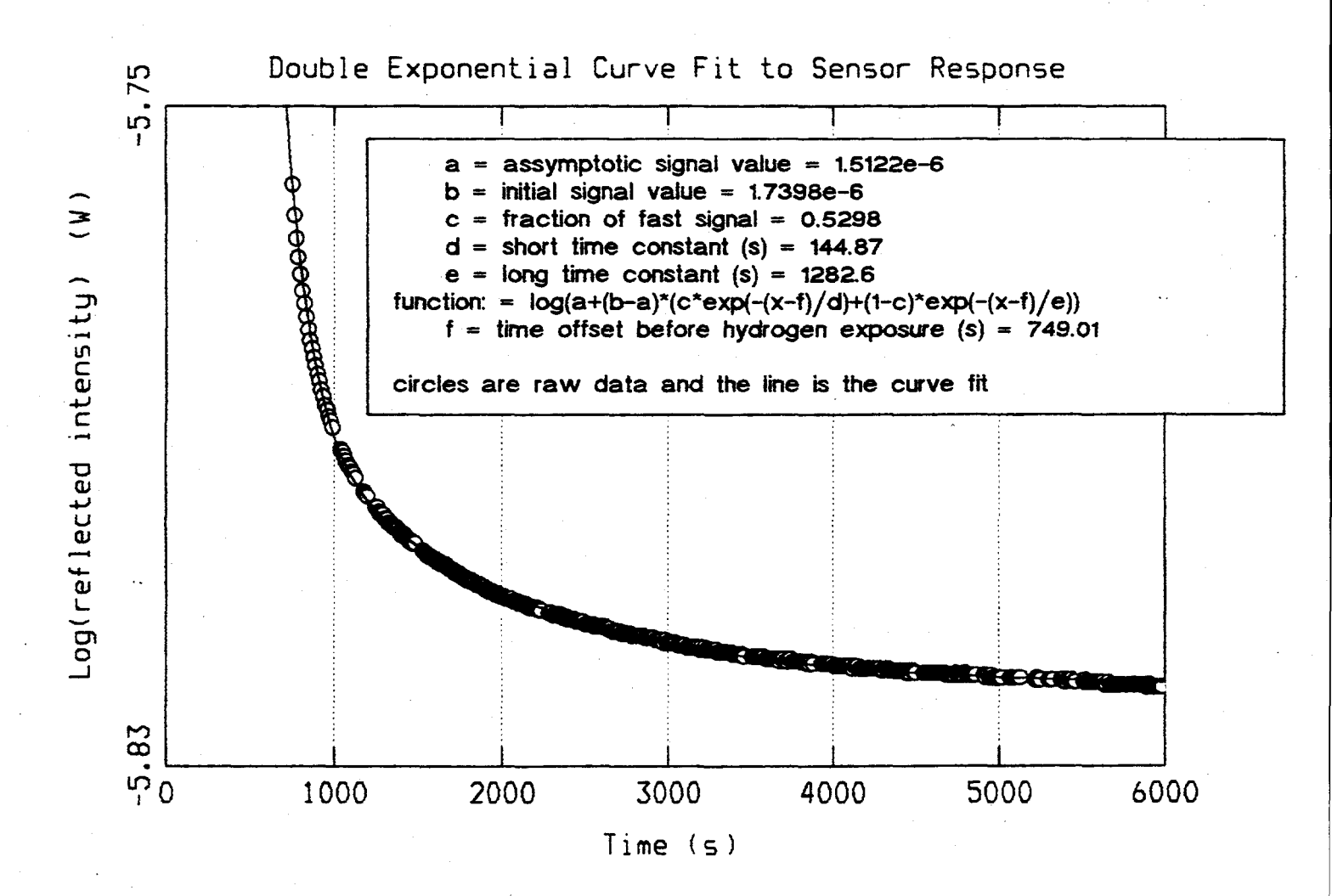


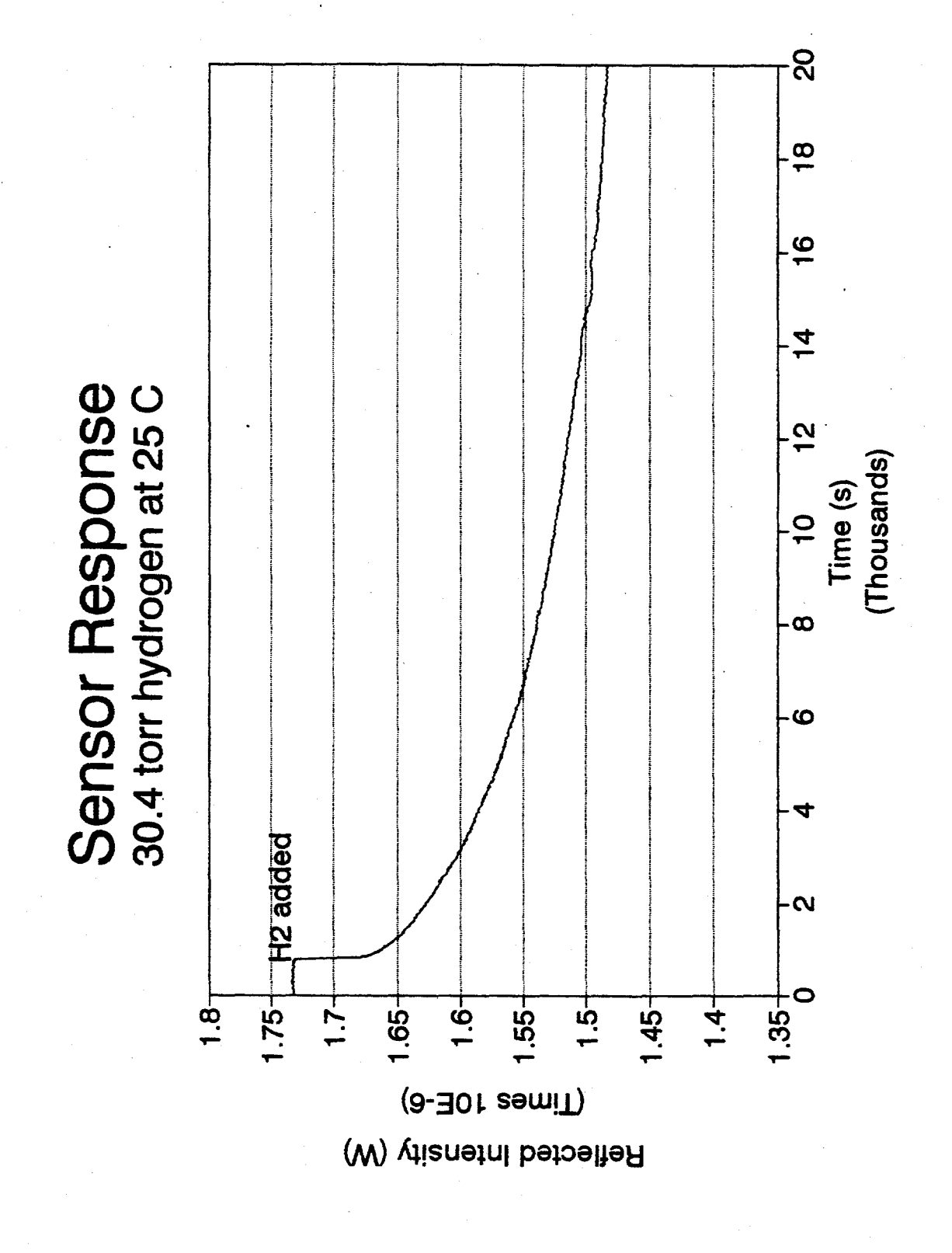
Test Apparatus Schematic



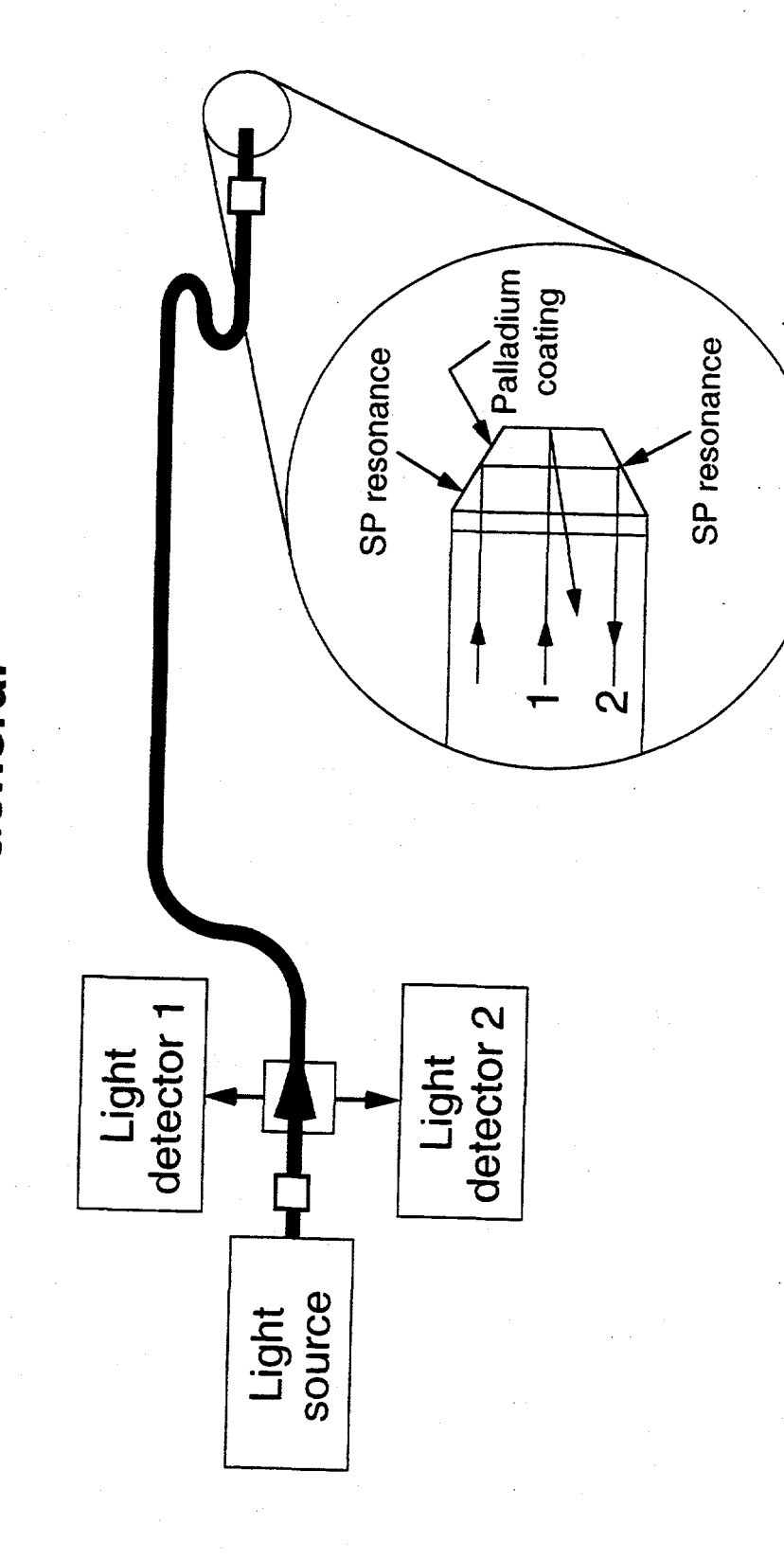
Sensor Response 7.6 torr hydrogen at 52 C





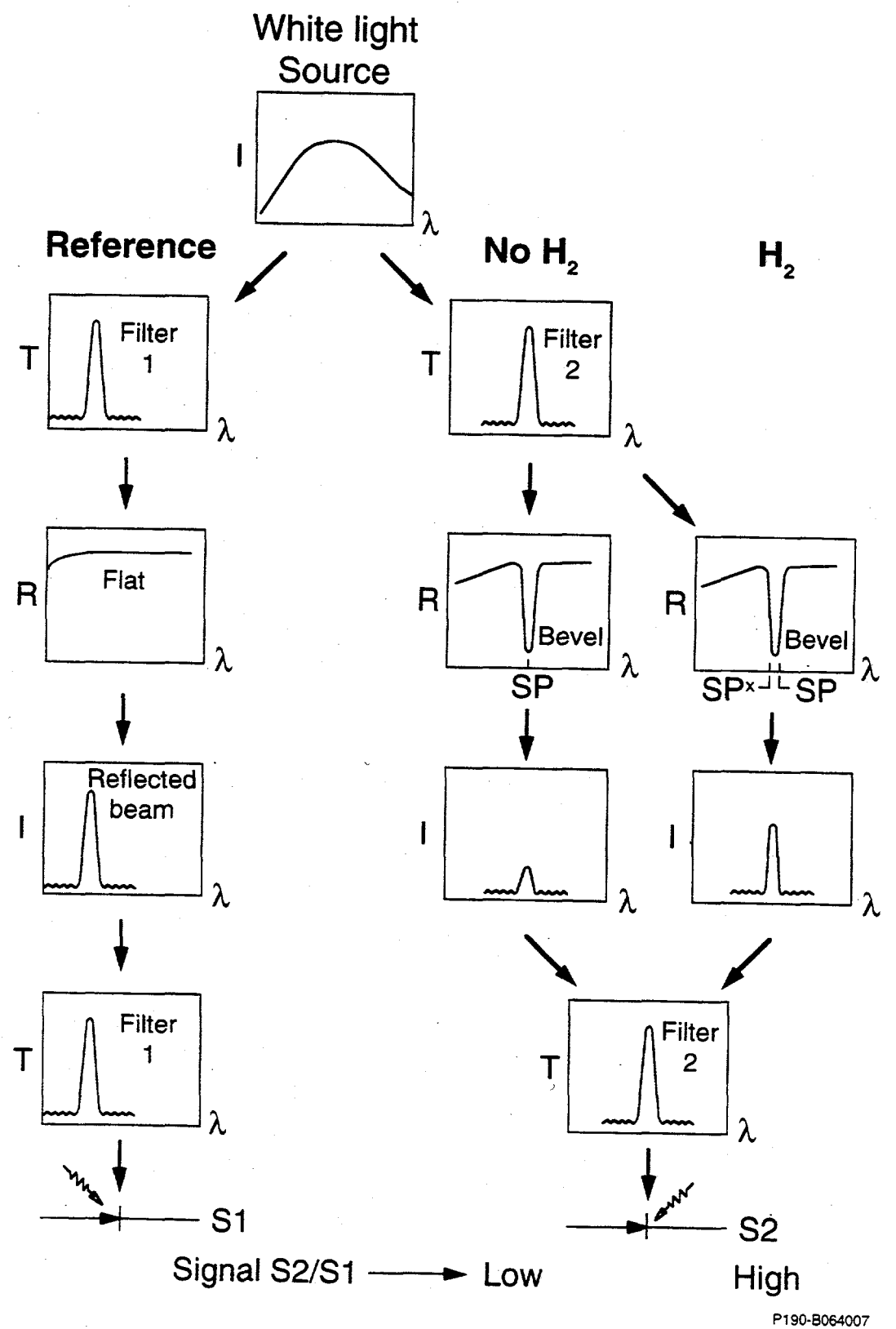


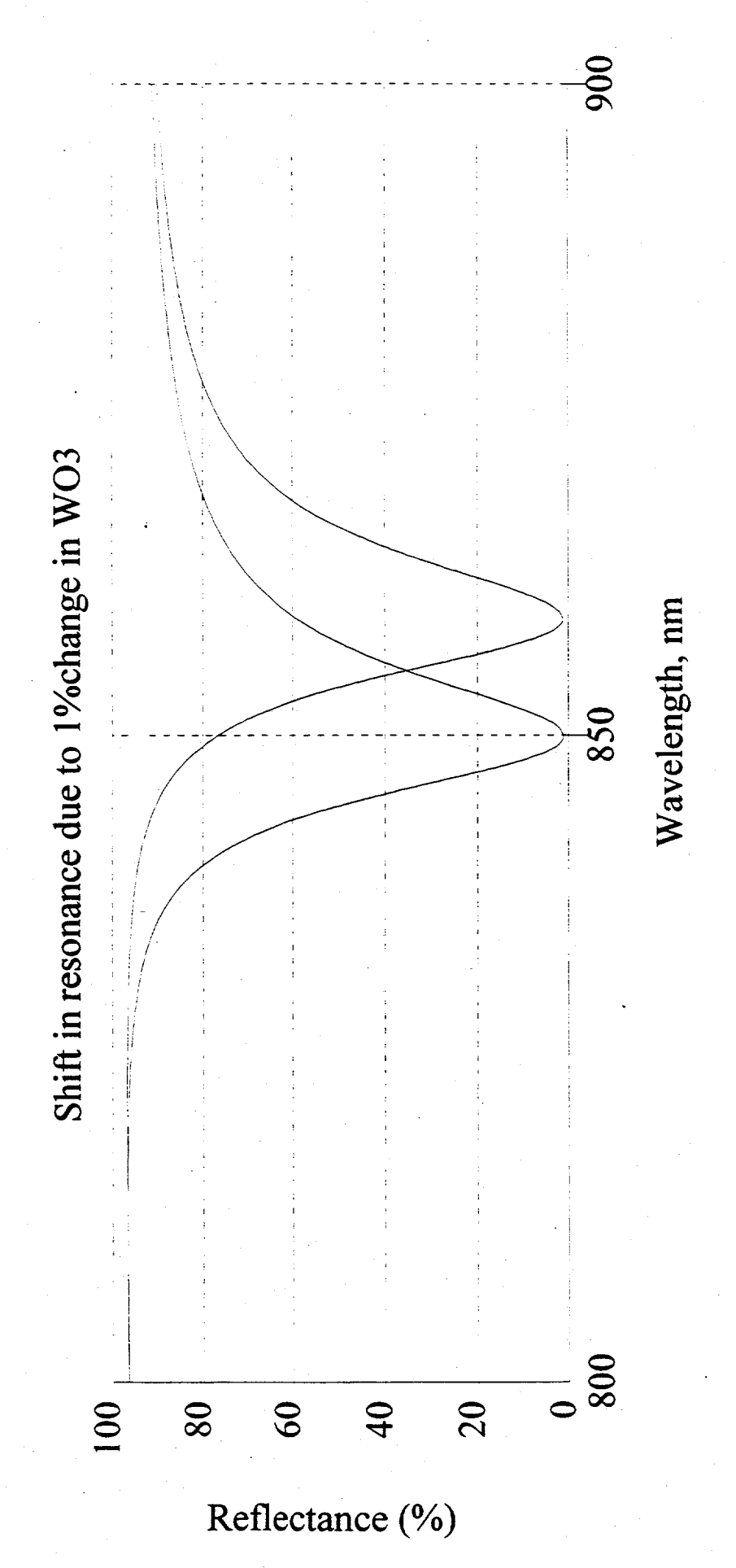
New Fiber-Optic Detector Design General



New Fiber-Optic Design

Optical Design Detail

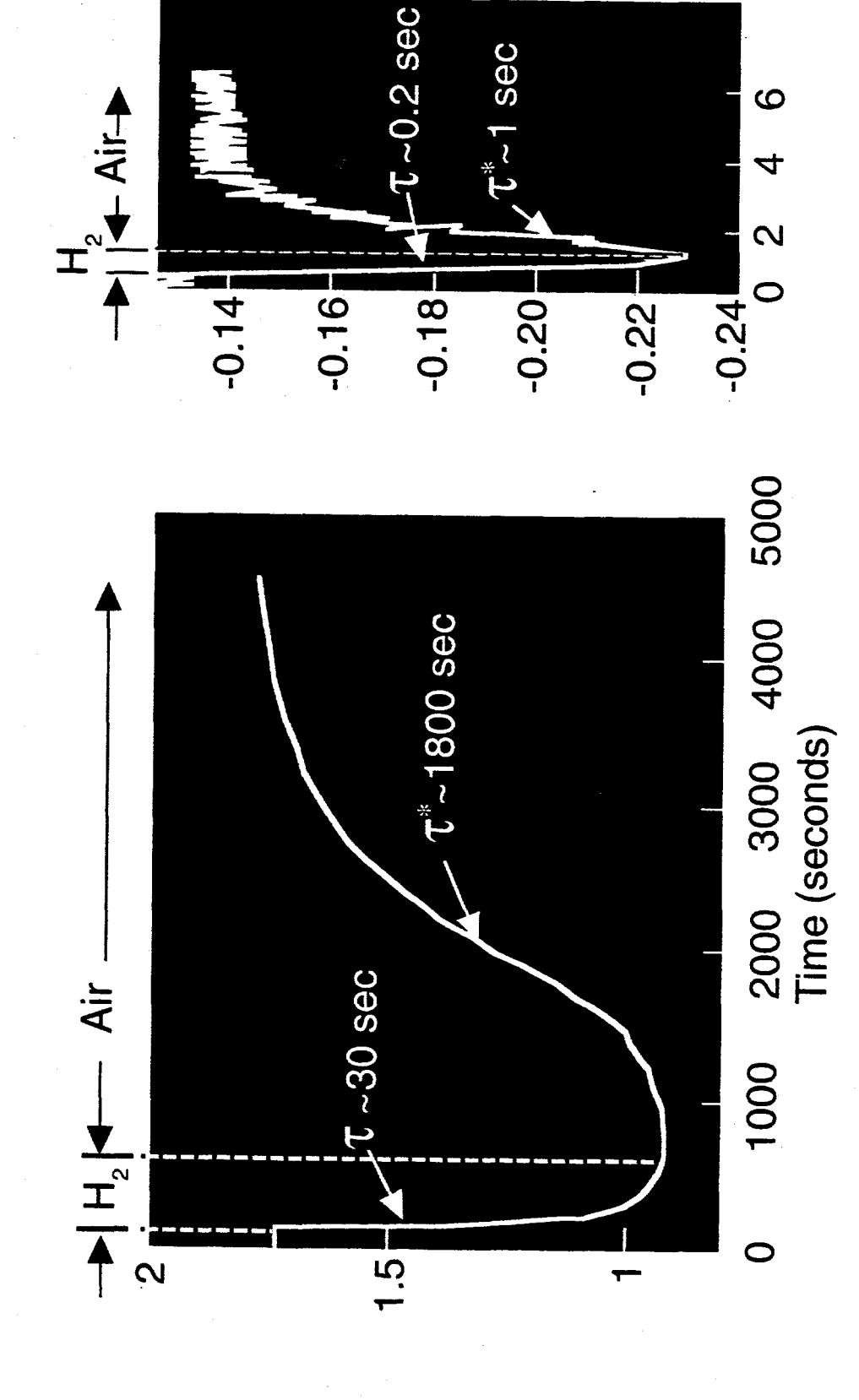




New Detector Design is Faster

Old Design

New



CHEMICAL KINETIC MODELING OF H2 APPLICATIONS

Charles K. Westbrook
Nick Marinov
William J. Pitz
Henry Curran
Lawrence Livermore National Laboratory
Livermore, CA 94550

Abstract

This project is intended to develop detailed and simplified kinetic reaction mechanisms for the combustion of practical systems fueled by hydrogen, and then to use those mechanisms to examine the performance, efficiency, pollutant emissions, and other characteristics of those systems. During the last year, a H2/NOx mechanism has been developed that gives much improved predictions of NOx emissions compared to experimental data. Preliminary chemical kinetic and equilibrium calculations have been performed in support of Br2-H2O experiments to be conducted at NREL. Hydrogen, hydrogen/methane and hydrogen/natural gas mixtures have been investigated in a knock-rating engine to assess their automotive knock characteristics. We are currently developing the simplified analog reaction mechanisms that are computationally simple, yet still reproduce many of the macroscopic features of flame propagation.

Summary of Approach/Rationale

This project is intended to provide theoretical and kinetic modeling support to a variety of current research programs being supported by DOE which involve combustion of hydrogen and hydrogen/hydrocarbon mixtures in practical systems. Kinetic modeling can reduce the overall cost of system development, and it can provide analysis of novel and innovative proposals before they are subjected to experimental studies. This project will provide reliable simplified reaction models for incorporation into large-scale CFD models, it investigates pollutant species production and combustion rates under fuel-lean conditions, and it investigates the features of hydrogen/hydrocarbon mixtures.

Past Results

We refined many of the elementary kinetic reaction steps in the detailed reaction mechanism for hydrogen oxidation. To extend the model to pressures characteristic of internal combustion engines, it was necessary to apply theoretical pressure falloff formalisms for several key steps in the reaction mechanism. Detailed and global chemical kinetics for hydrogen-air mixtures have been validated against data derived from flame propagation, flame structure and shock tube ignition delay time studies. The chemical kinetic mechanism for the detailed reaction model was critically reviewed and well-simulated the experimental measurements. We have continued development of simplified reaction mechanisms for hydrogen

oxidation, we have implemented those mechanisms into multidimensional computational fluid dynamics models, and we have used models of chemistry and fluid dynamics to address selected application problems. A global rate expression validated against hydrogen-air laminar flame speeds was developed for the single step reaction $H_2 + 1/2$ $O_2 = H_2O$. A two-dimensional fluid-dynamics computer program with detailed chemical kinetics has been developed and tested on a 1-D laminar flame. Detailed kinetics studies have investigated hydrogen flames and ignition of hydrogen behind shock waves, intended to refine the detailed reactions mechanisms.

Current Year Results

NO_x Calculations for Stirred Flames of Hydrogen

A detailed NO_X (where $NO_X=NO+NO_2$) modeling study for hydrogen-air mixtures in a jet-stirred reactor was performed for the purpose of NO_X model validation. The GRI- NO_X Model (Version 2.1), as obtained from the Internet (http://www.gri.org/), was initially used in order to compare the model's NO_X predictions to the NO_X measurements in stirred flames of hydrogen. The data source used for the model validation study was obtained from jet-stirred reactor experiments performed for the hydrogen-air equivalence ratio range of 0.6 to 1.6, at atmospheric pressure, and for a nominal residence time of 0.8 msec (Engleman et al., 1973). Figure 1 shows the experimental NO_X measurements and GRI- NO_X Model predictions. The breakdown of the contributing NO_X formation mechanisms to NO_X production is shown in the figure and suggests that both the Zeldovich (Thermal) NO_X mechanism and the NNH mechanism to NO_X production are effective NO_X production routes.

The GRI-NO_X Model tended to overpredict the NOx concentration by a factor of five over the full H₂-Air equivalence ratio range examined. The overprediction was due to a slightly fast kinetic rate assignment to the Zeldovich (Thermal) NO formation reaction N₂+O \rightarrow NO+N and NO production from the NNH submechanism (N₂+H \rightarrow NNH, NNH+O \rightarrow NO+NH). We tried correcting the GRI-Model to allow for a better NO_X prediction in the H₂-Air stirred reactor study but any correction greatly compromised the GRI-NO_X model predictive capability for NO_X in CH₄-Air mixtures. At this point we abandoned the GRI-NO_X Model and developed a NO_X Model based on our previous detailed H₂-Air mechanism validation work. We combined our detailed H₂-Air chemical kinetic model with the Miller-Bowman nitrogen chemistry. The kinetic rate to the N₂+O \rightarrow NO+N reaction was only adjusted in order to obtain good agreement with the NO_X measurements as shown in Figure 2. The LLNL NO_X Model predicted the NO_X concentration to within a factor of two of the experimental measurements and the major contributor to NO_X formation is from the Zeldovich (Thermal) NO pathway.

We have also successfully validated the LLNL NO_X model for CH₄-Air and C₃H₈-Air mixtures in an atmospherically operated jet-stirred reactor.

We will continue to model NO_X formation for a variety of conditions and experimental apparatus. In particular, we will be validating the LLNL NO_X Model for NO_X formation in low temperature ($T_{max}=1200K$) and pressure H₂ flames, and NO_X formation in a high pressure flame tube apparatus at ultra-lean H₂-Air conditions.

Chemical Kinetic and Equilibrium Calculations for HBr Yields in Br2 and H2O Mixtures

At the request of Hydrogen Program personnel at Sandia National Laboratories and University of Florida, we carried out preliminary chemical kinetic and equilibrium calculations in support of Br2-H2O experiments to be conducted at NREL. The motivation for this computational work is to examine the potential role of thermal reaction and photolysis in HBr production from Br2-H2O mixtures. The HBr formed by this process may then be electrolytically decomposed in a reversible fuel cell as a means for

mass production of molecular hydrogen. A parameter variation study was performed to verify the findings of previous experimental work conducted for Br₂-H₂O mixtures in a thermal reactor and to examine the potential role of Br₂ photolysis on HBr yields.

A quartz reactor was used to examine bromine-steam chemical reaction in the 900K - 1300K temperature range, Br₂ concentrations ranging from ca. 1.0% to 12.0% and for a reactor residence time of ca. 1.0 second. The experimental results were previously reported and may be summarized by two statements.

- (1) Experiments conducted for temperatures 1015K and below revealed HBr yields a factor of five to an order of magnitude lower than the equilibrium calculated HBr yields. Experimental HBr yields for temperatures greater than 1200K were a factor of 1.5 lower than the equilibrium calculated HBr yields. These results indicate that the reactor residence time of ca. 1.0 second was shorter than the time-scale required to reach equilibration of the reaction kinetics.
- (2) Experimental HBr yields increased with temperature and decreased with increasing Br₂ concentration in Br₂-H₂O mixtures.

Equilibrium calculations for HBr yield in the 1110K to 1250K temperature range are shown in Figure 3. The percent Br2 in the Br2-H2O mixture was varied from ca. 1.0% to 12.0% for three distinct temperatures, conditions similar to those reported in the earlier experimental study. The HBr yield at equilibrium increased with increasing temperature from 1100 to 1250 K.

We also examined the potential role of reactor residence time and Br2 photolysis on HBr production. In Figure 4, chemical kinetic and equilibrium calculations were performed at 1175K and Br2 concentrations varying from ca. 1% to 99% Br2 in H2O. The solid line refers to calculated equilibrium HBr yields per Br2 concentration in water. The dashed lines refer to time-dependent kinetic calculations performed using a plug flow reactor (PFR) code. Three different PFR calculations were performed to determine HBr yields by (1) thermal reaction for a PFR residence time of 1.0 second, (2) simulating Br2 photolysis through the adjustment of the Br2 dissociation rate constant for complete Br2 break up (the reverse Br recombination rate parameters were kept fixed), and (3) simulating Br2 photolysis with an order of magnitude increase in the PFR residence time.

The numerical computations revealed the following results:

- (1) The time-dependent PFR kinetic calculations (no Br2 photolysis simulation) indicated that reactor residence times on order of 1.0 second lead to approximately a factor of two less in HBr yield than compared to the equilibrium HBr yield. The modeling results are remarkably consistent with experimental HBr yields reported at the other temperatures examined and adds credibility to the computational model used in describing the experiments.
- (2) If photolysis could dissociate all the Br₂ found in the thermal reactor for a nominal residence time of 1.0 second and 1175K, then HBr yields may be produced at those levels attained by the equilibrated reaction kinetics. The calculations performed at these conditions show that Br₂ concentrations greater than ca. 12.5% would be needed in the photolysis and thermal reactor system in order to attain equilibrium HBr yield levels.
- (3) Superequilibrium HBr yields could be attained by a combination of Br2 photolysis and thermal reaction for a nominal reactor residence time on the order of 10.0 seconds at 1175K. Br2 concentrations greater than 2.5% in H2O would be required to achieve HBr yields greater than equilibrium at those operating conditions. Higher operating temperatures will allow for greater levels of superequilibrium HBr to be achieved or allow for shorter reactor residence times needed to achieve superequilibrium HBr when Br2 photolysis and thermal reaction are used in tandem.

A reaction flux analysis was conducted to determine the important HBr production pathways for the conditions examined in this study. HBr production was primarily controlled by the reaction sequence

$$Br_2 (+M) \rightarrow Br + Br (+M)$$

 $Br + H_2O \rightarrow HBr + OH$

and the secondary HBr production pathway was determined to be as follows

OH + OH
$$\rightarrow$$
 H₂O + O
Br₂ + O \rightarrow BO + Br
BrO + OH \rightarrow Br + HO₂
Br + HO₂ \rightarrow HBr + O₂

Photolysis of Br2 can lead to the production of ground state $Br(^2P_{3/2})$ and electronically excited $Br(^2P_{1/2})$. The electronically excited Br may react with H_2O to produce HBr and OH but such a reaction would have to overcome a ca. 24 kcal/mol activation energy barrier. A literature search was conducted to examine the possible role of electronically excited Br reacting H_2O and any other species. The work of Donovan and Husain (1966) showed electronically excited Br collisionally quenches to ground state Br by H_2O at a rate constant of 2.0E13 cm³/mol-sec. This would make electronically excited Br production by photolysis unimportant and would then suggest that photolysis need not be performed in the wavelength region which would produce electronically excited $Br(^2P_{1/2})$.

H2/CH4 Motored Engine Results

Octane ratings are important because they can be used to assess whether a fuel will produce knock in an automotive engine. Ultimately, the occurrence of knock determines the upper limit of compression ratio at which an automotive engine can operate. Compression ratio is a key factor that determines the thermodynamic efficiency of the engine and thus the fuel economy of the vehicle. Automotive engine knock affects spark-ignition engines using hydrogen as a fuel just as it affects those which are burning conventional hydrocarbon fuels.

Calculations were carried out to assess the octane ratings of hydrogen, methane, natural gas and their mixtures. A previously developed correlation for a knock-rating engine was used to obtain the octane ratings. This correlation was developed for a CFR engine operated by Dr. William Leppard at General Motors Research Laboratories. The fuel/air mixtures were stoichiometric mixtures, as required for octane ratings. Leppard has performed experiments to determine the critical compression ratio for primary reference fuels and hexanes with measured octane ratings ranging from 0 to 104. Critical compression ratio is the compression ratio at which a fuel/air mixture will autoignite due to compressional heating without the use of a spark plug. We have developed the capability to compute critical compression ratios with a chemical kinetic model for the fuel chemistry and a thermodynamic model for engine compression, expansion and heat transfer. Using a previously developed correlation curve (Curran et al., 1995, 1996) and computed critical compression ratios for methane, hydrogen, natural gas and methane/hydrogen and natural gas/hydrogen, predicted octane ratings were obtained (Fig. 5 and 6). The natural gas composition was based on an average composition as determined by the Gas Research Institute in their survey (Liss, et al., 1992). The average composition is 93.9% methane, 3.0% ethane, 0.7% propane, 0.2% n-butane, 0.2% iso-butane, 1.0% nitrogen and 1.0% carbon dioxide. As shown in Fig. 5, a predicted research octane rating (RON) for methane of 119 compared to an experimental value of 120 (Obert, 1973). Our predicted research octane rating (RON) for hydrogen is 111 compared to an experimental value of 100 (Phillips 66, 1962). The predictions show the correct experimental trend that hydrogen has a lower octane number than methane. Under slightly different experimental conditions, Naber and Siebers (1994, 1996) have found that hydrogen is slightly easier to ignite than methane, also consistent with our kinetic modeling predictions summarized here. Further study of both the prediction and the experimental uncertainty in the octane number for hydrogen needs to be made. Also shown in Fig. 5 is a prediction for a 50:50 mixture of methane and hydrogen, showing a perhaps anomalous behavior that a 50:50 mixture has a higher octane rating than either neat methane or hydrogen. This preliminary prediction will be investigated further in the coming year. Critical compression ratios for natural gas and natural gas/hydrogen mixtures were computed, and predicted octane ratings were obtained (Fig. 6). A predicted research octane rating (RON) for natural gas of 117 compares to a predicted value of 119 for pure methane. The higher

molecular weight components in natural gas (ethane, propane, and butanes) are more reactive than methane and cause natural gas to autoignite and knock more easily than pure methane. The natural gas mixture has an octane quality (117) that is higher than predicted for hydrogen (111). A 50/50 hydrogen/natural gas mixture was also examined and has an octane quality that is slightly higher than natural gas (Fig. 6). This is a synergistic effect where the mixture has a higher octane quality than either of the individual fuels contained in the mixture. Synergistic and antagonistic effects are often seen for binary mixtures of neat hydrocarbon fuels (Croudace and Jessup, 1988). The perhaps anomalous behavior of the 50/50 hydrogen/natural gas blend will be investigated further in the coming year.

Reduced Reaction Model for Multidimensional Codes

We have found that the single reaction kinetic model we had developed previously eventually became unreliable as the unburned hydrogen-air mixture reached the elevated temperatures and pressures characteristic of operations in internal combustion engines. The reason for this problem was traced to the relatively low activation energy (35 kcal/mole) of this reaction and the fact that this reaction led to significant heat release immediately. As a result, when we attempted to compute the propagation rate of a laminar flame where the unburned gas temperature was above 700 K and the pressure above 30 atm, the model could not arrive at a steady flame propagation rate. Another result of the difficulties with this single reaction model is, we believe, the type of premature ignition that is being predicted in model calculations at LLNL and by Norm Johnson at LANL.

To address this problem, we are now working on a reduced reaction model that begins with the fully detailed kinetic mechanism for hydrogen oxidation and retains only the five most important reactions. These include:

$$H_2 + O_2 = OH + OH \tag{1}$$

$$H_2 + O = H + OH \tag{2}$$

$$H + O_2 = O + OH \tag{3}$$

$$H_2 + OH = H_2O + H$$
 (4)

$$OH + OH = H_2O + O$$
 (5)

This set of reactions includes only the five chemical species H, H₂, O, O₂, and H₂O, and is not significantly more costly to compute than the original simplified system that included the three species H₂, O₂, and H₂O. In addition, it incorporates most of the elementary chemistry and the real kinetic rate expressions that apply to hydrogen ignition and combustion, so it is very likely to be reliable over a significant range of conditions. We are using the COYOTE code to do these studies, which are currently involving laminar, one-dimensional, flame models. The code is closely related to the KIVA model of LANL, but including a detailed kinetic solver adapted from the LLNL code HCT which is routinely used for solving kinetics problems for fuels up to hexanes and octanes. Results to date are very encouraging for flames at atmospheric pressure, and current tests are being carried out to ensure that computed results under other realistic operating conditions are also correct.

Free Piston Engine

Calculations and code development are being performed in support of the Free Piston Engine (FPE). The FPE operates at variable compression ratio and can take advantage of the high octane value of hydrogen. To achieve maximum thermal efficiency, the hydrogen-air mixture must autoignite near top dead center. The timing of the autoignition is controlled by parameters which include compression ratio, equivalence ratio, scavenging efficiency, intake pressure and temperature. A series of subroutines are being integrated into the HCT chemistry code to address the Free Piston Engine (FPE). These subroutines were written by

Scott Goldsborough and Peter Van Blarigan of SNL. With the above subroutines integrated into the HCT chemistry code, we will be able to assess the effects of the above engine parameters. The HCT code has the fully-detailed, chemical-kinetic mechanisms for hydrogen and C_1 - C_2 hydrocarbons, so that the new code will allow predictions concerning mixtures of hydrogen and natural gas.

Plans for Future Work

During the next 18 months, investigations will continue in the areas discussed above. We will continue to use detailed chemical kinetic models to investigate fuel-lean mixtures where hydrogen and hydrogen/natural gas mixtures exhibit low NO_x emissions. We will examine the NO_x emission with these models over a range of operating conditions. We will examine further the automotive knock characteristics of hydrogen and hydrogen/natural gas mixture under conditions found in a knock-rating engine. We will incorporate new subroutines in our combustion code (HCT) to treat a free piston engine, test those subroutines and simulate combustion in a free piston engine for comparison with upcoming experiments at Sandia National Laboratories. We will continue development of simplified mechanisms to be used in multidimensional models of practical systems. We will use existing and new models to provide direct support to program experimental efforts. For example, at the request of Hydrogen Program personnel, we will continue to support work on hydrogen production, catalyzed by Br₂ and solar radiation, being carried out at Sandia National Laboratories and University of Florida. We will be available to provide chemical kinetics and other modeling support to other contractors as directed by the DOE program manager.

Projected Goals/Basis for Goals

This work is intended to provide computational combustion modeling support for a variety of hydrogen combustion projects at LLNL and other contractors in this overall program. The goal is therefore to develop kinetic submodels and CFD methods, and then to use those models ourselves as well as to provide those models to others to use in simulations of actual systems. It is essential to identify the intended uses that these models must serve.

At LLNL, there are two major classes of use for hydrogen combustion models. The first involves the use of detailed chemical kinetics to analyze hydrogen combustion problems. This can include issues of critical conditions for ignition, production of oxides of nitrogen (NOx) from hot combustion products, combustion of mixtures of hydrogen with other fuels such as natural gas, and determination of flammability and other limits for combustion. In such problems, the physical model may be somewhat simplified, but the attention must be given to the chemical submodel. The second major class of models include larger systems which may combine a larger number of model elements in addition to the chemical factors. This may include problems with several spatial dimensions which may be important, such as internal combustion engines or industrial burners. In such systems, a more complex fluid mechanics treatment may be necessary, and a very detailed chemical model may be unnecessary or impossible to include. In such cases, a more simplified chemical model is required, but it is important that the simplified model still include the most important features of the hydrogen combustion chemistry.

Both of the above types of models are included in our program goals, and considerable progress has been made in providing them for general use. Following the development of these models, a final goal of this project is the application of those models to practical problems of hydrogen combustion that are identified by the program leaders as particularly important to its eventual success. During the past year, we have had success in meeting all of the above program goals. As described earlier in this report, the models themselves, both detailed and simplified chemistry models, have been improved and tested, and the resulting computer models have been used at LLNL and elsewhere to analyze practical hydrogen combustion problems of interest to the DOE hydrogen program. The same goals apply during the coming year, and we expect that our work will be able to meet those goals.

Major Barriers for Meeting Goals

At the present time, all of the computational models required for the LLNL work have already been developed and thoroughly tested. There is always room for improvement and addition of new capabilities, and these will be pursued as needed for specific types of applications. However, there are no major obstacles or technical breakthroughs required.

Since the LLNL effort in this topic area consists entirely of computational modeling, there is a continuing need for collaborators with reliable and detailed experimental results with which to compare model predictions and analysis. These results must be supplied by other contractors within the DOE program, as in the past. However, at the present level of financial support, the LLNL combustion modeling program is prepared to provide the overall Hydrogen Program with reliable modeling efforts and provide insights and analysis into the details of hydrogen combustion and pollutant emissions.

Acknowledgments

This work is supported by the U. S. Department of Energy, Office of Utility Technology, and was carried out under the auspices of the U. S. Department of Energy by the Lawrence Livermore National Laboratory under contract No. W-7405-ENG-48.

References

Croudace, M. C., and Jessup, P. J. "Studies of Octane Properties of Mixtures of Isomeric Hexanes" Society of Automotive Engineers Paper SAE# 881604, 1988.

Curran, H. J., Gaffuri, P., Pitz, W. J., Westbrook, C. K. and Leppard, W. R., "Autoignition Chemistry in a Motored Engine: An Experimental and Kinetic Modeling Study", In *Proceedings of the 26th Symposium (International) on Combustion*, The Combustion Institute, Pittsburgh, 1996.

Curran, H. J., Gaffuri, P., Pitz, W. J., Westbrook, C. K. and Leppard, W. R., "Autoignition Chemistry of the Hexane Isomers: An Experimental and Kinetic Modeling Study", Society of Automotive Engineers Paper SAE# 952406, 1995.

Donovan, R. J., and Husain, D., Trans. Faraday Soc., 62, 2987, 1966.

Engleman, V. S., Bartok, W., and Longwell, J. P., "Experimental and Theoretical Studies of NO_X Formation in a Jet-Stirred Combustor", In *Proceedings of the 14th Symposium (International) on Combustion*, The Combustion Institute, Pittsburgh, 1993.

Liss, W. E., Thrasher, W. H., Steinmetz, G. F., Chowdiah, P., and Attari, A. "Variability of Natural Gas Composition in Select Major Metropolitan Areas of the United States", Gas Research Institute Report No. GRI-92/0123, 1992

Naber, J., D., Siebers, D. L., Caton, J. A., Westbrook, C. K., and Di Julio, S. S. "Natural Gas Autoignition under Diesel Conditions: Experiments and Chemical Kinetic Modeling." Society of Automotive Paper SAE # 942034, 1994.

Naber, J., D., and Siebers, D. L. "Hydrogen Combustion under Diesel Conditions." To be presented at the 11th World Hydrogen Energy Conference, Stuttgart, Germany, June 23-28, 1996.

Obert, E. F., 1973. Internal Combustion Engines and Air Pollution. New York: Harper and Row, Publishers.

Phillips 66, 1962. Reference Data for Hydrocarbons and Petro-Sulfer Compounds, Phillips Petroleum Company, Bulletin No. 521, Reprinted 1984,

Figure Captions

- Figure 1. NO_X versus H₂-Air equivalence ratio. Experimental data are denoted by solid circles. Model predictions are denoted by solid symbols with curve drawn.
- Figure 2. NO_X versus H₂-Air equivalence ratio. Experimental data are denoted by solid circles. Model predictions are denoted by solid symbols with curve drawn.
- Figure 3. Equilibrium Calculations for various Br2 concentrations inwater at 1100K, 1200K, and 1250K. HBr Yield is defined as Yield = XHBr Formed / 2 times XBr2 Input, where X = Mole Fraction.
- Figure 4. HBr Yield versus percent Br₂ in Br₂-H₂O mixtures at 1175K. HBr yield is defined as Yield = XHBr Formed / 2 times XBr₂Input, where X = Mole Fraction.
- Figure 5: Research octane rating versus critical compression ratio for hydrogen/methane mixtures. The solid curve is a fit of Leppard's critical compression data for primary reference fuels and heptane isomers. The experimental data ranged from critical compression ratios of 6 to 19. The solid curve was linearly extrapolated from a critical compression ratio of 19 to 30. The squares are predictions for hydrogen/methane mixtures.
- Figure 6: Research octane rating versus critical compression ratio for hydrogen/natural gas mixtures. The solid curve is a fit of Leppard's critical compression data for primary reference fuels and heptane isomers. The experimental data ranged from critical compression ratios of 6 to 19. The solid curve was linearly extrapolated from a critical compression ratio of 19 to 30. The squares are predictions for hydrogen/natural gas mixtures.

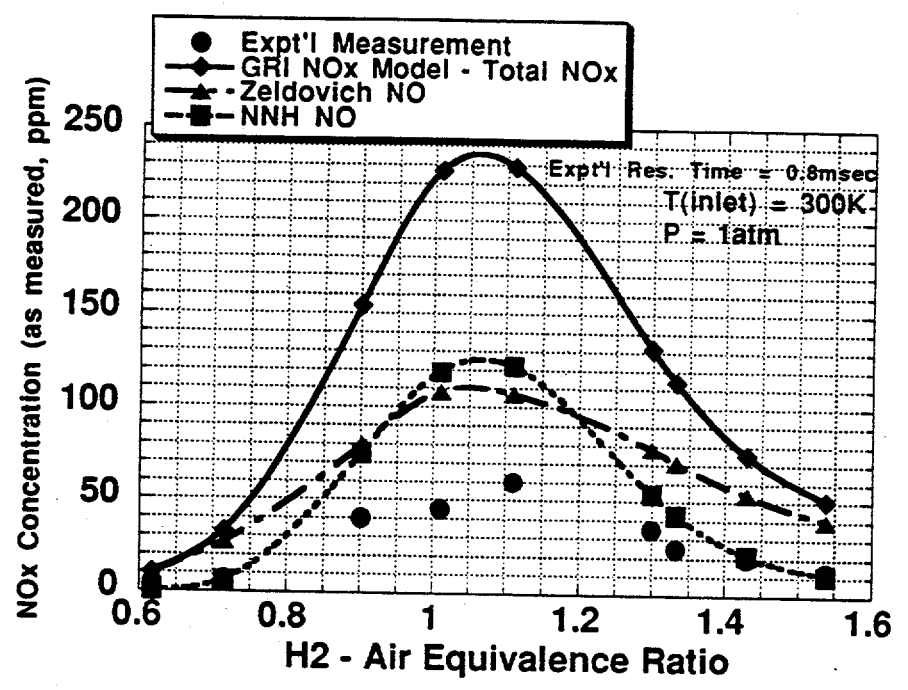


Figure 1. NO_X versus H₂-Air equivalence ratio. Experimental datadenoted by solid circles. Model predictions denoted by solid symbols with curve drawn.

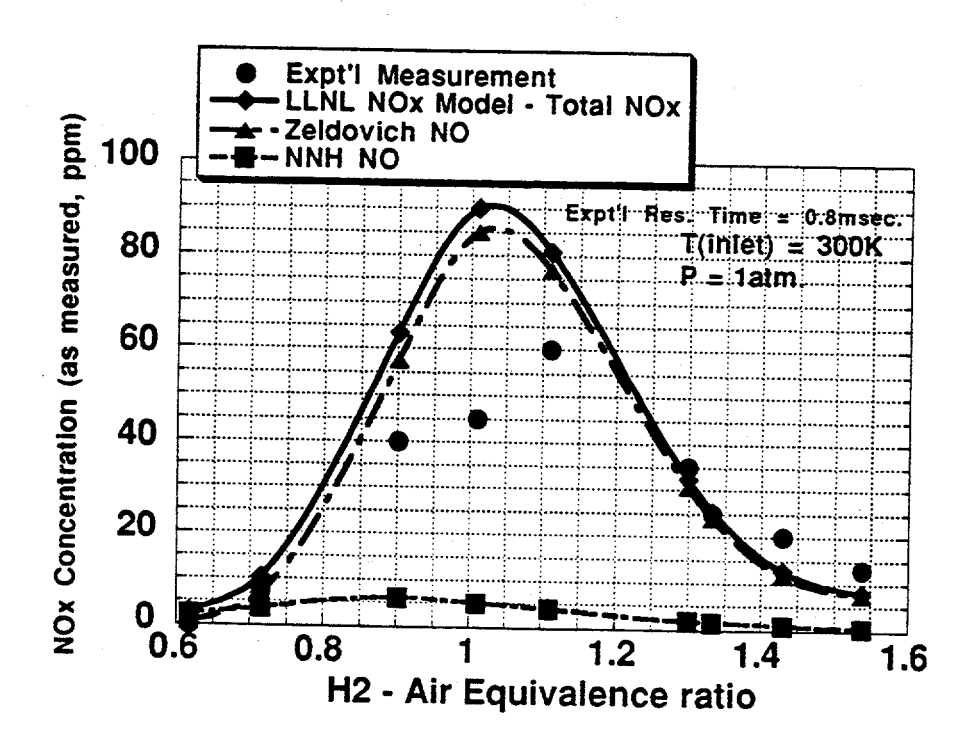
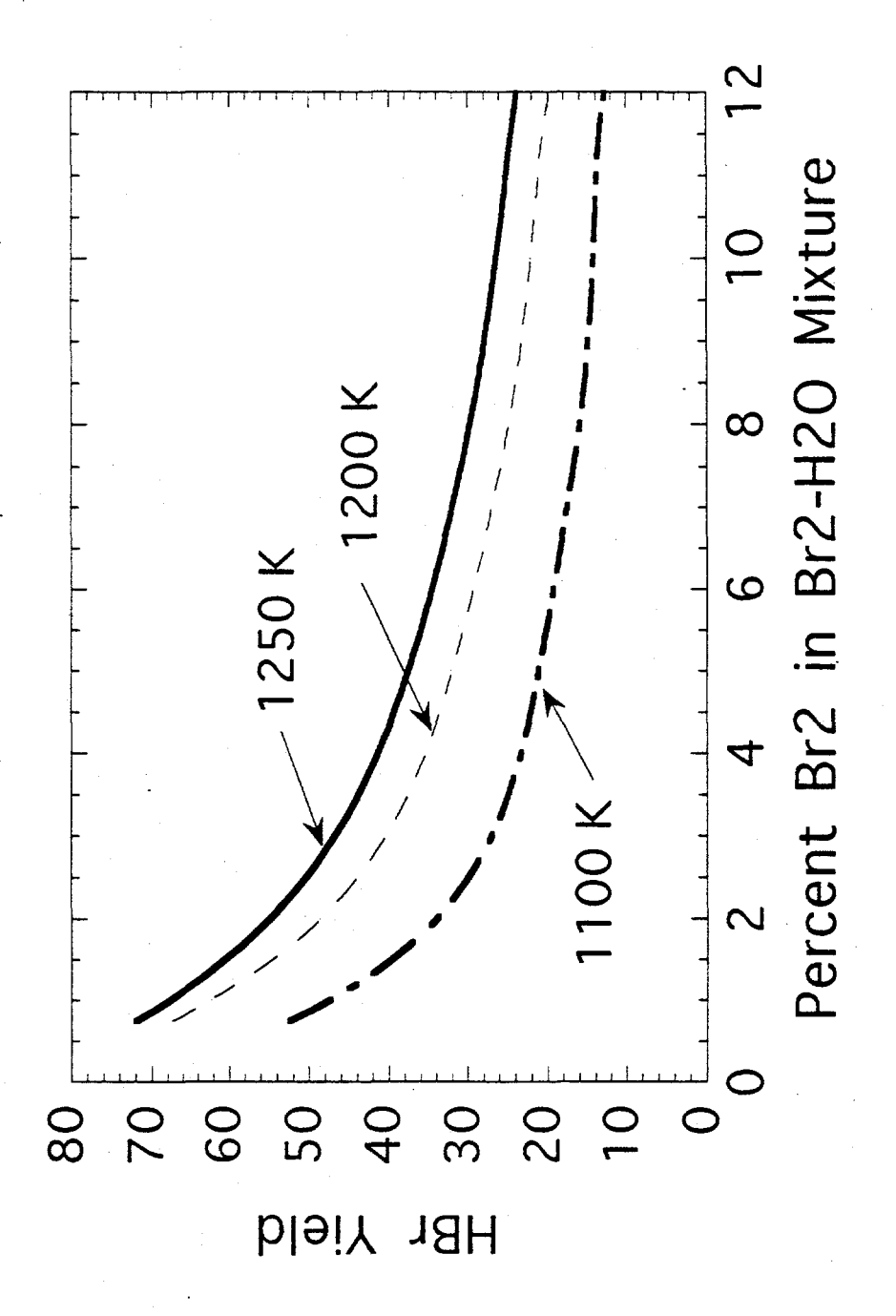
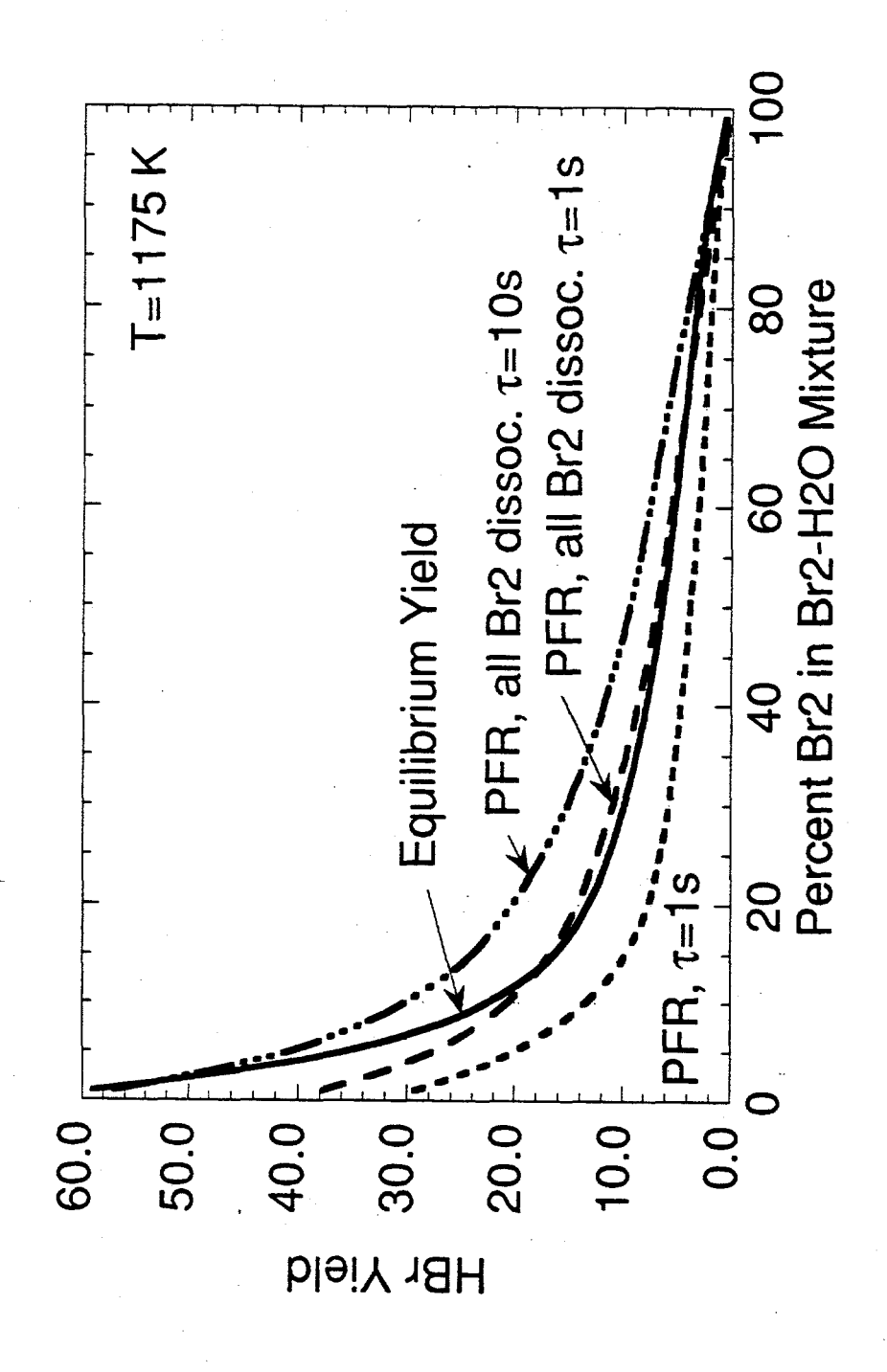
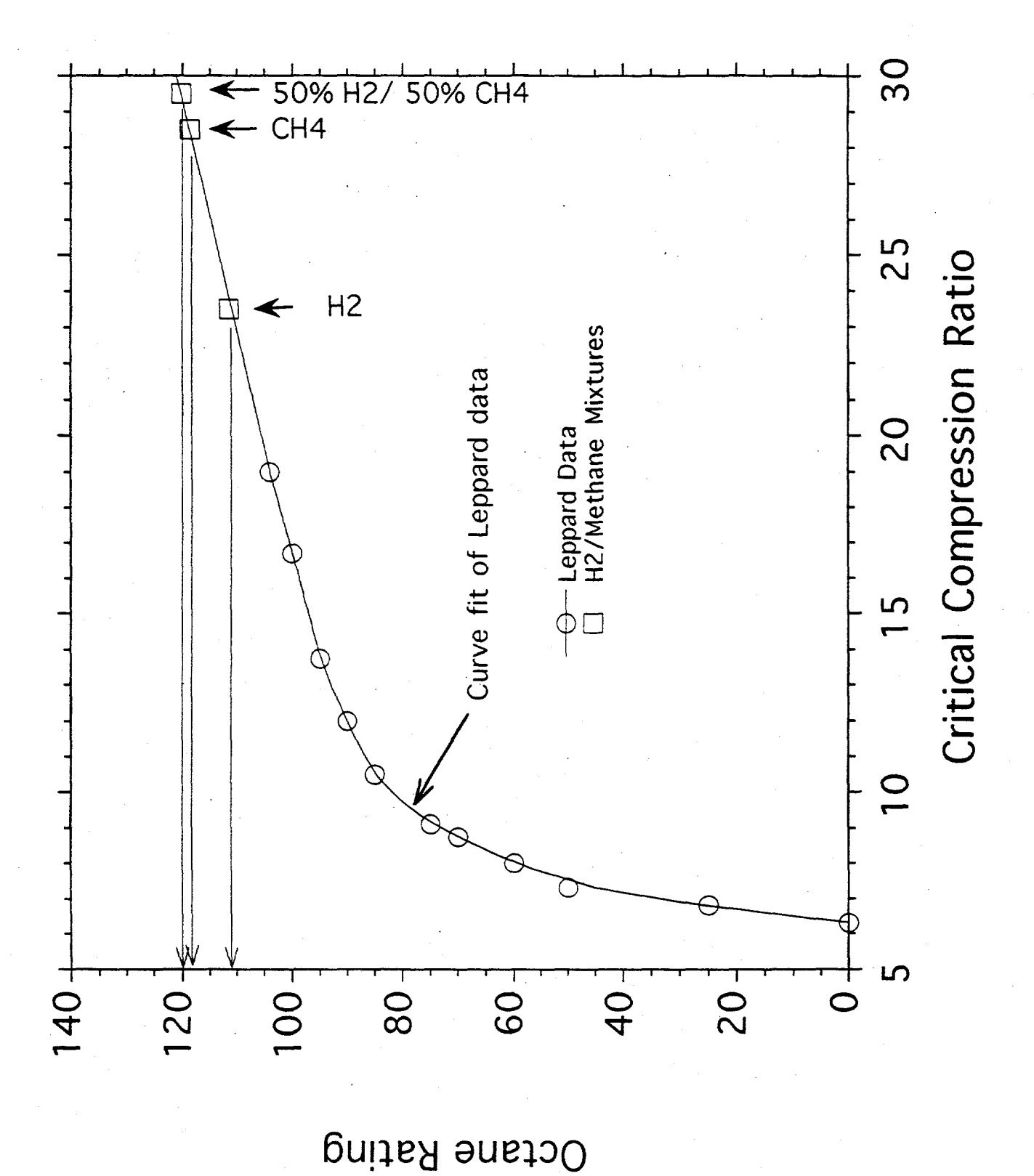
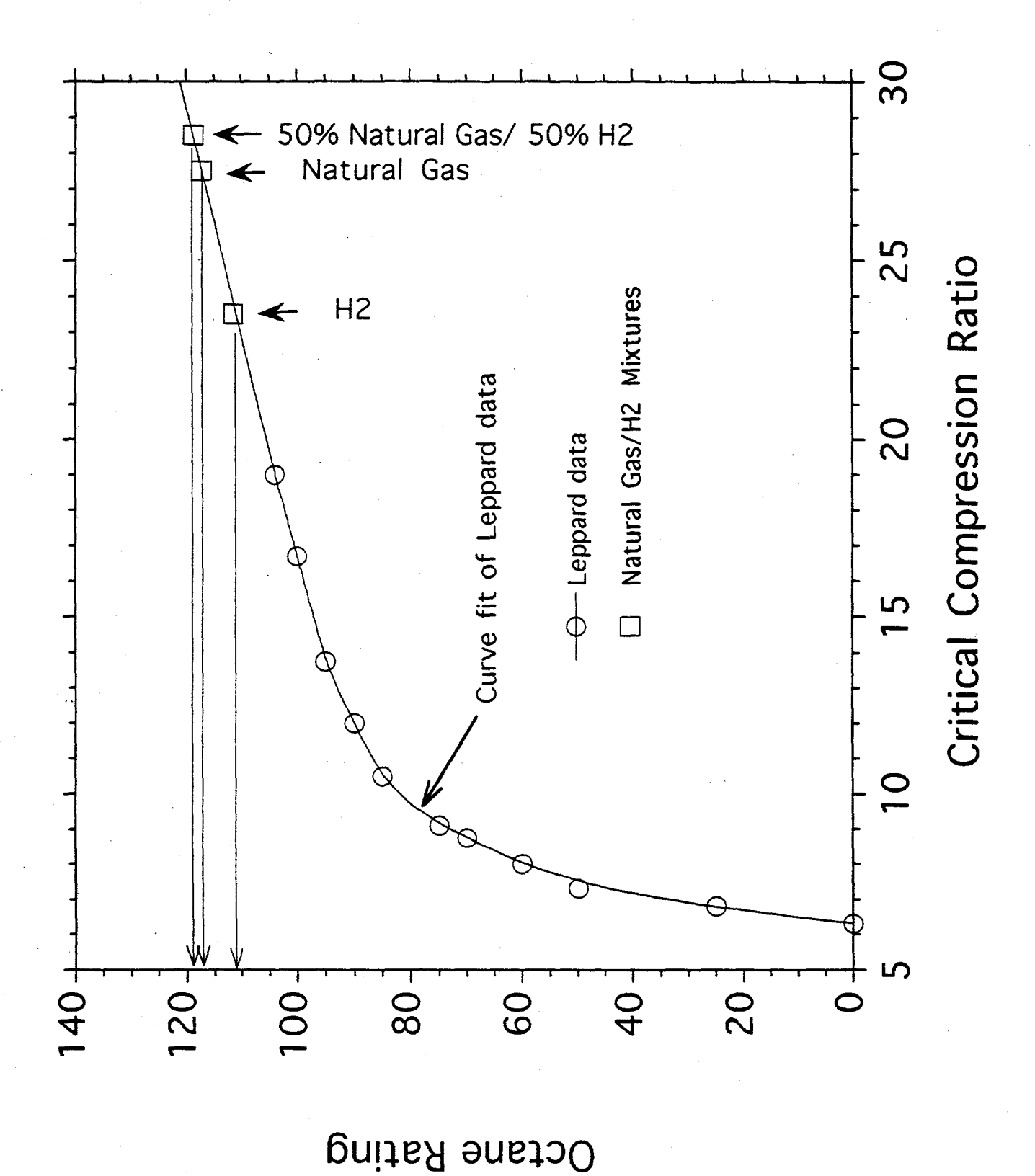


Figure 2. NO_X versus H₂-Air equivalence ratio. Experimental data denoted by solid circles. Model predictions denoted by solid symbols with curve drawn.









HYDROGEN ENGINE DEVELOPMENT: EXPERIMENTAL PROGRAM

Peter Van Blarigan Sandia National Laboratory Livermore, CA 94550

Abstract

In the continuing development of a hydrogen fueled IC engine optimized for application to a generator set or hybrid vehicle, experiments were performed at Sandia National Laboratories on two engine configurations. The intent is to maximize thermal efficiency while complying with strict emissions standards. The initial investigation was conducted utilizing a spark ignited 0.491 liter single cylinder Onan engine and has progressed to a spark ignited 0.850 liter modified for single cylinder operation Perkins engine. Both combustion chamber geometries were "pancake" shaped and achieved a compression ratio of 14:1. The engines were operated under premixed conditions. The results demonstrate that both engines can comply with the California Air Resources Board's proposed Equivalent Zero Emission Vehicle standards for NO_x during operation at an equivalence ratio of 0.4. The Onan engine achieved an indicated thermal efficiency of 43% at 1800 RPM, as determined by integration of the pressure-volume relationships. Initial experiments with the larger displacement Perkins engine have realized a gain, relative to the Onan engine, in indicated thermal efficiency of 2% at 1800 RPM, and 15% at 1200 RPM.

Introduction

Engine development in recent years has been guided by concerns for emissions, as well as depletion of world oil reserves. In an effort to address these concerns, Sandia National Laboratories is collaborating with Los Alamos and Lawrence Livermore National Laboratories (LANL, LLNL) to develop a hydrogen fueled IC engine for application to either a generator set or hybrid vehicle. The approach has been to utilize the fundamental differences between hydrogen and conventional fuels in their application to an internal combustion engine; to take advantage of hydrogen's unique fuel characteristics which include high flame speed, ignitibility of homogeneous mixtures at low

equivalence ratios, and high effective octane; and to design specifically for this constant speed, constant power application. The final design hopes to achieve high brake thermal efficiencies (over 40%) while realizing low emissions without the need for exhaust gas after treatment. The emissions goal is to comply with the California Air Resources Board's (CARB) proposed standard for Equivalent Zero Emission Vehicle (EZEV) limits (CARB 1995).

An approach in this manner, when combined with the aspects of energy storage for a hybrid power train, could allow operation in a constant power, on/off regime. It is anticipated that in an application of this type both the emissions and the thermal efficiency would be competitive with fuel cell power trains (Patil 1996), and thus offer a low cost interim solution in transition to the next generation of vehicles. In addition, the internal combustion engine approach may also allow operation using a blend of natural gas and hydrogen - an attractive option that could ease the transition to a hydrogen infrastructure.

The preliminary development of the research program included a characterization of hydrogen combustion in two lean burn spark ignited engines. The possibility of using natural gas and a blend of hydrogen and natural gas was also investigated in support of multi-cylinder engine experiments at the University of Central Florida (Hoekstra 1996). This paper outlines the engine development thus far and specifically details the progress of the experimental program at Sandia.

Background

The goal of the experimental program thus far has been to maximize the indicated thermal efficiency of a homogeneously charged, spark ignited engine operating on hydrogen fuel. Indicated thermal efficiency is defined here as the work done on the piston by the cylinder gases divided by the fuel energy content. The NO_x emissions have been reduced to the desired EZEV level by operating at a sufficiently low equivalence ratio. That this NO_x emission level can be achieved was verified by Sandia using a Cooperative Lubrication Research (CLR) engine at various compression ratios (Van Blarigan 1995).

In order to maximize the theoretical efficiency of the Otto cycle on which the SI engine is based, four conditions are desired (Heywood 1988, Edson and Taylor 1964):

- 1. Combustion should occur as close as possible to top dead center (TDC). This would approach the constant volume condition and result in a higher peak pressure.
- 2. Heat loss from the cylinder gases to the engine should be minimized. More energy could therefore be converted to useful work.
- 3. Compression ratio should be as high as possible.
- 4. The mixture should be lean to reduce the losses associated with the fuel availability.

The typical Otto engine cycle using homogeneous mixtures of conventional hydrocarbon fuels is a compromise of these ideals: typically combustion begins 10 - 30° before TDC and ends 40° after TDC (a burn duration of 50 - 70 crank angle degrees (CAD)), heat transfer losses account for 20 - 35% of the fuel energy, compression ratio is limited to about 10:1 due to autoignition (knock), and operation is not possible below an equivalence ratio of about 0.65.

Caris and Nelson (1959) investigated the effect of compression ratio on the efficiency of production General Motors Corporation V-8 engines modified for high compression ratio and found that brake thermal efficiency was maximized at a compression ratio of 17:1. They suggested that the increasing departure from theoretical behavior as the compression ratio is increased is due to a longer

burn duration at these higher compression ratios and/or the dissociation of the combustion products resulting in a pressure limit. Edson (1964) later studied the dissociation issue and concluded that this was a second-order effect at practical compression ratios. Thus it appears that Caris and Nelson effectively demonstrated that, in their engine geometry, burn duration is the major detriment to the efficiency increase expected with increasing compression ratio.

In contrast, Muranaka et al (1987) argued that heat loss from the combustion gases to the engine is a more significant loss mechanism at higher compression ratios provided a sufficiently rapid combustion occurs (40 CAD). Thus two schools of thought have materialized: one stating that in-cylinder turbulence and flow velocity should be minimized at the expense of burn duration (within limits), thereby reducing heat transfer losses. The other approach uses turbulence and in-cylinder flow to achieve rapid combustion, thereby reducing finite burn duration loss at the expense of higher heat loss, while allowing for operation with leaner mixtures.

Smith et al (1995) concluded that the most promising approach for optimizing the thermal efficiency in a hydrogen fueled engine is to design a quiescent combustion chamber with sufficient reaction rate achieved by utilizing multiple spark ignition. This would have the net affect of minimizing both heat transfer and timing losses. As a result of their efforts an Onan engine was modified and tested to verify their conclusion.

The efforts to achieve the goals of this program have thus concentrated on experimental and analytical studies of an optimum combination of flow induced turbulence, compression ratio, ignition site(s) and combustion chamber geometry specific to hydrogen fuel. The level of effort is approximately two full time employees.

Engines

To date two engines have been tested; their specifications are given in Table 1 and a brief discussion follows. The experimental procedures and diagnostics for both engines were essentially identical and are subsequently described.

Table 1: Engine Specifications

	Onan	Perkins
Bore	82.55 mm	91.44 mm
Stroke	92.08 mm	127.0 mm
Displacement	0.4928 L	0.834 L
Compression Ratio	14.04:1	14.04:1
Valve Timing	stock	stock
Spark Plugs	Champion 53R	Champion A49R
Ignition System	Mallory HyFire 667 CDI (2 systems)	Mallory HyFire 667 CDI (1 system)
	Mallory ProMaster	Mallory ProMaster
	28880 coils	28880 coils
Inlet System	Pressurized, Unthrottled	Pressurized, Unthrottled

Onan Engine - The Onan engine employed was a modification of a diesel engine used to power the cooling system of refrigerated truck trailers. Following (Smith 1995), the existing iron cylinder head was discarded and replaced with an aluminum unit designed and built by LLNL with provision for pressure measurement and two point ignition. Both the piston top and the cylinder head were flat, resulting in a "pancake" combustion chamber shape at top dead center. The spark plugs were located on a common diameter line equidistant from the wall and the cylinder center. The inlet runner was configured for low swirl (less than 15 RPM/CFM) by aligning it with the cylinder center.

Modeling of the in-cylinder flow was performed by LANL using the KIVA three dimensional computational fluid dynamics (CFD) code (Johnson 1995). The calculations suggested that a tumbling motion developed in the cylinder during induction of the fresh charge and that the combustion chamber was not quiescent.

Though this tumbling motion was not confirmed experimentally, an attempt was made to modify it by use of a shrouded intake valve. Each shroud was designed to allow flow through only 180 degrees of the valve circumference during a specified portion of the valve travel. Shrouded valves of various height were tested in the engine as well as characterized on a steady flow swirl test rig (Swain 1995). The flow test utilized an on-axis spinner in a transparent cylinder, where the rotational speed was measured stroboscopically. Figure 1 shows the results of these tests for three different shroud configurations (1.5, 3.1, and 6.2 mm high), as well as an unshrouded valve, and a standard high swirl 2.0 liter Chevrolet cylinder head. It can be seen from the figure that a wide range of swirl variation was possible.

Perkins Engine - After investigation of the Onan configuration a three cylinder Perkins 3.152D engine was selected to determine the effect of a larger piston displacement on thermal efficiency. Single cylinder operation was accomplished by removing the pushrods from Cylinders 2 and 3 and fabricating a new, separate intake manifold for Cylinder 1. The existing cast iron cylinder head was modified to provide a pressure transducer port, as well as allow spark plug access on Cylinder 1's central axis, through the diesel fuel injection port. As in the Onan engine, both the piston top and the cylinder head were flat which resulted in a "pancake" combustion chamber shape at top dead center.

An additional goal with the Perkins engine was to increase the cylinder clearance height at top dead center, the net result of which would be to decrease the surface area-to-volume ratio at TDC by 16%. The expected result of these changes was a reduction in heat loss from the combustion gases and a resulting higher thermal efficiency. Experience with the twin spark plug configuration on the Onan had shown that while more ignition advance was required for peak efficiency with one spark plug relative to two, the thermal efficiency for both cases was almost identical. In the Perkins engine the inlet port was configured tangential to the cylinder and this created conditions for high swirl generation, however the swirl level has not yet been quantified or optimized.

The compression ratio of each engine was determined by calculating the cylinder volume at top and bottom dead center and combining it with the free volume of the head, and that above the top piston ring. The volume of the cylinder head was determined by bolting the head to a flat plate and using a precision gas volume measurement system $(\pm 1.0\%)$.

The leakage of the engine through valves and past the piston was determined in a two step process. First, the flat plate fixture described above for determining the compression ratio was used in conjunction with a pressure/temperature instrumented reservoir to apply high pressures to the combustion chamber side of the cylinder head in a leakdown fashion. The mass leakage past the valves during this leakdown test as a function of time was then inferred by use of the reservoir pressure/temperature history. The mass leak rate versus reservoir pressure information was used to predict the total gas loss during a complete engine cycle by integrating a typical cylinder pressure history for both motoring and firing conditions.

Next, the leakage past the piston was determined by carefully sealing the engine crankcase and operating the engine under both motoring and firing conditions for a known length of time. The gases that escaped were collected from the crankcase breather tube (the only exit) in a bag. These gases were quantified by transfer to a known volume and then through use of well known pressure-volume-temperature (PVT) analysis.

The results of these tests are shown in Figure 2. Leakage past the valves, as a percent of displaced mass, for both the motoring and firing cases, is shown as a function of crank angle. Also listed are the conclusions of the bag measurement tests. When added together, the total $(2.25\% \text{ of displacement}, \pm 2.0\%$, for the firing case) is consistent with published results (Ferguson 1986). Though this method of determining engine leakage is unique, the author believes that assumptions made during the calculations lead to a comparable result.

No exhaust gas recirculation was employed in these tests.

Experimental Setup - The test engines were coupled to an Emerson Electric Company model 2110B321E00-DC dynamometer that maintained a constant engine speed regardless of engine output. A Lebow model 1604 torque transducer was located between the engine and dynamometer, the output indicated on a strip chart recorder. This record was useful for determining best torque vs. ignition timing, as well as engine roughness. This record was not used, however, to calculate thermal efficiency due to the large friction component present in these research engines.

Figure 3 is a system schematic of the fuel/air inlet system. The intent of the experiments with hydrogen was to operate in a fully homogeneous charge regime, and numerous steps were therefore taken to assure this condition. The hydrogen and air fed to the engine were supplied at 800 kPa. The hydrogen was controlled by an MKS model 1559A mass flow controller calibrated for hydrogen by MKS. Air and fuel were mixed in a stagnation chamber, passed through a sonic orifice and conveyed through the intake manifold to the engine. Stagnation chamber pressure was measured with a Heise model 901 pressure transducer (1,400 kPa full scale). The sonic orifice was machined to present a 2:1 elliptical contour to the upstream flow, and the diameter is measured to within 0.0025 mm.

The mass flow rate of the mixed gases could consequently be calculated using standard sonic orifice relationships; the air flow rate was determined by subtracting off the hydrogen flow.

This intake system had several attractive features. First, the pressure upstream of the orifice was steady; this resulted in a continuous mixing of the fuel and air devoid of the flow fluctuations characteristic of single cylinder engines. Second, the passage of the gases through a sonic orifice developed a violent mixing environment. Third, the engine could be either supercharged or run at sub-atmospheric pressure by adjusting the upstream air pressure. No inlet throttling, other than the sonic orifice, was employed.

Crankshaft position was determined by a BEI Motion Systems Company model H25E-F3-SS-720-ABZC-7406R-LED-EMI8 optical shaft encoder coupled directly to the crankshaft. This unit provided 720 position pulses every revolution of the crankshaft, as well as a top dead center pulse.

Pressure Measurement - The engine was equipped with an AVL model QC42D-X quartz pressure transducer for in-cylinder pressure measurement. The charge output of the transducer was converted to voltage by a Kistler type 5010A dual mode amplifier and fed to a Data Translation DT2821-F-16SE 12 bit analog-to-digital conversion board. A Pentium-based 90 MHz PC controlled the system and recorded the crankshaft position, as well as intake manifold pressure at two locations using Teledyne-Taber model 254 strain gage transducers, each amplified by Daytronic model 3270 signal conditioners. The AVL quartz transducer was set by the PC to a defined reference value at 150 degrees into each cycle (the end of the inlet stroke).

Calibration of the AVL transducer was accomplished by rapidly applying a pressurized gas and comparing the output to a calibrated Heise 901B transducer of appropriate range. Agreement between the two transducers was within 0.2% at full scale (8,000 kPa).

Emissions Measurements - The exhaust gases were continuously sampled 8 cm from the cylinder head. The gases were transferred first through a heated line (100°C), then through a cold trap, and finally to a Rosemont Analytical Inc. model 951A Chemiluminescent NO/NO, Analyzer. Calibration of this instrument with both zero emissions and 12 PPM NO calibration gases was performed both before and after each test series. Hydrocarbon based emissions from the engines were not quantified in these tests and will need to be addressed later.

System Flow Calibration - The fuel flow rate calibration of the MKS flow meter was verified by two methods. First, an orifice was manufactured to specifically measure fuel flow using the existing sonic flow diagnostic. As well, a 299.44±0.10 liter vessel was used with PVT analysis to measure the total fuel flow at a constant rate over a fixed time. Results of these two methods and the MKS flow meter agreed to within 1%.

A similar calibration procedure for the air flow system also verified agreement to within 1%.

Fuels and Air - The hydrogen used was at least 99.9% pure, supplied from pressurized cylinders. The natural gas was purchased as Tennessee Natural Gas, consisting of 93.6% methane, 3.6% ethane, 1.0% propane, 0.7% carbon dioxide, 0.5% nitrogen and 0.4% butane. The 30% hydrogen blend was made up containing 67.5% methane, 2.5% ethane and 30.0% hydrogen. The air was supplied from an air compressor, run through a desiccator and filtered.

Test Procedure - The Onan engine was operated until the coolant temperature had stabilized at 45 - 50 C (typically 45 minutes). While this temperature was less than typical for modern engines, concern for the aluminum head (due to rather small coolant passages) motivated this limit. The Perkins engine was stabilized at 75 C. During this time the NO, analyzer was calibrated with both zero emission gas and span gas. After the initial warm-up the test conditions were set and the engine was allowed to reach steady state. Following the stabilization, data was taken. Pressure data were recorded for 100 cycles and stored as the average at 0.5 degree sample point intervals.

Most tests were conducted at volumetric efficiencies of approximately 100% meaning that the mass of fuel/air charge inducted each cycle was equivalent to the mass that would be contained in the displacement volume at local atmospheric pressure and room temperature.

Experimental Results

The goals of the experimental program were to quantify and optimize the indicated thermal efficiencies and NO_x emissions from these hydrogen fueled engines. Indicated thermal efficiencies, based on integrated work and measured fuel flow rates, were compared. As well, the NO_x emissions results were compared to the CARB proposed EZEV standards.

Indicated mean effective pressure was calculated through two revolutions of the crankshaft - a full four stroke cycle. The average pressure from 100 cycles was integrated as a function of volume to determine the average work.

The indicated thermal efficiency was calculated using the average work and the lower heating value of the appropriate fuel. Where experimental results for volumetric efficiencies of other than 100% are presented the indicated thermal efficiency was calculated from the power stroke only (one

revolution of the crankshaft), removing from the calculation the work produced or absorbed by the inlet/exhaust process.

Since the proposed standards are specified as emissions in weight per unit distance, vehicle efficiency must be taken into account. Here a final conversion efficiency of 60 miles per gallon (MPG) gasoline equivalent is assumed, as this is generally believed to be reasonable for a hybrid vehicle (Moore 1995). The standards are therefore valid for any test cycle provided the vehicle achieves 60 MPG during that cycle. Equivalence ratio (ϕ) is also a factor when emissions are measured in parts per million (PPM). Additionally, the engine is assumed to operate in the constant power, on/off mode with startup/shutdown emissions the same as the operating emissions. Figure 4 portrays the NO_x level limit in PPM that must not be exceeded in order to meet the CARB proposed EZEV standards as a function of ϕ . The development for this plot is given in the Appendix.

Additional tests were conducted with the Onan engine to determine the minimum ϕ at which the engine would operate. This turned out to be $\phi = 0.20$ for hydrogen, $\phi = 0.48$ for the 30% hydrogen fuel and $\phi = 0.62$ for natural gas. These values were determined by the inability to ignite the fuel at lower equivalence ratios, meaning simply the engine abruptly failed to generate power.

While the absolute accuracy of the indicated thermal efficiency could not be quantified, the same diagnostics and analysis were performed on both engines. Repeatability of the measurements was excellent, and changes in engine performance were consistently detectable. Thus the use of these standards as a means of optimizing the performance of the combustion parameters is valid.

Onan Engine - To optimize the indicated thermal efficiency with regard to inlet flow generated swirl, each of the valve shrouds previously discussed was tested under similar operating conditions. Figure 5 presents the results of this investigation, showing that the intermediate size shrouds produced the best results. The following data was produced with the 1.5 mm shroud in place; the 3.1 mm shroud had cracked due to mechanical stresses induced during the welding process.

The Onan engine test results are presented for three fuels (hydrogen, 30/70% hydrogen/natural gas, and natural gas) at 1800 RPM for equivalence ratios which produced acceptable NO, levels.

Figure 6 presents NO_x and indicated thermal efficiency results as a function of spark advance before TDC for hydrogen at three equivalence ratios. The CARB proposed EZEV NO_x limit is included (the shaded line indicates the range). It can be seen that operation above $\phi = 0.4$ is not in compliance for the spark advances recorded. A similar presentation of results for natural gas is contained in Figure 7. From this plot it can be seen that the CARB proposed EZEV standards cannot be met with this fuel. Operation at $\phi = 0.62$ was erratic, but when increased to 0.64 engine smoothness and torque improved markedly.

The same type of plot for the 30/70% fuel is shown in Figure 8. Operation at $\phi < 0.52$ incurs a large efficiency penalty, however, when set at $\phi = 0.52$ the results seemed reasonable. From these series of plots it can be seen that operation near maximum brake torque (MBT) timing with hydrogen at $\phi = 0.40$ and with 30% hydrogen at $\phi = 0.52$ give similar NO_x results. This is more clearly demonstrated in Figure 9.

Perkins Engine - Experimental results from the Perkins engine are shown for 1800 RPM in Figure 10. These results are to be compared with the Onan results shown in Figure 6. An improvement of 2% in indicated efficiency is realized by the Perkins at this speed.

The improvement is more significant at 1200 RPM (an increase of 15%), as shown in Figure 11, which presents both Onan and Perkins results for 1200 RPM at an equivalence ratio of 0.4.

Discussion

The effort to optimize indicated thermal efficiency utilizing hydrogen fuel is producing a steady improvement in test engine performance. The Onan test series, which is now complete, has increased the indicated thermal efficiency relative to the CLR engine (Van Blarigan 1995) by 12% at useful operating conditions. The best results are shown in Figure 12, which presents the Onan performance at various volumetric efficiencies. Operation at boost levels typical of a turbocharged engine produces 44% indicated thermal efficiency with only a small NO_x penalty. This data was taken at MBT timing; slight spark retardation would reduce the NO_x levels significantly, in compliance with the proposed NO_x standards.

The Perkins experiment is intended to improve upon the indicated thermal efficiency of the Onan by utilizing an increased stroke and volume-to-surface area ratio, resulting in proportionally less heat loss from the gases to the engine. These results can be compared to the work of Olsson and Johansson (1995). Their work with natural gas in a large (1.6 liter) diesel converted to spark ignition engine reported an indicated efficiency of 49% for the most favorable combustion chamber geometry (similar to ours), at 1200 RPM and a compression ratio of 12:1. The Perkins engine displacement is smaller than this, but is thought to be a workable compromise for a hybrid vehicle engine, and has produced indicated thermal efficiency of 45% with hydrogen fuel in our first test series. It can be inferred, therefore, that the surface area-to-volume ratio is an important factor influencing the energy conversion efficiency.

In this research program, maximization of the indicated thermal efficiency at a specific speed has required the optimization of the in-cylinder flow conditions at that speed. Figure 13 displays the indicated efficiency of both the Onan and Perkins engines at an equivalence ratio of about 0.4, and 100% volumetric efficiency. It can be seen that the variation with engine speed is different for each engine. Interestingly though, the burn duration for each of the conditions shown was quite similar, as depicted in Figure 14.

It should be noted that the Onan engine has been optimized for operation with hydrogen, not a mixed fuel. The reaction rate and burn duration are not necessarily optimal for these slower burning mixtures. This effect may, however, cause the falloff in efficiency with reduced ϕ for the mixed fuel, as well as natural gas relative to hydrogen.

The indicated thermal efficiency penalty measured in the mixed gas test series (6% less for the 30/70% fuel relative to hydrogen) is both small and, possibly, correctable. The burn duration for the case of hydrogen and the hydrogen/natural gas blend operated at similar NO, emissions and speed were calculated from the cylinder pressure-volume data according to the method of Rassweiler and Withrow (January 14, 1938). Figure 15 shows that the burn duration of the blended fuel under these conditions is longer, perhaps too long for peak efficiency.

Finally, it should be mentioned that neither engine knocking nor preignition were a problem during the operation of these engines. While it was possible to achieve knocking with these engines by advancing the spark, the timing required was considerably advanced of MBT. This may be due to the precise mixing of fuel and air combined with the low equivalence ratio tested. The question of engine deposits forming ignition sites as the engine ages have not been addressed here.

Conclusion

It has been shown that the CARB proposed EZEV NO, standards can be met without exhaust gas after treatment using hydrogen fueled spark ignited IC engines operating at high compression

ratio (14:1) and low equivalence ratio (0.4) for application to a hybrid vehicle employing constant speed, constant power on/off engine operation. Other regulated emissions due to combustion of the lubricating oil have not yet been measured, but will be quantified in the future. Optimization of incylinder flow, engine speed, compression ratio, and combustion chamber geometry will further improve the indicated thermal efficiency of the Perkins research engine beyond the 45% reported here.

Acknowledgments

This work was performed at the Combustion Research Facility, Sandia National Laboratories / California and supported by the U.S. Department of Energy, Office of Energy Efficiency and Renewable Energy. Thanks are due to Dr. Robert Green of Sandia for the CLR results, Dr. Norman Johnson of Los Alamos National Laboratory for the KIVA calculations, and Professor Mike Swain of the University of Miami for the Onan swirl measurements. As well, Scott Goldsborough and David Zanini were of technical assistance throughout this program.

References

Caris, D. F. and Nelson, E. E. 1959. "A New Look at High Compression Engines", SAE Trans., Vol. 67, pp. 112 - 124.

California Air Resources Board (CARB). September 1995. Proposed equivalent zero emission vehicle standards, in IEEE Spectrum, page 72.

Edson, M. H. 1964. "The Influence of Compression Ratio and Dissociation on Ideal Otto Cycle Engine Thermal Efficiency", in Digital Calculations of Engine Cycles, SAE Progress in Technology, Vol. 7, pp. 49 - 64.

Edson, M. H., and Taylor, D. F. 1964. "The Limits of Engine Performance - Comparison of Actual and Theoretical Cycles", in Digital Calculations of Engine Cycles, SAE Progress in Technology Vol. 7, pp. 65 - 81.

Ferguson, C. R. 1986. Internal Combustion Engines. John Wiley & Sons. pp. 362 - 366.

Heywood, J. B. 1988. Internal Combustion Engine Fundamentals. McGraw-Hill.

Hoekstra, R. L., Van Blarigan, P. And Mulligan, N. 1996. "NO_x Emissions and Efficiency of Hydrogen, Natural Gas and Hydrogen/Natural Gas Blended Fuels", SAE Paper 961103.

Johansson, B. and Olsson, K. 1995. "Combustion Chambers for Natural Gas SI Engines Part 1: Fluid Flow and Combustion", SAE Paper 950469.

Johnson, N. L. 1995. Los Alamos National Laboratories, Private Communication.

Moore, T. C. and Lovins, A. B. 1995. "Vehicle Design Strategies to Meet and Exceed PNGV Goals", SAE Paper 951906.

Muranaka, S., Takagi, S. Y. and Ishida, T. 1987. "Factors Limiting the Improvement in Thermal Efficiency of S.I. Engines at Higher Compression Ratio", SAE Trans. 870548.

Olsson, K. and Johansson, B. 1995. "Combustion Chambers for Natural Gas SI Engines Part 2: Combustion and Emissions", SAE Paper 950517.

Patil, P. G. 1996. "Alternative Fuels in Future Vehicles", Automotive Engineering, pp. 39 - 43, January.

Rassweiler, Gerald M. and Withrow, Lloyd. January 14, 1938. "Motion Pictures of Engine Flames Correlated with Pressure Cards", SAE annual meeting, Detroit, MI, USA, January 14, 1938. Reprinted as SAE paper 800131.

Smith, J. R., Aceves, S. and Van Blarigan, P. 1995. "Series Hybrid Vehicles and Optimized Hydrogen Engine Design", SAE Paper 951955.

Swain, M. R. 1995. University of Miami, Private Correspondence of August 9.

Van Blarigan, P. and Green, R. 1995. "NO_x emission data verified in a hydrogen-fueled engine", Combustion Research Facility News, Vol. 17, No. 4, January/February.

List of Figures

Figure 1: The effect of valve lift on swirl in a steady flow swirl test rig.

Figure 2: Calculated mass loss through the power stroke at 1200 RPM.

Figure 3: Schematic of fuel/air inlet system.

Figure 4: NO_x limit vs Equivalence ratio to comply with CARB's proposed EZEV standard for NO_x for a vehicle attaining 60 MPG.

Figure 5: Indicated thermal efficiency vs Valve shroud height.

Figure 6: Indicated thermal efficiency and NO, vs Spark advance for hydrogen.

Figure 7: Indicated thermal efficiency and NO, vs Spark advance for natural gas.

Figure 8: Indicated thermal efficiency and NO, vs Spark advance for 30/70% blend.

Figure 9: Indicated thermal efficiency and NO, vs Spark advance. Hydrogen vs Blended fuel.

Figure 10: Indicated thermal efficiency and NO, vs Spark advance for the Perkins engine.

Figure 11: Indicated thermal efficiency and NO, vs Spark advance for the Onan and Perkins engines.

Figure 12: Indicated thermal efficiency and NO_x vs Indicated mean effective pressure for the Onan engine.

Figure 13: Indicated thermal efficiency vs Engine speed for the Onan and Perkins engines.

Figure 14: MBT timing and Burn duration vs Engine speed for the Onan and Perkins engines.

Figure 15: Burn duration vs Crank angle degree of the Onan engine using hydrogen and the 30/70% blend.

Appendix

CARB proposed EZEV NO_x standards are stated as weight per unit distance. For comparison of these standards to data taken from the NO/NO_x Analyzer, these figures were converted to parts per million (PPM) equivalent. This, however, assumes an overall vehicle conversion efficiency. The transformation of the CARB standards to PPM equivalent for hydrogen fuel follows. The same method was used for the natural gas and 30/70% hydrogen/natural gas fuels.

Realizing that the standards converted to PPM are more stringent for NO₂, the combustion equation can be written as,

$$H_2 + [1/2\phi] \{O_2 + 3.773N_2\} \Leftrightarrow H_2O + (Z/\phi)NO_2 + [(1.887/\phi) - (Z/2\phi)]N_2 + [(1-\phi)/2\phi - (Z/\phi)]O_2$$

Here it can be seen that the mole fraction of NO₂ in the product gases is given by,

$$NO_2$$
 (in PPM) = $[Z/\phi] / [1 + (1.887/\phi) + (1-\phi-Z)/2\phi] \times 10^6$

and the ratio of NO₂ formed per mole of hydrogen is expressed as

$$Z/\phi = [(PPM/2\phi)(\phi + 4.773)] / [1 \times 10^6 + (PPM/2)]$$

Using the lower heating value (LHV) of hydrogen, 0.242 MJ/mole, it can be shown that one gallon of gasoline energy is equivalent to 517 moles of hydrogen, where the LHV of gasoline is taken as 44.0 MJ/kg, and the average density is 2.84 kg/gal [4].

Therefore, the CARB proposed EZEV NO, standard can be expressed as

0.02 (gm NO₂/mile) =
$$Z/\phi$$
 (mole NO₂/mole H₂) * 517 (mole H₂/equivalent gallon gasoline) * 46.0 (gm NO₂/mole NO₂) * (1/MPG)

where MPG is the vehicle energy conversion efficiency in miles per gallon.

Finally, setting this limit as the maximum PPM that can be measured by the NO/NO, Analyzer to be in compliance, we have

$$PPM_{max} = [0.841 * MPG] / [(1/2\phi)(\phi + 4.773) - 4.3 \times 10^{-7} * MPG]$$

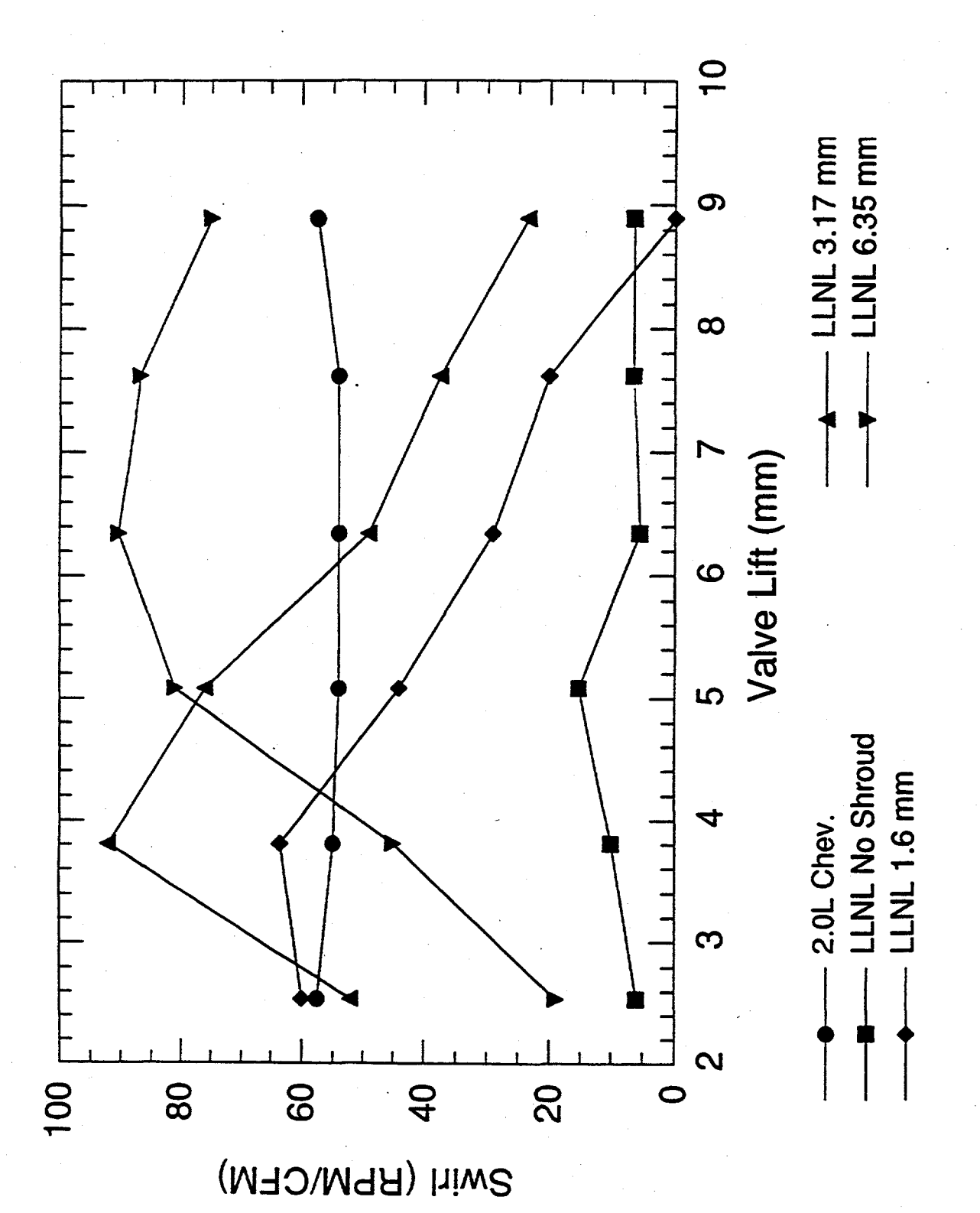


Figure 1: The effect of valve lift on swirl in a steady flow swirl test rig.

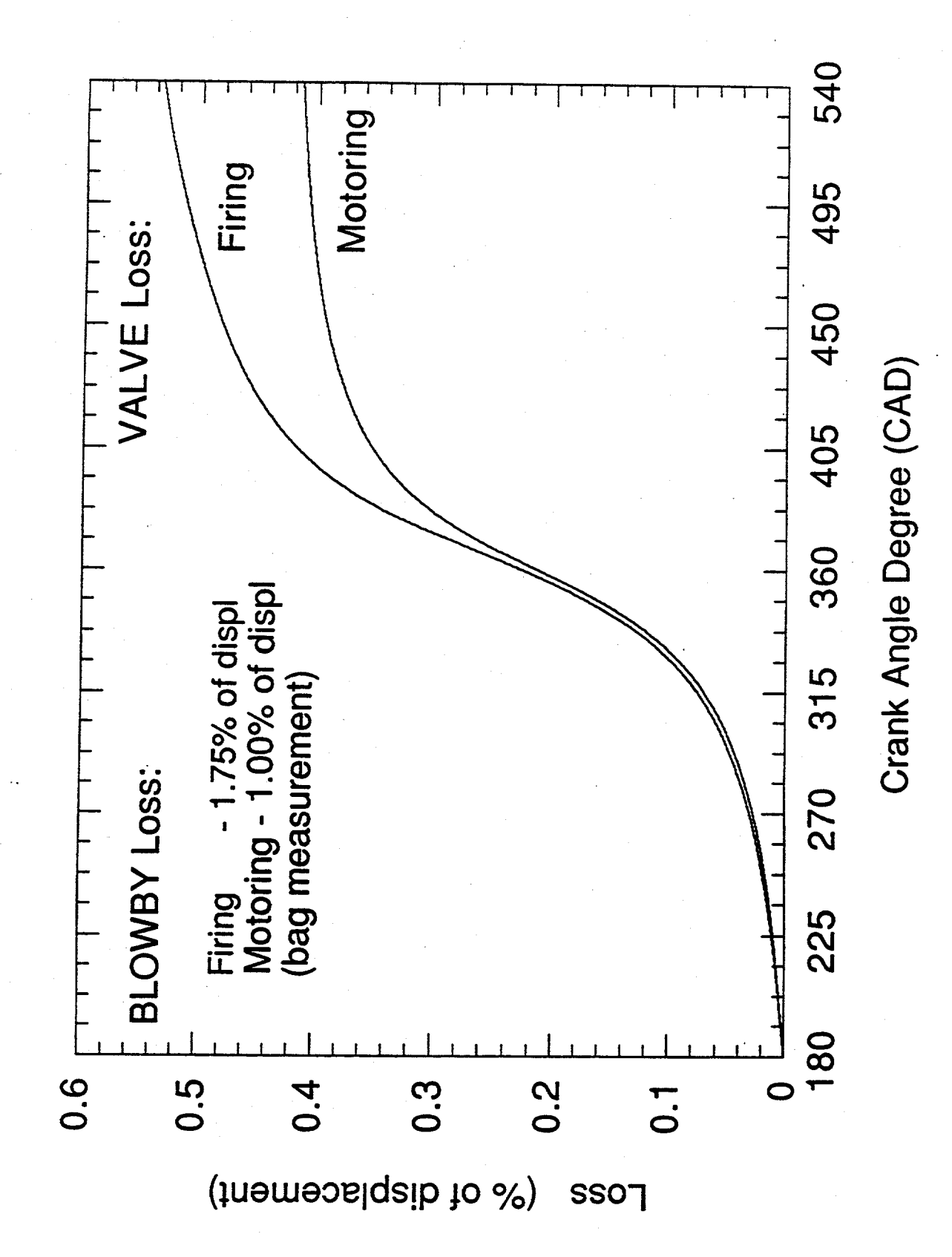


Figure 2: Calculated mass loss through the power stroke at 1200 RPM.

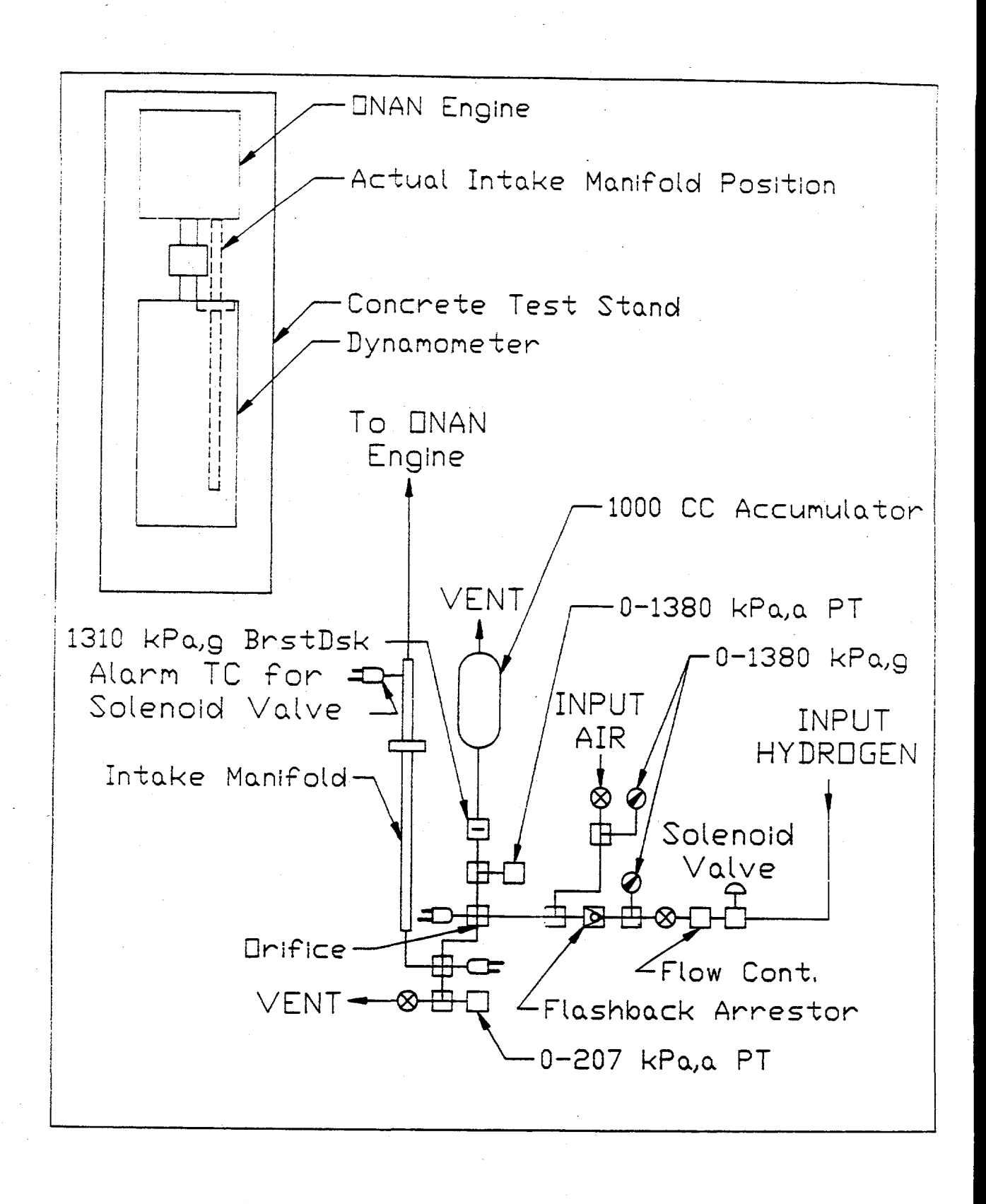
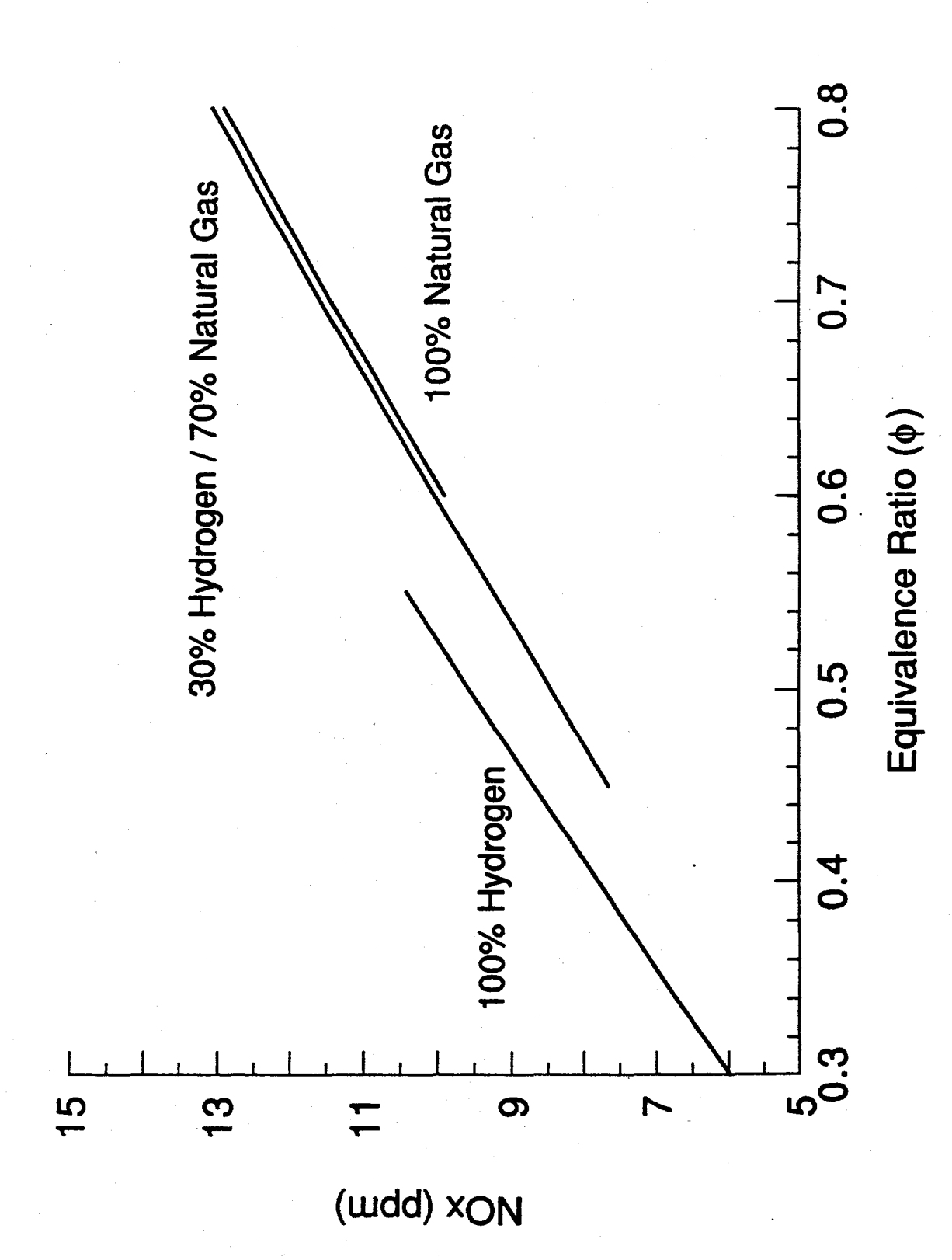


Figure 3: Schematic of fuel/air system.



proposed EZEV standard for NO, for a vehicle attaining 60 MPG Figure 4: NO, limit vs Equivalence ratio to comply with CARB's

Figure 5: Indicated thermal efficiency vs Valve shroud height

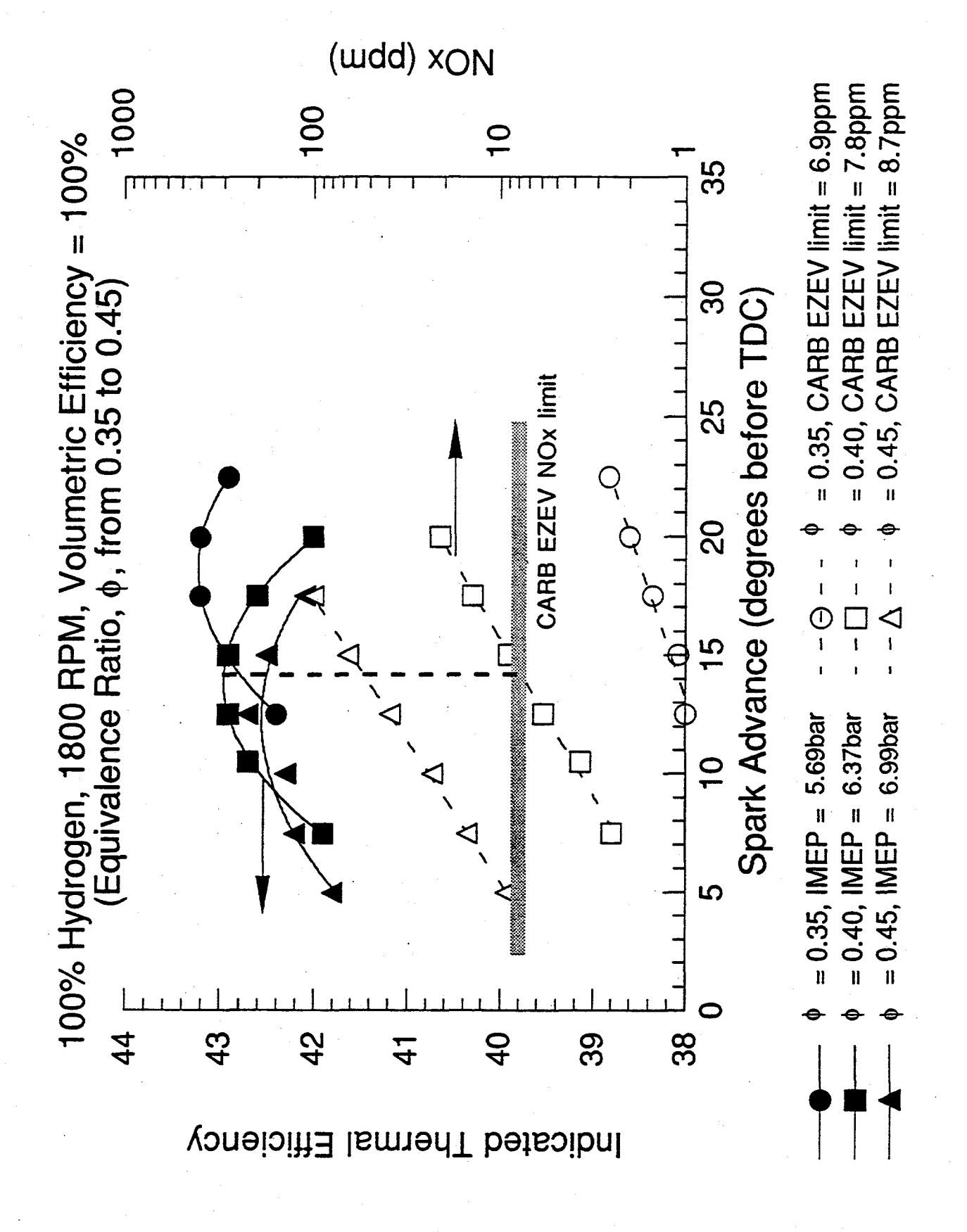


Figure 6: Indicated thermal efficiency and NO, vs Spark advance for hydrogen.

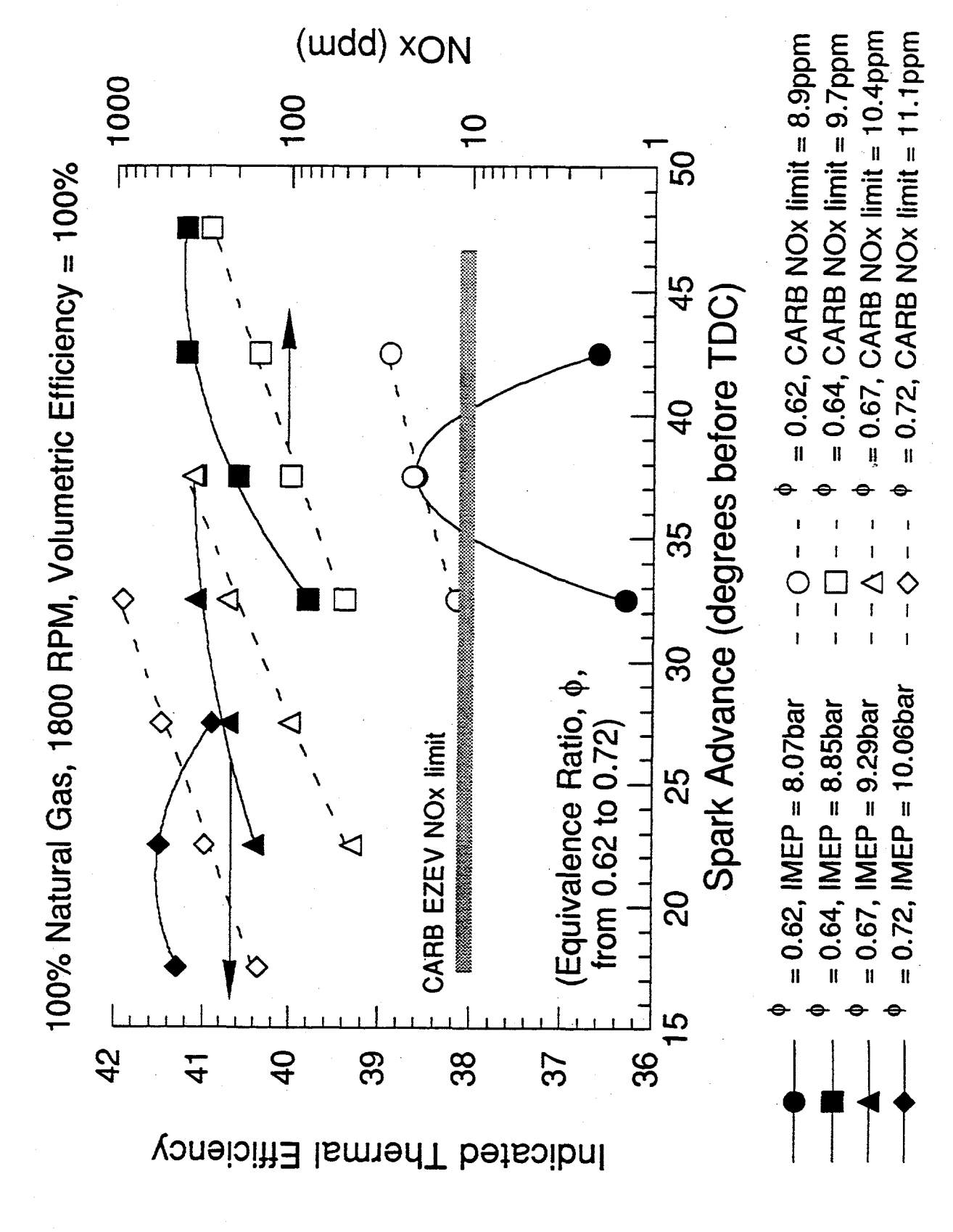


Figure 7: Indicated thermal efficiency and NO_{x} vs Spark advance for natural gas.

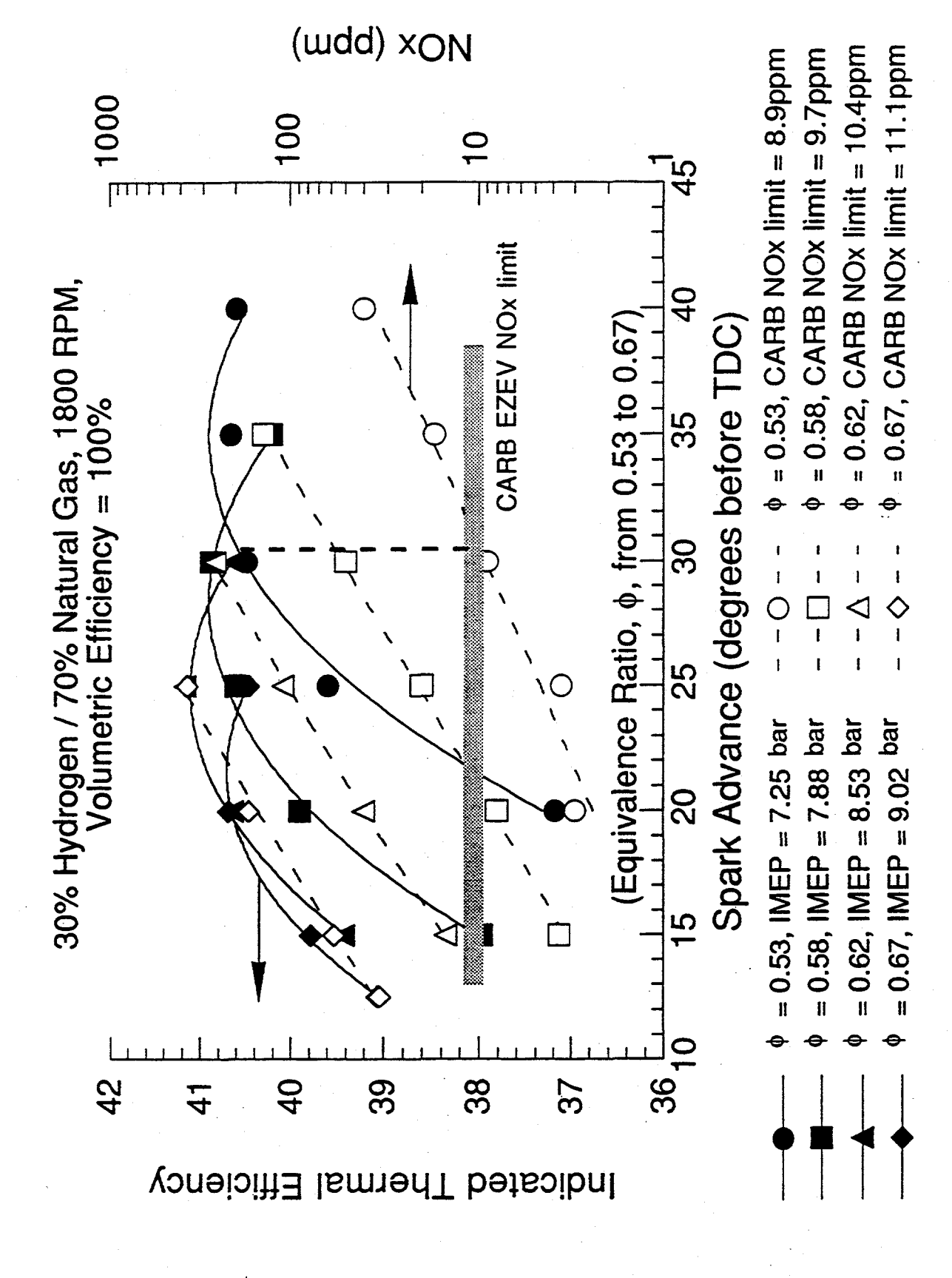


Figure 8: Indicated thermal efficiency and NO, vs Spark advance for 30/70% blend.

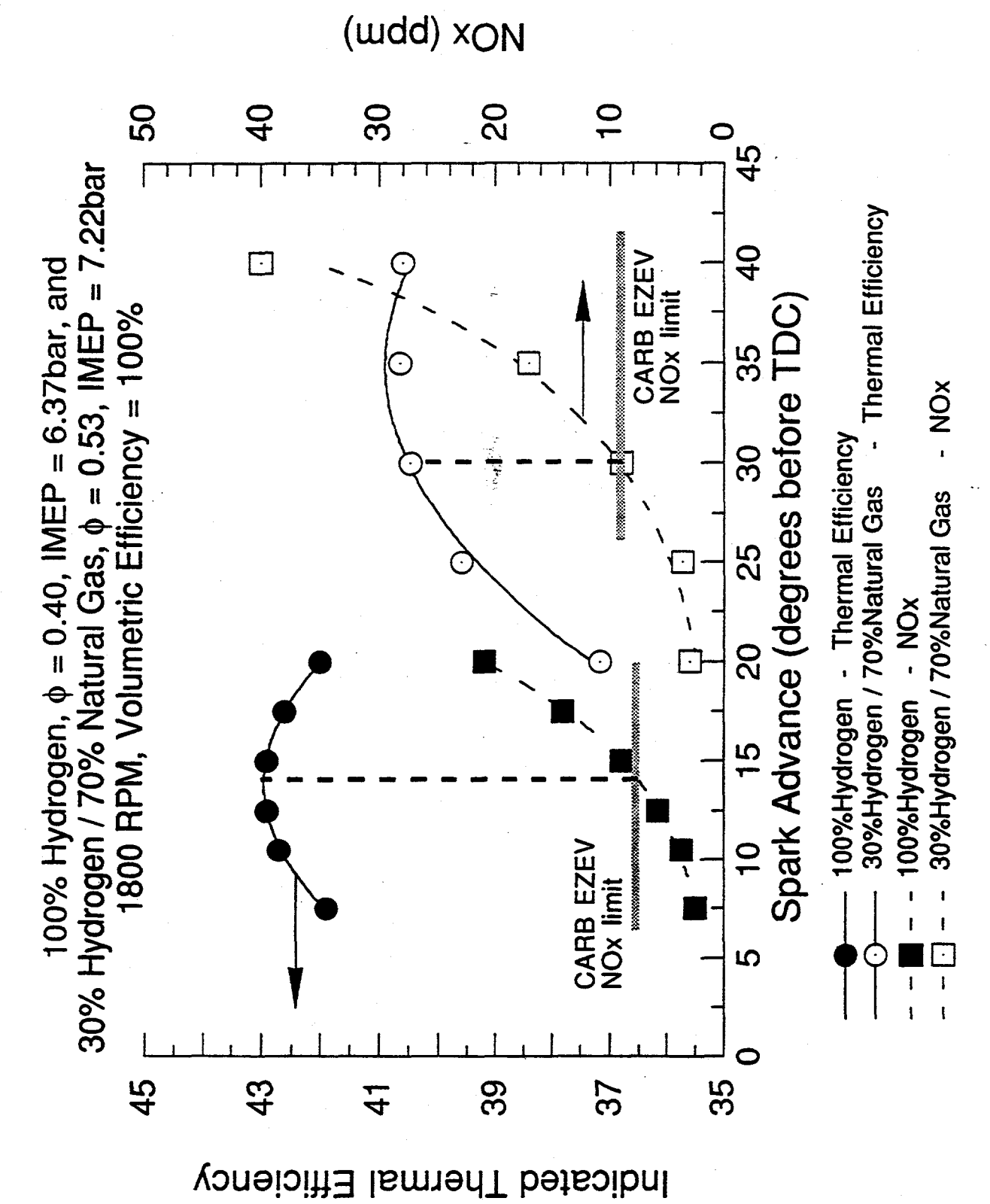


Figure 9: Indicated thermal efficiency and NO_{χ} vs Spark advance. Hydrogen vs Blended fuel.

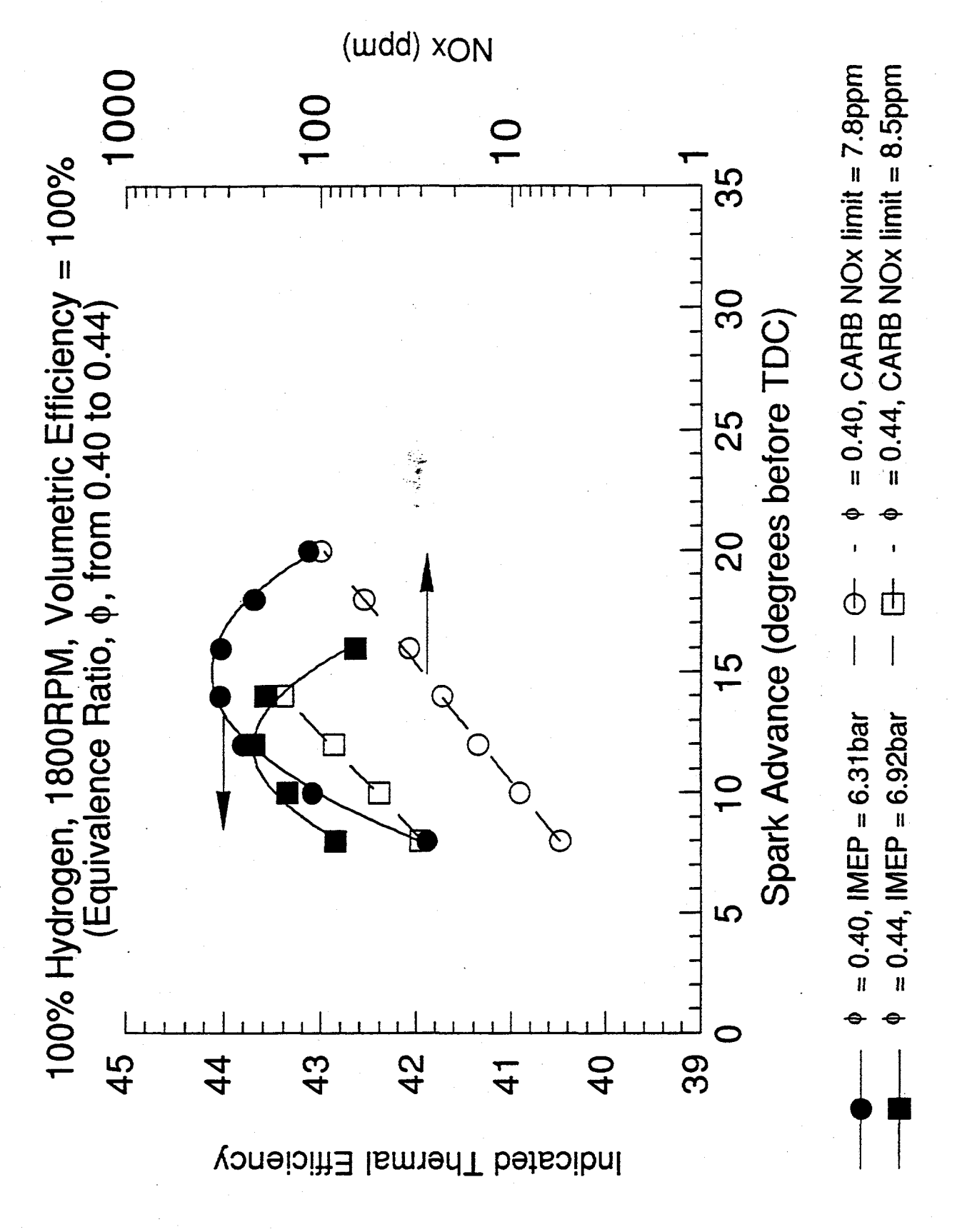


Figure 10: Indicated thermal efficiency and NO_x vs Spark advance for the Perkins engine.

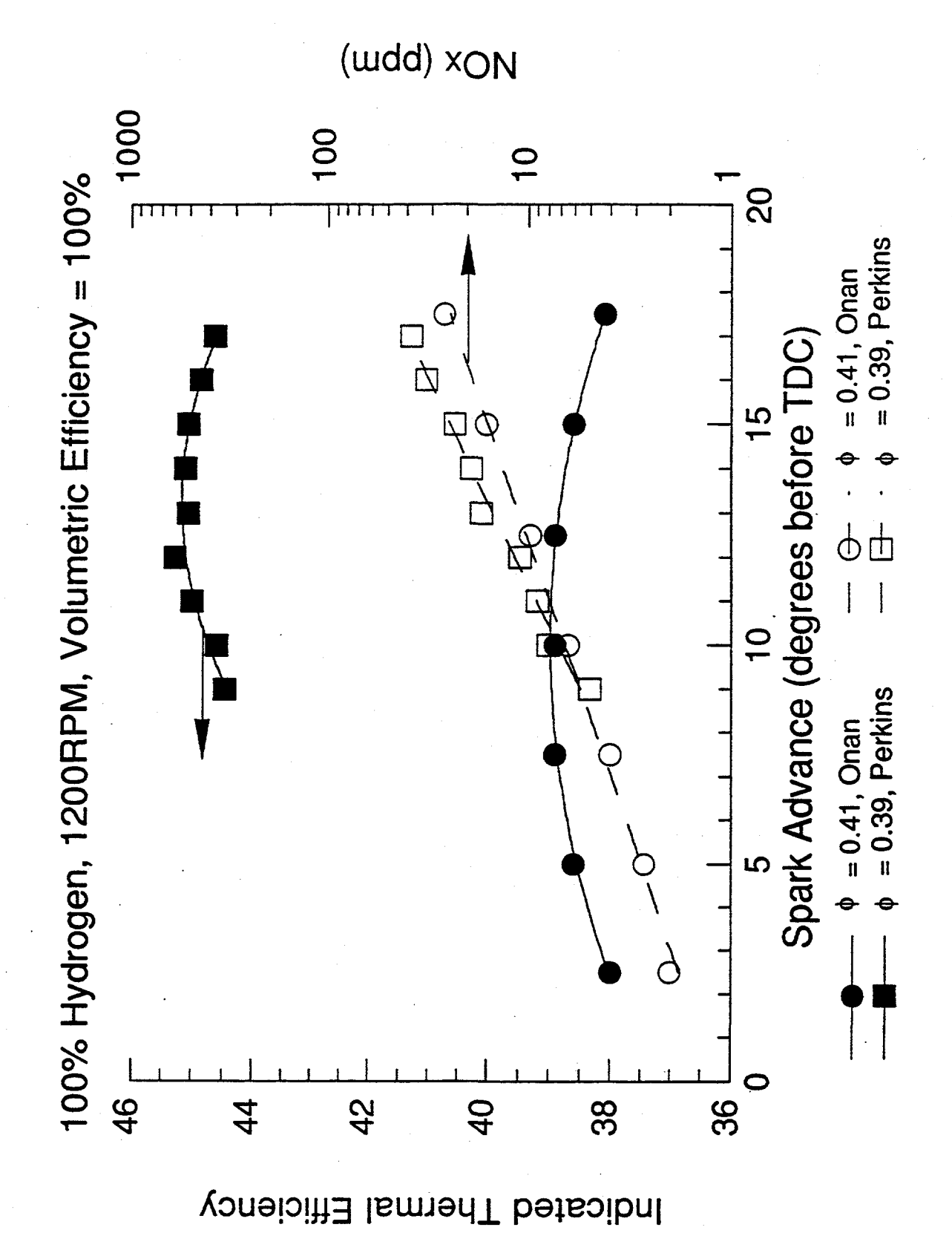


Figure 11: Indicated thermal efficiency and NO_x vs Spark advance for the Onan and Perkins engines.

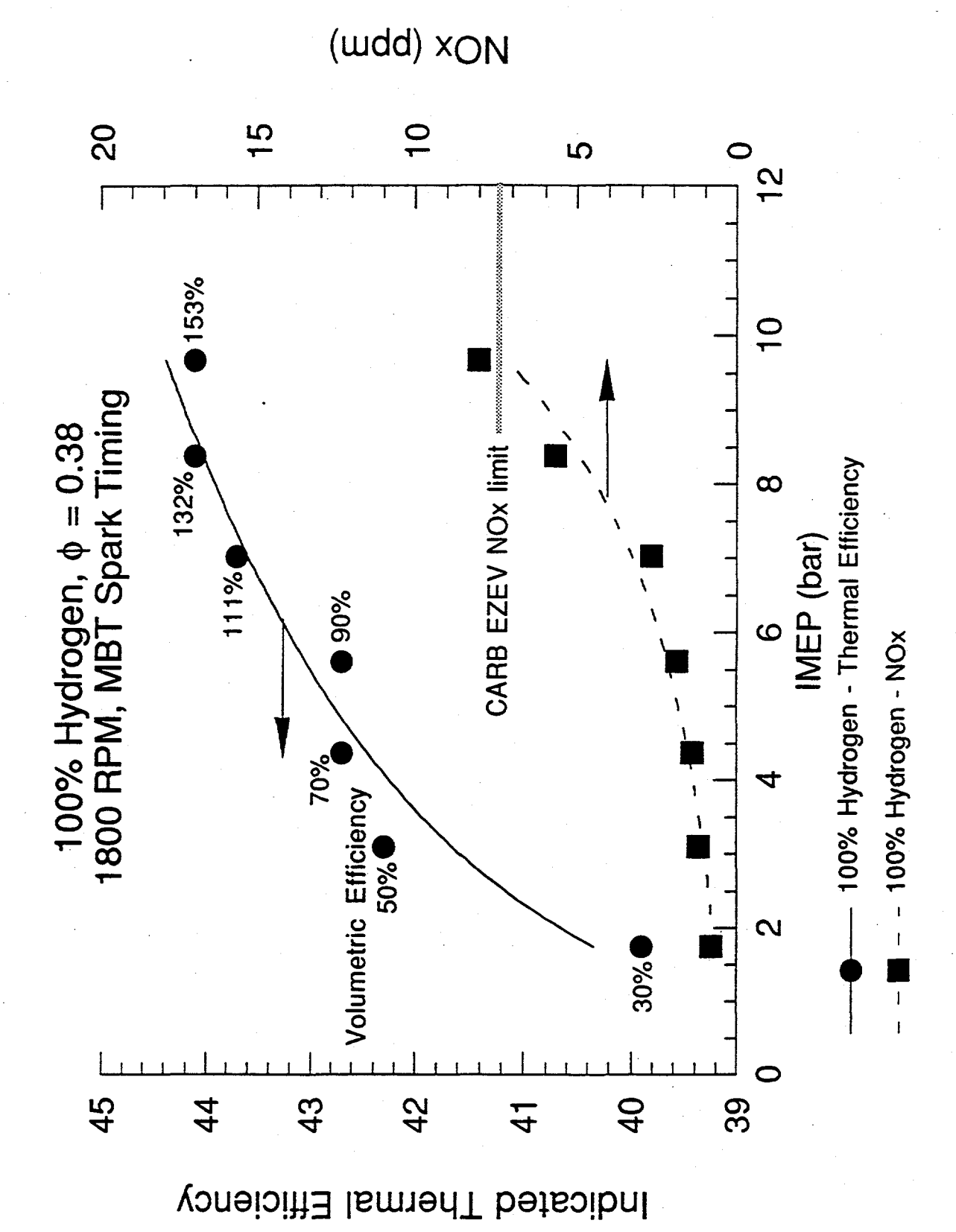


Figure 12: Indicated thermal efficiency and NO, vs Indicated mean effective pressure for the Onan engine.

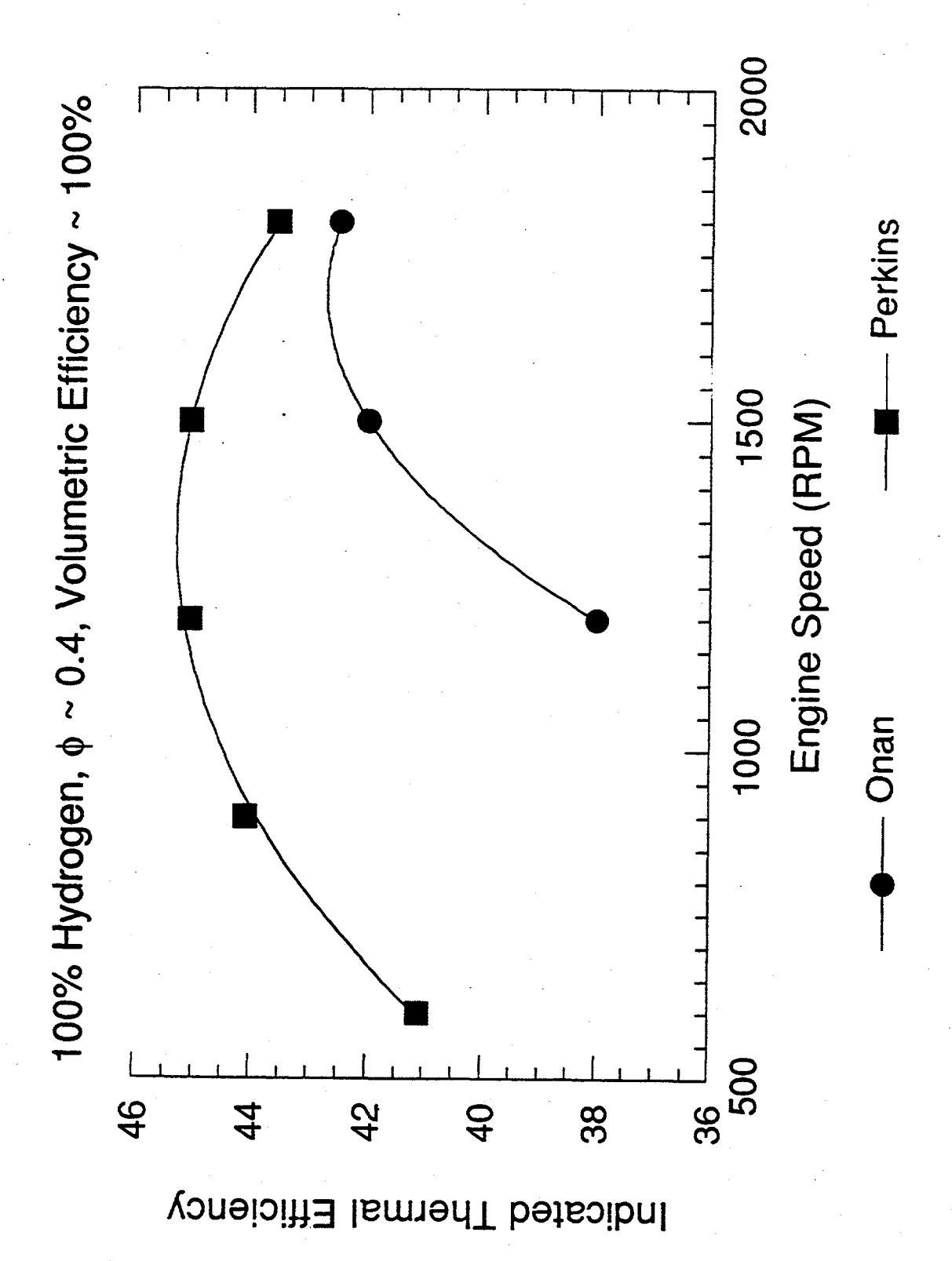


Figure 13: Indicated thermal efficiency vs Engine speed for the Onan and Perkins engines.

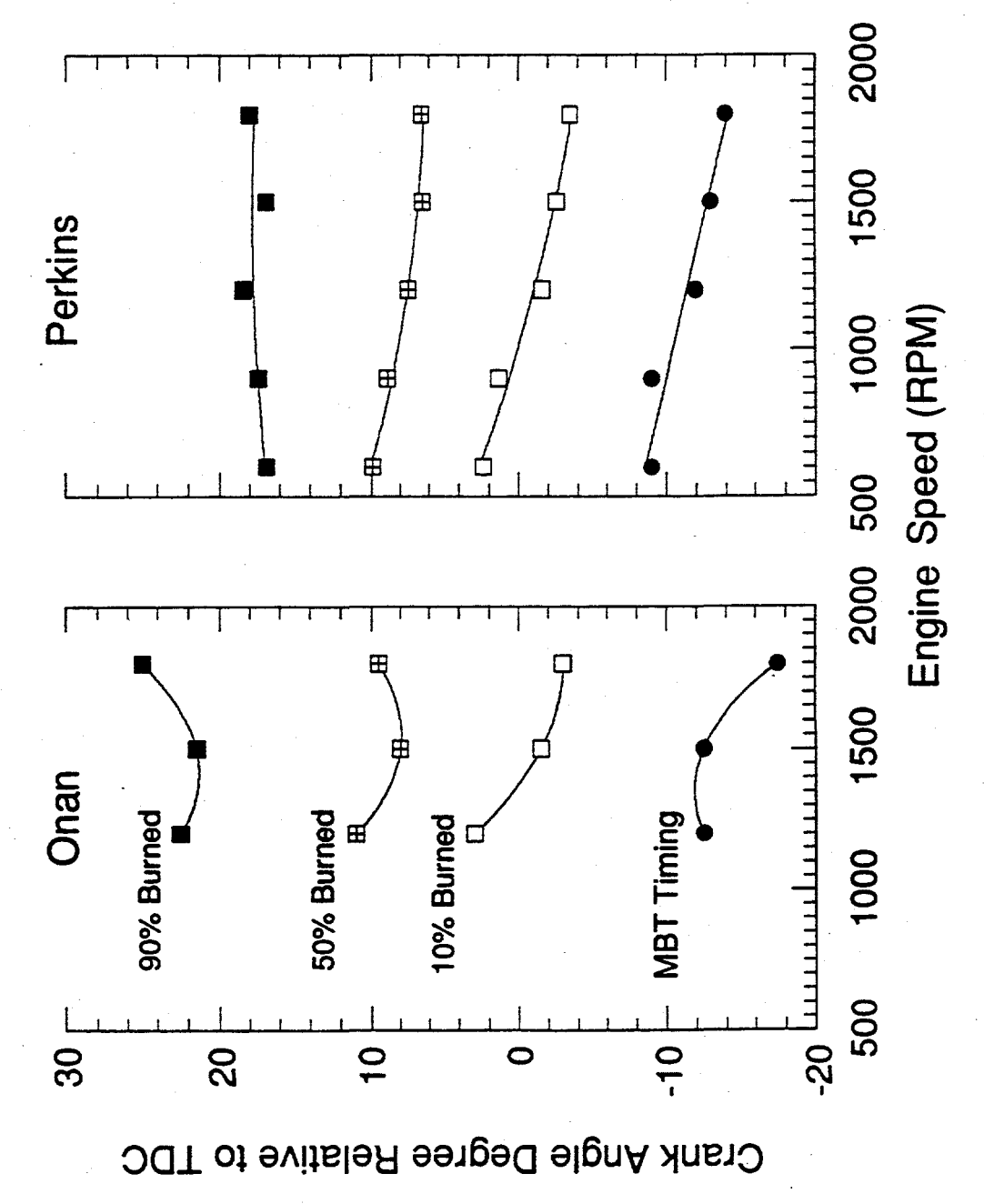


Figure 14: MBT timing and Burn duration vs Engine speed for Onan and Perkins engines.

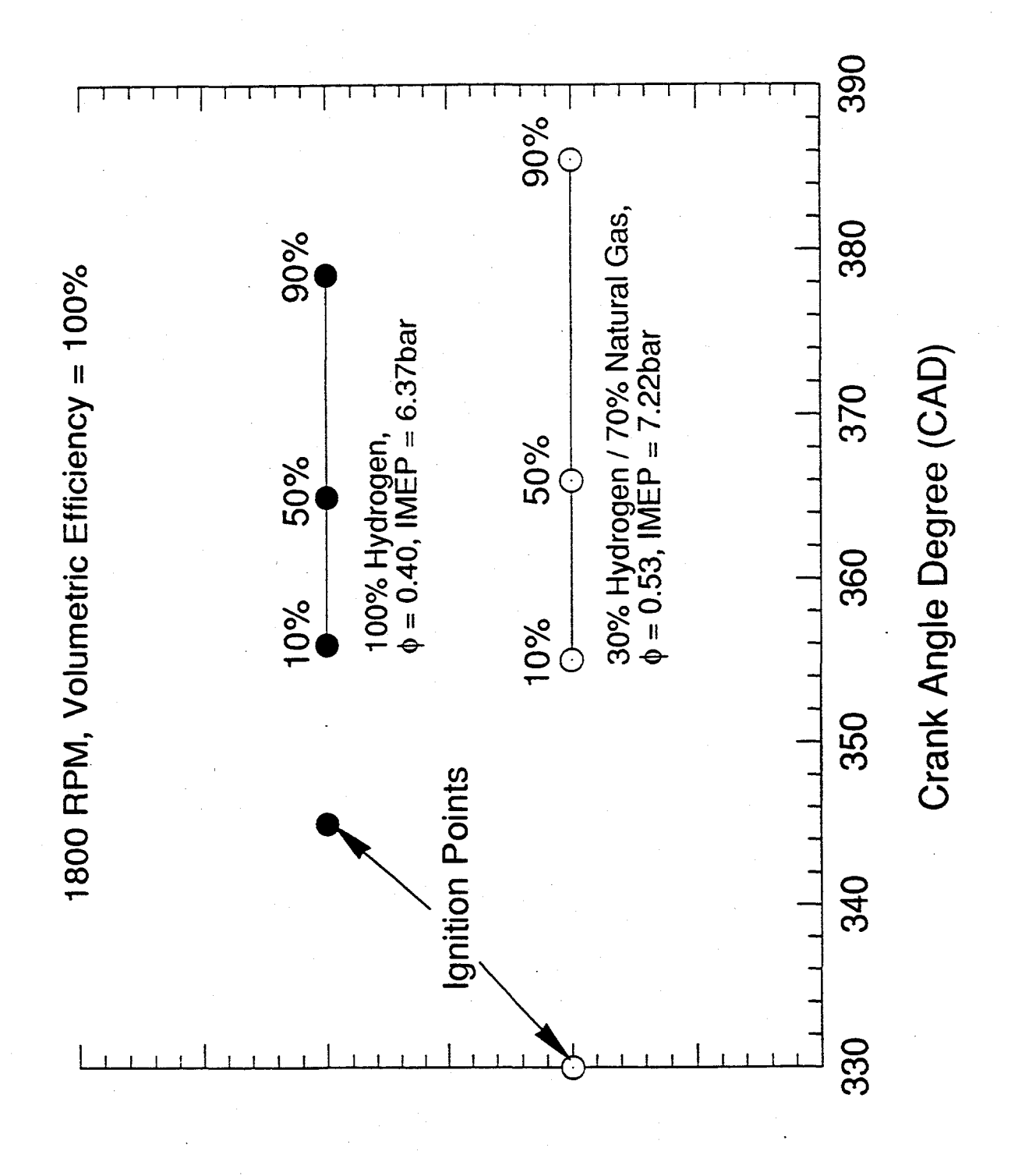


Figure 15: Burn duration vs Crank angle degree of the Onan engine using hydrogen and the 30/70% blend.

NUMERICAL MODELING OF HYDROGEN-FUELED INTERNAL COMBUSTION ENGINES

Norman L. Johnson, Anthony A. Amsden, and T. Daniel Butler Los Alamos National Laboratory Theoretical Division, Group T-3 Los Alamos, NM 87545 (NLJ@LANL.GOV)

Abstract

Major progress was achieved in the last year in advancing the modeling capabilities of hydrogenfueled engines, both in support of the multi-laboratory project with SNL and LLNL to develop a high-efficiency, low emission powerplant and to provide the engine design tools to industry and research laboratories for hydrogen-fueled engines and stationary power generators. The culmination of efforts on many fronts was the excellent comparison of the experimental data from the Onan engine, operated by SNL. These efforts include the following. An extensive study of the intake flow culminated in a major understanding of the interdependence of the details of the intake port design and the engine operating condition on the emissions and efficiency. This study also resulted in design suggestions for future engines and general scaling laws for turbulence that enables the KIVA results to be applied to a wide variety of operating conditions. The research on the turbulent combustion of hydrogen brought into perspective the effect of the unique aspects of hydrogen combustion and their influence on possible models of turbulent combustion. The effort culminated in a proposed model for turbulent hydrogen combustion that is in agreement with available literature. Future work will continue the development in order to provide a generally predictive model for hydrogen combustion. The application of the combustion model to the Onan experiments elucidated the observed improvement of the efficiency of the engine with the addition of a shroud on the intake valve. This understanding will give guidance to future engine design for optimal efficiency. Finally, a brief summary is given of the extensions and refinements of the KIVA-3 code, in support of future designers of hydrogen-fueled engines.

Introduction

The long-term goal of this applied research is to provide the engine design tools to industry and research laboratories for hydrogen-fueled engines and stationary power generators. Because many years are required to develop design tools for powerplants, this project will have tools ready for industry when its interest in hydrogen fuels is maturing. Los Alamos National Laboratory (LANL) is a significant contributor to the design tools for hydrocarbon-fueled powerplants through the development of the KIVA series of codes over the last 25 years (Amsden and Amsden 1993). These codes have proven their utility by reducing the reliance on costly experimental prototypes, thereby speeding the implementation of new designs into final products. Furthermore, they have contributed to a detailed understanding of the operating cycle of powerplants, which have resulted in reduced emissions, improved efficiency and longer engine life. These tools could not have been developed in industry due to the extended time and resource investment. The KIVA codes are currently used in all the major auto and diesel companies and scores of universities, as exemplified by the 21 technical papers that use KIVA in the 1996 Spring SAE Congress alone. Therefore, the dissemination of the hydrogen-design capability through the KIVA codes will rapidly reach all sectors of applied research and design groups. The secondary goal of the project is to validate the design tools by supporting a multi-laboratory development of a zero-emissions, high-efficiency engine, as described below. Successful completion of this goal will demonstrate to industry the feasibility and desirability of hydrogen-fueled engines.

The approach to achieving the above goals is a multi-laboratory-university project to develop a zero-emission, high-efficiency internal-combustion engine as an interim powerplant until economical fuel cell technology is available. Such engines are envisioned for both the transportation and stationary powerplant sectors, depending on size, with small engines for hybrid-powered automobiles and large ones for stationary electric power sources. SNL is constructing and operating the experimental test engines. LLNL is providing the systems analysis for the hybrid vehicle and the chemistry for combustion and pollution formation. University of Miami is collaborating in the prototype engine design. The planned work focuses on a tight coupling of experiments, simulation and analysis. The KIVA engine simulations done at Los Alamos will provide critical understanding of the engine operation while developing the design tools for future engines. Concurrent with the engine development, Los Alamos will use existing ties with industry and universities to disseminate the advances to the KIVA design tools, in preparation for future designs of hydrogen-fueled engines.

Prior Work

Earlier concepts for a high-efficiency combustion engine sought to take advantage of the higher efficiency of diesel engines. Carefully executed hydrogen and methane injection experiments were done at SNL into a fixed volume with optical access, resulting in penetration histories and pressure rises, with and without combustion. These experiments were simulated with KIVA and produced the following results (Johnson, Amsden et al. 1995). (1) A computational approach was developed that accurately modeled the gas penetration in mesh resolutions comparable to those used in full engine simulations by industry. (2) The combustion rate was accurately modeled, but only after the standard kinetics model for hydrocarbon fuels was modified in order to reproduce the experimentally observed autoignition delay (simulations using a similar model for methane combustion did not require modification, illustrating the additional challenges presented by hydrogen kinetics). (3) The NOx production was quite high due to the heterogeneous combustion and high burning temperatures, even though the overall fuel equivalence ratio was low. It was concluded that the NOx emissions were too high to continue using the diesel approach and focus was shifted to lean, homogeneous-charged, spark ignited (SI) engines.

A hydrogen-fueled. SI engine (the Certified Lubricating Research "CLR" engine) was operated at SNL and simulated using KIVA. The geometry of the cylinder and combustion chamber were accurately modeled in KIVA, but the intake flow through the valve was not included; consequently, in the absence of better information the standard practice of initializing the turbulence was used: the

turbulence intensity (u') at the beginning of the simulation was specified to be one-tenth of the maximum piston velocity. The CLR engine, in the experiments and simulations, showed large reductions in NOx levels at lean fuel mixtures, sufficient to satisfy the "zero-emission" standard without a catalytic converter. In the KIVA simulations, we found that modifications to the standard hydrogen kinetics were required for the CLR simulations, as were required for the injection simulations. Because the experimental results suggested that the bulk flow from the intake process was influencing the performance of the engine and that the combustion rate in SI engines, and subsequently the emissions and engine efficiency, is dependent on the turbulence levels at the time of combustion, it was concluded that a predictive simulation capability was needed to include the intake flow. A valve model for KIVA was begun in late 1994 and mostly completed in FY95. The addition of the valve model into KIVA is one of the more important improvements in KIVA over the last decade and has attracted significant attention in industry and academia. A pre-released version of KIVA with the valve model is currently being tested at two major diesel manufacturing companies, two universities, and a government engine design laboratory. A national release of the version with documentation is expected within this fiscal year.

Preliminary results of the modeling of the Onan engine, the second experimental engine at SNL, were reported in last year's annual review (Johnson, Amsden et al. 1995). The intake flow and valve configuration of the experimental Onan engine was designed by LLNL to result in a quiescent flow at the time of combustion in order to maximize the efficiency by minimizing heat transfer to the walls. An additional spark plug was added to offset the slower ignition duration. In the absence of experimental data on the Onan engine at the time, a computational investigation was undertaken to evaluate the importance of modeling the intake flow on the combustion and NO_x emissions. A simulation that began with the compression of a quiescent hydrogen-air mixture was compared to a simulation of the air induction process with resolved opening and closing of the intake valve. Although moderate differences were observed in the cylinder-averaged pressure, temperature, bulkflow kinetic energy and turbulent kinetic energy, large differences were observed in the hydrogen combustion rate and NO_x emissions. We conclude that (1) the Onan engine is not a typical quiescent engine, (2) the flow state at combustion is heterogeneous and sensitive to the details of the bulk and turbulent flow, and consequently an accurate simulation of the Onan engine must include the modeling of the air-fuel induction and (3) the single-equation hydrogen combustion model is deficient for modeling the Onan engine due to unrealistic precombustion. Results from this study suggested that minor changes to the engine geometry by the addition of a shroud on the inlet valve would have the desirable effect of switching the dominant tumble flow to a more swirling flow, thereby producing less heat transfer and a higher efficiency. This modification was implemented in the Onan engine in the following months and did result in an increase in the efficiency of the engine (details of these experiments can be found in the annual review paper by Van Blarigan). The success of this collaboration between the experimental and computation program illustrates the importance of the simulations in understanding in the details of the engine dynamics, which are not experimentally available. More details of these results are provided in the section below on the intake flow and shrouded-valve simulations.

Hydrogen Combustion

Introduction

The combustion characteristics of hydrogen are the unique aspects of hydrogen that differentiate the modeling of hydrogen-fueled engines from all other fuels, including hydrocarbon gases, such as methane, and liquid hydrocarbon fuels. In the absence of these differences, the existing techniques for non-hydrogen fuel could be directly applied to hydrogen engines. Because of the unique combustion properties of hydrogen, we address this aspect of the project first, even though it is the most recent area of study and is not yet completed.

Our goal is to provide a combustion model that accurately describes the dependencies of turbulence, fuel-oxygen ratio, fuel mixtures, temperature and pressure, but that is also applicable to repetitive, full-engine simulations, required by industry. An accurate combustion model, that is too complex and computationally intensive, has limited application, both in the current project and by engine

designers in industry. While we are now focusing on hydrogen-air mixtures, later work will include mixtures of hydrogen with hydrocarbon gases.

The main questions to be answered in this section are: How does turbulent combustion of hydrogen differ from that of hydrocarbon gases? Can the models for hydrocarbon turbulent combustion be used accurately for hydrogen combustion? Fortunately, the answer appears to be that turbulent hydrogen combustion does differ from hydrocarbon combustion, but not in a way that invalidates the use of the hydrocarbon combustion models.

The Unique Behavior of Hydrogen Laminar Combustion

Most researchers of combustion of gases are familiar with the low flammability limit of hydrogen and very high flame speeds or burning velocities of hydrogen, about 3.5 m/s in air at STP (Al-Khishali and Bradley 1983, Koroll et al., 1993), about ten times the flame speed as found in low molecular weight hydrocarbon gases (Liu and MacFarlane 1983; Tseng, Ismail et al. 1993). What is not broadly known is the origin of these differences, and this section focuses on the results of a thorough literature search on laminar and turbulent combustion, both as the basis of the current research, and as a resource for other researchers concerned with hydrogen combustion. Unfortunately the needed information in the literature is not complete, but the existing literature was generally found to be consistent. As an aid to other researchers, relationships are given between the various measures of hydrogen concentration used in the literature in an attached Appendix and will aid in comparisons of experimental data.

The extremely high molecular diffusivity of hydrogen produces many of the unique properties of hydrogen, such as the desirable traits of flammability and robust combustion at lean mixtures for both hydrogen-air and hydrogen-hydrocarbon gas-air mixtures. The high mobility of the hydrogen also contributes to an instability in a laminar flame front at lower values of φ , the fuel equivalence ratio (here, an unstable flame front means that a protuberance in the flame front will speed up and a trough will slow down - making a wrinkle grow in size). The instability occurs because the hydrogen is depleted in the troughs and collects in the tips, coupled with the fact that the flame speed increases with increasing hydrogen concentration in this regime. Although an instability in a planar flame front occurs for all combustion gases at some concentration, due primarily to the difference in molecular weight of oxygen and any gaseous fuel, what is unusual for hydrogen is that this instability in air occurs at values of φ in the normal operating conditions of engines, at a φ less than 1.5 at standard temperatures and pressures (STP). This is in contrast to the region that is unstable for methane ($\varphi < 0.74$), propane ($\varphi > 1.44$), ethane (>1.68) and ethylene ($\varphi > 1.95$) (Wu, Kwon et al. 1991; Kwon, Tseng et al. 1992; Tseng, Ismail et al. 1993). The existence of the laminar flame instability has been generally neglected in theories of laminar flame propagation for hydrogen and generally brings into question the validity of a thin, resolved flame front assumed in most treatments of turbulent combustion. This will be discussed again in the later section on turbulent combustion.

Another unique aspect of hydrogen combustion, which is not currently understood, is the separation of the value of φ where the maximum temperature (1.0) and the maximum flame speed (1.8) occurs (Kwon, Tseng et al. 1992); for all hydrocarbon fuels, the φ for these maximums coincide and occur in the range of values for φ between 1.0–1.2. Detailed information that is comparable for hydrogen-hydrocarbon mixtures is not available, but the combustion properties of a hydrocarbon gas have been found to change greatly with a small addition of the highly mobile hydrogen (Apostolescu and Chiriac 1996).

The kinetics of hydrogen combustion have been extensively studied, although comparisons between theory and experiments have been complicated by the diffusive instabilities described above. A successful effort in producing a limited reaction set of eighteen equations (Warnatz 1981) concluded the following on the concentration, temperature, and pressure dependence of hydrogen-air mixtures. 1) The existence of two competing mechanisms for hydrogen oxidation significantly complicates the laminar kinetics and is the source of unexpected sensitivity to initial temperature, pressure and equivalence ratio. The addition of a third species (N_2 to H_2 and O_2) reduces these dependencies. As a consequence, the laminar flame speed has a strong dependence on initial temperature, rising from 3.5 m/s for stoichiometric conditions ($\varphi = I$) in air at STP to about 23 m/s at 1000K, typical of

temperatures at ignition in the high compression Onan engine. The higher pressure at the time of combustion also increases the laminar flame speed, but to a weaker power $(p^{0.2})$. 2) The Zel'dovich model for NOx production is better suited to hydrogen combustion than hydrocarbon combustion due to the absence of HC radicals which encourage the formation of "prompt" NOx. About half of the NOx is produced in the flame region and the rest in the post-flame region. This was also observed in the KIVA simulations, as noted below.

Overview of Modeling Turbulent Combustion

All spark-ignited engines have flame fronts that propagate in the presence of turbulence, and hence it is essential that an accurate combustion model include the effects of turbulence. For hydrocarbon fuels, the typical approach in large scale SI engine simulations is to neglect the laminar kinetics entirely and use models that include just the effect of turbulence on the flame front, e.g., the Magnussen or eddy-dissipation model (Magnussen and Hjertager 1978). For diesel engines the occurrence of the ignition delay requires a detailed kinetics model for its prediction, but once ignited, the kinetics model is typically replaced with a simplified turbulence combustion model.

In recent years, some progress has been made in understanding some of the details of the turbulent combustion by the introduction of flamelet or coherent flame models (Dillies, Marx et al. 1993) for turbulence that add to the turbulence equations, evolution equations for the generation and destruction of flame surface. Tables of laminar flame speed as a function of pressure, temperature, and composition are then used to determine the reaction rate at any time. The key assumption of the flamelet approach is that the flame thickness is thin compared to the dimensions of the turbulent eddies. The complication of the unstable nature of the laminar flame front for hydrogen has not been examined for the flamelet model and may violate the thin flame assumption.

Another alternative to understanding turbulent flame fronts, but one that is not practical for large engine simulations, is the technique of Direct Numerical Simulation (DNS) of both the turbulence and combustion (Rutland, Ferziger et al. 1990). In the DNS approach, all scales are resolved on the continuum level and no stochastic averaging is made. The systems that can be examined are limited in size and complexity, but full fidelity information is obtainable to test assumptions in stochastic theories, as required for simulations of more complex geometries.

Given this background in the current state of modeling turbulent combustion, the occurrence of the unstable laminar flame front in the regime of interest would seem to question the validity of applying models developed for hydrocarbon turbulent combustion to hydrogen. Furthermore, one would expect that the sensitivity to turbulence would be greater for hydrogen combustion because turbulence wrinkles the flame front, and once wrinkled, the flame front would become unstable and more wrinkled, hence increasing the flame speed and the consumption of fuel.

In the following sub-sections, the existing experimental information, performance of the standard turbulent combustion models, and development of a simplified model for turbulent combustion for hydrogen are presented.

Experimental Data for Turbulent Combustion of Hydrogen

Little experimental information is available on the turbulent combustion of hydrogen, and what is available is at conditions different than typical engine regimes. The most complete set of data was found in (Koroll, Kumar et al. 1993) as needed to support the nuclear reactor safety studies, with less complete data in (Al-Khishali and Bradley 1983; Kwon, Driscoll et al. 1990; Wu, Kwon et al. 1991; Kwon, Wu et al. 1992; Meier, Köhler et al. 1994; Apostolescu and Chiriac 1996; Collier, Hoekstra et al. 1996). Some relevant data on lean methane turbulent combustion can also be found in (Ting, Checkel et al. 1995).

In an effort to develop correlations for hydrocarbon turbulent combustion, many of these researchers present the experimental information for hydrogen combustion using use correlations developed for hydrocarbon combustion, but the fits tend to be poor at lower hydrogen concentrations, presumably

due to the unstable nature of the laminar flame front extending the lean burn limit. A major conclusion by Koroll et al. (1993) is that the effect of turbulence is large for slow burning mixtures. and small for fast burning mixtures. For the Onan and future hybrid engines, the planned operating conditions (φ around 0.4) are in the unstable regime (φ < 1.5). Consequently, the laminar flame speed is in an intermediate regime and is predicted to have moderate sensitivity to turbulence, with increases from 0 to 10 times for a range of turbulence intensity of 0-2.4 m/s. For very lean mixtures, the laminar flame speed can be 0-23 times for the same range of turbulence. At the maximum laminar flame speed, the increase is only 7 times at 2.4 m/s. Note that the typical turbulence intensities for the Onan engine during ignition as found from the KIVA simulations is in the range of 1-3 m/s. The second major conclusion made by Koroll et al. is that some additional mechanism, either the flame generated turbulence or preferential diffusion effects, must be included for accurate correlations for the flame speed; the increase of flame surface by pre-existing turbulence, which is generally argued to increase as $k^{0.5}$, is not sufficient. At fuel concentrations around $\varphi = 0.4$, the turbulent flame velocity in air is found to scale according to $k^{0.5}$, with a smaller exponent for lower concentrations and a larger exponent for higher concentration up to $\varphi = 1.5$, and then declining again for higher concentrations. Because the Onan engine is expected to operate in the range around $\varphi = 0.4$, this gives us some guidance as to how the turbulent flame speed should vary with turbulence intensity in the regime of interest.

One-Dimensional KIVA Runs of Turbulent Combustion and NOx Production

To better understand and verify the standard turbulence combustion model on initial turbulence intensity, pressure, temperature, and fuel equivalence ratio, we have done a series of one-dimensional KIVA-3 runs at parametric values of pressures (1-5x10⁷ dynes/cm²), turbulence intensity (10²-10⁶ cm²/s²), and fuel equivalence ratios (0.4–0.8) and evaluated the flame speed, time to steady ignition, final combustion temperature, peak temperature, temperature at ignition, and NOx production. The initial gas temperature was taken to be 900K, the typical gas temperature at the time of ignition in the Onan engine. The one-dimensional configuration was chosen to have approximately constant pressure combustion conditions (unlike an actual engine that has significant increased in pressure), and the simulation was forced to have a constant turbulence intensity (k) and dissipation rate (ε) . The enforcement of constant turbulence levels prohibits the occurrence of flame generated turbulence, which can increase the flame speed (Koroll, Kumar et al. 1993). Although we will examine this effect later for generality, it is expected to be small for lean fuel mixtures of current interest. The KIVA simulations use a variation of the eddy-dissipation model (Magnussen and Hjertager 1978) that has successfully been applied to turbulent combustion of hydrocarbon fuels for large simulations, for both pre-mixed and injected fuels. Although we expect the unmodified model to underestimate the flame speed, our primary interest is to determine functional dependence on the independent variables.

A least-squares fit to the steady-state turbulent flame speed, s_t , gave a good fit and provides a compact summary of the simulations results:

$$s_t = 1.70 \ k^{0.487} \ \varphi^{0.366} \ p^{-0.027} \ \text{in cm/s}$$

in which k is the turbulent kinetic energy (cm^2/s^2) , φ is the fuel equivalence ratio, and p is the pressure $(dynes/cm^2)$. The adjusted correlation coefficient, r^2 , for the fit is 0.9997, indicating an excellent fit of the data.

The expected exponent of k is 0.5, based on an analysis of the model, and more importantly approximately duplicates the observed coefficient for hydrogen combustion (Koroll, Kumar et al. 1993) for $\varphi = 0.4$, as described in the previous section. The pressure dependence is observed to be almost zero $(p^{-0.027})$ as expected from an analysis of the model. No experimental information on the pressure dependence of the turbulent flame speed could be found, but one might expect that the dominant effect of pressure is on the laminar flame speed in the turbulent eddies, and, consequently, the pressure dependence would be the same as the laminar flame speed, or approximately

proportional to $p^{0.2}$ (Warnatz 1981). The steady-state temperature was observed to depend only on the fuel equivalence ratio, as expected, since this determines the net heat released. Finally, no dependency was observed on the eddy dissipation rate, ε , as expected from the formulation of the model.

In the original development of the eddy-dissipation model (Magnussen and Hjertager 1978), the turbulent combustion rate is proportional to a constant A, that is held constant during a simulation, but is typically adjusted to match experimental data for operating conditions of the engine. Because it appears as a premultiplier of the turbulent combustion rate, A is expected to have a similar dependence on fuel equivalence ratio, initial pressure and temperature as the laminar flame speed. For the one-dimensional simulations, A is taken to equal 18, a value typically used for diesel engine combustion. Ideally, the parameter A should be a function of the fuel equivalence ratio, initial pressure and temperature and not require modification for different operating conditions.

The above correlation gives a flame speed of 160.0 cm/s for $(k, \varphi, p) = (5.0 \times 10^4 \text{ cm}^2/\text{s}^2, 0.4, 1.0 \times 10^6 \text{ dynes/cm}^2)$, in comparison to the experimentally observed value for hydrogen in air of 230 cm/s (Koroll, Kumar et al. 1993) (note that the experimental laminar flame speed is 60 cm/s). This difference was expected, because the flame speeds for hydrogen are larger than for diesel fuels. This suggests that the parameter A in the eddy-dissipation model should be increased to 25 from 18 for constant pressure ignition at 900K. In an actual engine simulation where temperatures continue to increase during combustion, the flame speed would increase, and A would be correspondingly larger. This was observed in the full engine KIVA simulations, as noted below.

We also examined the dependence of the NOx formation in the parametric study using the standard Zel'dovich model. NOx was produced in the flame front. Behind the flame front, the NOx production was constant with time under these constant pressure and temperature conditions. Because of the time for significant NOx to be produced was much longer than the simulation time, no useful conclusions could be made in these simulations about the NOx formation of in the presence of turbulence.

Direct Numerical Simulation of Turbulent Combustion of Hydrogen

The final source of information on turbulent combustion of hydrogen can be obtained from detailed computer experiments of the turbulent combustion in a continuum fluid, in which no stochastic models for turbulence are used. The direct numerical simulations (DNS) provide information that is unavailable from experiments that can be used to better understand the details of turbulent combustion and thereby to improve stochastic turbulence models. One preliminary study (Rutland and Trouve 1993) has been done on the effect of the preferential diffusion instability, as occurs in lean hydrogen combustion, on turbulent combustion. The conclusions of the study are very significant to the present research. A strong, almost linear, correlation was found between the local flame speed and the curvature of the flame front, supporting the observation that the local flame front is unstable. In contrast, no correlation was found between the flame speed and local strain rate. Most significantly, the enhanced curvature effects, observed at the local level, were found to cancel on the average or global level. Hence, the front instability affects the local flame front, but not the overall propagation of the turbulent flame. It was also observed that the preferential diffusion causes hot spots to form and persist in the flame front, which would likely affect the kinetics of the NOx production. From this study, we can tentatively conclude that the global turbulence reaction rates may not be affected by the preferential diffusion instability, but quantities that depend on the details of the local flame front may be sensitive to this effect. This gives us some hope that a global turbulence combustion model, such as the eddy-dissipation model, that has been applied to stable laminar flames, may also be applicable to lean turbulent hydrogen combustion.

Conclusions and Future Work on Turbulence Combustion Modeling

The above review of the literature and of the one-dimensional KIVA simulations suggest that a straightforward modification of the model used for hydrocarbon-based fuels may be appropriate for turbulent, hydrogen combustion in the regime of operation of the Onan engine. In the following

section on the three-dimensional simulations of the Onan engine, the eddy-dissipation model is applied directly to the hydrogen turbulent combustion in KIVA-3, with understanding that the parameter A must be increased to account of the increased flame speed. Because A is taken to be a constant and not dependent on the changing conditions during ignition, we expect there to be some deficiencies in the details of the model. Comparable difficulties arise in the application of the same model for hydrocarbon fuels. Preliminary results with the modified parameter look promising, as is reported in the next section.

Future work will include the addition of the dependence on the fuel equivalence ratio, pressure and temperature on the parameter A, through the known dependence of the laminar flame speed on these variables. We believe that this should significantly improve the predictability of the model. Although not necessary for the simulation of the spark-ignited engines, a simplified model for the laminar hydrogen kinetics is still needed to complete the model for both compression ignited and sparkignited engines. This work will be done in collaboration with LLNL.

Intake Flow, Turbulence, and Scaling Studies of the Onan Engine

Introduction

The majority of the effort in the last year has focused on the importance of accurate modeling the intake flow in a spark-ignited engine and the effect of various design choices on the performance of the engine. Because of the sensitivity of the combustion rate and pollutant formation on the intake port design and turbulence level (Khalighi, El Tahry et al. 1995; Kühn, Abthoff et al. 1996; Neußer and Geiger 1996), little progress could be made on the turbulent combustion modeling for the Onan engine until we were confident about the turbulence levels at the time of combustion. The modeling issues of concern were the accuracy of the newly implemented valve model and the best model for the intake port to duplicate the experimental driving conditions. The following subsections describe the KIVA-3 simulations that model the intake flow and the turbulence generation. These naturally divide into three topics: the study of the scaling of the turbulence intensity, the effects of the intake port changes and the simulations with and without shrouded valves. The discussion of the simulations with combustion are described separately in the following section.

Description of the Onan Engine, the KIVA Mesh and Motored Simulations

Details of the SNL Onan engine can be found in (Van Blarigan 1995; Hoekstra, Van Blarigan et al. 1996). The Onan engine is a converted diesel engine with a modified head containing two valves and two spark plugs. Table 1 summarizes the engine specifications. Note that the compression ratio has changed from the last annual report, reflecting a better measurement of the combustion volume.

Table 1. Modified Onan Engine Specifications

Bore	82.55 mm
Stroke	92.08 mm
Displacement	493.0 cm ³
Geometric compression ratio	14.04:1

Details of the KIVA mesh and initial conditions for the Onan engine are given in the last year's annual report (Johnson, Amsden et al. 1995) and are summarized here. The mesh and one time of the simulation are shown in Fig. 1. The mesh was generated with 41 pseudo-blocks, resulting in 5 logically hexahedral blocks of mesh with about 75,000 cells in the full 360° mesh or half this number

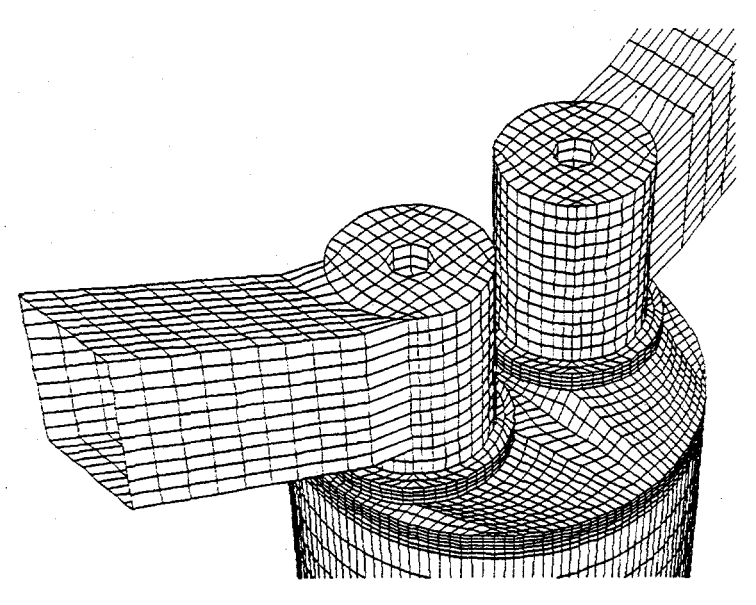


Fig. 1a. A detail of the exterior of the mesh for the Onan engine.

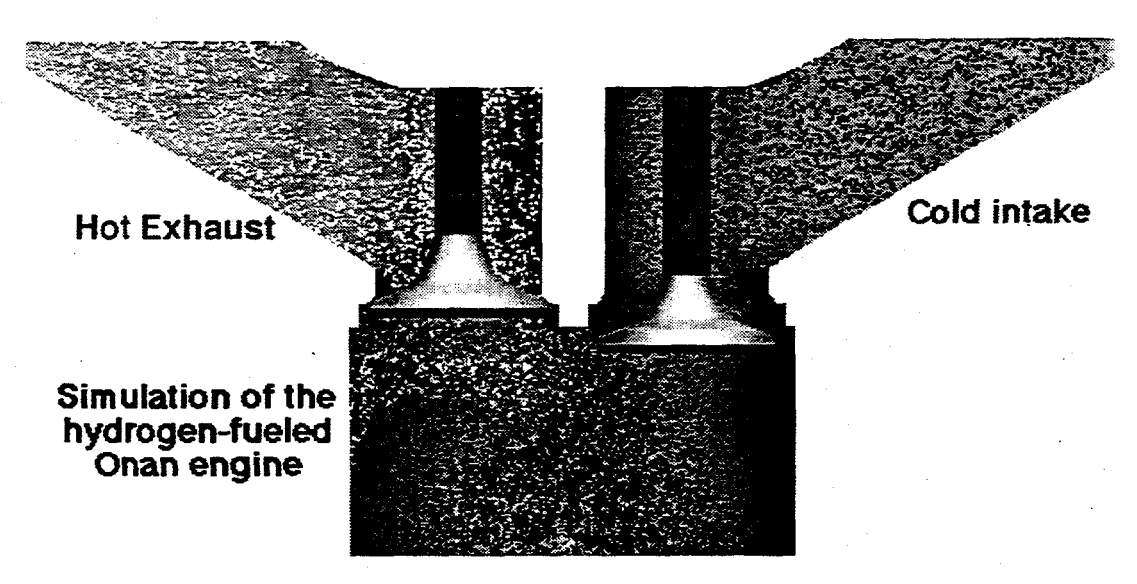


Fig. 1b. The intake flow at one time during the KIVA simulation. The cold air represented by the dark dots is compressing the hot residual gases, represented by the white dots. Note the exact rendering of the valve shapes and pockets.

for the simulations that model only half of the engine. The full mesh of the Onan engine includes a slight azimuthal twist of 27° in the intake port as occurs in the Onan engine. Without this twist in the intake port, the flow and combustion is symmetric through a plane passing through the two valves. Because the effect of this twist was found to be negligible (see the section on the intake flow modeling, below), for simulations that do not use a shroud to induce swirling flow, the half mesh was used, thereby reducing computational times by half.

The only major simplifications made in the computational mesh were the square cross-section of the intake and exhaust manifolds (See Fig. 1a). To reduce the effect of the simplification, the flow area of the simulated and actual manifolds are identical. Other simplifications are the omission of the

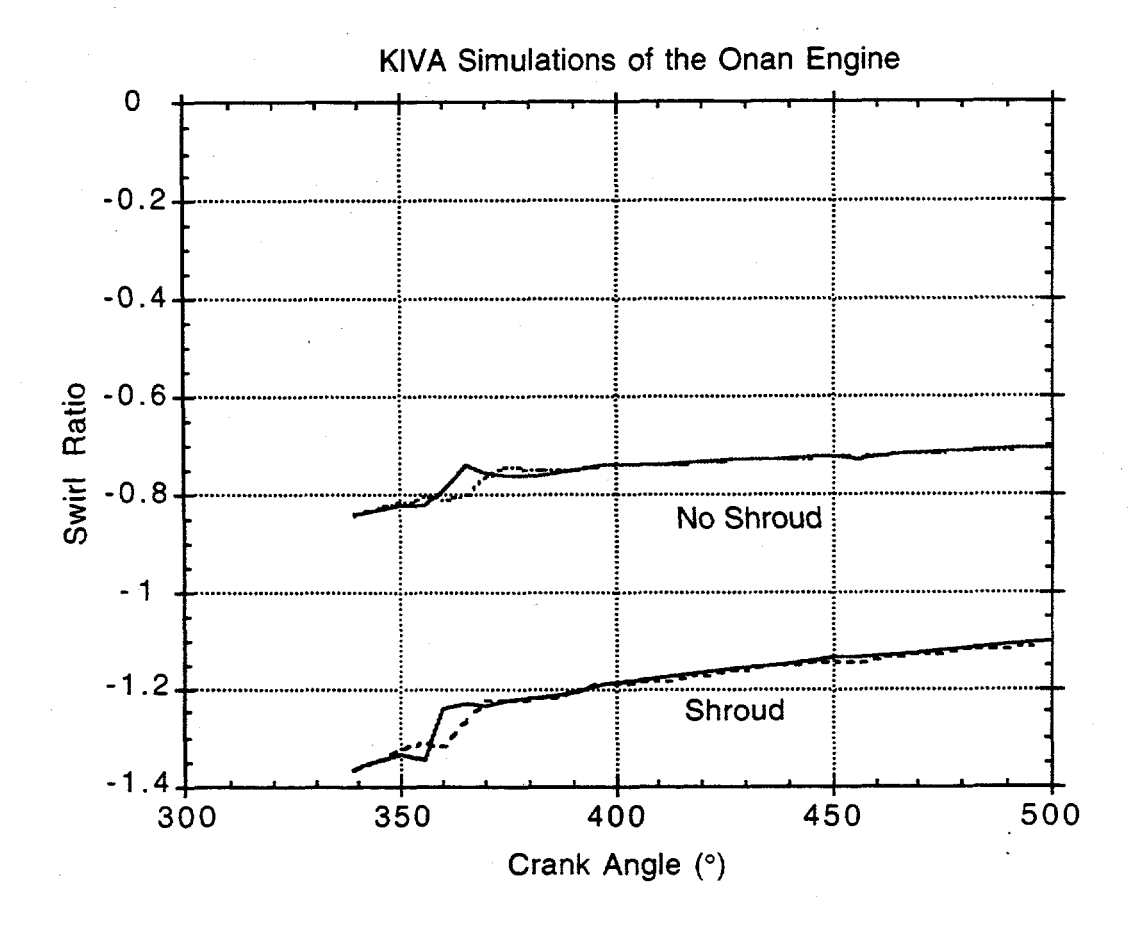


Fig. 4. The swirl ratio for KIVA-3 simulations with and without a 1.5 mm shroud and for two ignitions timings (20° (solid lines) and 12.5° (dashed lines) BTDC). The swirl ratio is the angular momentum in the cylinder divided by the product of the total mass in the cylinder and the angular velocity of the piston.

though the simulations with the shroud have a higher heat loss to the wall, the more optimal pressure histories of the runs with the shroud compensate of the additional heat loses, thereby either improving the efficiency at 12.5° case or keeping the efficiency constant in 20° case.

The plot of the hydrogen mass in Fig. 8 as a function of crank angle illustrates that even though all the simulations have similar turbulence intensities, the consumption of hydrogen is faster for the simulations with the shroud than without, even though the turbulence levels and hence the local combustion rates are comparable. The source of the different combustion rates is the stretching of the flame front by the slow swirling flow. The increased efficiency with the shrouded valve, as explained by the KIVA simulations, is due to the faster combustion rate from the bulk flow from the gentle swirl, thereby producing more work near TDC, but with not too large a swirl that causes a loss of efficiency due to increased heat loss. With this understanding of the delicate balance between competing effects, an optimal design can be made of the intake port in the final prototype engine.

volume associated with the spark plugs (3.5% of the minimum cylinder volume) and the volume above the piston rings (0.7% of the minimum volume). The valve shapes and seating were modeled accurately to within the resolution of the mesh (See Fig. 1b). Two types of boundary conditions were used to model the intake flow of the Onan engine: a constant pressure boundary condition and a time-varying boundary condition as taken from the experimental pressure measurements in the intake port. For studies of the comparison between different simulation runs, the former was used. The latter boundary condition was used for comparison to the Onan experiments and is discussed in more detail in the section on intake flow modeling. Other boundary conditions for the engine simulation with combustion are specified as in the prior annual report (Johnson, Amsden et al. 1995).

As a test of the proper compression volume, simulations were done of the motored Onan engine (operation without combustion) and the pressure shape and maximum pressure agree well with the experimental data, as in Fig. 2. For these simulations the temperature of all surfaces in the engine were taken to be room temperature since the engine was operated cold. The cold surfaces tend to cool the hot, compressed air, thereby reducing the maximum pressure expected from purely adiabatic compression. The slight difference in the maximum pressure between the experiment and simulation is due likely due to the temperature of the cylinder walls and piston being lower than in the experimental engine, which are slightly heated by the compressed gas.

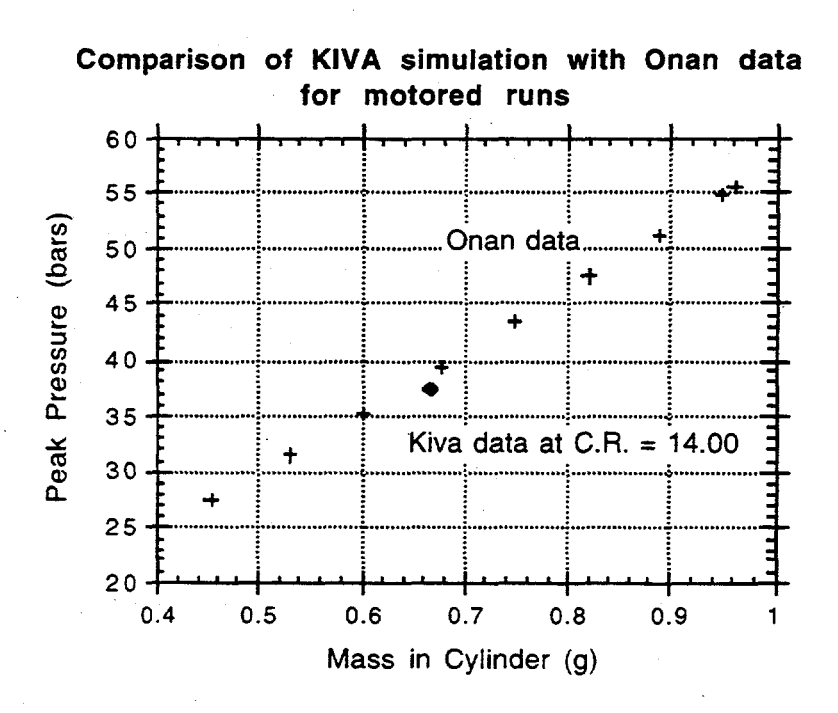


Fig. 2. Comparison of the KIVA simulations with motored Onan experiments of the peak cylinder pressure versus the air mass in the cylinder.

Scaling of Turbulence Levels in the Onan Engine Simulations

Prior to the availability of experimental results for the Onan engine, simulations were done to examine the dependence of the turbulence levels on many design parameters, such as the engine rpm and intake geometries and the twist in the intake port, as mentioned above. It was observed that for a given engine geometry and intake conditions (e.g., a given intake port length, or for shrouded or unshrouded valves), the turbulence levels of the cylinder gas simulated over the operating cycle of the engine can be superimposed if they are scaled by the maximum piston velocity (or engine rpm) and mass of cylinder air/fuel charge. This superposition applies for a wide range of volumetric efficiencies, engine speeds or operating temperatures. The scaling applies if the bulk flow does not

differ too greatly, as illustrated in Fig. 3 with the good comparison, with and without an angled port and with a cold and hot engine. Furthermore, during combustion, only a 20% increase in the scaled turbulence levels is observed over the motored simulations, although the bulk flow kinetic energy is significantly increased (detail in Fig. 3). (The increase in the bulk flow kinetic energy is due to the compression of the unreacted gases by the higher pressure combusting gases, thereby, causing a bulk flow.) This suggests that the turbulent levels in the unburned fuel during combustion do not change significantly for the Onan geometry for these lean operating conditions. The scaling does not apply if the bulk flow is drastically changed between simulations, as occurs with the addition of a shroud on the intake valve. This scaling law enables a single KIVA turbulence history to be applied to a variety of other operating conditions, as needed in the zero-dimensional, thermodynamic simulation codes. This has been done by Salvador and Smith at LLNL in support of the project, and they have found that the burning duration correlates well with average turbulence intensity during combustion (see their contribution to the annual review).

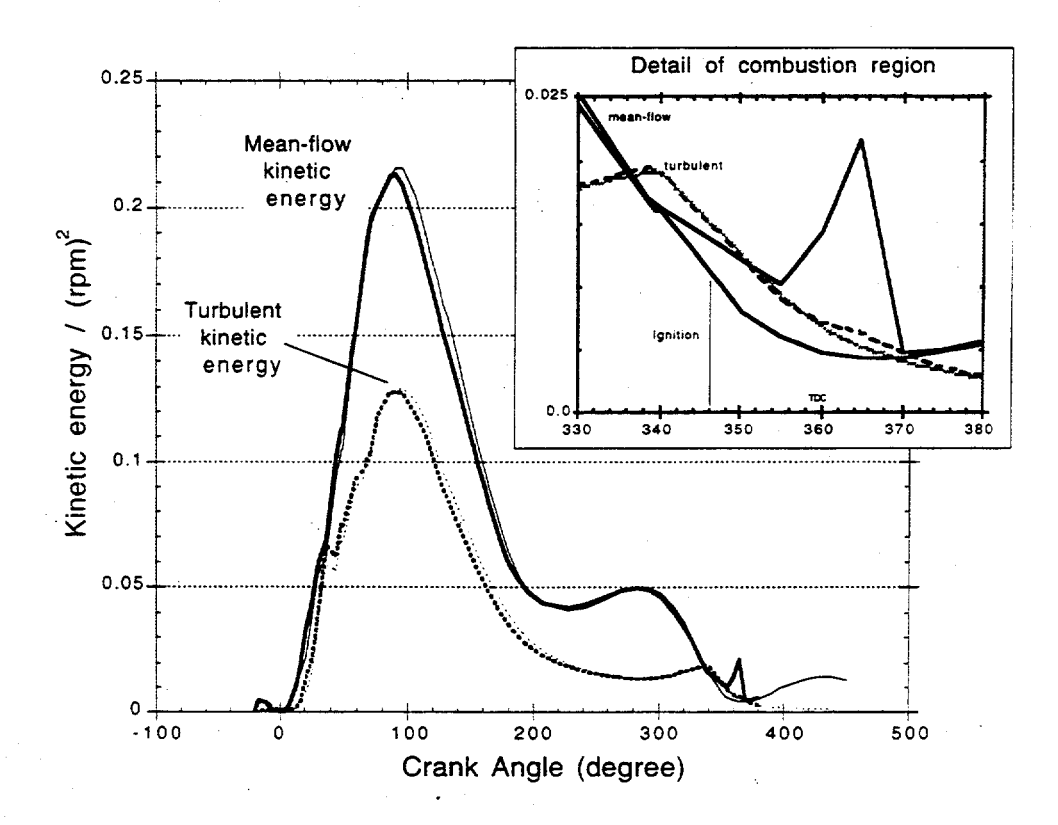


Fig. 3. Illustration of the scaling of kinetic energy in KIVA simulations for different operation conditions. The heavy lines are for a run with combustion in a hot engine and an angled port with minor swirl at 1206 rpm. The thin lines are for a run with no combustion and no swirl in a cold engine at 1500 rpm.

Modeling of the Intake Ports and Cylinder Pressure Oscillations

Intake Port Modifications

One of the challenges of any engine simulation is the approach used to duplicate the experimental conditions for the air delivery. The complication is that the computational mesh for the simulation must be terminated at some point and an appropriate boundary condition applied. This is

additionally complicated by the fact that the experimental information available is pressure histories at various points in the experimental setup, but momentum flux and thermodynamic state, as is needed to fully determine the inlet conditions in the simulation (i.e., the pressure at a point gives no information about the momentum flux through a point, nor the temperature or density of the gases). The use of the experimentally available information to duplicate the conditions and amount of the air/fuel charge in the cylinder is an outstanding problem in engine modeling (Stephenson and Rutland 1995). Because of the sensitivity and complexity of the cylinder pressure on details of the intake port geometry and driving history (Kühn, Abthoff et al. 1996; Neußer and Geiger 1996), the trend in engine modeling is to forgo direct comparisons and use simulations generically to design engines (Stephenson and Rutland 1995; Bauritaud 1996).

A study of the intake flow in the Onan engine was undertaken and moderate success in comparing with the experimental data was achieved. An unexpected result of this study was the discovery that tuning the intake port on a naturally aspirated engine can significantly increase the charge density; in one simulation, with no attempt to optimize the charge density, a 7% increase above ambient density was observed in a particular combination of port length and experimentally-derived, pressure-history boundary condition. This indicates that significant supercharging can be obtained for the hybrid engine, because the intake port design can be optimized for just one engine speed. This is in contrast to multiple-speed engines that compromise performance at one RPM in order to operate at many engine speeds.

In order to aid in the computer modeling of the Onan engine, SNL added additional pressure diagnostics in the intake port and a more sensitive cylinder pressure transducer. This data significantly clarifies the operation of the air/fuel delivery system of the Onan engine and illustrated dynamics that were not previously observed: the cylinder pressure during the early intake flow (0–100 CA) oscillates with a frequency of 180–260 Hz and a large amplitude of 1–3 psi (data 101895AB). To understand the origin and effect of these oscillations, a KIVA simulation was done with a much longer intake port (from 7.4 cm to 37 cm). This simulation clearly exhibits the same amplitude oscillations, but with an even lower frequency (90–130 Hz). The simulation with the longer port also resulted in 4.5 percent lower mass in the cylinder and a 16 percent increase in the turbulent kinetic energy per unit mass at the time of combustion. Additional simulations showed that the dynamics of the intake flow are more sensitive to small changes in the initial state and geometry than expected, with large variations possible in magnitude and frequency and significantly different cylinder mass charges and turbulent levels. For example, a 20°C temperature increase of the gas in the port (a 7% decrease in density) results in a 20% increase in the amplitude of the first oscillation of the cylinder pressure.

These observations highlight the difficulty of matching the experimental data and the need for accurate experimental operating conditions. The source of the oscillations was found to occur in the simulations with the long, narrow intake port, and could likely be eliminated by larger diameter ports. The sensitivity and the difficulty of matching just one set of Onan data has led us to suggest that the intake manifold for future experimental engines needs be modified to eliminate or reduce this phenomenon. The experimental operation that is ideal for the KIVA simulations is a steady or slowly varying driving pressure and temperature, measured in a mostly stagnant volume near the intake valve. But, as mentioned in the opening of this section, these intake port simulations also suggest that the port dynamics can be exploited to provide supercharging in a naturally aspirated engine.

In addition to modifying the dimensions of the inlet port and the initial density, KIVA simulations were also done that duplicated the slight twist (27° from the plane through the two valves) in the intake port. These simulations did not change the prior conclusions concerning the dominant flow at time of combustion, a tumble flow, which is many times the intensity of the swirling flow. Steady-state swirl intensity was measured for the Onan engine (Swain 1995) for various valve lifts and flow rates. The KIVA simulations produced similar swirl characteristics: low swirl at small and large valve openings, larger swirl at moderate valve openings. More details are given on these simulations in the following section on the effect of the addition of a shroud on the intake valve.

Shrouded-Valve Simulations

As discussed in the introduction of this section, earlier KIVA simulations of the Onan engine lead to the conclusion that by inducing a swirling flow in the cylinder, in the place of the dominant tumble flow that was observed in the KIVA simulations (Johnson, Amsden et al. 1995), the efficiency of the engine might be improved. The experimental technique of inducing the swirl that was suggested by LANL was the addition of a shroud on the intake valve. Various shroud heights and extents on the edge of the valve were tried experimentally, and it was found that the apparent introduction of a moderate amount of swirl increased the efficiency of the engine (Hoekstra, Van Blarigan et al. 1996). The reason for this increased efficiency, as elucidated by the KIVA simulations, is the focus of this section. But first the technique for implementing a shroud in KIVA is presented.

A simple scheme was used to model a shroud on a valve in KIVA-3: a zero-thickness wall at an element boundary was added at the perimeter of the valve to duplicate the blocking of the flow by the shroud. For a full-height shroud, this wall extended up into the valve pocket, thereby preventing all flow through the valve gap at that azimuthal angle. For a lower-height shroud that allows flow past the shroud at large valve openings, a constant number of element sides above the edge of the valve were similarly blocked. The number of element sides that were blocked where chosen such that the average height of the numerical shroud was similar to the experimental height of the shroud. For example, for the 1.5 mm high shroud, the sides of two elements were blocked. This approach allowed for full blockage of the flow for small valve openings and allowed the flow over the shroud at large valve openings.

During the past year many KIVA simulations were done comparing the effects of different shroud heights and orientations, and it was found that the shroud caused significant changes in the turbulence level, combustion time, and NOx emissions. Experimentally it was observed that the engine had its peak efficiency with the 1.5 mm shroud and had lower efficiency for either higher shroud heights or no shroud. It was thought that the shroud introduced more swirl into the engine, which resulted in a more ideal turbulence intensity history, since it is known that tumble, as predicted to be the dominant flow in the Onan engine by KIVA, tends to create high turbulence intensity at maximum compression, where swirl tends to produce turbulence uniformly during combustion (Khalighi, El Tahry et al. 1995). Because excessive turbulence can increase heat transfer to the wall, it was thought that the efficiency increased with the shroud because of the more favorable turbulence intensity history.

To resolve the question as to the cause of the increased efficiency, four simulations were compared: with and without the 1.5 mm shroud and for two ignition timings of 20° and 12.5° BTDC. Fig. 4 illustrates that the addition of the shroud does indeed increase the swirl, although these values are low for engines designed to have swirl (Floch, Frank et al. 1995; Swain 1995). The indicated thermal efficiencies were calculated for all of the simulations by integrating over the compression, combustion and expansion cycle the work done by the cylinder pressure due to the change of cylinder volume and then dividing by the total energy produced by the hydrogen fuel. An identical method was used to calculate the thermal efficiencies of the Onan experiments (Hoekstra, Van Blarigan et al. 1996). The resulting efficiencies are plotted in Fig. 5. Although experimental data does not exist for the same operating conditions, preliminary Onan data with and without the 1.5 mm shroud tended to exhibit a 3% increase in the thermal efficiency, when it was observed to have an effect. What is of primary concern here is to understand the improved efficiency at the ignition timing of 12.5° BTDC in the simulation with the shroud.

In Fig. 6 the turbulence intensity is plotted for all of the simulations during the time of combustion and expansion. It is immediately apparent that the turbulence intensity, and hence the turbulent flame speed, would be similar for these four simulations. In fact, a more careful examination of the turbulence intensity shows that the different timing of ignition has a larger effect on the turbulence intensity than the presence or absence of the shroud. An examination of the heat transfer to the wall in Fig. 7 yields a similar conclusion that the dominant effect is the ignition timing. Note that even

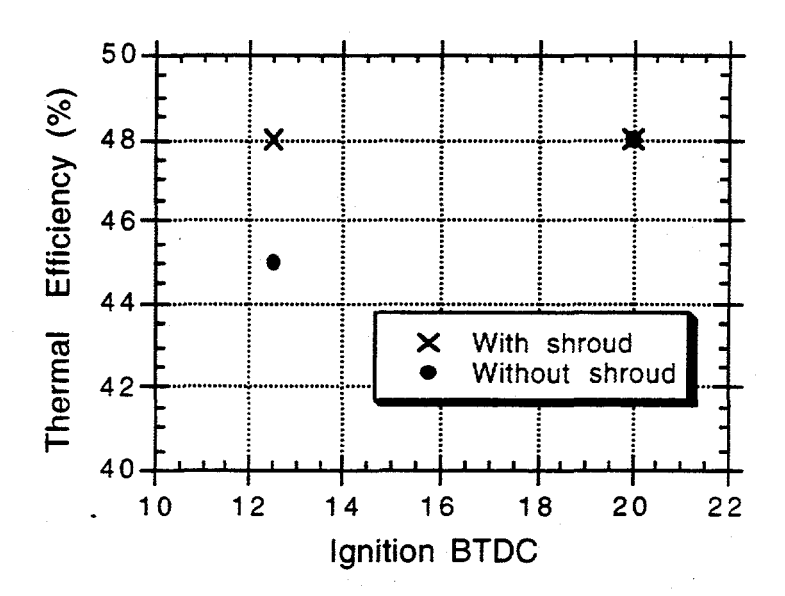


Fig. 5. The indicated efficiencies for the KIVA simulations.

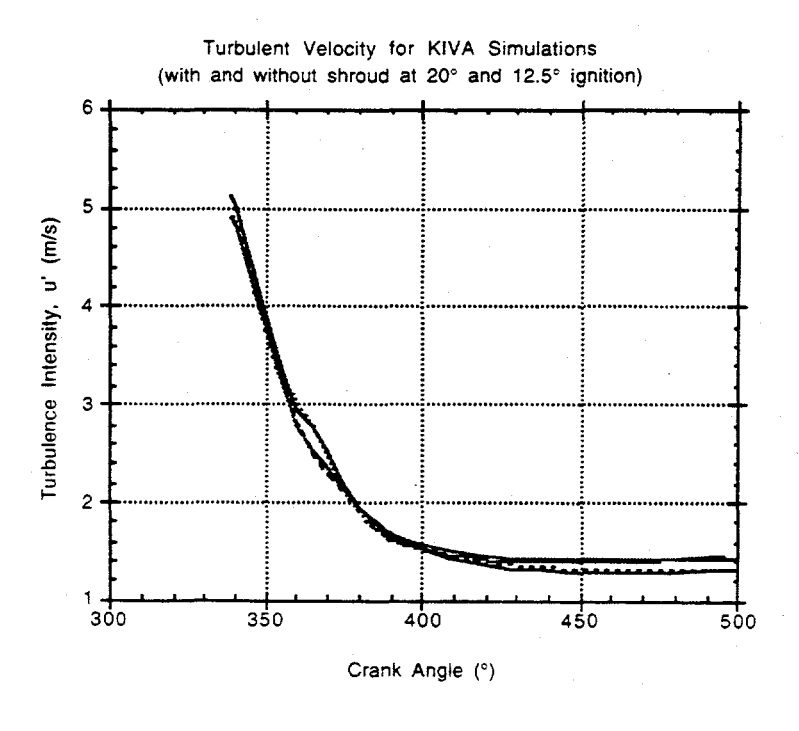


Fig. 6. The turbulence intensity for four simulations are shown, illustrating that the turbulent intensities are almost the same for all the simulations.

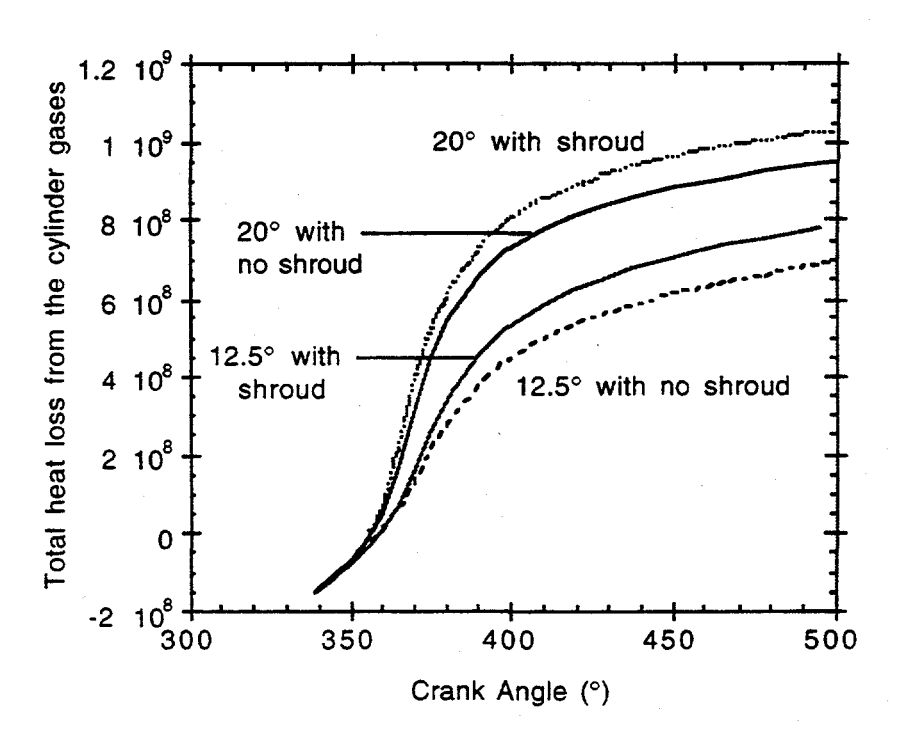


Fig. 7. The accumulated heat transferred to the wall from the cylinder gases in ergs.

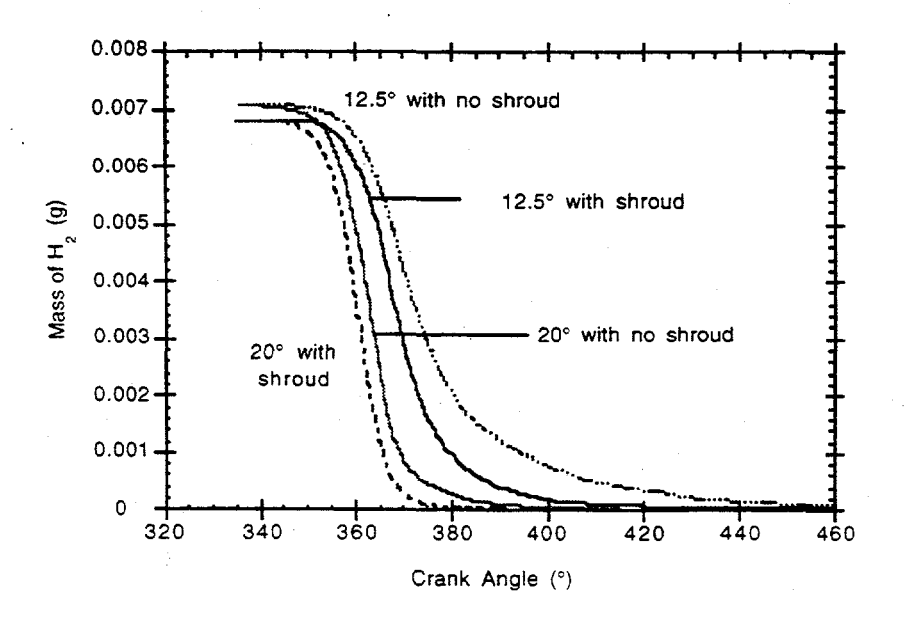


Fig. 8. The mass of hydrogen for the four KIVA simulations.

Comparison to the NOx and Efficiency of the Onan Engine

The ability to compare the KIVA simulations with the Onan engine data is a culmination of all the successes in modeling the intake flow with a short shroud and the development of a turbulent combustion model for hydrogen. The experimental comparison was also made possible by the large parametric set of data for the Onan engine made available by SNL. The large data set circumvented the problem of matching the intake flow history in order to achieve the same cylinder charge. Instead, an experimental data set could be chosen that most closely matched the volumetric efficiency in the KIVA simulations. The KIVA simulations were done at both 1200 and 1800 rpm and at a variety of ignition timings (from 20° to 7.5° BTDC) at an equivalence ratio of 0.4. The results presented here are for the 1800 rpm simulations.

As discussed in the section on modeling turbulence combustion, the eddy-dissipation model in its current undeveloped form has one free parameter that must be determined from a comparison to the experiments, and is comparable to determining the laminar flame speed for a specific hydrogen-air mixture at a certain temperature and pressure. This was accomplished by picking a value for A that best matched the pressure history of one Onan simulation (Run 111495fa). The parameter A was then held constant for all other simulations with different ignition times, but at the same equivalence ratio and volumetric efficiency. By then applying the model to a variety of ignition times, a fairly severe test of the model is achieved because by changing the ignition times, the conditions during combustion - the turbulence, pressure and temperature - also change significantly.

The resulting NO_x values from the simulations compare excellently with the experimental values, without any adjustment of the NO_x model for hydrogen (Fig. 9 below). Because NO_x is very sensitive to the burn rate and flame temperature, this is a sensitive test for the accuracy of the turbulent combustion model. This comparison is better than is generally found for hydrocarbon simulations and supports the conclusion in the literature (Warnatz 1981) that the slow NO_x kinetics are more accurate for hydrogen combustion. The difference in the slope between the simulations and experiments is likely due to keeping A constant when it should be varying with the changing conditions at ignition and during combustion. Inclusion of these effects would increase the flame speed and the combustion temperature at later spark timing, and hence the NO_x levels, resulting in even better agreement at other spark timings.

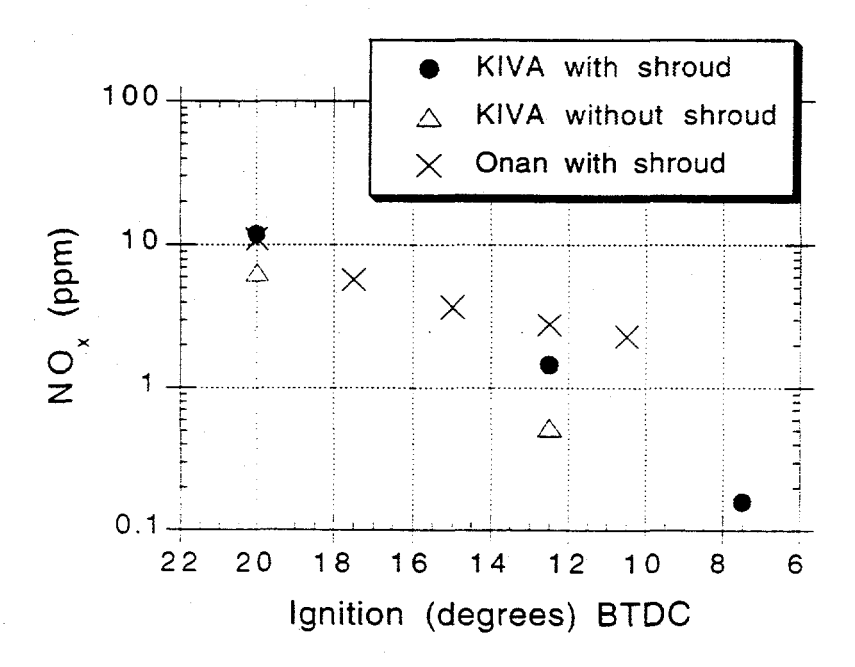


Fig. 9. Comparison of the NOx for the KIVA simulations and Onan experiments.

Comparisons of the efficiencies and pressure histories between experiments were also made (Fig. 10 below). The trend in the indicated thermal efficiencies duplicates the Onan data, but the values in the KIVA simulations are about 4% higher than in the experimental data. Because of the uncertainty in the wall temperatures in the engine and the difficulty in experimental determination of efficiencies, the offset is not unexpected. The duplication of the trends is an important validation of the turbulence and combustion model in KIVA. The rapid drop in the efficiency of the data at small ignition advance is generally seen to occur in other experimental data and is an expected trend in the simulation results.

All the results for the five simulations in Fig. 9 were obtained with about 15 hours of Cray YMP time. A large reduction in the required computing time was achieved by running the simulation to just before the earliest ignition time and then restarting the simulation from this time for the different ignition times.

In summary, KIVA simulations of the Onan engine agreed very well with the experimental results and largely validates the chosen approach for the intake flow modeling and the turbulence combustion modeling. Indeed, fewer "adjustments" of the models in KIVA were required than is typically necessary for modeling hydrocarbon-fuel engines. As additional comparisons with the Onan data are made and as data from the larger experimental engine are made available, the performance of KIVA will be reassessed and improvements in the models will be made.

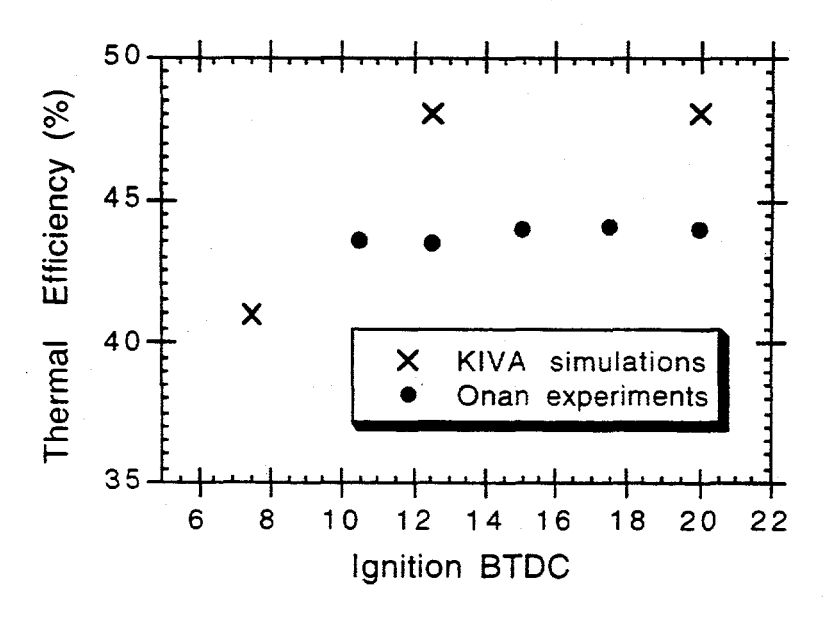


Fig. 10. Comparison of the indicated thermal efficiency for the KIVA simulations and Onan experiments.

Improvements in the KIVA-3 Code

Extensions to the Valve model

The implementation and testing of the valve model was covered in the prior annual report (Johnson, Amsden et al. 1995). Prior KIVA-3 simulations were limited to vertical intake and exhaust valves. Given that the turbulence and bulk flow patterns significantly affect the combustion in homogeneous-charged hydrogen engines, as demonstrated in the current Onan engine simulations, the capability to model valves at any inclined angle is essential for future hydrogen engine modeling. With some modification of the prior vertical-valve model, this capability has been added to the current setup and simulation codes and an angled-valve version of the Onan engine is shown in Fig. 11. This is a significant extension of the KIVA capability, because inclined values are used in almost all gasoline-fueled engines and likely will be used in many future hydrogen-fueled engines.

Improvement of Ease-of-Use of the KIVA-3 Code

Two additional features have been added to the KIVA-3 code that reduce the time needed to simulate a new engine. One is the addition of a "no-hydro" option that quickly runs through the opening and closing of the valves and the movement of the piston, in the exact manner as a full simulation, except no hydrodynamics are calculated. Thus, the integrity of the mesh can be checked in a few minutes, instead of hours. This is particularly useful for complex meshes in order to avoid the common difficulty of running a problem many hours, only to discover a difficulty with the mesh connectivity or entanglement late in the simulation and then have to redo the entire simulation. The second user-friendly feature is the simplification of different initial conditions within the computational mesh by specification in the input file. Prior versions required that the source code be modified to, for example, have a different state in the intake port than in the cylinder volume. Included in this feature is the direct specification of the air composition and temperature, along with the fuel equivalence ratio, thereby making the input variables similar to those typically specified in the experimental setup.

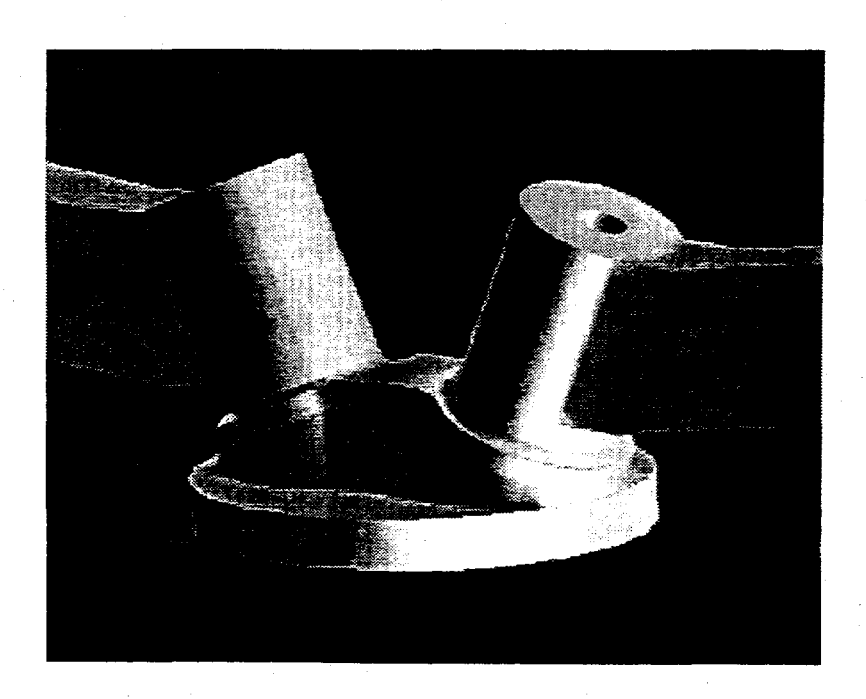


Fig. 11. An outside view of an angled-valve variation of the Onan engine. (Compare with Fig. 1.)

Improved Wall Heat-Transfer Model

Research done for future versions of the KIVA family of codes has improved the wall heat transfer model and has been implemented in the current version of KIVA-3. Analysis shows that the improved treatment gives better agreement with the experimentally observed wall heat flux.

Improved State Conservation During Mesh Remapping

An accuracy problem with KIVA during valve and piston movement was characterized and corrected. During the simulation of the Onan engine, mesh is added or removed from the calculation during the movement of the piston and valves. At these times, information (mass, momentum, energy, turbulence, etc.) must be remapped from the old mesh to the new mesh. Ideally all quantities are conserved during the remapping, but in practice the complexity of the process (multiple dimensions and multiple, but interrelated, variables) allows for only approximate conservation. It was observed that the prior method for remapping resulted in unexpected jumps in the state of the gas. in particular the velocity, during remapping. Because of the additional remeshing required by the new valve treatment in KIVA, this difficulty became more obvious than in prior simulations.

A better remapping scheme was formulated and tested. The worst case of momentum nonconservation was reduced to a tenth of prior change, and the new formulation usually resulted in no changes during remapping. Past Onan simulations were redone to assess the errors made previously. The turbulent energy levels in a typical Onan simulation differed by at most 10 percent between the old and new versions, although at the time of combustion the turbulent levels were negligibly different. The problem of nonconservation was a concern, because combustion flame velocities are proportional to the square of the turbulent kinetic energy. With this improvement in KIVA, we are more confident in the turbulence levels, and hence the hydrogen combustion rates, in the simulations.

Conclusions

Technical Presentations of the Project and Outreach to Industry

During the last year, many technical presentations of the project were made at conferences, universities and industry, to many attendees which had not previously heard of the Hydrogen Program. These are now summarized. A paper on the hydrogen injection modeling was presented at the '95 High Performance Computing Conference at Phoenix. A similar talk on "Three-dimensional modeling of hydrogen injection and combustion" was given at The 8th International Symposium on Transport Phenomena and Combustion at San Francisco. A technical paper, "Progress toward an Optimized Hydrogen Serial-Hybrid Engine," was presented in the Alternative Fuels Session at the ASME Internal Combustion Engine Conference in Milwaukee. The presentation covered the contributions of LLNL, LANL and SNL. Many of the attendees represented management and technical personnel from the major engine manufacturers. Requests for the research papers and video of a simulation of the Onan engine were made from industry and universities. A similar presentation was made at the Engine Research Center at the University of Wisconsin, Madison, briefing their modeling group on the unique challenges and opportunities in the hydrogen program.

In the last six months, the version of KIVA-3 that has been modified for the hydrogen project has been distributed to selected industrial and university collaborators for final testing and evaluation. The version will be more broadly released to our collaborators in the current fiscal year, followed by an official release to all the current users of KIVA-3, estimated to be more than two hundred users, as based on the KIVA email mailing list. The KIVA email list was developed to facilitate communication among KIVA users and to quickly disseminate information about the code. Currently over 220 subscribers have registered and represent industry, universities and national laboratories in the US and around the world.

Progress in the Project

During the past year, three milestones were achieved:

- The prediction of the NO_x and efficiency of the Onan experiments.
- The implementation and successful testing of a simplified chemistry model for hydrogen combustion.
- The transfer of the modified KIVA-3 code to industry and academia.

Future Work

The planned work over the next two years falls in three broad areas: the development of the KIVA simulation code for powerplant design, the support of the design and interpretation of the optimized, low-emission powerplant and industrial outreach and collaboration. These activities are concurrent and mutually supportive.

The extension of the KIVA code focuses on two areas: the continued development of the advanced chemistry and combustion modeling for hydrogen and hydrogen-hydrocarbon mixtures and the additions to the code for broader application and more user-friendly features. While the latter is straightforward and largely completed, the former is a significant challenge and is at the forefront of current research. The goal is to provide a combustion model that not only accurately describes the dependencies of turbulence, fuel-oxygen ratio, temperature and pressure, but that is applicable to repetitive, full-engine simulations, required by industry.

The engine modeling capability will be validated by comparisons with the data from the prior and current SNL engines. The current SNL engine has a similar combustion chamber geometry as the Onan engine, but with about double the total volume. The two data sets will enable a test, both experimentally and computationally, of the expected scaling of efficiency with engine volume. Furthermore, the different intake port geometry, and the subsequent different turbulence levels during combustion, will provide further understanding on the optimum intake port design for maximum engine efficiency. The simulation capability is an essential component for understanding the performance in experimental engines, because the simulations provide details and causal effects that are not experimentally measurable. A unique design opportunity is presented because the operating conditions of the powerplant is at constant RPM: the engine geometry, in particular the intake port and valves, can be optimized for maximum efficiency, in contrast to all existing engines which are a compromise of performance over a wide RPM range. The KIVA simulation capability can economically examine many possible geometries and is an essential component to the success of the final engine design.

Concurrent with the above tasks, the transfer of the technology to industry and universities and the collaboration with industrial partners will be undertaken. Outside participation on the development of the hydrogen simulation capability in KIVA is ongoing and will easily continue, due to the active interest of our collaborators.

Appendix A - Useful Relationships between Different Measures of Concentration

Hydrogen concentration can be given as:

 φ = fuel equivalence ratio, the moles of fuel divided by the moles of fuel that would exactly be consumed by the available oxygen,

 f_{H2} = the mole fraction of hydrogen,

 n_{H2}/n_{O2} = the number of moles of hydrogen divided by the moles of oxygen

= f_{H2}/f_{O2} , assuming an ideal mixture.

% (molar) hydrogen concentration = $100 \times f_{H2}$

The assumption is made in the following that hydrogen mixtures can be assumed to be an ideal mixture of gases, i.e., the gases are non-interacting and hence the volume fraction is equal to the mole fraction $(V_{H2}/V_{O2} = n_{H2}/n_{O2} = f_{H2}/f_{O2})$. This is a good assumption at typical pressures and temperatures encountered in combustion engines. For hydrogen the fuel equivalence ratio is given by:

$$\varphi = (1/2) f_{H2} / f_{O2}$$

independent of the presence of a diluent, such as nitrogen.

For hydrogen-oxygen mixtures, the above concentration measures are related by:

$$\frac{n_{H2}}{n_{O2}} = \frac{f_{H2}}{f_{O2}} = \frac{f_{H2}}{1 - f_{H2}} = 2\varphi$$

$$\varphi = \frac{1}{2} \frac{f_{H2}}{1 - f_{H2}}$$
 or $f_{H2} = \frac{2\varphi}{1 + 2\varphi}$

The following table gives representative values between these measures:

φ	f _{H2}	nH2/nO2
0.4	0.44	0.8
1.0	0.66	2.0
1.8	0.78	3.6

For hydrogen-air mixtures, with an composition of air assumed to be 77% N2, 22% O2 by mass or 79% N2, 20% O2 by volume or moles, with the average molecular weight of air taken to be 28.90. The above concentration measures are related by:

$$\varphi = \frac{1}{0.44} \frac{f_{H2}}{f_{gir}}$$
 or $\frac{f_{H2}}{f_{gir}} = 0.44 \varphi$

$$f_{H2} = \frac{0.44\varphi}{1 + 0.44\varphi} \text{ or } \varphi = \frac{2.\overline{27}f_{H2}}{1 - f_{H2}}$$

The following table gives representative values between these measures:

φ	f _{H2}	nH2/nO2
0.4	0.15	0.176
1.0	0.306	0.44
1.8	0.442	0.792

References

Al-Khishali, K.J. and D. Bradley. 1983. "Turbulent Combustion of Near-Limit Hydrogen-Air Mixtures." Comb. and Flame, 54: 61-70.

Amsden, D.C. and A.A. Amsden. 1993. "The KIVA Story: A Paradigm of Technology Transfer." *IEEE Transactions on Professional Communication*, 36(4): 190-195.

Apostolescu, N. and R. Chiriac. 1996. "A Study of Combustion of Hydrogen-Enriched Gasoline in a Spark Ignition Engine." SAE Technical Paper Series (960603).

Bauritaud, T. 1996. Personal communication on Intake Flow Modeling at IFP.

Collier, K., R.L. Hoekstra, N. Mulligan, C. Jones and D. Hahn. 1996. "Untreated Exhaust Emissions of a Hydrogen-Enriched CNG Production Engine Conversion." SAE Technical Paper Series (960858).

Dillies, B., K. Marx, J. Dec and C. Espey. 1993. "Diesel Engine Combustion Modeling Using the Coherent Flame Model in Kiva-II." SAE Technical Paper Series (930074).

Floch, A., J.V. Frank and A. Ahmed. 1995. "Comparison of the Effects of Intake-Generated Swirl and Tumble on Turbulence Characteristics in a 4-Valve Engine." SAE Technical Paper Series (952457).

Hoekstra, R.L., P. Van Blarigan and N. Mulligan. 1996. "NOx Emissions and Efficiency of Hydrogen, Natural Gas and Hydrogen/Natural Gas Blended Fuels." SAE Technical Paper Series (961103).

Johnson, N.L., A.A. Amsden and T.D. Butler. 1995. "Hydrogen program combustion research: three dimensional computational modeling." In *The 1995 DOE/NREL Hydrogen Program Review, Vol. II*, 285–304. Coral Gables, Florida: National Renewable Energy Laboratory.

Johnson, N.L., A.A. Amsden, J.D. Naber and D.S. Siebers. 1995. "Three-Dimensional Computer Modeling of Hydrogen Injection and Combustion." In *High Performance Computing* '95 Conference. Phoenix, Arizona: Society for Computer Simulation.

Khalighi, B., S.H. El Tahry, D.C. Haworth and M.S. Huebler. 1995. "Computation and Measurement of Flow and Combustion in a Four-Valve Engine with Intake Variations." SAE Technical Paper Series (950287).

Koroll, G.W., R.K. Kumar and E.M. Bowles. 1993. "Burning Velocities of Hydrogen-Air Mixtures." Comb. and Flame, 94: 330-340.

Kühn, M., J. Abthoff, R. Kemmler and T. Kaiser. 1996. Influence of the Inlet Port and Combustion Chamber Configuration on the Lean-Burn Behavior of a Spark-Ignited Gasoline Engine. SAE Technical Paper Series (960608).

Kwon, M.S., J.F. Driscoll and G.M. Faeth. 1990. "Turbulent Premixed Hydrogen/Air Flames at High Reynolds Numbers." Comb. Sci. and Tech., 73: 327-350.

Kwon, S., L.K. Tseng and G.M. Faeth. 1992. "Laminar Burning Velocities and Transition to Unstable Flames in H2/O2/N2 and C3H8/O2/N2 Mixtures." Comb. and Flame, 90: 230-246.

Kwon, S., M.S. Wu, J.F. Driscoll and G.M. Faeth. 1992. "Flame Surface Properties of Premixed Flames in Isotropic Turbulence: Measurements and Numerical Simulations." *Comb. and Flame*, 88: 221-238.

Liu, D.D.S. and R. MacFarlane. 1983. "Laminar Burning Velocities of Hydrogen-Air and Hydrogen-Air-Steam Flames." Comb. and Flame, 49: 59-71.

Magnussen, B.F. and B.H. Hjertager. 1978. "On Mathematical Modeling of Turbulent Combustion with Special Emphasis on Soot Formation and Combustion." In 16th Symposium on Combustion, The Combustion Institute.

Meier, F., J. Köhler, W. Stolz, W.H. Bloss and M. Al-Garni. 1994. "Cycle-Resolved Hydrogen Flame Speed Measurements with High Speed Schlieren Technique in a Hydrogen Direct Injection SI Engine." SAE Technical Paper Series (942036).

Neußer, H.-J. and J. Geiger. 1996. Continuous Variable Tumble - A New Concept for Future Lean Burn Engines. SAE Technical Paper Series (960607).

Rutland, C.J., J.H. Ferziger and S.H. El Tahry. 1990. "Full Numerical Simulations and Modeling of Turbulent Premixed Flames." Comb. Inst., : 621-627.

Rutland, C.J. and A. Trouve. 1993. "Direct Simulations of Premixed Turbulent Flames with Nonunity Lewis Numbers." Comb. and Flame, 94: 41-57.

Stephenson, P.W. and C.J. Rutland. 1995. "Modeling the Effects of Intake Flow Characteristics on Diesel Engine Combustion." SAE Technical Paper Series (950282).

Swain, M. 1995. Measurements of Swirl in the Onan Engine.

Ting, D.S.-K., M.D. Checkel and B. Johansson. 1995. "The Importance of High-Frequency, Small-Eddy Turbulence in Spark Ignited, Premixed Engine Combustion." SAE Technical Paper Series (952409).

Tseng, L.K., M.A. Ismail and G.M. Faeth. 1993. "Laminar Burning Velocities and Markstein Numbers of Hydrocarbon/Air Flames." Comb. and Flame, 95: 410-426.

Van Blarigan, P. 1995. "Experimental Program for the Development of the Hybrid Engine." In *The* 1995 DOE/NREL Hydrogen Program Review, Vol. II, Coral Gables, Florida: National Renewable Energy Laboratory.

Warnatz, J. 1981. "Concentration-, Pressure-, and Temperature-Dependence of the Flame Velocity in Hydrogen-Oxygen-Nitrogen Mixtures." Comb. Sci. Tech., 26: 203-213.

Wu, M.S., S. Kwon, J.F. Driscoll and G.M. Faeth. 1991. "Preferential Diffusion Effects on the Surface Structure of Turbulent Premixed Hydrogen/Air Flames." Comb. Sci. Tech., 78: 69-96.

ANALYSIS OF EXPERIMENTAL HYDROGEN ENGINE DATA AND HYDROGEN VEHICLE PERFORMANCE AND EMISSIONS SIMULATION

Salvador M. Aceves Lawrence Livermore National Laboratory Livermore, CA 94550

Abstract

This paper reports the engine and vehicle simulation and analysis done at Lawrence Livermore (LLNL) as a part of a joint optimized hydrogen engine development effort. Project participants are: Sandia National Laboratory, California (SNLC), responsible for experimental evaluation; Los Alamos National Laboratory (LANL), responsible for detailed fluid mechanics engine evaluations, and the University of Miami, responsible for engine friction reduction.

Fuel cells are considered as the ideal power source for future vehicles, due to their high efficiency and low emissions. However, extensive use of fuel cells in light-duty vehicles is likely to be years away, due to their high manufacturing cost.

Hydrogen-fueled, spark-ignited, homogeneous-charge engines offer a near-term alternative to fuel cells. Hydrogen in a spark-ignited engine can be burned at very low equivalence ratios, so that NO_x emissions can be reduced to less than 10 ppm without catalyst. HC and CO emissions may result from oxidation of engine oil, but by proper design are negligible (a few ppm). Lean operation also results in increased indicated efficiency due to the thermodynamic properties of the gaseous mixture contained in the cylinder. The high effective octane number of hydrogen allows the use of a high compression ratio, further increasing engine efficiency:

In this paper, a simplified engine model is used for predicting hydrogen engine efficiency and emissions. The model uses basic thermodynamic equations for the compression and

expansion processes, along with an empirical correlation for heat transfer, to predict engine indicated efficiency. A friction correlation and a supercharger/turbocharger model are then used to calculate brake thermal efficiency. The model is validated with many experimental points obtained in a recent evaluation of a hydrogen research engine. The experimental data are used to adjust the empirical constants in the heat release rate and heat transfer correlation. The adjusted engine model predicts pressure traces, indicated efficiency and NO_x emissions with good accuracy over the range of speed, equivalence ratio and manifold pressure experimentally covered.

The validated model is applied to conditions that are considered to be of interest to vehicular applications in hybrids as well as conventional cars. It is recognized that using the engine model for conditions far from the experimental points may result in inaccuracies. Therefore, cylinder geometry is kept constant in the analysis, and only engine speed is varied beyond the range for which experimental data points are available. It is expected that such an extrapolation does not introduce large errors.

The results present information that can be used to predict engine performance for vehicular applications, and are expected to serve as a first-order guide for engine sizing (number of cylinders) and control strategy selection. The results indicate that hydrogen lean-burn sparkignited engines can provide Equivalent Zero Emission Vehicle (EZEV) levels in either a series hybrid or a conventional automobile.

Nomenclature

A cylinder surface area

B cylinder bore

 C_1 , C_2 constants in Equation 4.

h heat transfer coefficient

n shape parameter for burn fraction curve

p pressure

q heat transfer rate

S_p mean piston speed

T temperature

V volume

w gas velocity parameter

x fraction of burn

 θ crank angle

Subscripts

d displacement

m motored

r reference

w wall

Introduction

Fuel cells have been recognized as the optimum power source for the light-duty fleet, due to their high efficiency and low (near zero) emissions (DeLuchi, 1992). Fuel cells provide the near-zero-emission benefits of electric vehicles, with the potential for long range and performance comparable to that of conventional cars. The major obstacles in the way of generalized use of vehicular fuel cells are their high cost, and the lack of an adequate fueling infrastructure. The need for a new fueling infrastructure can be reduced if a fuel reformer is installed onboard the vehicle, to convert a liquid fuel (e.g. methanol) to the high-purity hydrogen fuel required in PEM fuel cells (Appleby, 1993).

Hydrogen can also be used in spark-ignited piston engines. Hydrogen has very special properties, including a very high laminar flame speed, a high effective octane number, and no toxicity or ozone-forming potential (Smith, 1994). Homogeneous-charge spark-ignited piston engines can be designed to take advantage of these characteristics. The high laminar flame speed allows the use of very low equivalence ratios (as low as 0.2), reducing NO_x emissions to near-zero levels without requiring a catalytic converter, that may deteriorate with time. The use of low equivalence ratios also increases the indicated efficiency, and reduces the need for throttled operation (Heywood, 1988). The engine can have a high compression ratio, due to the high hydrogen octane number. Piston engines do not require a high-purity fuel, and can burn mixtures of hydrogen, carbon monoxide, and other gases.

Hydrogen piston engines can therefore be optimized to yield a high efficiency and near-zero emissions. While fuel cells have the potential for greater improvements in efficiency as well as emissions, piston engines are an inexpensive and well-known technology that can be applied in the short-term for obtaining basically the same benefits as fuel cell utilization.

This paper analyzes the applicability of hydrogen homogeneous-charge spark-ignited piston engines to Equivalent Zero Emission Vehicles (EZEV). The analysis uses an engine model that is calibrated to match the data obtained in a recent experiment (Van Blarigan, 1996). The model is then used to generate engine performance maps for supercharged and turbocharged operation. These maps are applied for predicting fuel economy and emissions for conventional and series hybrid vehicles.

Ford Motor Company has publicly stated that piston engines can be produced for \$20/kW, which provides the economic incentive to evaluate piston engine technology for hydrogen utilization.

Based on our engine modeling and vehicle simulation work, we believe that we can develop the design rules for building 40% efficient hydrogen engines with emissions that are lower than those from electric vehicles when power plant emissions are accounted for

This research work has two major parts:

1. Analysis of hydrogen engine experimental data: This task consists of using a simplified engine model to evaluate the experimental results obtained by Sandia National Laboratory/California, for the current generation of optimized hydrogen spark-ignited

¹ Equivalent Zero Emission Vehicles are defined here as those that generate less emissions when operating inside the Los Angeles Basin than the power plant emissions generated as a result of electric car operation. These emission levels have been estimated as being one tenth of CARB ULEV standards, and are being considered for approval by CARB (CARB, 1995).

engine. The simplified engine model is used in conjunction with an optimizer, to obtain optimum fits for the pressure traces obtained by the SNLC researchers. Burn duration and burn fraction parameters are then obtained from the optimum pressure trace fits. Pressure traces are always fitted to within a very good approximation, indicating that the heat release parameters obtained from the simplified engine model can be considered reliable:

2. The results of the analysis of the combustion obtained in (1) are then used to develop an engine model that can predict hydrogen engine performance and emissions for conditions not tested in the experimental work. Friction, supercharger and turbocharger models are incorporated into the engine model, to predict brake thermal efficiency (ratio of net output work to chemical energy input). The engine model can then be incorporated into a hybrid and conventional vehicle simulation code, to predict hydrogen vehicle fuel economy and emissions. Hydrogen vehicle fuel economy is a necessary input to infrastructure studies and fuel storage design.

The purpose of this work is to generate a design guide for hydrogen spark-ignited engines that a user may consult for selecting a hydrogen engine (especially for sizing the engine) for a particular application and for the efficiency and emissions constraints of the given application. The guide will indicate the performance of vehicles built with an existing engine, and point to engine designs that will result in improved performance and emissions.

This project complements the ongoing experimental work at Sandia National Laboratory/California (SNLC), the detailed fluid mechanics and combustion analysis done at Los Alamos National Laboratory (LANL), and the friction reduction work at University of Miami, without duplicating any of the work.

Past Results

This project has resulted in a set of design guidelines for high efficiency and low emission hydrogen engines and vehicles. These guidelines include: extremely lean engine operation for high indicated efficiency and very low nitric oxide (NO_x) emissions; high compression ratio for high efficiency; long piston stroke, controlled turbulence, and big cylinders for reduced engine heat transfer losses; relatively low engine speed for reduced friction; supercharged operation for improving power output and efficiency; and the use of a series hybrid vehicle configuration for maximum fuel economy, thus reducing the problem of on-board fuel storage for vehicular use.

This project has also demonstrated that an optimized hydrogen spark-ignited engine built according to the guidelines listed above, offers most of the emissions and efficiency benefits of using fuel cells, without the cost and packaging restrictions of current PEM fuel cells. Optimized hydrogen spark-ignited engines are a current technology that can be used in approaching the 80 mpg goal of the Partnership for a New Generation of Vehicles (PNGV), as well as the Equivalent Zero Emission Vehicle (EZEV) standards being considered by the California Air Resources Board (CARB).

The results of this project have been reported in 6 publications in the open literature. One of these papers was written jointly with SNLC, and another was written jointly with LANL.

Experimental Engine Evaluation

The engine used in the experimental evaluation is an Onan engine which was modified by incorporating a head containing two spark plugs, along with the original two valves. The combustion chamber is a simple right circular cylinder with no squish and a flat top piston. This geometry has been shown to be the most efficient shape for reducing heat transfer losses

in lean-burn engines (Olsson and Johansson, 1995). Engine characteristics are listed in Table 1, along with the range of conditions used in the experiment. The design of the Onan engine is based on the arguments set forth by Smith et al., 1995, to obtain a high efficiency, low emission engine. These guidelines include: extremely lean engine operation for high indicated efficiency and very low NO_x emissions; high compression ratio for high efficiency; long piston stroke, controlled turbulence, and big cylinders (low surface area to volume ratio) for reduced engine heat transfer losses; relatively low engine speed for reduced friction; and supercharged or turbocharged operation for improving specific power output and efficiency.

Figures 1 and 2 show the most important experimental results. Figure 1 shows indicated efficiency as a function of equivalence ratio, for all the experimental points at MBT timing obtained in the analysis. Engine speeds and supercharged operation are indicated with different symbols. A 0.39 equivalence ratio was selected for most supercharged runs. The figure shows that indicated efficiency increases as a function of engine speed, as a consequence of reduced heat transfer losses. The variation of indicated efficiency with equivalence ratio is best observed for 1200 rpm operation, for which the greatest fuel/air range was used. Indicated efficiency reaches a maximum near a 0.40 equivalence ratio. Increasing the equivalence ratio from this point results in a decreased indicated efficiency, due to a decreased specific heat ratio ($\gamma = c_p/c_v$) for the gas inside the cylinder (Heywood, 1988). Decreasing the equivalence ratio from the optimum point increases the timing losses, due to slower heat release, thereby reducing the indicated efficiency. Supercharged operation results in small indicated efficiency gains due to slightly lower heat transfer losses per unit mass of fuel at the higher densities. Supercharged operation has a larger effect on brake thermal efficiency by increasing the output work relative to the frictional work.

Figure 2 shows NO_x emissions as a function of equivalence ratio. The figure shows that NO_x emissions are very insensitive to engine speed and supercharged operation, and correlate very well with equivalence ratio. It is concluded that the modified Zeldovich mechanism (Heywood, 1988) describes NO_x production well. Spatial simulations using a 2-dimensional version of KIVA (Amsden, 1993) indicate that 80% of the NO_x is produced by the first 20% of the burned gas when the last-burned gas recompresses the first-burned gas.

Engine Model

The engine model uses first principles and correlations to predict piston engine efficiency and power output. The engine model is a lumped (zero-dimensional), time-dependent model which solves the basic differential equations for the compression and power strokes. The following empirical expression is specified for the shape of the heat release curve (Ferguson, 1986):

$$x = x_{\text{max}} \left[1 - \exp\left(\frac{\theta - \theta_{i}}{\theta_{b}}\right)^{n} \right]$$
 (1)

where θ is the instantaneous crank angle, θ_s is the ignition angle, and θ_b and n are shape parameters for the heat release curve. The values of θ_s , θ_b , and n are determined for each experimental run by using an optimizer (Haney et al., 1992) to find the combination of the three parameters that minimizes the differences between the experimental pressure trace and the pressure trace calculated by the model. The results have been very satisfactory. The relative errors in matching the pressure traces have been of the order of 0.5%, with a maximum error of 1% over all engine speeds, equivalence ratios and manifold pressures. The ranges for θ_b and n are: $15^{\circ} \le \theta_b \le 30^{\circ}$ and $1.15 \le n \le 1.45$.

The engine model uses Woschni's correlation (Woschni, 1967) to estimate engine heat transfer. This correlation is given as:

$$q = h A (T - T_w)$$
 (2)

with

$$h = 3.26 B^{-0.2} p^{0.8} T^{-0.55} w^{0.8}$$
 (3)

where q is the overall heat transfer rate, A is the cylinder area, h is the heat transfer coefficient in W/m²K, B is the cylinder bore in m, p is the pressure in kPa, T is the mass-averaged temperature in K, and w is a measure of the gas velocity inside the cylinder, given as:

$$w = C_1 S_p + C_2 V_d T_r (p-p_m)/p_r V_r$$
 (4)

Where $C_1 = 2.28$ during the compression and expansion periods; S_p is the mean piston speed; $C_2 = 0.00324$; V_d is the displaced volume; T_r , p_r and V_r are temperature, pressure and volume at a reference state; and $p-p_m$ is the difference between the cylinder pressure and the motored pressure. The variables are a function of time, and are calculated for each crank angle degree of engine rotation. It was found during the analysis that the heat transfer correlation underpredicts heat transfer losses. Therefore, the original values of the constants C_1 and C_2 given above were multiplied by 1.8, resulting in a better match with the experimental data.

The engine model includes a friction model and a supercharger/turbocharger model to predict brake thermal efficiency. The friction model uses a detailed correlation developed by Patton et al., 1989. Supercharger and turbocharger performance is calculated by using a thermodynamic model and assuming a constant (0.7) isentropic efficiency for both the turbine and the compressor. Selection of a supercharger to match the energy control demands is outside the current experience of the authors. However, a detailed supercharger map could be incorporated into the model if further refinement is desired. A water-cooled intercooler is assumed with a thermal effectiveness of 0.7. A model for NO_x emissions prediction is incorporated in the engine model. Emissions of NO_x are calculated as a function of engine equivalence ratio (Figure 2). A correction is used for supercharged and turbocharged operation, to take into account the higher intake temperature resulting from the compression process and the less than perfect effectiveness of the intercooler. Based on reported data for typical engines (Heywood, 1988), volumetric efficiency is assumed to vary from 85% at low engine speeds, to a maximum of 95% at 4000 rpm, down to 90% at 5000 rpm.

The engine model is validated by comparing the calculated and experimental indicated efficiencies. Figure 3 shows experimental (from Figure 1) and model results as a function of equivalence ratio. The figure indicates that the model predicts absolute values as well as trends with good accuracy for engine indicated efficiency, over the whole range of operating conditions, with the maximum error of the order of 1%. NO_x emissions are also predicted to within a good approximation with the correlation of NO_x as a function of equivalence ratio. No validation is done for brake thermal efficiency, because the Onan engine used in the experiment has substantially more friction per cylinder than a current automotive engine, for which Patton's correlation applies.

The engine model is then applied to predicting the engine and vehicle performance that result if a 4-cylinder (1.97 liter) hydrogen engine is built with the same cylinder characteristics of the Onan engine. The geometry of the engine cylinders is not changed in

the analysis, because small changes in geometry may result in significant changes in efficiency. It is expected, however, that larger engine cylinders will improve engine efficiency.

Using the engine model for predicting vehicle performance requires extrapolating from the engine speeds used in the experiment (1200-1800 rpm) to engine speeds that are required for vehicle operation. A maximum engine speed of 5000 rpm is assumed. It is recognized that this extrapolation may result in errors. Errors are due to turbulence variations with engine speed which influence heat release rate, thus changing both timing losses and heat transfer losses. However, Figure 3 shows that the model predicts the efficiency trends with good accuracy for the range in which experimental data exist, and it is considered that the model can do a reasonable job at predicting efficiency for high engine speeds. In addition to this, engines in conventional and series hybrid vehicles are most often operated at low to moderate speeds, which is the range for which the model has been validated. For the conventional vehicle analyzed in a later section of this paper the mean engine speed is 1500 rpm for the urban cycle and 2700 rpm for the highway cycle. Maximum engine speed for the driving cycles is 3300 rpm. The series hybrid vehicle is set to operate at a constant 2400 rpm during the driving cycles.

Engine brake thermal efficiencies are required for applying the engine code to vehicle calculations, and brake thermal efficiencies are calculated with a friction and a supercharger/turbocharger model that have not been validated for this particular application. While the model cannot replace experimental runs, it is considered that the brake thermal efficiencies calculated with the model give a good idea of the performance that can be obtained with such an engine. Engine emissions are very insensitive to engine operating conditions other than maximum temperature within the cylinder (Figure 2), and it is therefore expected that the engine NO_x model can provide accurate predictions for emissions levels throughout the operating range.

The engine model is applied to generate engine emissions and performance maps, necessary for predicting vehicle performance. A conventional engine has only one degree of freedom for controlling the output torque at any given speed: the inlet manifold pressure. This is due to the use of three-way catalysts that require near-stoichiometric operation for high conversion efficiency. A hydrogen engine has two degrees of freedom, because equivalence ratio can also be varied. Generating an engine map therefore requires determining a control strategy that specifies how to adjust these two parameters to obtain the desired torque for any given engine speed. In this analysis, an optimizer (Haney et al., 1992) is used to determine the combination of equivalence ratio and inlet manifold pressure that satisfies the torque requirement while providing the maximum engine brake thermal efficiency. Equivalence ratio in the optimization is restricted to values less than 0.5, and inlet manifold pressure is kept under 2 bar. Another constraint is used in the optimization: engine NO_x emissions are less than 10 ppm under all operating conditions. An engine generating 10 ppm of NO_x is below the EZEV standards, provided that it is installed in a vehicle with a fuel economy of 40 mpg or higher.

Lean operation results in low power output, and therefore turbocharged or supercharged operation is required for providing a reasonably high power output. Both supercharged and turbocharged operation have been considered for generating the engine performance map. The performance maps for both cases are very similar, with turbocharged operation having a slight efficiency advantage over supercharged operation. Only the results for supercharged operation are shown in this paper. Supercharged operation is preferred to turbocharged operation due to the lag time that may exist in turbocharged operation.

Results

Figures 4-7 show the predictions for engine efficiency and emissions maps, as well as the optimum control strategy for inlet equivalence ratio and pressure, for the 4-cylinder supercharged engine.

Figure 4 shows lines of constant brake thermal efficiency (in percent) as a function of engine speed and engine torque. The figure also shows a dotted line corresponding to the conditions at which the engine generates 10 ppm of NO_x, and a dashed line that indicates the maximum torque that can be obtained within the upper bounds of equivalence ratio (0.5) and inlet pressure (2 bar) used in the analysis. The 10 ppm NO_x curve is the lower of the two, and therefore sets the limit on the maximum torque and power that can be obtained from the engine. The maximum power that can be obtained while satisfying the NO_x restriction approaches 60 kW at 5000 rpm. The contour lines in this and the following figures spread beyond the 10 ppm line, to show the potential power gains obtained by relaxing this restriction. A square in the figure indicates the approximate range of experimental conditions covered.

Figure 4 shows that the engine is predicted to have a broad area of high efficiency, for intermediate speeds and high torques. The efficiency drops for lower speeds due to increased heat transfer losses, and for higher speeds due to increased friction. As expected, the efficiency drops to zero as the load is reduced. However, the drop occurs more slowly than in conventional engines, because the equivalence ratio can be reduced as the load is reduced, resulting in lower throttling losses.

Figure 5 shows contours of NO_x emissions in ppm as a function of engine speed and torque. Engine levels are near zero (<2 ppm) over the low load range, which is the range at which the engine is operated most of the time during city and highway driving in conventional cars. Emissions increase slowly as the torque increases, until the restriction of 10 ppm is approached. When this restriction is approached, the operating conditions in the engine are adjusted so that the 10 ppm line is pushed as high as possible by increasing the manifold pressure without further increases in equivalence ratio, at the cost of some losses in efficiency. This explains the great distance between the 8 ppm and the 10 ppm lines shown in the figure. Emission levels shown in the figure are expected to be valid over the lifetime of the engine, since no catalytic converter is used to control emissions. Emission levels are only a function of equivalence ratio and manifold pressure, and are therefore not expected to increase with use, as occurs in gasoline engines due to catalytic converter deterioration.

Figure 6 shows contour lines of equivalence ratio as a function of engine speed and torque. Equivalence ratios shown in the figure are optimum values, that result in the maximum possible brake thermal efficiency, while meeting the 10 ppm NO_x limit. The figure includes a dotted line for the 10 ppm NO_x limit, and a dashed line for maximum engine torque for the maximum equivalence ratio (0.5) and pressure (2 bar) considered in the analysis. Figure 6 shows that engine equivalence ratio is reduced down to 0.23 at the low load conditions, to reduce throttling losses. Equivalence ratio is then increased as the torque is increased, until the 10 ppm NO_x limit is approached. At this point, equivalence ratio cannot be increased any further, and additional power is obtained by supercharging (Figure 7). Equivalence ratio has to be reduced as the inlet pressure increases, to compensate for the higher temperature of the intake gases. The reduction of equivalence ratio with increasing torque appears in the figure as sharp corners in the equivalence ratio lines at about 80 Nm.

Figure 7 shows contour lines of optimum inlet pressure (in bars) as a function of engine speed and torque. Pressures in the figure are selected to provide the maximum possible brake thermal efficiency, while meeting the 10 ppm NO_x limit. The figure includes a dotted line for the 10 ppm NO_x limit, and a dashed line for the maximum engine torque. Inlet pressure is kept relatively high (0.5 bar) at the very low load conditions to reduce throttling losses. The engine operates without supercharging over most of the low-load conditions that are required for typical urban and highway driving. When the 10 ppm NO_x limit is approached, pressure is increased rapidly to provide the required power without increasing equivalence ratio (which would increase combustion temperature and therefore NO_x).

Application to Conventional and Series Hybrid Vehicles

The engine efficiency and NO, maps presented in the previous section are now used in predicting vehicle fuel economy, performance and emissions for a conventional and a series hybrid vehicle. This is accomplished by incorporating the engine maps into an existing vehicle evaluation code (Aceves and Smith, 1995). The main characteristics of the two vehicles are listed in Table 2. Both vehicles have a low weight, with the series hybrid vehicle weighing 100 kg more than the conventional car, due to the additional components required in the series hybrid power train. The engine and the hydrogen storage tank for the series hybrid vehicle can be downsized to reduce the weight differential between the two cars. This possibility, however, is not considered in this analysis. It is assumed that liquid hydrogen cryogenic storage is used, since hydride storage would result in a substantially increased vehicle weight. Liquid hydrogen storage also has a reasonable volume (about 110 liters, 30 gallons, for 5 kg of hydrogen), compared with the volume required for compressed hydrogen (about 220 liters, 60 gallons, at 34 MPa, 5000 psi). The conventional engine has a 5-speed transmission, and the series hybrid a single-speed transmission. Both transmissions have been optimized by finding the reduction ratios (and shift points for the conventional car) that result in maximum vehicle efficiency. The series hybrid car uses a high efficiency flywheel (Post et al., 1993), a permanent magnet generator, and an induction motor.

Conversion between ppm of NO_x , obtained from the engine maps, and grams per km (mile), specified in the emissions regulations, requires a knowledge of the composition of NO_x (fraction of NO and NO_2 in the mixture). It was found in the experiment that NO_2 emissions are a significant part of the total NO_x emissions, due to the very low equivalence ratios used. The calculation of grams/km of NO_x done in this analysis assumes that half of the NO_x produced per unit volume is NO_2 . This is a conservative assumption, since NO_2 emission levels are lower over most operating conditions.

Table 3 shows the results of the analysis. Fuel economy is given as gasoline-equivalent energy consumption. The conventional vehicle has a reasonably high fuel economy (17.4 km/liter, 41 mpg). The vehicle range (330 km, 205 miles) is lower than obtained in gasoline vehicles, but is still high enough to not represent a limitation on the applicability of the vehicle to most circumstances. The conventional vehicle has reasonable acceleration and hill climbing performance. The most desirable feature of the conventional car is the emission levels. Emissions are projected to be a factor of 75 lower than the CARB ULEV requirements, and therefore a factor of 7.5 lower than EZEV. The reason for the emissions to be so low is that the engine is operated most of the time at low torque, generating much less than the 10 ppm maximum allowable NO_x (Figure 5). Using the 10 ppm NO_x restriction guarantees that any driver obtains EZEV emissions, regardless of how aggressively they may drive.

The four cylinder engine has also been optimized considering a 100 ppm maximum NO_x , to observe how this change affects vehicle performance and emissions. It is found that changing the maximum NO_x limit causes very little change in driving cycle emissions and fuel

economy, because the urban and highway cycles are driven at low torque conditions, for which the NO_x limit does not have an effect. The major difference is an increase in the maximum engine power, from 60 kW to 75 kW, which results in a significant gain in performance (the time for 0 to 97 km/hr acceleration drops to 7.9 s, and the maximum continuous slope at 97 km/h increases to 16%). However, an aggressive driver may operate the vehicle at conditions that result in NO_x emissions that do not meet the EZEV limits.

The series hybrid vehicle has a very high fuel economy (26.9 km/l, 63.2 mpg), a range similar to conventional gasoline vehicles (508 km, 316 miles) and reasonable performance. Emissions are higher than for conventional cars, but still within EZEV limits. Emissions are higher than for conventional cars because the engine in a series hybrid vehicle operates at or near maximum efficiency, to maximize fuel economy. In this case, maximum engine efficiency (36%) is obtained near the 10 ppm emission limit (Figures 4 and 5).

Fuel economy projected for the series hybrid engine vehicle is low compared to the 33.5 km/l (79 mpg) predicted for a hydrogen series hybrid vehicle in a previous work by the authors (Aceves and Smith, 1995). The results are different because the engine model used in this analysis is based on experimental data for a particular engine (Onan), while the previous work indicates improvements that are likely to be obtained in a future optimized hydrogen engine.

Conclusions

This paper presents the development and validation of a simplified (zero-dimensional) engine model. The model is applied to a hydrogen engine which has been experimentally tested. The model predicts accurately engine efficiency and NO_x emissions over the full range of operating conditions. The validated model is then used to generate engine performance and emission maps for supercharged engine operation. The performance maps are then incorporated into a vehicle evaluation code to obtain performance and emissions for hydrogen-fueled conventional and series hybrid vehicles. Analysis of these two vehicles yields the following results:

- 1. The conventional vehicle has a high fuel economy, reasonable acceleration and hill climbing performance and a short but acceptable range. Emissions out of the conventional car are projected to be a factor of 75 lower than the CARB ULEV requirements, and therefore a factor of 7.5 lower than EZEV. The engine control strategy presented in this paper guarantees that the conventional vehicle achieves EZEV emissions levels regardless of how the car is driven.
- 2. The series hybrid vehicle has a very high fuel economy, a range similar to conventional gasoline vehicles, and reasonable performance. Emissions are higher than for conventional cars, but still within EZEV limits. Emissions in a series hybrid vehicle are intrinsically independent of driver's input.

These results indicate that lean-burn hydrogen spark-ignited engines provide basically the same benefits as a fuel cell, with a technology that is well-known and can be applied immediately. Emission control is achieved without a catalytic converter, and emission levels are therefore not expected to deteriorate with time.

Plans for Future Work

We plan to continue with the analysis of the experimental data generated by the SNLC researchers for the next generation of optimized hydrogen engine (a modified Perkins engine). Analysis of a different engine will allow us to compare the combustion and turbulence characteristics existing in the two engines, and to evaluate how these conditions affect engine efficiency and emissions. These comparisons are very important in achieving the goal of establishing a design guide for optimized hydrogen engine design. It is expected that the larger combustion chamber of the Perkins engine will show lower heat transfer losses and hence higher efficiency.

We also plan to use the results of the engine performance and emissions analysis with our vehicle simulation code and optimizer to determine vehicle and engine characteristics that result in an optimum vehicle design and point to desired engine and vehicle characteristics that result in better performance.

A third activity is to work jointly with the Los Alamos researchers in correlating the engine ignition characteristics with the turbulence characteristics obtained with KIVA. This activity is expected to improve the level of understanding of the flame propagation process in the engine, which will result in improved efficiency of future engine designs.

References

- 1. Aceves, S.M., and Smith, J.R., 1995, "A Hybrid Vehicle Evaluation Code and Its Application to Vehicle Design," SAE paper 950491.
- 2. Amsden, A.A., 1993, "KIVA-3, A KIVA Program with Block-Structured Mesh for Complex Geometries," Los Alamos National Laboratory Report LA-12503-MS.
- 3. Appleby, A.J., 1994, "Fuel Cells and Hydrogen Fuel," International Journal of Hydrogen Energy, Vol. 19, pp. 175-180.
- 4. California Air Resources Board, Mobile Sources Division, 1995, "Proposed Ammendments to the Low-Emission Vehicle Regulations to Add an Equivalent Zero-Emission Vehicle (EZEV) Standard and Allow Zero-Emission Vehicle Credit for Hybrid Electric Vehicles," Preliminary Draft Staff Report, CARB, El Monte, CA, July 14.
- 5. DeLuchi, M., 1992, "Hydrogen Fuel Cell Vehicles," University of California Davis Institute of Transportation Studies Report UCD-ITS-RR-92-14.
- 6. Ferguson, C.R., 1986, "Internal Combustion Engines, Applied Termosciences," John Wiley and Sons, New York.
- 7. Haney, S.W., Barr, W.L., Crotinger, J.A., Perkins, L.J., Solomon, C.J., Chaniotakis, E.A., Freidberg, J.P., Wei, J., Galambos, J.D., and Mandrekas, J., 1992, "A SUPERCODE for

- Systems Analysis of Tokamak Experiments and Reactors," Fusion Technology, Vol. 21, p. 1749.
- 8. Heywood, J.B., 1988, Internal Combustion Engine Fundamentals, McGraw-Hill, New York.
- 9. Olsson K., and Johansson, B., 1995, "Combustion Chambers for National Gas SI Engines Part 2: Combustion and Emissions," SAE paper 950517.
- 10. Patton, K.J., Nitschke, R.G., and Heywood, J.B., 1989, "Development and Evaluation of a Friction Model for Spark-Ignition Engines," SAE Paper 890836.
- 11. Post, R.F., Fowler, T.K., and Post, S.F., 1993, "A High-Efficiency Electromechanical Battery," Proceedings of the IEEE, Vol. 81, pp. 462-474.
- 12. Smith, J.R., 1994, "Optimized Hydrogen Piston Engines," Proceedings of the 1994 International Congress on Transportation Electronics, Convergence 1994, SAE, pp. 161-166.
- 13. Smith, J.R., Aceves, S.M., and Van Blarigan, P., 1995, "Series Hybrid Vehicles and Optimized Hydrogen Engine Design," SAE Paper 951955.
- 14. Van Blarigan, P., 1996, "Development of a Hydrogen-Fueled Internal Combustion Engine Designed for Single Speed/Power Operation," Submitted to the 1996 SAE Future Transportation technology Conference and Exposition, Vancouver, BC.
- 15. Woschni, G., 1967, "Universally Applicable Equation for the Instantaneous Heat Transfer Coefficient in the Internal Combustion Engine," SAE Paper 670931.

Table 1. Modified Onan engine characteristics and experimental conditions.

Bore, mm	82.55
Stroke, mm	92.08
Displacement, cm ³	493.0
Geometric compression ratio	14.0
Experimental range for equivalence ratio	0.2-0.5
Experimental range for engine speed, rpm	1200-1800
Experimental range for volumetric efficiency, %	90-215

Table 2. Main parameters for hydrogen-fueled conventional and series hybrid vehicles.

Vehicle parameter	conventional	series hybrid
test weight, kg (empty wt. + 136 kg)	1136	1236
frontal area, m ²	2.04	2.04
aerodynamic drag coefficient	0.24	0.24
coefficient of rolling friction	0.007	0.007
transmission efficiency	0.94	0.95
transmission gears	5	1
accessory load, W	1000	1000
hydrogen storage capacity, kg	5	5
engine idling speed, rpm	600	, -
launch engine RPM, maximum effort acceleration	n 3600	•
regenerative braking	no	yes
generator type	-	permanent magnet
motor type	- .	AC induction
energy storage device	-	flywheel
motor maximum torque, Nm	•	95
motor maximum speed, rpm	-	11000
flywheel energy storage, kWh	•	1
flywheel maximum power, kW -		100

Table 3. Performance and emissions results for the conventional and series hybrid hydrogen-fueled vehicles.

Vehicle parameter	conventional	series hybrid
fuel economy ¹ , urban cycle, km/liter (mpg)	15.0 (35.3)	24.7 (58.2)
fuel economy ¹ , highway cycle, km/liter (mpg) 21.7 (51.1) 30.0	(70.6)
fuel economy ¹ , combined cycle, km/liter (mpg)	17.4 (41.0)	26.9 (63.2)
NO _x emissions, urban cycle, g/km (g/mile)	0.0020 (0.0032)	0.012 (0.019)
NO _x emissions, highway cycle, g/km (g/mile)	0.0013 (0.0020)	0.0097 (0.015)
NO _x emissions, combined cycle, g/km (g/mile) 0.0016	(0.0027) 0.01	11 (0.018)
time for 0-97 km/h (0-60 mph), s	10.0	10.0
maximum climbing slope at 97 km/h (60 mph), %	13.1	6.0
vehicle range, combined cycle, km (miles)	330 (205)	508 (316)

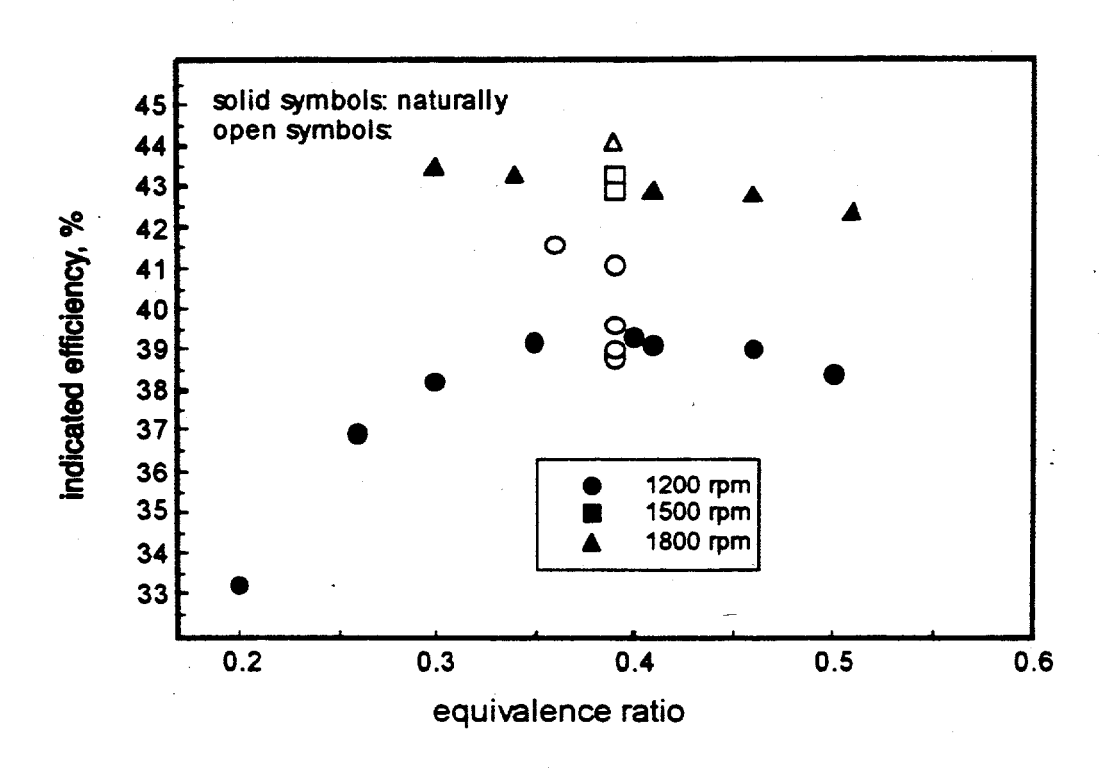


Figure 1. Indicated efficiency for the Onan engine as a function of equivalence ratio, for all the experimental points at MBT timing obtained in the analysis. Engine speeds and supercharged operation are indicated with different symbols.

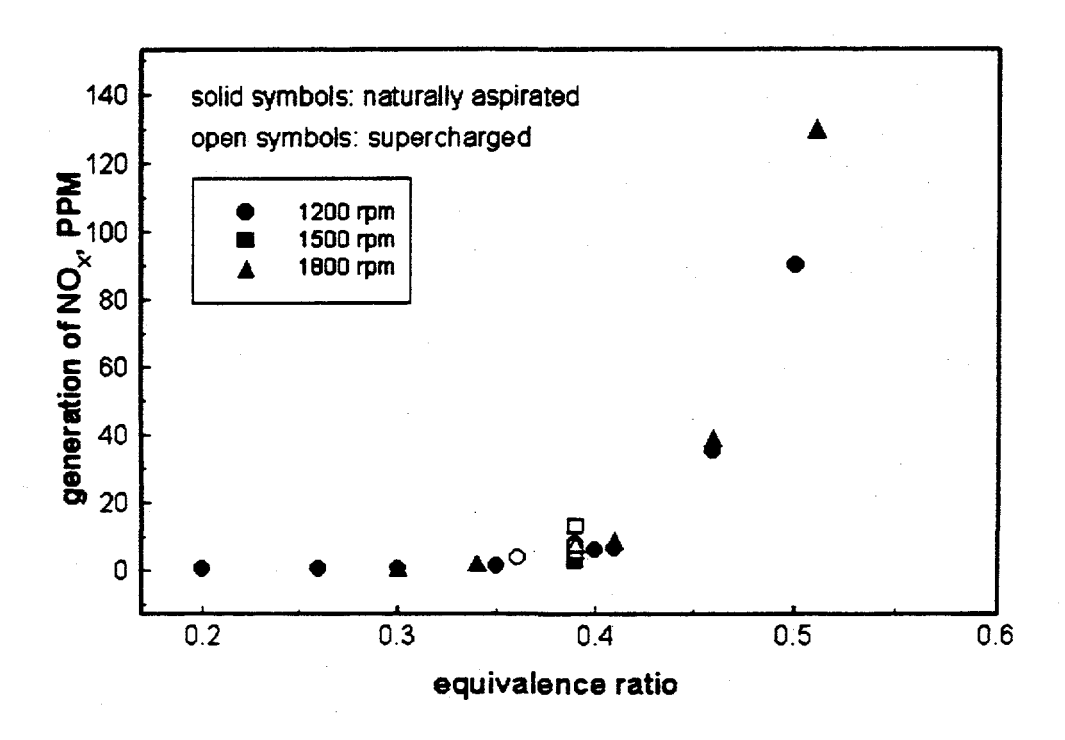


Figure 2. Emission of NO_x in parts per million for the Onan engine as a function of equivalence ratio, for all the experimental points at MBT timing obtained in the analysis. Engine speeds and supercharged operation are indicated with different symbols.

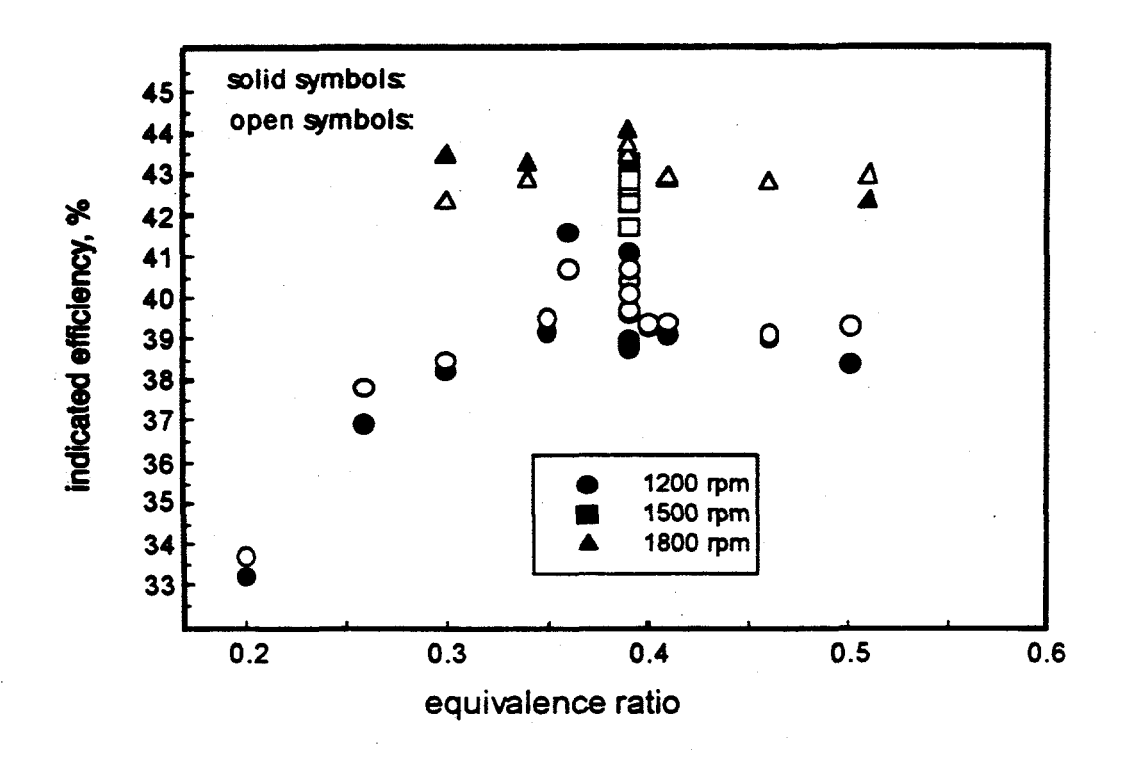


Figure 3. Indicated efficiency for the Onan engine as a function of equivalence ratio. The figure includes both the experimental results and the model predictions.

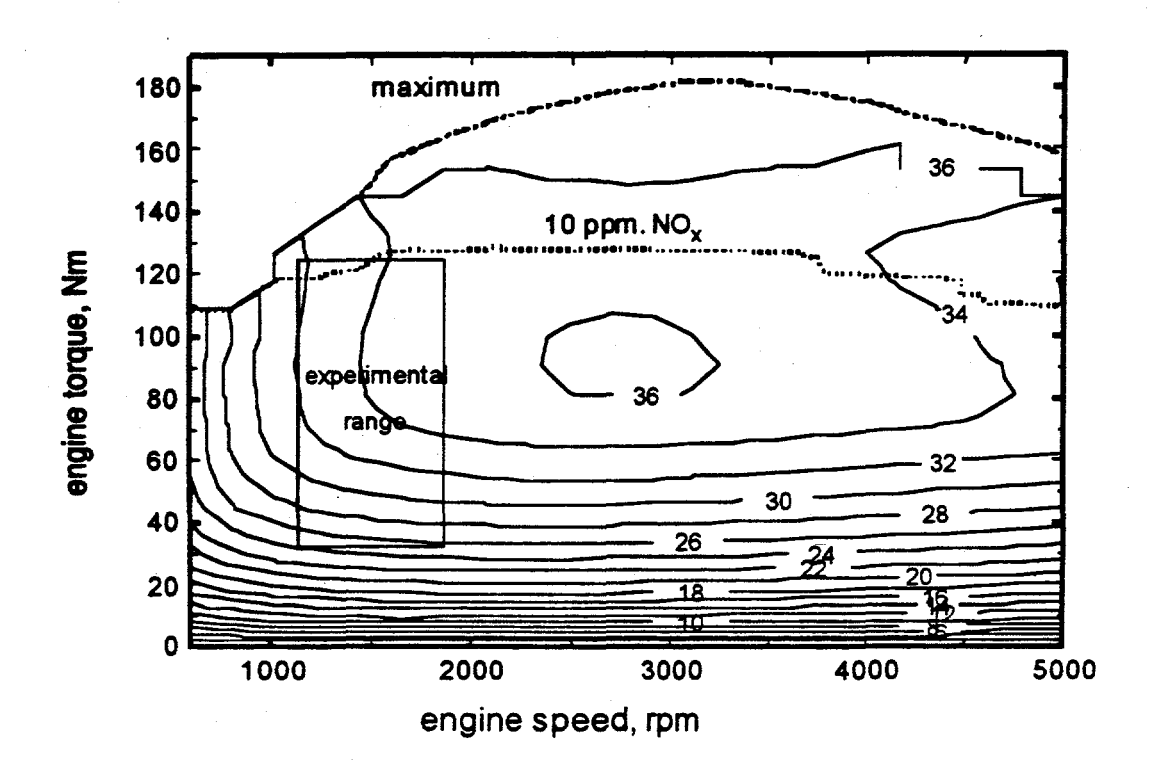


Figure 4. Contour lines of constant brake thermal efficiency (in percent) as a function of engine speed and engine torque. The dotted line corresponds to the conditions at which the engine generates 10 ppm of NO_x; the dashed line indicates the maximum engine torque that can be obtained within the constraints of maximum equivalence ratio (0.5) and inlet pressure (2 bar); and the square indicates the approximate area in which the experimental data were taken.

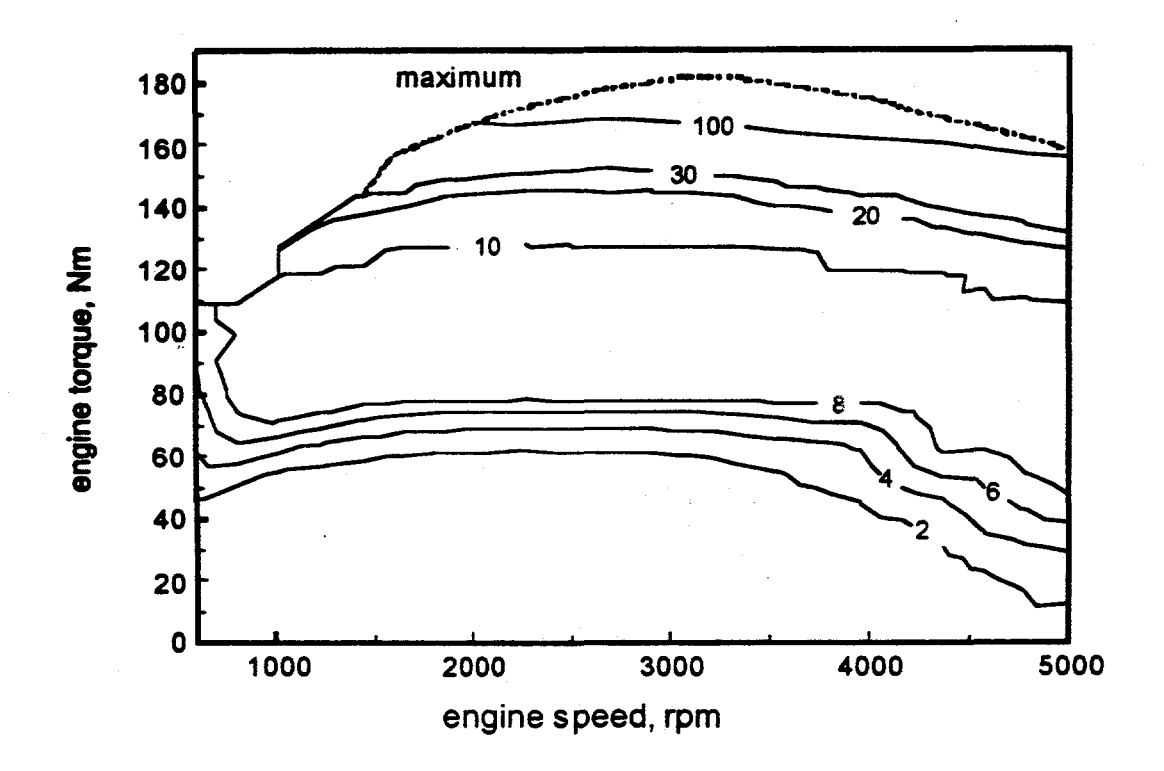


Figure 5. Contours of NO_x emissions in ppm as a function of engine speed and torque, for the optimized hydrogen engine. The dashed line indicates the maximum engine torque that can be obtained within the constraints of maximum equivalence ratio (0.5) and inlet pressure (2 bar).

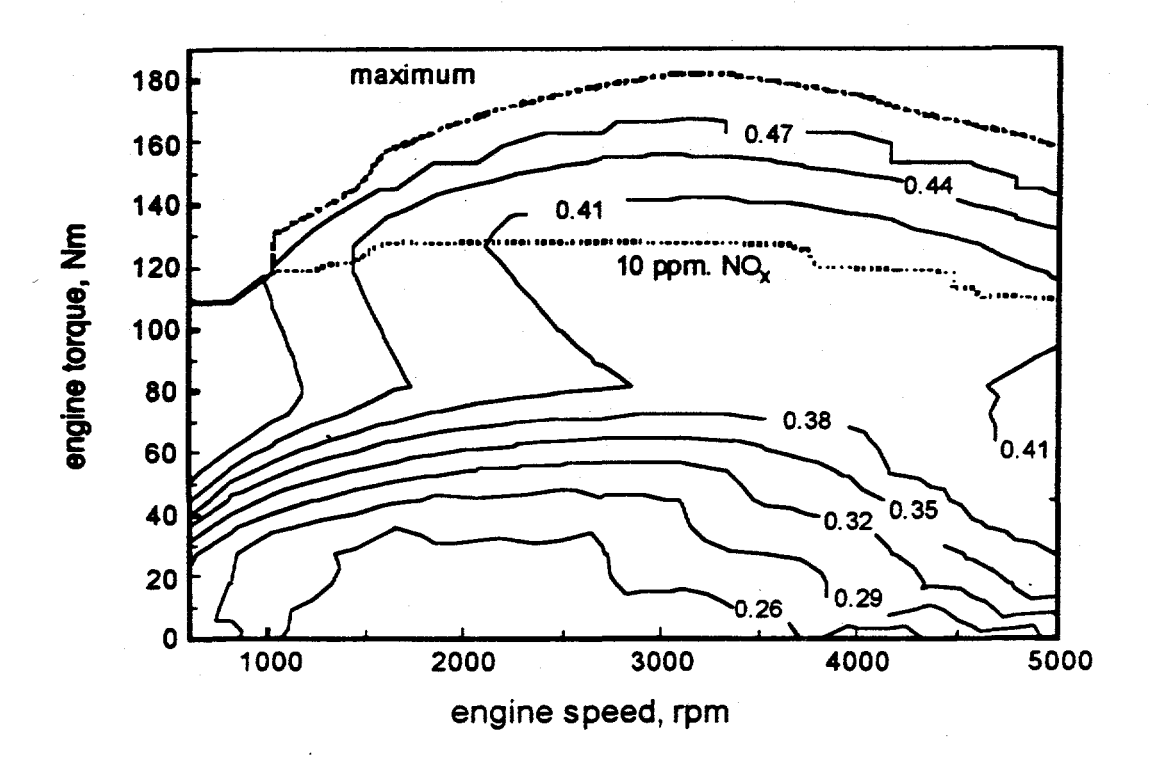


Figure 6. Contour lines of equivalence ratio as a function of engine speed and torque. Equivalence ratios shown in the figure are optimum values, that result in the maximum possible brake thermal efficiency, while meeting the 10 ppm NO_x limit. The figure includes a dotted line for the 10 ppm NO_x limit, and a dashed line for the maximum engine torque that can be obtained within the constraints of maximum equivalence ratio (0.5) and inlet pressure (2 bar).

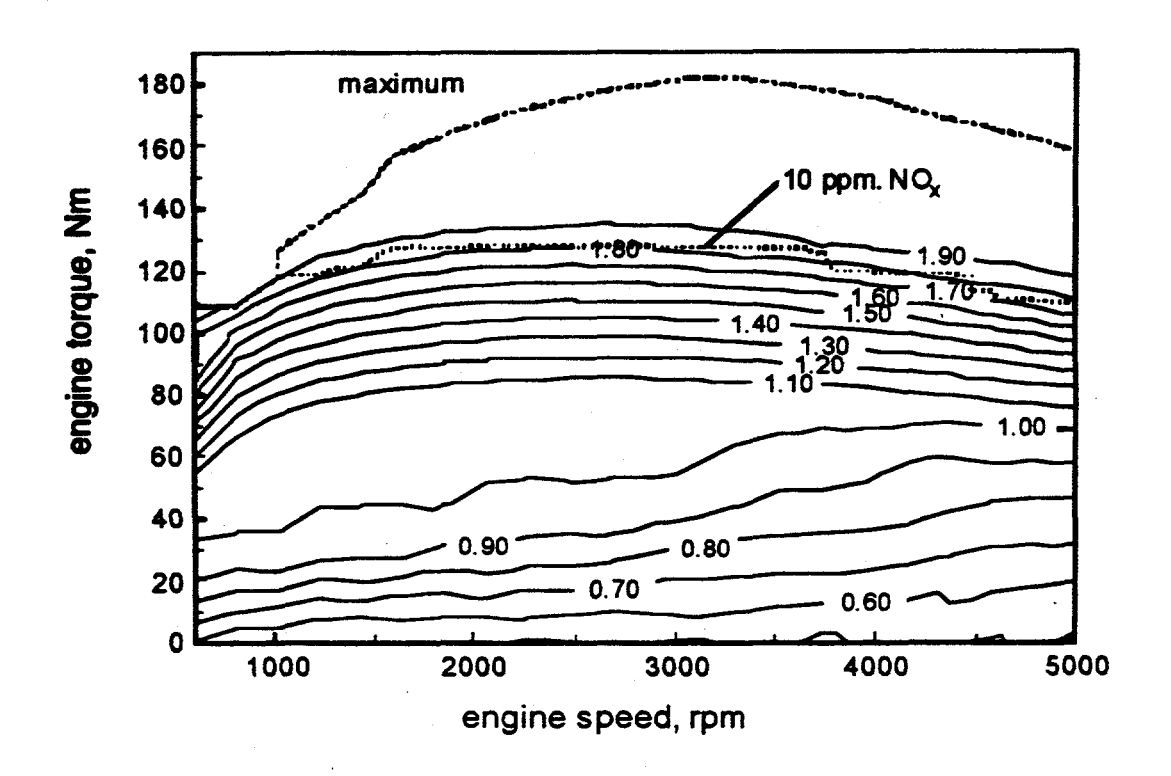


Figure 7. Contour lines of optimum inlet pressure (in bars) as a function of engine speed and torque. Pressures in the figure are selected to provide the maximum possible brake thermal efficiency, while meeting the 10 ppm NO_x limit. The figure includes a dotted line for the 10 ppm NO_x limit, and a dashed line for the maximum engine torque that can be obtained within the constraints of maximum equivalence ratio (0.5) and inlet pressure (2 bar).

DEVELOPMENT OF A LEAN PREMIXED BURNER FOR HYDROGEN UTILIZATION

Presented by: Jay O. Keller

Sandia National Laboratories Livermore, CA 94551-0969

Abstract

The long-term mandate of the hydrogen program is to develop the technologies needed to establish a hydrogen economy. Although a hydrogen fueled automobile has been established as a demonstration project, there are at least three other end use sectors that are recognized by the H₂ program and that are addressed by this project. These end uses are: 1) power generation from stationary turbines, 2) generation of process heat or steam, and 3) commercial and residential direct use applications.

Eliminating carbon from the fuel will remove carbon containing species from the emissions, however, NO_x resulting from thermal NO production cannot be ignored. Thermal NO production is minimized by reducing the peak combustion temperature and the residence time at the peak temperature. NO can be reduced to extremely low levels (a few ppm) by operating sufficiently lean to reduce the peak combustion temperatures below 1700 to 1800 K. The objectives for this project to:

- develop an environmentally benign and safe burner operating on hydrogen in a lean premixed mode.
- provide a facility in which fundamental investigations can be performed to support other programs.

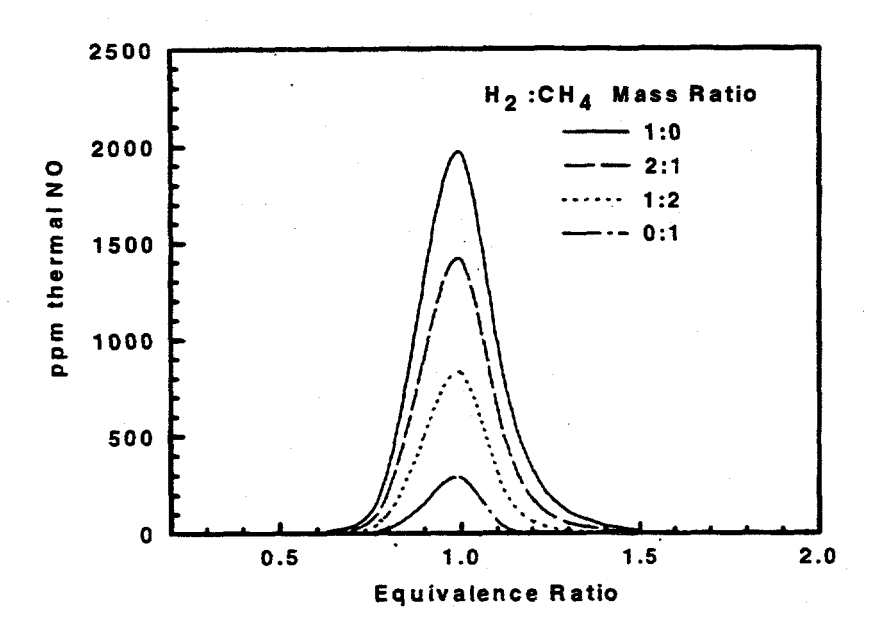


Figure (1) Estimates for thermal NO produced during premixed combustion of mixtures of H₂ and CH₄ assuming 30 msec residence time.

Approach and Rationale

 NO_x emissions from combustion devices are regulated by state and federal agencies. Typical requirements of the California South Coast Air Quality Management District are 15 ppm (15% O_2) for stationary gas turbines and 30 ppm (3% O_2) for refinery heaters. Due to its high flame temperature, stoichiometric combustion of H_2 and air produces levels of NO_x in the range of 10^3 ppm. Various control strategies are available including low-excess air, staged-combustion, oxy-gas, catalytic reduction, and diluent addition. Lean-premixed combustion is an approach which utilizes excess air as diluent to manage flame temperature. Figure(1) illustrates the benefits of lean premix operation on NO_x emissions.

In conventional premixed systems a significant volume is required in order to ensure thorough mixing of the fuel and oxidizer. If flashback should occur the resultant explosion can be hazardous to life and property. This lean premixed combustion program is designed to systematically investigate the combustion fluid dynamic characteristics necessary to provide a fully premixed system capable of completely oxidizing hydrocarbon/hydrogen fuels in a safe and environmentally benign manner. Systems that exploit the mixing characteristics of coherent vortical structures and the associated large strain fields

will be investigated. The goal of this work is to develop fluid dynamic mixing technologies so that combustion occurs in a controlled, safe and fully premixed mode.

In this work we will capitalize on the fluid dynamic features necessary to: 1) suppress the reaction (through controlling the fluid dynamic strain rates), 2) provide a controlled mixing environment to rapidly mix reactants on a macroscopic scale (through controlling large scale coherent vortical structures), and 3) provide a controlled mixing environment to rapidly and thoroughly mix reactants on a microscopic scale (through controlling the three-dimensional breakdown of the large structures, and enhanced fine scale velocity fluctuations to promote thorough microscopic mixing). Static and periodic methods of controlling vorticity deposition rate and subsequent behavior of the resulting large scale coherent structure will be investigated. Control over the rate and quality of the three-dimensional breakdown of these coherent structures will be achieved through careful deposition of additional components of vorticity and/or by promoting the natural breakdown of these large scale structures by introducing flow features that promote the natural breakdown phenomenon. We are starting with the simplest mechanical design that will still allow us to control the fluid dynamic featrues of choice. Figure 2 presents a sketch of the first burner installed in the laboratory for investigation. This configuration is comprised of three annular tubes configured with the fuel seperated by the oxidizer in such a way so that the shear rates between the air and the fuel can be controlled (creating Kelvin-Helmholtz instabilities) along with the vorticity deposition rate and shear zones associated with a roll up toroidal vortex down stream of the stagnation plate. This particular burner is also equipped with swirl generation vanes so that we may independently vary the stream wise vorticity of the flow. This burner is now installed in the laboratory and will be operational by early summer 1996.

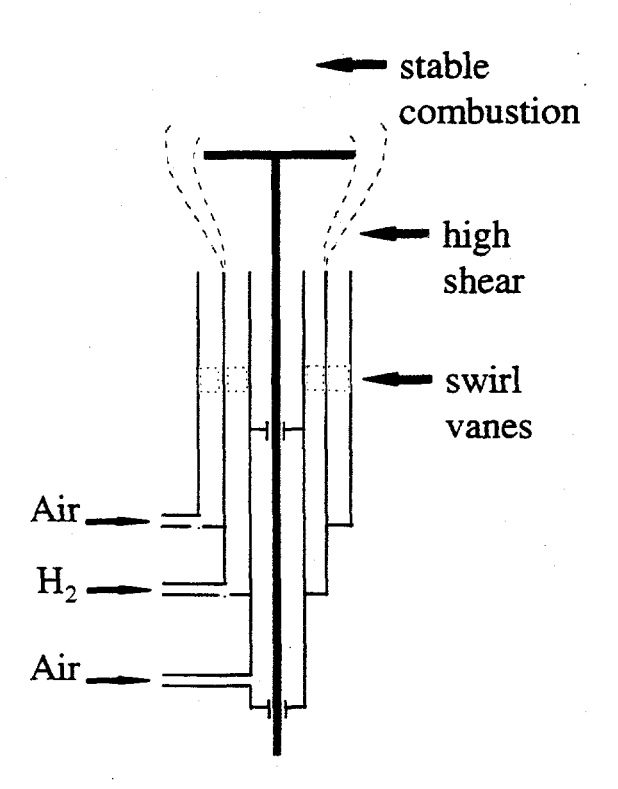


Figure 2 Initial test burner.

This work is performed by careful systematic investigations of the detailed fluid dynamics, thermodynamics, and the subsequent combustion characteristics of the flow field. The diagnostics that will be used during this investigation include, but are not limited to, two component LDV for velocity, Rayleigh scattering for temperature, laser sheet mie scattering, schlieren phase resolved images and exhaust emission measurements of pollutant species (NO_x). Selective laser sheet mie scattering and planar laser induced fluorescence (PLIF) will be used to measure the degree to which the reactants have mixed.

As a direct result of this effort, a facility capable of performing investigations into the fundamental behavior of premixed combustion systems will be created. Hence, providing this community a sought after capability. In this capacity, we will work collaboratively with Lawrence Livermore Laboratory (C.

Westbrook) in the development of chemical kinetic mechanisms associated with hydrogen and hydrogen/methane mixtures. A detailed combustion fluid dynamic modeling program with W. Kollman at University of California at Davis is planned to be synergistic with the experimental program. Information from the experimental portions of this work will be used to improve the fundamental understanding of the controlling physics necessary to guide the development of this technology, and will provide valuable support to the further development of the models. In return, the models will provide valuable insight into the fundamental fluid dynamic mixing mechanism controlling the combustion process of hydrogen and hydrogen/methane mixtures

The resulting burner will have the ability to thoroughly mix the reactants in an fluid dynamic environment that suppresses reaction. After mixing has occurred combustion will proceed in a fully premixed mode. The mixing process will be dominated by large scale flow features that result from the momentum flux of the reactants. In all combustion systems of choice (hydrogen and hydrogen/methane mixtures) the oxidizer's (air) momentum flux dominates the problem by 10 to 20 times that of the fuel. Hence, the operation of this burner should result in a system that is fuel type insensitive (this should accelerate the utilization of hydrogen). These investigations will first be performed at the laboratory scale, with the goal of scaling up to industrial scale (1MW) and if successful to utility size (10 MW).

This newly developed capability will be well positioned to perform fundamental investigations at the request of other investigators from the hydrogen community at large. For example; in collaboration with the Florida Central University/Florida Solar Energy Center (FSEC) we will investigate the combustion fluid dynamics of hydrogen/methane mixtures, providing fundamental insight to explain some of their intriguing Internal Combustion Engine emission and performance results. Complimentary to this program are other collaborations with Lawrence Livermore Laboratory, Los Alamos National Laboratory, the Florida Central University/Florida Solar Energy Center, the College of Engineering/Center for Environmental Research Technologies, the University of Miami, to develop ultra low emission engines for hydrogen and hydrogen/methane applications ranging from generator sets for series hybrid vehicles to stationary power systems. This lean premixed combustion program provides the needed vehicle to provide the community at large first principles information on hydrogen and hydrogen/methane mixtures combustion processes.

CITY OF CHULA VISTA HYDROGEN FUEL CELL BUS DEMONSTRATION PROJECT

Bill Gustafson, Transit Coordinator Barbara Bamberger, Environmental Resources Manager

Project Rationale

Hydrogen as an energy carrier and fuel has potential for various uses including electricity, commercial, residential, transportation, and industrial. It is an energy carrier that can be produced from a variety of primary sources and potentially can accomplish these various uses while significantly reducing pollution by substituting for or reducing the use of fossil fuels. One of the most immediate and potentially viable roles for hydrogen as an energy carrier will be its use as a transportation fuel, especially in densely populated urban areas where automotive emissions contribute significantly to air pollution. The Department of Energy's commitment to research and development of hydrogen as an alternative fuel, and California's Zero Emission Vehicle (ZEV) requirements, both provide the impetus and favorable circumstance for demonstrating hydrogen as a transportation fuel on an urban bus system.

The purpose of this project is to demonstrate the feasibility of using solid polymer fuel cells in a hydrogen-powered electric drive system for an urban transit bus application. Fuel cell buses use hydrogen fuel and oxygen from the air to produce electrical power with the only byproduct being pure water. Proton Exchange Membrane (PEM) fuel cells are proposed for this project. Current evidence suggests that fuel cells, which rely on hydrogen and a process known as proton exchange to generate their power, appear to have an infinite life span. All exhaust pollution is completely eliminated, resulting in a Zero Emission Vehicle (ZEV). An urban bus system offers the potential for developing a market for the production of hydrogen propulsion technology due to extensive vehicular use in densely populated areas experiencing pollution from numerous sources, and because the central garaging facilities or the bus system facilitates fueling and maintenance functions.

PEM technology, once commercialized, will also be attractive to operators of centrally fueled fleets covered by the Clean Fuel Fleet Program as part of the 1990 Clean Air Act Amendments. With the longer term development of hydrogen fueling infrastructure, PEM fuel cells potentially could provide a viable alterative to the internal combustion engine for most automotive applications, including passenger cars and trucks.

Project Approach

The City of Chula Vista intends to purchase three zero emission hydrogen fuel cell buses from a business consortium including New Flyer Industries, and Ballard Power Systems-California Office. These buses will operate on high ridership Chula Vista Transit (CVT) routes for a combined total of 804,500 kilometers, a time period of approximately three years. The project will include a hydrogen fueling station, field support for CVT personnel, and coordination, analysis, and reporting on the performance, cost, and reliability of the business. Chula Vista is the only city on the west coast to develop a collaborative effort of this nature. It is also one of two cities in the United States to demonstrate these vehicles, the other of which is Chicago. These three buses will operate on two CVT revenue service routes. The buses will provide significant data as part of a major research and development effort to convert NASA aerospace technology to a practical commercial application; the project will also provide valuable information on the feasibility of using this technology in a "real world" public transportation operating environment.

The City of Chula Vista is the second largest city in the County of San Diego (after the City of San Diego), with a population of approximately 165,000. The City is located midway between downtown San Diego and the United States/Mexico border. Chula Vista is served by four local and regional public transportation systems, including CVT, San Diego Transit, and the San Diego Trolley which has three stations within the city. CVT service provides two functions: it is a local public fixed-route bus system serving the City of Chula Vista; and it is a "feeder" system to the San Diego Trolley, and the two other regional bus services operating from near the U.S./Mexico border area to San Diego through Chula Vista. CVT has one of the highest suburban system riders in the San Diego region, carrying over 9,500 passengers daily on twelve routes. Over 60% of these riders transfer to the San Diego Trolley and to the two other regional bus routes. Within the city are numerous uses that generated significant current and potential public transportation ridership, including commercial areas and shopping centers, a community college, and the country's first all-year round Olympic Training Center. CVT plans to operate the three fuel cell buses on two routes: a new route from the vicinity of Southwestern Community College to the Olympic Training Center; the two other buses will operate on an existing route with high ridership that connects to the San Diego Trolley, thereby generating public interest and providing maximum exposure for this technology (Table 1).

Table 1. Hydrogen Fuel Cell Bus Routes

One bus: New service from Southwestern College to Olympic Training Center

Estimated one-way VKT*	9.654
Estimated daily ridership	300
Estimated daily VKT*	322
Estimated annual ridership	80,000
Estimated annual VKT	115,850

Two buses: One additional bus and one replacement** bus on CVT Route 709, service from the H Street Trolley Station to Eastlake via Southwestern College

Estimated one-way VKT	35
Estimated daily ridership	1,000
Estimated daily VKT	700
Estimated annual ridership	200,000
Estimated annual VKT	180,200

Three buses: estimated statistics

Total daily ridership	•	1,300
Total daily VKT		1,022
Total annual ridership		280,000
Total annual VKT		296,050

^{*} VKT = Vehicle kilometers traveled

The PEM fuel cell uses a thin piece of special plastic, which allows current to flow in the fuel cell, without the need for high temperature or corrosive environments. It is the high temperature (>2,500C) combustion process of the internal combustion engine which creates much of the exhaust pollution. This contrasts with the low temperature (80 C) electro-chemical process of the PEM fuel cell in which the exhaust products are

^{**} Replacement buses are 1984 Orion with 6V92 Detroit diesel engines

air and water vapor. Fuel cells may offer the best solution to environmental problems posed by transportation vehicles, and the PEM fuel cell currently is the only system which can provide the performance characteristics required in transportation applications. The requirements include: low operating temperature, use of ambient air (so the vehicle does not have to carry tanks of pure oxygen), and use of non-caustic fuel, in this case hydrogen.

Ballard Power Systems is the world leader in the development of solid polymer fuel cell technology and builds 5, 13, and 30 kW SPFC stacks. A 120 kW propulsion power system has been integrated, and a 200 kW system has been integrated. Ballard has over two years of operation with a 30 foot bus with no history of incidents. The bus fuel system is designed for safety, using approved cylinders comparable to those used for CNG vehicles. The buses will have roof-mounted storage, passive ventilation systems and built-in detection devices in the unlikely event of a gas leak.

The PEM fuel cell runs on pure molecular hydrogen (H2) and oxygen which it gets from ambient air. For the Chula Vista project, liquid hydrogen will be delivered by truck to a fueling facility to be located at the City's maintenance yard, which is the current location where the CVT fleet is parked and maintained. The liquid hydrogen will be stored in a cryogenic tank, and pumped to an evaporator as needed where it will resume its gaseous state, and in the process, build enough pressure to fuel buses without additional compressors. The compressed hydrogen gas stored on board the bus and used to fuel the PEM cell, is similar to compressed natural gas (CNG). The hydrogen vendor will be Praxiar, a firm with over 35 years experience in merchant liquid hydrogen production.

Past Results

There are no past results for the Chula Vista project. However, as was mentioned earlier, Ballard Power Systems has over two years operating experience with a 30 foot bus powered with hydrogen fuel cell technology, with not adverse incidents.

Current Year Results

The City currently is raising the necessary funds and developing strategic partnerships for the demonstration project. The City currently has partnerships with the California Energy Commission, the State of California Legislature, the Department of Energy, and the City of Chula Vista Transit Division. The cost of the project is estimated at \$6.4 million, which includes: 3 hydrogen fuel cell buses, manufactured by New Flyer Industries, with PEM cell supplied by Ballard Power Systems; installation of a hydrogen fueling station at the City's maintenance yard; fuel for the 804,500 km demonstration project (estimated at 2.5 to 3 years of operation); fuel cell spare parts and maintenance; on-board data collection and analysis; on-site field support from Ballard Power Systems personnel for the duration of the project.

Plans for Future Work

The City of Chula Vista is encouraging commercialization of promising emerging environmental technologies. Ballard Power Systems has strategic relationships with major international corporations and

governments to integrate this technology into their products and operations. The plan calls for the testing of fuel cell demonstration units, commercially targeted applications development, and final product definition. Accordingly, if the PEM technology is found to be workable and cost-competitive, CVT would consider replacing its diesel buses with PEM fuel cell powered buses during the regular bus replacement cycle. CVT plans to replace its entire fleet of 34 buses over the next 10 years. This replacement cycle would remove 34 diesel buses which travel approximately 1.3 million miles annually, and use about 325,000 gallons of diesel fuel.

Over the long term, the next generation of this technology may be appropriate for use in the personal automobile. As fueling infrastructure develops, PEM technology could provide one option for replacing the internal combustion engine in urban highway applications, thereby significantly reducing mobile source emissions and improving regional air quality.

Major automotive manufacturers are working with Ballard Power Systems pertaining to Electric Vehicles (EVs) using PEM technology. Each of these firms has specific programs and goals for fuel cell powered vehicles. Ballard is under contract with General Motors on a program funded by the U. S. Department of Energy (DOE) for a methanol fueled PEM vehicle to be operated with a target field test date in 1996. Ballard also has a partnership with Daimler-Benz. This research and development program for PEM systems for transportation applications consists of multiple projects and project phases. Key technologies encompass the PEM, the fuel processor/reformer, system engineering, and integration of system components into the PEM fuel cell automobile power plant.

The Chula Vista project will provide operating experience and data in conjunction with other ongoing research and development programs.

Status of Economic Evaluation and System Analysis

The specific parameters for economic evaluation and system analysis will include existing data collected for CVT operations and maintenance as well as additional data to permit evaluation of PEM technology in urban transit system operations. The test program will focus on performance, cost and reliability of the fuel cell engine, including air, fuel, cooling, electrical, control, safety subsystems, and ancillary bus subsystems.

The program will also include a comparative analysis of the PEM and diesel technologies relative to energy efficiency, operating cost, and reliability.

Fuel cell system operating data will be automatically collected on-board the buses by a Data Acquisition Computer (DAC). Real-time system monitoring data will automatically be reduced to produce summary statistics and operation profiles. Data will also be available for on-line display. Fueling and service information will be collected from fueling and service activity logs.

Operating data will be downloaded from the DAC on a regular basis and integrated into an ongoing field performance database. Key input and derived parameters in the DAC system include:

- Total system output power
- subsystem power allocations

- air, fuel, and coolant pressures
- system and component temperatures

Fueling logs will use standardized forms to collect data on fuel delivered to the storage tank, fuel loaded onto each bus, time taken to fuel the bus, and breakdowns of fuel handling equipment.

Service activity logs will use standardized forms, including shop work orders, to collect data on unscheduled and scheduled maintenance activity. Data to be collected include the following:

Unscheduled Maintenance

- date/mileage/run-time event identifier
- description of breakdown
- location of breakdown
- repair action and parts used
- person-hours required

Scheduled Maintenance

- date/mileage/run-time event identifier
- results of scheduled inspections
- description of malfunctions (if any)
- repair action and parts used (if any)
- person-hours required

Fuel consumption, operating cost, and reliability data on the New Flyer buses will be obtained from standard CVT data sources. Data not available from standard sources will be collected using forms and techniques adapted from those being applied to the fuel cell buses. All buses in the CVT fleet adhere to a four-stage Preventative Maintenance and Inspection (PMI) schedule, classified as level A, B, C, and D. Each level progressing from A to D is a more detailed check of specific components and systems. The A and B PMI's are scheduled every 3,000 miles; the C PMI every 24,000, and the D PMI every 48,000 miles. Applying the PMI schedule to the demonstration fuel cell buses, as well as to the rest of the fleet, will insure that all buses receive comparable maintenance, thereby establishing a base for future comparison and evaluation.

In addition to the established scheduled maintenance for the CVT fleet, which includes recording of unscheduled maintenance, breakdowns, repairs, down time, and repair time that occur during the test period for the three fuel cell buses will be documented, and classified into four categories as follows:

Type 1: A malfunction that represents a potential crash situation and could lead directly to passenger or driver injury.

Type 2: A malfunction that results in test interruption because the bus cannot be operated. Service is discontinued until the bus is repaired at the location of the malfunction or is towed to the service workshop.

Type 3: A malfunction that results in temporary interruption of testing, and the bus must return, under its own power, to the garage for repair.

Type 4: A malfunction that degrades bus operations but does not require immediate removal of the bus from testing.

Analysis and Reporting

On-site technical support personnel will assist CVT personnel with routine data and trouble shoot data systems if necessary. On-site technical personnel will carry out analysis work including data transfer and quality assurance, database management, statistical profiling, analysis, and evaluation of performance results and reporting.

Data from DAC, fueling, and service logs, will be transferred according to defined protocols, checked and confirmed for errors, and maintained in the field program database.

Summary operating statistics will be generated weekly and monthly reports compiled. Analysis of costs derived from service and fueling logs, together with system efficiency, fuel consumption and subsystems performance statistics will be prepared monthly.

Interim reports will be prepared semiannually, with a major interim report prepared after two years of operation. A final report will be prepared at the conclusion of the three year test period. The report will include overall results, including technical performance of system, reliability, and cost of components, and fuel consumption. A major outcome of the analysis will be to estimate life-cycle costs over a 12 to 15 year period.

Economic Feasibility

The buses, including related infrastructure and technical assistance used in this project, are estimated to cost \$1.4 million each. Since Ballard anticipates producing only approximately ten buses for their three demonstration cities, Chula Vista, Vancouver, and Chicago, this low volume of units accounts for the high cost.

One important issue for the City of Chula Vista is whether this technology has the reasonable potential to become cost-effective on a life-cycle basis. For example, a high capital cost might be offset by lower operating and maintenance costs over the life of the vehicle. In high volume production, Ballard estimates a fuel cell bus would cost about \$300,000 in current dollars, compared with a diesel powered bus at \$240,000 and a CNG powered bus at approximately \$280,000. At the estimated high production cost of \$300,000, the fuel cell bus would be competitive with a CNG alternative fuel bus which still pollutes. When considering the PTEM fuel cell bus is a ZEV, and there may be life-cycle maintenance costs savings, the PEM bus may be cost-competitive with diesel technology. The three year/804,500 km test should provide information to partially, if not completely, answer the life-cycle cost question.

Projected Goals/Basis for Goals

Goals

The project goals include:

- The reduction of new and existing mobile source emissions by the use of three hydrogen fuel cell buses.
- To pioneer the use of fuel cell bus technology in the San Diego region and further the development of fuel cell technology and commercialization.
- To develop and refine the database on performance, cost, and reliability of zero emission fuel cell buses.
- To contribute to the development of fuel cell propulsion as a viable alternative to the internal combustion engine.
- To become a leader in utilizing fuel cell buses in an urban transit system.

Basis for Goals

The Chula Vista program relates directly to one of the Department of Energy's Hydrogen Program near term goals of expanding the use of hydrogen as a fuel for surface transportation. California legislation requires an increasing percent of non-polluting vehicles be offered for sale within the next six years. Therefore, both Federal and State of California programs and mandates provide the impetus to develop non-polluting vehicles, and one viable energy source is hydrogen power. The Chula Vista program also provides an opportunity for a public/private partnership to advance hydrogen systems to a point where they are cost-effective, and eventually integrated into the energy economy.

The length of the project, estimated at three years/804,500 km, will results in estimated annual net energy savings of approximately 5,000 million BTU. The buses will use an estimated 1,664,000 liters of hydrogen during the course of the project. The demonstration fuel cell buses will replace two diesel buses which currently use about 55,150 liters of diesel fuel per bus annually. In addition, the third bus will be used on a new route, thereby eliminating the need for a diesel fuel bus. The total estimated diesel fuel not consumed annually will be 198,450 liters, resulting in the elimination of 2,258 million BTU per diesel bus and substituting 596 million BTU per bus.

Major Barriers to Meeting Goals

General

Securing additional funding in the amount of approximately \$1.5 million for the demonstration project - In order to accomplish the goals of the project, both Ballard Power Systems and the City of Chula Vista concur that a minimum of three hydrogen fuel cell buses should be tested. The City and Ballard currently are attempting to secure the remaining funding to implement the demonstration program.

Space constraint - CVT currently operates out of the City of Chula Vista's maintenance yard and shares this facility with other City maintenance functions. Space limitations at the yard and in the garage will require coordination and cooperation with the City's other maintenance functions with regard both to the siting of the hydrogen fueling facility and pertaining to vehicle storage and maintenance.

Technical

The main area of technical risk is in the stack integration itself. To limit program cost and overall technical risk, the initial phase of the bus program used a proven DC traction motor, carried pure hydrogen in compressed gas bottles, required about 25% of typical transit bus range, and used a smaller 30 foot bus. The Chula Vista program will use a 40 foot vehicle. The brassboard power plant has been built and successfully tested. The prototype for the Chula Vista buses was completed in April 1995 and is currently in a rigorous test program.

Technical challenges in the propulsion system include designing and building an efficient air compression system, hydrogen recirculation, reduction of parasitic loads, material selection for water purity, volume, weight, and low-cost materials and component designs. Within the bus system integration, technical challenges include fault-tolerant controls, axle loading, safety systems, and design for reliability and maintenance.

Acknowledgments

The authors would like to thank Scott Kaltrider (Praxair), Colleen Kelly (City of Chula Vista), Neil Otto (Ballard Power Systems), and Jose Palomo (California Energy Commission) for assistance and comments.

References

Otto, Neil, Ballard Systems, Private Communications, 1995-1996.

Praxair, "Data Source: Your Guide to Industrial Gases and Cryogenic Fluids," Praxair Technology, Inc., 1993.

National Renewable Energy Laboratory, "Hydrogen Energy for Tomorrow," Report No. DEO/GO-10095-067, August 1995.

National Renewable Energy Laboratory, "Hydrogen Program Overview," Report No. DEO/GO-10095-088, February 1995.

U. S. Department of Energy, Office of Conservation and Renewable Energy, "Hydrogen Program Plan: FY 1993-FY 1997," Report No. DOE/COMMISSIONER HOKE 10093-147, June 1992.

B: PAPER.WMG

A POLYMER ELECTROLYTE FUEL CELL STACK FOR STATIONARY POWER GENERATION FROM HYDROGEN FUEL

Christine Zawodzinski, Mahlon Wilson and Shimshon Gottesfeld

Materials Science and Technology Division Los Alamos National laboratory Los Alamos , NM 87545

Abstract

The fuel cell is the most efficient device for the conversion of hydrogen fuel to electric power. As such, the fuel cell represents a key element in efforts to demonstrate and implement hydrogen fuel utilization for electric power generation. A central objective of a LANL/Industry collaborative effort supported by the Hydrogen Program is to integrate PEM fuel cell and novel stack designs at LANL with stack technology of H-Power Corporation (H-Power) in order to develop a manufacturable, low-cost/high-performance hydrogen/air fuel cell stack for stationary generation of electric power. A LANL/H-Power CRADA includes Tasks ranging from exchange, testing and optimization of membrane-electrode assemblies of larger areas, development and demonstration of manufacturable flow field, backing and bipolar plate components, and testing of stacks at the 3-5 cell level and, finally, at the 4-5 kW level. The stack should demonstrate the basic features of manufacturability, overall low cost and high energy conversion efficiency.

Central achievements in this project which started in 1995 have been:

- (1) CRADA: * Crada agreement with H Power was signed 11/95; * Controlled fabrication of membrane/electrode assemblies (M&Es) of 100 cm² or larger has been demonstrated at LANL using computer controlled direct catalyst ink application to the ionomeric membrane; * The first Task of the CRADA: M&Es exchange and testing, has been completed; Cell testing results have shown that at 57%-65% energy conversion efficiency hydrogen-to-electricity (DC), the power density achievable in the stack can be 0.6 kW/liter.
- (2) Additional LANL Activities: *Building blocks for a manufacturable, low cost stack technology were demonstrated, based on off-the-shelf stainless steel screen & foil for flow field and bipolar plate, respectively; * Analysis of the gas flow pattern with a metal screen revealed even distribution of the gaseous reactant; * Enhanced energy conversion efficiency was demonstrated by increasing catalyst loadings to 0.8 mg/cm².

Our plans for future work are to continue the CRADA work along the time line defined in a two-year program, to continue the LANL activities of developing and testing stainless steel hardware for longer term stability including testing in a stack, and to further enhance air cathode performance to achieve higher energy conversion efficiencies as required for stationary power application.

Background

The high efficiency combined with very low environmental emissions and modular construction have fostered continued interest for the last thirty years in fuel cell technology for utility, customer-side-of-the-meter and transportation applications. Among the family of fuel cell technologies, polymer electrolyte (PEM) fuel cells have some uniquely attractive features, including a combination of high power density and high chemical-to-electric energy conversion efficiency, fast and easy start-up, high reliability and highly durable and benign materials of construction. Nevertheless, the application of PEM fuel cell technology for utility and /or stand alone applications was judged in the past to be too expensive for any terrestrial applications and, also, to be too sensitive to low levels of carbon monoxide in reformed carbonaceous (most likely natural gas) fuel feed streams. Both of these barriers for implementation of PEM fuel cells in utility and/or stand alone applications have been significantly lowered in the last few years but a remaining important barrier has been the need for a PEM fuel cell stack technology which is (a) of lower intrinsic cost, and (b) lends itself easily to large scale manufacturing.

To express the requirements from a viable stack technology in specific terms, the lowering... of the cost means primarily lowering of intrinsic materials costs, including catalyst, membrane and stack hardware materials. The latter include primarily the flow field/bipolar plate. The "manufacturability" of the stack is improved as the complexity of the forming processes, particularly forming of the bipolar plate/flow field, is minimized. Typically, minimization of the complexity in such forming processes is achieved when machining is completely eliminated, replacing it by processes based, e.g., on stamping and punching for metal hardware, or on molding for carbon based composites. Although machining is understood to be unsatisfactory for large scale and low cost manufacturing, present day fuel cell stack technology is based on machined graphite plates as the bipolar plate/flow field combination. A typical machined flow field is quite intricate, as shown in figure 1, and thus requires elaborate machining to manufacture. No other reliable PEM fuel cell hardware technology has been demonstrated to date which would compete favorably in terms of lower materials costs and better manufacturability. To achieve the central target of our project, the demonstration of low cost PEM fuel cell stack technology of clear manufacturability advantages, we have focused on the following elements:

- (a) Demonstrate at LANL the fabrication and quality of larger scale membrane/electrode assemblies (M&Es) based on low catalyst loadings. Such M&Es have been developed previously at LANL but demonstrated only in smaller cells of several cm² in area,
- (b) comparatively evaluate such and other (H-Power) M&Es in cells and in baseline stacks at LANL and at H-Power, using baseline stack components provided by both H-Power and LANL.
- (c) use some advanced stack technologies at H Power to further test baseline stacks with selected types of M&Es
- (d) develop and demonstrate at LANL innovative stack technologies which would best satisfy the combined requirements of low cost materials and manufacturability.

Tasks (a) to (d) are to culminate in a demonstration of a 4-5 kW prototype stack with the combined properties of low cost and manufacturability after two years from the onset of the joint program (12/97).

In addition to the above tasks, LANL is also involved in an effort devoted to enhancement of the air cathode performance in the stack developed, as required particularly in stacks for stationary power generation where the energy conversion efficiency is of highest priority. An additional LANL effort is devoted to the development and use of a code for effective diagnostics of losses in the fuel cell stack.

Progress This Year

(1) CRADA Efforts: The CRADA agreement with H-Power was signed in November 1995, and a kick-off meeting took place at the end of that month. By now, the first Task of the CRADA: M&Es exchange and their testing, has been completed. The conclusions from results obtained at LANL have been: (1a) LANL M&Es are a viable basis for the planned "baseline stack" fabrication and testing; (1b) At 57% energy conversion efficiency hydrogen-to- electricity (DC), the power density achievable in our stack should be, at least, 0.6 kW/liter; (1c) At H Power's suggestion, a carbon paper preparation was developed at LANL matching the properties of expensive carbon cloth backing material used previously with LANL M&Es; (1d) Optimized humidification conditions for maximum cell performance are strongly dependent on the nature of both backing and catalyst layers. Therefore, different humidification conditions, and, particularly, different "break-in routines" seem to be required depending on the specific membrane/electrode assembly employed. The latter points were fully revealed during a recent 2 days visit of two H Power personnel to LANL, devoted to clarification of such technical details and to achievement of effective coordinated testing routines.

(2) Additional LANL Activities: Stack technology based on off-the-shelf stainless steel screen / stainless steel foil combination, has been demonstrated at LANL to enable good fuel cell performance for durations of the order of 1000 hours (test beyond 1000 hours still ongoing). This demonstration followed a stepwise process of first using machined metal bipolar plates to test the viability of metal hardware without changing the conventional machined flow field (figure 1) which was then followed by complete replacement of the machined metal plate by a metal foil / metal screen combination. The basic structure of this PEM fuel cell stack hardware, that requires no machining and is based on inexpensive offthe-shelf stainless steel components, is shown in figure 2. The performance of the cell has been highly satisfactory, enabling 60% energy conversion efficiency hydrogen-toelectricity at a projected stack power density of about 0.6 kW/liter. Figure 3 compares the performance of a 100 cm² cell based on stainless steel screen/stainless steel foil structure (as shown in figure 2) with that obtained in a 5 cm² cell based on conventional machined graphite plate hardware. Although the 100 cm² cell uses a thinner ionomeric membrane (Nafion 112, 2 mil thick) than that used in the 5 cm² cell (Nafion 105, 5 mil thick), giving the metal hardware cell some performance advantage, the very similar performance shown demonstrates that the metal screen flow field hardware has been successful in achieving effective reactant distribution and low and stable cell resistance in a cell of significant dimensions.

The effective distribution of the gas by the metal screen without any further machining in the bipolar plate has been a "pleasant surprise" but required some better understanding.

Analysis of the gas flow pattern with the metal screen flow field was performed in a transparent cell built especially for the direct observation of the flow field. The reasons for the beneficial features of these extremely simple metal screen flow fields have been revealed: the gas enters in one corner of the flow field and leaves through a diagonally opposed corner, but flow can take place in the x and y directions only because of the configuration of the screen. Flow thus occurs across screen wire barriers of equal number for routes passing through the far corners of the flow field or along the diagonal. This is the reason for similar flow impedances for such different routes, explaining the equally distributed flow across the surface.

Other than the novel stainless steel hardware components, the cell we have tested employed membrane/electrode (M&E) assemblies of ultra-low platinum catalyst loadings, developed previously by us at LANL in a program supported by DOE/OTT.

Earlier tests we performed in this project with 304 stainless steel components resulted in excessive contact resistances. In contrast, our most recent cell has been built with 316 stainless steel screens and foils, and showed excellent performance, as described above. Stack design which completely avoids direct steel/electrolyte contact (see figure 2), as well as operation of the cell on air (no neat oxygen) in stationary power applications, apparently provide conditions for very low stainless steel surface reactivity. The initial results have suggested that 316 stainless steel could satisfy hardware requirements in well designed PEM fuel cell stacks, without further need for surface treatment or precious metal coating. Having said that, careful further testing is required of possible failure modes, associated with either metal surface passivation or with membrane poisoning by ions originating from metal corrosion processes. Of particular value would be accelerated corrosion tests, planned for this year. Such accelerated tests will be performed with the 316 SS screens exposed to water of residual conductivities, rendered by very small concentrations of sulfuric acid and HF (expected membrane degradation products), at somewhat elevated temperatures.

The stack building block demonstrated by us (figure 2) could serve as basis for low-cost PEM stack technology of great manufacturing advantages. Compared with present day PEM fuel cell stack technologies, based on machined flow fields, the metal screen flow field demonstrated provides simplicity, off-the-shelf availability, and very low cost. This flow field would cost 1-2 \$/kW, vs. 100 \$/kW projected for machined graphite flow fields. This brings the total cost of fuel cell materials down to the cost of just the M&E assembly which today is about 300 \$/kW at 60% energy conversion efficiency but is expected to drop significantly with increase in fuel cell market, and/or with industrial development of less expensive fuel cell membranes known to proceed at this point. Even the present day cost estimate of 300 \$/kW would be acceptable considering a stationary power generation market entry cost target of around 2000 \$/kW, projected by both J. Ogden and coworkers (1995 Hydrogen Program Review) as well as by an A.D. Little document prepared for DOE/OBT.

Formal disclosure of this metal screen technology has been made by Mahlon Wilson and Christine Zawodzinski of our Group to a LANL patent lawyer in the fall of 1995. When a patent is awarded to us for this hardware, intellectual property for a complete low cost stack (M&E assembly and hardware components) will be owned by LANL.

Finally, as part of the effort on enhanced performance of the air cathode to further improve energy conversion efficiency we have demonstrated that some increase of the catalyst loading increases the current density at 0.8V by factor two. This is shown in Figure 4. Such a cathode should still fulfill cost requirements and enable 65% energy conversion efficiency.

Future Plans

(1) CRADA:

Central Milestones for FYs 96, 97 are:

(i) 3-5 cell "baseline stack" fabrication (6/96),

(ii) 3-5 cell "baseline stack" testing (10/96),

(iii) optimized manufacturable M&E of high-performance/low cost (2/97),

(iv) low cost backing and flow field demonstrated on 1000 hours time scale (5/97),

(v) 3-5 cell prototype stack fabrication (8/97), and

(vi) 20-cell prototype stack demonstration (12/97).

(2) Additional LANL Activities:

We plan to test the cell with the 316 stainless steel hardware for about 5000 hours. We plan also accelerated corrosion tests performed with the 316 SS screens exposed to water of residual conductivities (Kohm cm level), rendered by very small concentrations of sulfuric acid and HF (expected membrane degradation products), at somewhat elevated temperatures.

In addition to our planned demonstration of a stack with conventional machined graphite plates, we now plan to pursue stack building and testing with this novel metal screen hardware. We would like to achieve complete demonstration of a stack based on this manufacturable and inexpensive design by the end of 1997, i.e., together with the target of prototype stack based on H Power/Lanl joint effort which will most probably use a more conventional hardware.

References

- 1. Mahlon Wilson, Christine Zawodzinski, Shimshon Gottesfeld and Albert Landgrebe, Stationary Power Applications for Polymer Electrolyte Fuel Cells, Proceeding of the Eleventh Annual IECEC Battery Conference on Applications and Advances, pp.107-122, Long Beach CA, January 1996
- T.E. Springer, T.A. Zawodzinski, M.S. Wilson and S. Gottesfeld, Characterization of Polymer Electrolyte Fuel Cells Using AC Impedance Spectroscopy, J.Electrochemical Soc., 143, 587-599 (1996)
- C. Zawodzinski, M.S. Wilson and S. Gottesfeld, PEM Fuel Cell Stack development Based on Membrane-Electrode Assemblies of Ultra-Low Platinum Loadings, in Proton Conducting Membrane Fuel Cells I, Edited by Shimshon Gottesfeld, Gerald Halpert and Albert Landgrebe, The Electrochemical Society Pennington, NJ, Oct 95, pp.57-65
- M.S. Wilson, T.E. Springer, J.R. Davey and S. Gottesfeld, Alternative Flow-Field and Backing Concepts for Polymer Electrolyte Fuel Cells, in Proton Conducting Membrane Fuel Cells I, Edited by Shimshon Gottesfeld, Gerald Halpert and Albert Landgrebe, The Electrochemical Society Pennington, NJ, Oct 95, pp.115-126

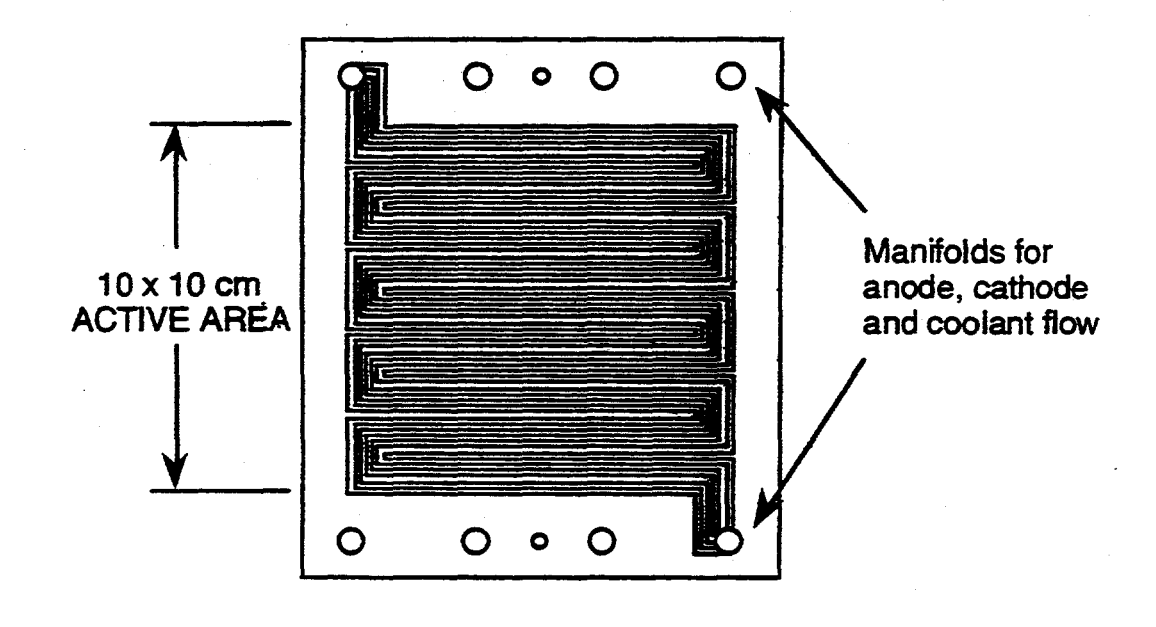


Figure 1: Example of a machined flow field used in earlier experimentation this year with metal bipolar plates. We employed in these experiments either stainless steel or titanium plates machined to yield this flow field pattern. Machining of stainless steel or titanium to generate such flow fields was highly time consuming and costly, and directed us to alternative much simpler flow field configurations — see Figure 2.

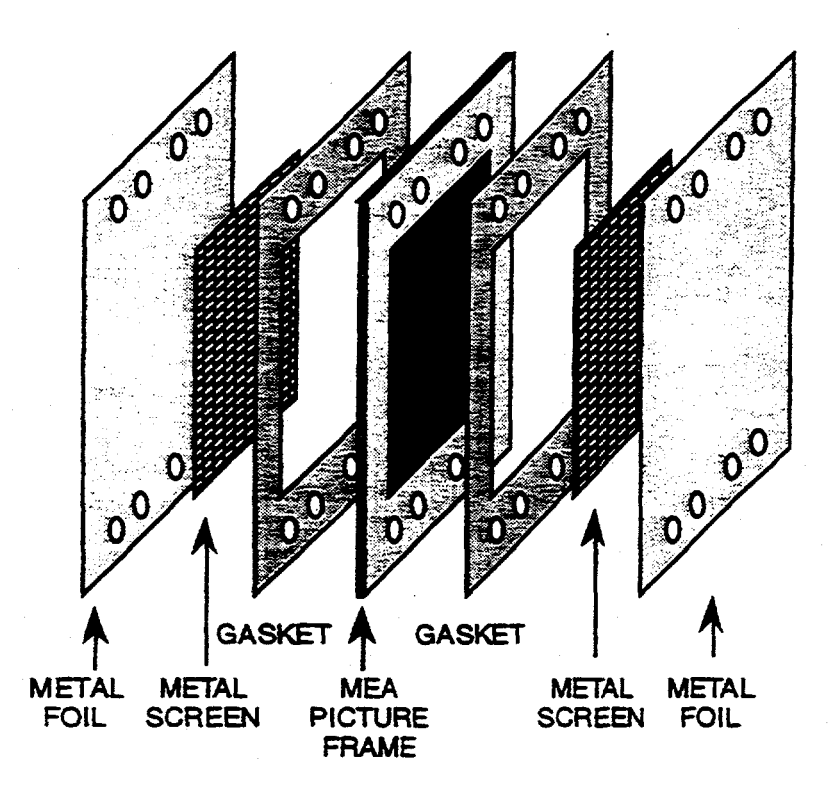


Figure 2: Scheme of a non-machined metal hardware demonstrated at LANL this year as potential building block for low cost, manufacturable PEM fuel cell stack. (MEA - membrane electrode assembly including carbon paper backing layers).

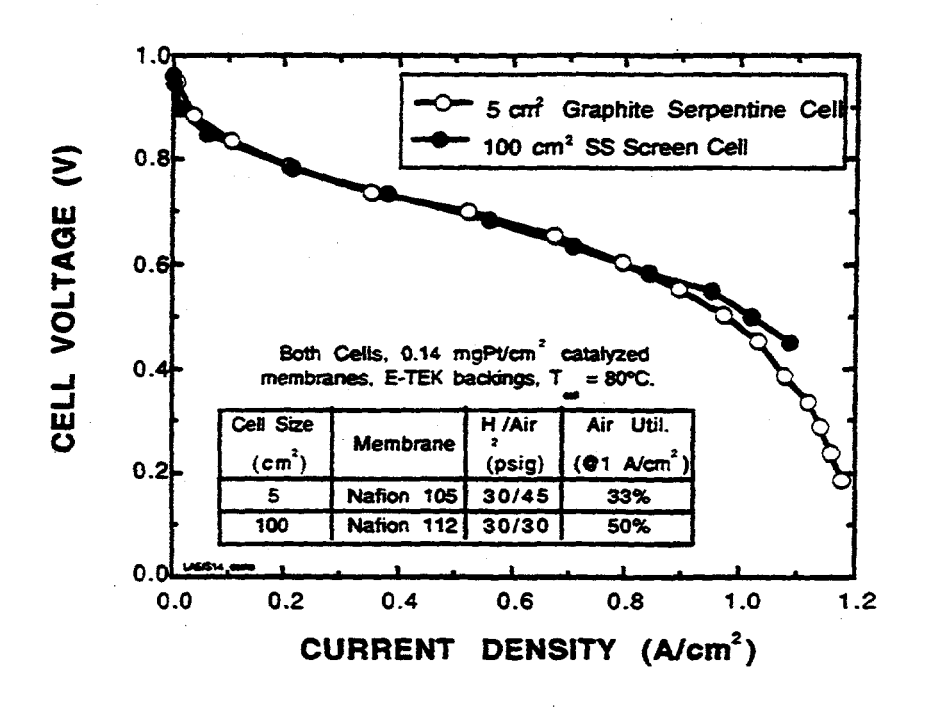


Figure 3: Comparison of performance of PEM cell with 100 cm² active area employing the 316 stainless steel (SS) screen as flow field (and Nafion 112 membrane) to that of PEM cell with 5 cm² active area employing machined graphite plate as flow field (and Nafion 105 membrane). The performances are seen to be comparable showing the effectiveness of the screen as simple, non-machined flow field in cells of larger area

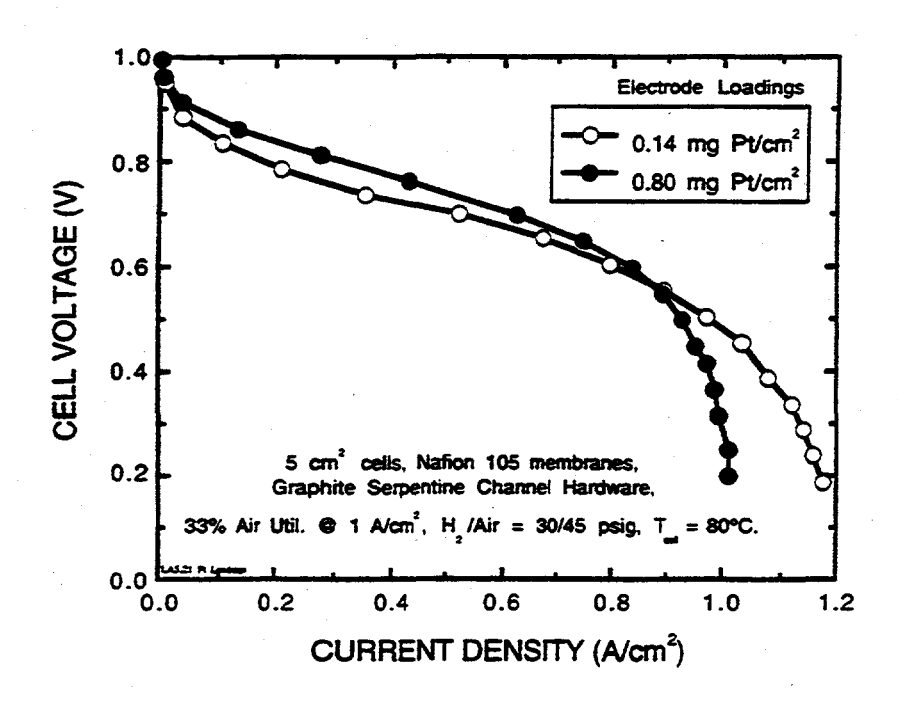


Figure 4: At somewhat higher loading of Pt in the thin-film catalyst applied to the membrane, the power density at 0.8V can be doubled and reaches 0.25 W/cm2. Such power density may enable operation at 0.8V, corresponding to an energy conversion efficiency of 65% hydrogen-to-electricity (DC)

THE PALM DESERT RENEWABLE HYDROGEN TRANSPORTATION SYSTEM

Peter Lehman, Ph.D. Schatz Energy Research Center Humboldt State University Arcata, CA 95521

Abstract

The present paper describes, for purposes of the Department of Energy (DoE) Hydrogen Program Review, Schatz Energy Research Center (SERC) progress on the Palm Desert Renewable Hydrogen Transportation System Project for the period January through June 1996. This period represents the first six months of the three year project. The estimated cost over three years is \$3.9M, \$1.859M of which is funded by the DoE (\$600 k for fiscal year 1996).

The goal of the Palm Desert Project is to develop a clean and sustainable transportation system for a community. The project will demonstrate the practical utility of hydrogen as a transportation fuel and proton exchange membrane (PEM) fuel cells as vehicle power plants. This transportation system will be developed in the City of Palm Desert in southern California and will include a fleet of 8 fuel cell powered vehicles, solar and wind powered hydrogen generating facilities, a consumer-ready refueling station, and a service infrastructure. The system holds the promise of a clean environment and an energy supply that is predictable, domestic, safe, and abundant.

During the first part of 1996 we at SERC have nearly completed building a fuel cell powered personal utility vehicle, which features an upgraded safety and computer system; we have designed and built a test bench that is able to mimic golf cart loads and test fuel cell system auxiliary components; we have begun the design of the solar hydrogen generating station; we have worked with Sandia National Laboratory on an advanced metal hydride storage system; we have increased the power density of the SERC fuel cell by as much as 50%; and we have reached out to the rest of the world with a new fact sheet, world wide web pages, a press release, video footage for a television program, and instruction within the community.

Approach:

The goal of the Palm Desert Renewable Hydrogen Transportation System Project is to develop a clean and sustainable transportation system for a community. The project will demonstrate the practical utility of hydrogen as a transportation fuel and proton exchange membrane (PEM) fuel cells as vehicle power plants. This transportation system will be developed in the City of Palm Desert in southern California and will include a fleet of 8 fuel cell powered vehicles, solar and wind powered hydrogen generating facilities, a consumer-ready refueling station, and a service infrastructure. The system holds the promise of a clean environment and an energy supply that is predictable, domestic, safe, and abundant. Total funding for the project is \$3.9M, \$1.859M of which is funded by the DoE (\$600 k for fiscal year 1996). The Schatz Energy Research Center began work in January of 1996.

One of the main motivations to implement a pollution free transportation system in the City is poor air quality. The City of Palm Desert lies in Region 30 of the South Coast Air Quality Management District (SCAQMD), a 13,350 square mile area consisting of Los Angeles, Orange, and parts of Riverside and San Bernardino Counties. This area is the smoggiest in the nation despite California's strict air pollution control program. Most of this pollution originates in and around the city of Los Angeles, where the air quality failed to meet federal standards for ozone, carbon monoxide, or PM10 (particulates smaller than 10 microns) on about one out of two days in 1993.

The population in the SCAQMD has risen from 5 million in 1950 to the present 13 million, and is projected to reach 18 million by the year 2010. At present there are 9 million registered motor vehicles, which travel nearly 300 million miles each day, consuming 13 million gallons of gasoline and 1.5 million gallons of diesel fuel. These vehicles are the predominant cause of poor air quality; approximately 60% of the air pollution in the area is due to motor vehicles [1].

The photochemical smog formed by the interaction of vehicle emissions, sunlight, and stagnant air can have serious health effects. Ozone, nitrogen oxide, nitrogen dioxide, and PM10's can add stress to the body by constricting the airways and forcing the respiratory system to work harder in order to provide oxygen. Long term exposure to air pollutants can permanently damage the alveoli (air sacs) in the lungs, reducing lung capacity. [8] Children in Pasadena were recently found to have 15% less lung capacity than children nationwide [1].

In order to improve the air quality in California and especially in the SCAQMD, CARB originally mandated that by the year 1998, 2% of all new passenger vehicles sold in California must be zero emission vehicles (ZEV's). This mandate was relaxed in early 1996. (New York and Massachusetts, which also adopted the ruling, are still battling to keep it.) At present the car companies are only required to institute demonstration programs for electric vehicles. However, the last part of the original mandate was retained: by the year 2003, 10% of all new cars sold in California must be ZEV's.

We have used the American Automobile Association's estimate of new passenger vehicle registrations for 1993 as an estimate of new car sales in the year 2003. Assuming the ZEV mandate is also effective in New York and Massachusetts, we estimate that there will be 200,000 electric vehicles per year sold starting in 2003. [3]

Because the only ZEV's are those that run on electricity, the CARB mandates are driving the development of battery and fuel cell powered electric vehicles. These technologies have the potential to reduce air pollution from fossil fuels while offering comparable range and power, much lower noise levels, and the opportunity to use renewable energy as the ultimate source of power. This last point is important. Vehicles powered by either batteries or fuel cells will be truly

zero emission only if renewable energy, such as solar or wind power, is used to charge the batteries or produce the hydrogen for the fuel cells. [4]

An important factor in producing technological progress is a venue where the technology can be usefully employed, effectively demonstrated, and rigorously tested. The City of Palm Desert is such a venue. The City has exhibited, through its legislation and its policies, a commitment to promote the development of environmentally benign technologies. This commitment has already manifested itself in several ways: 1) The City Council, on December 22, 1994, passed resolutions supporting the participation of the City and its staff in this project and committing the City to a cash contribution of \$300k and an in-kind contribution of the City's corporation yard and a building; 2) The California legislature, through Assembly Bill #1229, established Palm Desert as the first test locale in which golf carts used as PUV's are street legal; 3) Resolution number 94-63 was passed by the City Council in order to encourage research and development in the areas of alternative energy and alternative transportation and to attract related industry; 4) The public transportation system servicing the City, SunLine Transit, is the only one in the U.S. that is completely fueled by compressed natural gas; and 5) The local community college, College of the Desert, has the only compressed natural gas mechanics training program in the nation. [4]

The DoE hydrogen program plan states several goals, three of which are met by this project:

- 1) "The program will favor R& D investment in approaches where hydrogen can be shown (via pathway analysis) to exhibit potential advantages over competing energy approaches when considering the totality of energy efficiency, environmental quality, domestic availability of energy source, and cost information.
- 2) "The program will limit its technology development efforts to those pathways and applications for which the primary energy source in entirely or substantially of domestic origin.
- 3) "A significant thrust of the federal R&D effort will be placed on the development of improved methods for storing hydrogen." [2]

The Palm Desert Project fulfills these goals. Hydrogen technology, if adopted, will exhibit significant advantages over the current fossil fuel and battery technologies: Hydrogen fuel cells have a 40 to 50% efficiency, compared to the 15% efficiency of the internal combustion engine. [4] In terms of environmental quality, fuel cells offer many advantages over fossil fuel burning engines and batteries: the only byproduct of fuel cells is pure water and they have long lives, whereas internal combustion engines emit carbon monoxide and dioxide, oxides of nitrogen, toxic air contaminants, and particulate matter. Batteries require recycling every 3 to 5 years.

In addition, hydrogen for fuel cells can be made using solar or wind energy, predictable and domestic energy sources, whereas much of our conventional fuel (over 50%) is imported. Other advantages of fuel cells over batteries, which make a great deal of difference to the user, are expanded range and fast refueling.

Finally, for the Palm Desert project, SERC is integrating advanced hydrogen storage systems into vehicles. Sandia National Laboratories is developing, with help from SERC, a metal hydride hydrogen storage system, designed specifically for the project.

Past Results:

During the years of 1990 to 1995, SERC built and continues to operate an automatic solar hydrogen-fuel cell energy system, which powers an air compressor at the HSU Telonicher Marine Laboratory. [9] In addition, SERC developed a fully equipped fuel cell laboratory and production

facility and built its first fuel cells, as well as a first prototype fuel cell powered personal utility vehicle (PUV). The prototype PUV was completed on schedule and debuted on November 5, 1995 at the Palm Desert Golf Cart Parade. The cart performs well and meets our initial goals. [5]

Current Year Results:

During the first part of 1996 SERC has nearly completed building a second fuel cell powered PUV, which will be delivered in July, 1996. This PUV features an upgraded safety and computer system, with the ability to collect data. In addition, the SERC laboratory facility now has a newly designed and built test bench, which is able to mimic golf cart loads and test fuel cell system auxiliary components. SERC has also begun the design of the solar hydrogen generating station and coordinated activities with Sandia National Laboratory on an advanced metal hydride fuel storage system. Finally, SERC is testing several types of electrode and membrane materials in order to increase the power density of the fuel cell. So far this year, SERC has seen a 50% improvement in fuel cell performance. [6]

SERC's second prototype fuel cell powered PUV is the first of the vehicles deliverable to the City of Palm Desert. Design of the fuel cell power system involved:

- designing, building, and testing a 5.0 kW proton exchange membrane (PEM) fuel cell as a
 power plant for the PUV.
- designing, building and testing peripherals including the air delivery, fuel storage and delivery, refueling, water circulation, cooling, and electrical systems.
- devising and implementing a control algorithm for the fuel cell power plant in the PUV.
- designing and building a test bench in which running conditions in the PUV could be simulated and the fuel cell and its peripheral systems tested.
- installing an onboard computer and associated input/output electronics into the PUV and debugging.
- assembling and road testing the PUV (still in progress). [5]

PUV System and Fuel Cell Design

As the first step in the design and construction of the SERC prototype fuel cell PUV, we selected the E-Z-GO golf cart to serve as the platform because it was already established and accepted in the Palm Desert community and used an efficient motor and motor controller. We then acquired, instrumented, and tested an original, battery powered E-Z-Go Golf Cart. This provided information on the performance and power demands that the PUV fuel cell power plant would have to satisfy and allowed preliminary system design and sizing of the proton exchange membrane (PEM) fuel cell stack required for the prototype. [5]

Based on these tests, we developed a parallel hybrid design for the system that incorporates three small lead acid batteries to provide power for acceleration and hill climbing. In this role, the batteries provide a small buffer for short term power demands and are recharged during normal cruising and idling conditions. Control of the system was assigned to an on-board computer that permits the PUV operator to start and drive the cart in a straightforward manner. The control computer also provides a lap-top computer with real-time information on the status of all PUV systems. The lap-top both displays and stores the data for further analysis. The design of the PUV

systems and the control software have been reviewed and revised to protect the operator and the PUV by the use of inherently safe hardware design and numerous software safety interlocks. [5]

The PEM stacks developed and operated by SERC have been designed to be simple and to have high **net** efficiency. Consequently, they are designed to run efficiently on air at very low pressure. Although this entails some sacrifice in performance relative to high pressure fuel cells, a simple, low power blower (vs. a compressor) can be used to provide the air supply. [5]

The fuel cell stack developed for and used in the prototype was designed:

- to operate throughout the entire range of driving conditions at a voltage compatible with the E-Z-GO motor controller,
- to provide sufficient power to cruise at constant speed up a moderate incline and still charge the batteries,
- to require low parasitic loads for auxiliary systems such as air supply, water circulation, control computer, solenoids, sensors, etc., and
- to operate efficiently. [5]

To meet these demands, the resulting fuel cell stack contains 64 cells with 300 cm² active area and delivers more than 5.0 kW peak power. During cruising conditions, the stack operates at 0.71 volts/cell which corresponds to a 57% stack efficiency (LHV). The required stack air inlet pressure is less than 2 psig. [5]

The fuel cell stack for the PUV has run well since early March and, because of a more effective electrode design, exceeds the output of the stack that powers SERC's prototype PUV by 25%. The stack has run on SERC's test bench since the third week in March with excellent performance. We will install this fuel cell stack into the cart by July, 1996. [6]

Because improvements in power density are critical to the eventual use of fuel cells in cars, SERC is developing a fuel cell that produces more power, yet weighs less and occupies less volume. DuPont is beginning to make a new Nafion® membrane of intermediate thickness, which SERC will be testing soon. E-TEK, an electrode manufacturer, has sent SERC a set of electrodes with a lower platinum loading. We have made membrane-electrode assemblies (MEA's) using these E-TEK electrodes. The fuel cell made with these MEA's has only been running for a week and a half, but already exhibits a power density that is 35% greater than that of the improved 5 kW stack. We continue to plan and carry out experiments to develop a fuel cell with greater power density. [6]

All of the energy to power the cart comes from the hydrogen stored onboard in two compressed gas cylinders that together hold about 0.16 kg H₂. The hydrogen plus air from a low power, high efficiency blower combine in the fuel cell stack and provide power to the traction bus through a DC-to-DC converter. The power to the PUV's 1.5 kW series DC motor is controlled by the driver via the E-Z-GO motor controller. Power from the traction bus also charges the batteries during normal idling and cruising conditions and power is provided to the traction bus from the batteries during periods of acceleration and hill climbing. Although the batteries store about 30 amp-hrs, only a small fraction of this capacity is normally utilized. Power for all of the auxiliary systems is drawn from the traction bus through a small DC-to-DC converter. The control algorithm for the fuel cell power plant in the PUV manages the power demand on the fuel cell stack plus the air flow, battery charging/discharging, and system heat management. [5]

PUV Construction

Following testing of the original battery powered cart and the design of the PUV system and fuel cell, the fuel cell stack was constructed and tested and the individual PUV auxiliary or peripheral subsystems were designed and individually tested and calibrated. The PUV peripheral subsystems include:

- · air delivery,
- fuel storage, delivery, and refueling,
- water circulation and cooling,
- electrical systems, and
- on-board computer hardware and software. [5]

In the design and testing of each of these subsystems, component safety, reliability, size, and parasitic power demands were important considerations. [5]

Prior to assembly in the PUV, the complete system including the onboard computer was installed on a specially designed test bench so that PUV running conditions could be simulated and the fuel cell, the peripheral systems, and the control algorithm could be tested as they functioned in a complete system. The test bench incorporated duplicate and redundant data acquisition, safety checks, and system controls. This facilitated debugging of the system hardware and software and optimizing the control algorithms in a safe and convenient manner. A 12 kW programmable electronic load was used to impose on the traction bus different steady-state and transient loads that were patterned after those observed during the testing of the original golf cart. Near the completion of the bench testing, the actual cart motor controller and motor were used to load the traction bus while the cart was operated on a dynamometer. [5]

As the component selection and later the bench testing were taking place, the original cart was stripped to the chassis and structurally modified. A fiberglass cover was designed and crafted to cover the fuel storage compartment and the air delivery, fuel storage/delivery/refueling, and the water circulation subsystems were installed. After bench testing, the electrical and on-board computer system were installed. While still in the lab, the PUV system was tested and debugged under idling and low power steady state conditions using a small dynamometer. [5]

The development and testing of the PUV systems were greatly facilitated by the use of specially designed software that permitted real-time monitoring during bench, lab, and finally, on-road testing. [5]

We have developed, using Labview software, the ability to control the fuel cell and related subsystems and to simulate the cart driving cycles on our prototype test bench. This involved thinking through and simulating various fault scenarios, using an electronic load in place of the fuel cell, as well as writing new software. We have rebuilt the bench (air, hydrogen, water, and electrical systems), adding improvements in the areas of data acquisition and control (such as the ability to produce polarization curves) and the flexibility to test subsystems (e.g., calibrate sensors). [6]

Our in-cart software, Portable Cart Monitoring Tool, allows the screen to display fuel cell stack current, the average cell voltages for 4-cell blocks in the stack, the air flow to the stack, the stack temperature, the current to/from the battery, the hydrogen storage pressure, and many other useful sensor readings. [5]

PUV Testing

After the lab evaluation is completed, the PUV will be further tested at a nearby race track where the original cart trials took place. In a series of runs, the PUV will begin at a standing start, accelerate to its maximum speed, and then continue cruising through the remainder of the 0.25 mile course on a level track. [5]

Other Accomplishments

In addition to work directly related to the Palm Desert Project, SERC has developed a Fuel Cell Fact Sheet, completed construction of world wide web pages, written a press release, been featured on *Tomorrow's World* (a British science program), established an independent accounting system, and been active in the community by holding informative talks and discussions to grade school, high school, and university students.

Economic Evaluation

The cost of PEM fuel cells (\$5,000-\$20,000/kW) is the biggest barrier to commercialization in vehicles when compared with the \$50/kW of an ICE. Simple economies of scale will help reduce PEM production costs somewhat, but developments are still required to drive the manufacturing and materials costs to the point where they are competitive. [7]

The SERC Palm Desert Project is for research and demonstration purposes only and therefore is difficult to analyze for an internal rate of return or in terms of cost/benefit. In order to discuss the cost of fuel cells (or any other new technology), it is necessary to consider: 1) an appropriate learning curve ratio for the product, and 2) the point in the product life cycle (how many cumulative units have been produced). SERC's first fuel cell power system (in a golf cart) had a materials cost of \$45,000. The learning curve ratio for the fuel cell industry is generally accepted to be around 15%. This means that a fuel cell power system (such as SERC's) will cost \$20,000 by the 32nd unit, \$10,000 just after the 512th unit, and \$2,000 at the 525,000th unit. Note that other factors that affect price, such as economies of scale, need to be considered. (For simplicity, labor costs have been excluded.) The decline in cost as cumulative production increases may be seen in the table below.

Table 1. Cost of SERC's 4 kW Fuel Cell at various Levels of Cumulative Production

Cumulative	Fuel Cell
Production	System Cost
(# of Units)	(LC=.15)
1	45,000
2	38,250
4	32,513
8	27,636
16	23,490
32	19,967
64	16,972
128	14,426
256	12,262
512	10,423
1,024	8,859
2,048	7,530
4,096	6,401
8,192	
16,384	4,625
32,768	
65,536	<u> </u>
131,072	
262,144	
524,288	
1,048,576	
2,097,152	
4,194,304	
8,388,608	1,071

The most important benefits that a hydrogen economy (the eventual result of sufficient investment and progress in a project such as this one) would have on the country are difficult to quantify in terms of dollars and are sometimes referred to as externalities. Nevertheless, they greatly impact the quality of life in America. They include the following:

- America would be politically and economically independent from Persian Gulf countries.
- Our nation's economy would not be subject to the enormous shifts that occur with large increases in the price of oil.
- The 75% of Americans who live in urban areas would breathe cleaner air (reducing lung and heart disease, as well as crop losses from smog) and see bright skies.
- Our nation's environment would no longer suffer from oil spills, refining effluent, and the addition of greenhouse gases to the atmosphere.

Projected Goals:

The outcome of this project will be a complete, operating model transportation system based on hydrogen and fuel cell power plants. This is the first time that solar and wind derived hydrogen will be produced and used, at the same location, in fuel cells to power motor vehicles. The project provides the opportunity to collect data to help understand how differences in system components can affect overall performance, thus gaining information directly relevant to the nation's future transportation system. Success will also result in new materials and manufacturing techniques for fuel cell power systems that will help commercialize the technology. [7]

In order to achieve the overall goal, the following specific objectives will be met. They are:

- to complete the design, building, testing, and operation of the current PUV, plus 4 additional units and 3 neighborhood electric vehicles (NEVs) powered by hydrogen fueled PEM fuel cells. Development of an advanced metal hydride storage system is progressing in a companion project undertaken in cooperation with Sandia National Laboratory.
- to design, build and operate a refueling infrastructure relevant to future hydrogen based transportation systems. This will include two hydrogen generating facilities and one refueling station. One generating station will be solar powered; the second (to be designed by Lawrence Livermore National Laboratory) will be wind powered.
- to design and construct a PEM fuel cell service and diagnostic center. The center will be located in a refurbished building in the City of Palm Desert corporation yard and service personnel will be trained through this project. The center will serve as an incubator to attract fuel cell manufacturing industry to the City. [7]

Of the total \$3.9M cost of the project, approximately \$2.0 M is provided mainly by SERC, the South Coast Air Quality Management District, and the City of Palm Desert. Other contributors include DuPont (providing membrane material for the fuel cells), ASE Americas (providing the photovoltaic panels at a discount), Wintec (providing a wind turbine, building, and engineering services), Sandia National Laboratory (providing expertise in advanced hydrogen storage techniques), Teledyne-Brown Engineering (providing electrolyzers at a discount), and Lawrence Livermore National Laboratory (providing engineering services). The remainder, \$1.9M, is provided by the U.S. Department of Energy.

Acknowledgments

The authors gratefully acknowledge generous grant funding from Mr. L.W. Schatz of General Plastics Manufacturing Co., Tacoma, WA, USA, and the assistance of SERC's Co-director, Dr. C. Chamberlin, as well as the staff: P. Barger, A. Cohen, S. Cohen, S. Ebers, R. Glover, R. Herick, T. Herron, A. Jacobson, A. La Ven, R. Mayberry, C. Parra, G. Pauletto, M. Rocheleau, L. Reid, R. Reid, and J. Zoellick.

References

- 1. Wedaa, H. (1994). Fuel Cells and Activities by the AOMD To Promote Them, a presentation outline, Palm Desert, Cal.
- 2. Hydrogen Program Plan, FY 1993-FY 1997, U.S. Department of Energy, Office of Conservation and Renewable Energy, 1993.
- 3. Facts and Figures '93. ©1993, American Automobile Manufacturer's Association, Washington, D.C.
- 4. Lehman, P., Olmstead, P., and Parra, C., Fuel Cell, Battery, and Gasoline Golf Carts: A Comparative Analysis, 1994. A report to the City Council of the City of Palm Desert.
- 5. Chamberlin, C., Design and Performance of SERC's Prototype Fuel cell Powered Vehicle, presented at the National Hydrogen Association Meeting, April 2-4, 1996.
- 6. Parra, C., May 1996 Status Report., a report to the U.S. Department of Energy, June 7, 1996.
- 7. Lehman, P., Development of a Renewable Hydrogen Transportation Project for the City of Palm Desert, a proposal to the U.S. Department of Energy, April 7, 1995.
- 8. Facts about Air Pollution and Health, 1991, Air Resources Board Public Information Office, El Monte, Cal.
- 9. Lehman, P. and Parra, C., <u>Solar Todav</u>, Vol.8, No.5, September/October 1994, "Hydrogen Fuel from the Sun," American Solar Energy Society.

CARBON NANOTUBE MATERIALS FOR HYDROGEN STORAGE

A.C. Dillon, K.M. Jones, and M.J. Heben National Renewable Energy Laboratory Golden, CO 80401-3393

Abstract

Hydrogen burns pollution-free and may be produced from renewable energy resources. It is therefore an ideal candidate to replace fossil fuels as an energy carrier. However, the lack of a convenient and costeffective hydrogen storage system greatly impedes the wide-scale use of hydrogen in both domestic and international markets. Although several hydrogen storage options exist, no approach satisfies all of the efficiency, size, weight, cost and safety requirements for transportation or utility use. A material consisting exclusively of micropores with molecular dimensions could simultaneously meet all of the requirements for transportation use if the interaction energy for hydrogen was sufficiently strong to cause hydrogen adsorption at ambient temperatures. Small diameter (~ 1 nm) carbon single-wall nanotubes (SWNTs) are elongated micropores of molecular dimensions, and materials composed predominantly of SWNTs may prove to be the ideal adsorbent for ambient temperature storage of hydrogen. Last year we reported that hydrogen could be adsorbed on arc-generated soots containing 12 Å diameter nanotubes at temperatures in excess of 285 K. In this past year we have learned that such adsorption does not occur on activated carbon materials, and that the cobalt nanoparticles present in our arc-generated soots are not responsible for the hydrogen which is stable at 285 K. These results indicate that enhanced adsorption forces within the internal cavities of the SWNTs are active in stabilizing hydrogen at elevated temperatures. This enhanced stability could lead to effective hydrogen storage under ambient temperature conditions. In the past year we have also demonstrated that single-wall carbon nanotubes in arc-generated soots may be selectively opened by oxidation in H2O resulting in improved hydrogen adsorption, and we have estimated experimentally that the amount of hydrogen stored is ~ 10% of the nanotube weight. We have also correlated hydrogen adsorption capacities with nanotube densities, prepared cobalt-doped carbon targets for high-yield and potentially low-cost production of SWNTs, and are the first to demonstrate the use of concentrated solar radiation for the formation of SWNTs by a new and potentially less expensive route.

Statement of the Problem / Relevance of the Work

Background

With the 1990 Clean Air Act and the 1992 Energy Policy Act, the United States recognized the need for a long term transition strategy to cleaner transportation fuels (Cannon 1995). This realization comes while the U.S. continues to increase petroleum imports beyond 50% of total oil consumption, with nearly 50% of the total oil consumed being used in the transportation sector (N.E.S. 1991/1992). Because of the potential for tremendous adverse environmental, economic, and national security impacts, fossil fuels must be replaced with pollution-free fuels derived from renewable resources. Hydrogen is a ideal candidate as it is available from domestic renewable resources, and usable with virtually no pollution. It could therefore provide the long-term solution to the problems created by Nation's dependence on fossil fuel.

Interest in hydrogen as a fuel has grown dramatically since 1990 and many advances in hydrogen production and utilization technologies have been made. However, hydrogen storage technology must be significantly advanced in performance and cost effectiveness if the U.S. is to establish a hydrogen based transportation system. As described in the U.S. DOE Hydrogen Program Plan for FY 1993 - FY 1997, compact and lightweight hydrogen storage systems for transportation do not presently exist.

Hydrogen provides more energy than either gasoline or natural gas on a weight basis. It is only when the weight, volume, and round-trip energy costs of the entire fuel storage system and charging/discharging cycle is considered that hydrogen's drawbacks become apparent. New approaches enabling more compact, lightweight, and energy efficient hydrogen storage are required in order for the wide-spread use of hydrogen powered vehicles to become a reality.

Research and development geared towards implementation of a national hydrogen energy economy has many indirect economic benefits. With almost 600 million vehicles in the world in 1992 - double the number in 1973 - the conflict between energy requirements, power generation, and environmental concerns is felt on a world-wide basis (Flavin and Lessen 1994). Thus, in addition to providing domestic energy alternatives, investment in hydrogen energy research will result in opportunities for U.S. technologies in over-seas markets.

Currently Available Hydrogen Storage Technologies

Hydrogen can be made available on-board vehicles in containers of compressed or liquefied H₂, in metal hydrides, or by gas-on-solid adsorption. Hydrogen can also be generated on-board by reaction or decomposition of a hydrogen containing molecular species (Dillon et al. 1995). Although each method possesses desirable characteristics, no approach satisfies all of the efficiency, size, weight, cost and safety requirements for transportation or utility use. The D.O.E. energy density goals for vehicular hydrogen storage call for systems with 6.5 wt % H₂ and 62 kg H₂/m³ to provide a 350 mile range in a fuel cell powered vehicle. This requirement amounts to the storage of ~2.9 kg of H₂ in the weight and volume occupied by a conventional gasoline tank. These storage density goals will only be met with significant advances in the capabilities of hydrogen storage technologies.

Gas-on-solid adsorption is not only inherently safer than physical hydrogen storage methods but also has the potential to be more energy efficient than physical storage methods. Consequently, the hydrogen storage properties of high-surface-area "activated" carbons have been extensively studied (Schwarz 1; Carpetis and Peschka 1980; Schwarz 1993). However, activated carbons are ineffective in hydrogen storage systems because only a small fraction of the pores in the typically wide pore-size distribution are small enough to interact strongly with gas phase hydrogen molecules.

Technical Approach and Summary of Past Work

The gas adsorption performance of a porous solid is maximized when all pores are of similar size and not larger than a few molecular diameters (Gregg and Sing 1982). Under these conditions the potential fields from the walls of the so-called micropores overlap to produce a stronger interaction than would be possible for adsorption on a semi-infinite plane. At sufficiently low temperatures, where the escaping tendency of the gas is much less than the adsorption potential, the entire micropore may be filled with a condensed adsorbate phase. For the case of hydrogen, with a van der Waals diameter of 2.89 Å (Breck 1974) pores would be required to be smaller than ~40 Å to access this nanocapillary filling regime. Sufficiently small pores would exhibit an adsorption potential strong enough to localize H₂ at relatively high temperatures. Ideally, the entire porous volume of an adsorbent would be of the microporous variety, and the volume and mass of the adsorbent skeleton would be the minimum necessary to develop the adsorption potential and provide sufficient thermal conductivity for management of heat fluxes associated with adsorption and desorption.

In 1993, we initiated a research program based on the idea that aligned and self-assembled single wall carbon nanotubes could serve as an ideal hydrogen adsorbent. A simple calculation indicated that a single isolated 20 Å diameter tube could meet both DOE energy density targets by storing H₂ at densities of 7.8 wt% and 65 kg/m³. The calculation considered a close-packed arrangement of H₂ molecules as a first monolayer on the interior surface of the nanotube, with subsequent volume filling by a condensed H₂ phase. Additional storage in the interstitial spaces between assembled tubes was neglected. Theoretical calculations by Pederson and Broughten (Pederson and Broughton 1992) further suggested that adsorption forces for hydrogen within SWNTs would be stronger than for adsorption on ordinary graphite, indicating that high H₂ storage capacities could be achieved at relatively high temperatures and low pressures as compared to adsorption on activated carbons.

In the Proceedings of the 1994 Hydrogen Program Review, we presented microbalance data which demonstrated gravimetric hydrogen storage densities of up to 8.4 wt% at 82 K and 570 torr on carbon nanotube samples. This substantial uptake at low hydrogen pressures demonstrated the strong interaction between hydrogen and these materials. The behavior is consistent with higher heats of adsorption than can be found with activated carbons, and suggests that these materials could be optimized for efficient use in hydrogen storage.

In the 1995 Hydrogen Program Review Proceedings, we presented the results of our temperature programmed desorption (TPD) studies which showed significant H₂ adsorption near room temperatures. The adsorption energies on nanotube materials were shown to be a factor of 2-3 times higher than the maximum that has been observed for hydrogen adsorption on conventional activated carbons. To our knowledge, these are the first results which demonstrate the existence of stable adsorbed hydrogen on any type of carbon at temperatures in excess of 285 K. We also presented an analysis of nanotube production yields versus rod translation rate in our spark-gap SWNT generator. The research reactor was specifically designed and constructed for the controlled generation on SWNT material.

This year we have significantly advanced our understanding and control of the highly unique hydrogen adsorption properties of single-wall carbon nanotube materials. We performed a detailed comparative investigation of the hydrogen adsorption properties of SWNT materials, activated carbon, and exfoliated graphite. We also determined that the cobalt nanoparticles which are present in our arc-generated soots do not play a role in the observed hydrogen uptake. We determined the amount of hydrogen which is stable at near room temperatures on a SWNT basis is ~ 10 wt%, and found that an initial heating in vacuum of single-wall carbon nanotubes samples is essential for producing high temperature hydrogen adsorption. Further experiments revealed that SWNTs are selectively opened by oxidation during this heating, and that H_2O is more selective in oxidation than O_2 due to hydrogen termination of dangling bonds at the edges of opened nanotubes. Purposeful oxidation in H_2O resulted in hydrogen storage capacities which were improved by more than a factor of three. We also correlated the measured

nanotube densities produced by specific synthesis rod translation rates during arc generation with hydrogen storage capacities determined by TPD. Finally, we utilized NREL's High Flux Solar Furnace to form nanotubes by a new and potentially less expensive route for the first time. The methods used and findings made during the past year are presented in detail in the remainder of this report.

EXPERIMENTAL

SWNT Synthesis by Spark-gap Evaporation

As discussed previously (Dillon et al. 1995) our arc-generated carbon nanotube soots were produced by co-evaporating cobalt/carbon mixtures in a spark-gap evaporator (SGE) (Bethune et al. 1993; Iijima and Ichihashi 1993). Two graphite electrodes of differing diameters (6 and 13 mm) were mounted on the base plate of the evaporator by electrically isolated positioners. The 6 mm graphite rod was doped with cobalt by drilling-out and refilling a 2.9 mm hole with mixtures of cobalt and carbon. The cobalt density averaged across the entire rod was ~ 3 at %. Prior to all synthesis runs, the evaporator was evacuated to $\sim 10^{-6}$ torr with a diffusion pump and back-filled with helium to ~ 500 torr.

Electrical feedthroughs connected the graphite rods to a multi-tapped transformer capable of supplying more than 5 kW. The two graphite rods were held co-axially, and the small rod was moved linearly by a rotational feedthrough with a pinion/rack gear arrangement. The spark gap could be initiated by advancing the 6 mm rod towards the 13 mm rod with ~16 volts between the rods. Electronic feedback circuitry was employed to perform three different types of 10 minute runs with rod translation rates of 1.5, 2.5 and 4.5 mm/min. and a fixed potential of 16.2 volts. The carbon soots produced in each of the different runs were analyzed by TEM. In general, the soots contained varying amounts of amorphous carbon, graphitic fragments, cobalt nanoparticles and 12 Å diameter SWNTs.

Transmission Electron and Atomic Force Microscopies

Samples were prepared for TEM by suspending ~ 1 mg in 86 ml of acetone. The solutions were sonicated for at least 5 min., and 1 cc was charged into a 1.5-1.8 x 100 mm micro-capillary and atomized onto carbon coated copper grids. The copper grids were sprayed with the solution three times to insure a adequate quantity of material. Transmission electron microscopy images were obtained on a Phillips CM-30 TEM/STEM operating at 200 kV with a 50 µm objective aperture for improved contrast. The images were taken at magnifications from 4.4k to 340 k and recorded on a 1024 x 1024 CCD camera. Each sample was surveyed for ~45 min. and ~ 5 images were recorded to ensure a true representation of the material.

AFM studies were performed on a Park Autoprobe CP in contact mode with a 100 Å diameter cantilever and a force of 5 nanoNewtons. SWNT material was dissolved in isopropyl alcohol and sprayed onto highly ordered pyrolytic graphite substrates. Each sample was surveyed for ~ 45 min., and average heights of the various soot components were obtained.

Temperature Programmed Desorption

The ultra high vacuum (UHV) chamber employed for the TPD studies is shown in Fig. 1. The sample is mounted at the bottom of a liquid nitrogen cooled cryostat (George 1986), and a mass spectrometer provides for line-of-site detection of desorbing species. An ion gauge and capacitance manometer are employed to monitor pressure. Gas exposure is controlled with a variable conductance leak valve. Isolation gate valves separate the sample compartment during high-pressure gas exposures. A leak valve was used to transfer species to the mass spectrometer.

Carbon samples weighing ~1 mg were placed in a packet formed from 25 µm thick platinum foil. Pin holes in the foil enabled gas diffusion into and out of the packet. The packet could be cooled to ~90 K by the liquid nitrogen cryostat, and resistively heated with a programmable power supply. The sample temperature was measured with a thin thermocouple spot-welded to the platinum packet.

Except where noted, the samples were heated in vacuum at 1 K/s to 970 K prior to TPD studies. Various hydrogen (99.999% purity) exposures were employed to elucidate the H_2 adsorption properties of the samples. Oxidation of the nanotube material was studied at various pressures and temperatures employing both H_2O and O_2 . The chamber was evacuated to $\leq 5 \times 10^{-8}$ torr before each TPD run. TPD spectra were obtained with a heating rate of 1 K/s, and mass spectra were recorded every 2 s.

RESULTS AND DISCUSSION

Hydrogen Adsorption on SWNTs, Activated Carbon, and Exfoliated Graphite

Figure 2 is a TEM image of arc-generated SWNT material obtained with a rod translation rate of 2.5 mm/min. As discussed in detail later, this translation rate resulted in the highest nanotube content in the arc-generated soots. The TEM image clearly displays the characteristic fibrous network in which SWNTs are found. The network consists of 20-100 nm rounded soot particles linked together by fine nanotube fibers. The fibers are covered with a thin layer of amorphous carbon and can be traced across the full TEM image. Inspection of the fibers at higher magnification revealed bundles of individual SWNTs with diameters of -12 Å. Note that the cobalt nanoparticles which catalyze the SWNT formation are -5-70 nm in diameter and clearly visible inside the soot particles.

Activated carbon was studied for comparison with SWNT materials. The activated carbon (AC), supplied by Spectracorp Limited was synthesized from pitch precursors and activated by KOH. Figure 3 is a typical TEM image of the AC showing a collection of relatively short, large-inner-diameter (50-100 Å) multi-walled tubes agglomerated with amorphous carbon. Other TEM images (not shown) revealed the presence of isolated graphitic fragments and amorphous carbon particles. However, no SWNTs were observed.

Figure 4 displays H₂ TPD spectra obtained from both SWNT materials and AC. Figure 4a shows the H₂ TPD spectrum from SWNT material after a 300 torr, 10 min hydrogen exposure at 133 K. After the H₂ exposure, the chamber was evacuated and the sample was cooled to ~90 K. TPD spectroscopy measured a hydrogen peak at 148 K. The signal is apparently due to desorption from only those sites in the tail of a broad distribution which could not be populated at 133 K.

Figure 4b shows the TPD spectrum from a SWNT sample after exposure to 300 torr of H₂ for 10 min at 273 K, followed by cooling to 133 K in the presence of the hydrogen gas. As before, the sample temperature was reduced to ~90 K when the chamber was evacuated. Two well-defined hydrogen desorption signals are apparent in Fig. 4b at 148 and 288 K. The low temperature signal is similar to the peak produced by the 133 K dose (Fig. 4a). The striking feature in Fig. 4b is the appearance of hydrogen desorption which is peaked at 288 K. In contrast to the 148 K signal, the feature is a complete TPD peak representing a population of distinct and structurally unique sites for hydrogen adsorption. These sites were not populated with H₂ exposures at 133 K, suggesting that access to the more stable sites is limited by diffusion kinetics. As discussed later, the high temperature TPD peak is due to H₂ adsorption within the cavities of SWNTs. The diffusion limitation may be due either to slow diffusion along the long internal surface of the SWNTs, or to the inability of H₂ to enter the SWNTs through the amorphous carbon coating around their ends.

Figure 4c shows H_2 TPD data after exposure to 300 torr H_2 for 10 min at 273 K and evacuation with the sample temperature held at 223 K. The sample was cooled to ~ 90 K when the pressure is below $\sim 5 \times 10^{-8}$ torr. In contrast to Figs. 4a & b, no hydrogen desorption signal at 148 K was observed after these procedures. However, the H_2 desorption peak at 288 K is still clearly evident. The data demonstrates two significant features of the hydrogen species occupying these sites; (i) the adsorbed species in the high temperature sites are stable at 223 K while in contact with low hydrogen partial pressures (5 x 10^{-8} torr), and (ii) the species do not redistribute to other sites on the SWNT material during evacuation and cooling.

Figure 4d shows the TPD data from AC after an exposure identical to that used to produce the data in Fig. 4b. An H₂ desorption peak similar to that in Fig. 4b is observed at 148 K, but no higher temperature desorption signal is apparent. The adsorption sites responsible for the hydrogen desorption peak at 288 K on SWNTs are evidently not present in activated carbon. The internal cavities of the multi-walled tubes may be too large to produce the nanocapillary interactions ascribed to SWNTs (Pederson and Broughton 1992)

Extensive TEM examinations showed that the AC material is very similar in structure and overall morphology to the arc-generated soots except for the absence of the 12 Å diameter SWNTs and the cobalt nanoparticles. The graphitic/amorphous carbon ratio is higher in AC, but these two fractions are clearly the largest part of both types of material. Consequently, it is reasonable to assign the TPD signal at 148 K observed for both materials to hydrogen desorbing from sites associated with these ubiquitous carbon structures. The source of the 148 K peak can be further identified by noting that H₂ is unstable on planar graphite under the pressure and temperature conditions employed here (Pace and Siebert 1959). Thus, the signals must be due to desorption from porous environments at the edges of graphitic fragments or within amorphous carbon. This interpretation is consistent with the area of the peak in Fig. 4d being 10% of the corresponding area in Fig. 4a, reflecting a reduced porosity and a higher graphitic/amorphous ratio in the AC. Measurements on exfoliated graphite supported this reasoning by yielding H₂ desorption signals at 150 K which were only 25% of those observed for AC materials. As with the AC sample, the TPD peak at 285 K was not observed from exfoliated graphite.

Hydrogen Adsorption on Cobalt

At last years Program Review Meeting there was concern expressed from a reviewer that the TPD peak centered at 285 K might simply be do to hydride formation with the cobalt nanoparticles present in the arc-generated soots (Fig. 2a). We entertained this possibility thoroughly by performing an extensive literature review and detailed experimental investigation.

Hydrogen TPD studies of cobalt single crystals (Ernst et al. 1994), powders (Cabrera 1993), and polycrystalline samples (Lisowski 1989; Cabrera 1993) report spectra which differ significantly from those we observe for SWNT samples. Most notable are peaks reported at temperatures greater than 350 K (Lisowski 1989; Cabrera 1993; Ernst et al. 1994) and near 500 K (Cabrera 1993). In contrast, our TPD measurements on SWNT materials yielded only two peaks at 148 K and 288 K for sample temperatures between 100 and 700 K (Dillon et al. 1995).

Additional experiments performed in our laboratory preclude any significant role for Co in the TPD signals we observe. Electron diffraction performed on as-produced SWNT soots yielded metastable face-centered-cubic Co patterns (Bethune et al. 1993)). After heating in vacuum to develop the high-temperature peak, blurred diffraction rings were observed in agreement with a superposition of hexagonal Co₃O₄ and Co patterns. The composite pattern is consistent with cobalt metal particles coated with a thin oxide, which may explain the lack of H₂ uptake by the cobalt nanoparticles. Control experiments on the micron-sized cobalt powders used to prepare the filled anodes, and on the cobalt nanoparticles remaining after complete oxidative removal of the carbon fraction from SWNT samples, did not yield H₂ desorption signals between 100-400 K. These experiments confirmed that the hydrogen adsorption at near ambient temperatures is unrelated to the cobalt nanoparticles present in the SNWT samples.

Quantitation of Hydrogen Adsorption

The integrated area of the high temperature H_2 desorption peak corresponds to an amount of hydrogen between $\sim 0.005-0.02$ wt% on a total soot weight basis. The broad range in the hydrogen storage capacities is a function of both the heterogeneity of the samples and sample pre-treatments (vide infra).

Transmission electron microscopy and atomic force microscopy (AFM) were used to determine the volume fractions of the various components in an oxidized SWNT soot which adsorbed ~0.005 wt% hydrogen at near ambient temperatures. This particular sample had been oxidized in 1 torr H₂O until not only the tube caps but also the nanotubes themselves were consumed in order to ensure that all tubes were opened (vide infra).

The cross sectional areas of the amorphous carbon, graphitic fragments, cobalt nanoparticles, and carbon nanotubes were measured from TEM images. Average heights of these same structures were measured with AFM. The volume of each fragment was multiplied by the corresponding density to estimate the weight fraction of each component in the 1 mg soot samples. The nanotube content within the soot was estimated to be -0.05 wt%. This determination enabled the amount of adsorbed hydrogen per nanotube to be estimated as -10 wt%. These results are consistent with predictions that complete filling of a SWNT should result in gravimetric storage density of -6.5 wt% H₂ (Heben 1993).

Opening of Single-wall Carbon Nanotubes During Initial Degassing

During our early hydrogen uptake investigations SWNT soots were outgassed in vacuum to 970 K at 1 K/s as part of a standard experimental protocol. Experiments performed without this initial degassing were quite revealing as no high temperature desorption signal could be observed. Figure 5 compares the hydrogen TPD spectra of as-synthesized (Fig. 5a) and degassed (Fig. 5b) SWNT materials. The samples were exposed to H₂ at 300 torr for 10 min at 273 K, and then cooled to 133 K (the minimum temperature achievable with the cryostat and the gas load) for 3 min. The chamber was evacuated with concurrent cooling of the sample to 90 K prior to TPD. Figure 5a shows a single H₂ peak centered at 148 K in the TPD spectrum from a sample that was not initially outgassed. Once again, this signal is likely the tail of a much broader desorption peak which would be observed with hydrogen exposures at lower temperatures. Fig. 5b also shows a low temperature signal at 148 K which is similar to the peak observed in Fig 5a, and is therefore attributed to desorption from the same sites. However, the outgassed SWNT sample displays an additional feature in the TPD spectrum: a well-defined hydrogen desorption signal at 288 K. Unlike the 148 K signal, the desorption feature at 288 K is a complete TPD peak representing distinct sites for H₂ adsorption.

During degassing, the pressure in the chamber increases by two orders of magnitude over the base pressure of 10^{-8} torr. The CO, H_2O , CO_2 , H_2 and N_2 evolve as a function of temperature during this initial heating is shown in Figure 6. The CO_2 and H_2O signals increase significantly above 400 K due to either the desorption of physisorbed species, or the thermal decomposition of surface carbonyl and hydroxyl species according to the mechanisms shown in Figure 7. Multiple internal reflectance infrared (MIRIR) spectra revealed carbonyl groups, CH_x species, physisorbed CO and H_2O , and hydrogen-bonded hydroxyl species on the initial carbon nanotube material, and confirmed a loss in carbonyl groups and an increase in CH_x and C-O-C species after degassing in agreement with the proposed mechanisms. Unfortunately, changes in the surface hydroxyl coverage could not be monitored due to the presence of physisorbed H_2O (Dillon et al.).

Water and CO_2 pressures decrease dramatically above 560 K where CO evolution becomes dominant during degassing (Fig. 6), suggesting that evolved CO_2 and H_2O is reacting with surface carbon (C_s) to generate CO (Chelliah 1996). The reaction between H_2O and C_s should liberate H_2 increasingly as more water becomes available for the reaction: $C_s + H_2O \longrightarrow CO + H_2$. Instead, the H_2 pressure increases

only above 400 K and decreases after 560 K. The lack of a continued increase in the H_2 signal is consistent with hydrogen termination of carbon dangling bonds. This view is supported by an increase in the C- H_x stretching vibration in the MIRIR spectrum of the degassed material (Dillon et al. 1996). Desorbing N_2 is also observed in Fig. 6, but not in proportion to the amount of O_2 that would be expected for equilibration of the sample with laboratory atmosphere prior to degassing. The absence of O_2 in Fig. 6 indicates that the molecule is reacting as it is evolved, and contributing to CO or CO_2 production.

Degassing allows the high-binding energy sites with a TPD peak at 288 K to become apparent. The presence of such sites is consistent with the enhanced physical attractive interactions predicted for molecular species within the internal cavities of small diameter carbon nanotubes (Pederson and Broughton 1992). The mass spectroscopy data and MIRIR studies show that carbon present in the sample is converted to gaseous CO and CO₂ by the procedure, and that remaining portions of the sample are hydrogen terminated. Although difficult to observe by TEM, it is likely that the SWNTs are oxidatively opened during the degassing procedure allowing H₂ adsorption within the nanotube internal cavities (Dillon et al. 1996). Multi-walled carbon nanotubes are selectivity opened by oxidation due to the strong local curvature, imperfect geometry, or the presence of five-membered rings in the tube caps (Ajayan et al. 1993). The caps of small diameter SWNTs should be especially reactive for the same reasons. It is also possible that some fraction of the SWNTs are always open and that outgassing simply produces a clean substrate for hydrogen adsorption.

Controlled Oxidation of SWNT Carbon Soots in Water and Air

Degassing of SWNT carbon soots in vacuum results in the oxidative opening of the single-wall carbon nanotubes and enables high temperature H_2 adsorption. We endeavored to oxidize SWNT soots further to determine if the amount of H_2 stored at high temperatures could be maximized. As a starting point for these investigations a degassed carbon nanotube sample was exposed to H_2 at 300 torr for 10 min at 273 K and 3 min at 133 K prior to chamber evacuation and cooling to 90 K. The subsequent H_2 TPD spectrum revealed the characteristic low and high temperature hydrogen desorption signals (Fig. 8a). The sample was then heated between 325-975 K at 1 K/s in 1 torr H_2 O. As was found for the original degas above 600 K (Fig. 6), the CO partial pressure increased as the H_2 O pressure decreased indicating the oxidation of the carbon material. Although some H_2 was also detected by the mass spectrometer, the evolution did not scale with the produced CO indicating at least partial hydrogen termination of the carbon surface dangling bonds and the same reaction mechanism observed during the degas.

Following this oxidation in water the sample was degassed to 970 K in vacuum, and dosed with hydrogen in a manner identical to that used for the un-oxidized degassed material. The TPD spectrum (Fig. 8b) displayed a substantial increase in the high temperature desorption signal indicating the opening and filling of additional carbon nanotubes. The low temperature hydrogen desorption signal decreased indicating that amorphous carbon had been consumed by reaction with water.

Hydrogen TPD studies after exposure to 1×10^{-5} torr H_2O at 825 K for 10 min were also performed. Comparing Fig. 9a & 9b shows the high temperature H_2 signal is increased by approximately a factor of three by the process. In addition, an increase and slight shift to -180 K is observed for the low temperature peak. The dramatic increase in the high temperature peak suggests that some carbon nanotubes may have been fully consumed during oxidation with water at 1 torr (Fig. 8). The increase in the low temperature peak may be attributed to the development of increased porosity within the amorphous carbon portions of the material. The more vigorous oxidation of Fig. 8 may have resulted in consumption of both highly porous amorphous material as well as some carbon nanotubes.

For comparison, the oxidation of carbon nanotube material by heating between 325-975 K at 1 K/s in 5 torr of air was also examined. An increase in the partial pressure of CO₂ corresponding to a decrease in the O₂ pressure was detected above 600 K again indicating the oxidation of the carbon substrate. In sharp contrast to TPD after oxidation in water, hydrogen TPD studies identical to those of Figs. 8 & 9 did not

display a high temperature hydrogen desorption signal. Subsequent TEM investigations revealed that the SWNTs had been completely consumed during the oxidation. In another experiment, oxidation of SWNT material in 5×10^{-5} torr of air for 10 min at 825 K resulted in a significant decrease in both the high and the low temperature hydrogen desorption peaks indicating the consumption of both the carbon nanotubes and other material fractions in the soot (Dillon et al. 1996). Our studies indicate that water is a gentler and more selective agent for removal of nanotube caps. The selectivity for cap removal demonstrated by water can be attributed to hydrogen termination of the opened nanotube dangling bonds.

Optimization of Nanotube Content in Arc-generated Soots

Carbon soots were generated in a spark gap evaporator with rod translation rates of 1.5, 2.5 and 4.5 mm/min (Dillon et al. 1995). Relative SWNT contents were determined with a rigorous TEM analysis (Fig. 10) which shows that no single-wall nanotubes are produced for a rod translation rate of 4.5 mm/min The TEM images of the 4.5 mm/min material displayed high concentrations of graphitic fragments, amorphous carbon and multi-walled tubes and were similar to images of activated carbon (Dillon et al.). In contrast, a fibrous network of single-wall carbon nanotubes was observed for both the 2.5 and 1.5 mm/min runs with the tube density in the 2.5 mm/min run being ~ 20% higher (Fig. 2). During the 1.5 and 2.5 mm/min runs the gap spacing between the two rods was ≥ 1 mm, and a blue plasma between the rods extended 1-2 cm. During the 4.5 mm/min run the gap between the rods was ≤ .5 mm and a well defined plasma was not observed. Thus, it appears that in the faster run the current in the gap is predominantly carried by an arc with a high current density rather than a uniform plasma. The evaporation rate of material from the small diameter rod is enhanced over the sputtering rate with slower translation speeds. This effect may be attributed to a more uniform hot zone extending across the small rod at the slower translation speeds. Annealing of carbon fragments within such a hot zone appears to be essential for the production of single-wall carbon nanotubes.

The two carbon soots produced at 1.5 and 2.5 mm/min were dosed with hydrogen under the conditions which produce a maximum amount of adsorbed H_2 in the high temperature sites (vide infra). Figure 11 shows the subsequent TPD data. The hydrogen desorption peak for the 2.5 mm/min run is $\sim 20\%$ larger than the corresponding H_2 desorption signal for the 1.5 mm/min run, in good agreement with the estimated tube densities for these materials (Fig. 10). As expected, no hydrogen adsorption was detected following an equivalent hydrogen exposure to the 4.5 mm/min material.

Production of SWNTs in NREL's Solar Furnace

We have demonstrated the production of carbon single-wall nanotubes using concentrated solar radiation. Unique doping schemes were developed to prepare carbon targets containing highly-divided cobalt. The solar route offers the potential for low-cost photon and/or heat delivery, and the possibility of spatially separating the generation of critical gas phase species from the annealing of these species to achieve high SWNT yields. The details of these investigations are beyond the scope of this report, and are presented elsewhere (Heben et al. 1996). Future experiments with next generation reactors will continue to access the viability of a solar-based approach to the cost-effective synthesis of SWNTs.

Summary and Conclusions

This year we have greatly broadened our understanding of the highly unique adsorption hydrogen properties of single-wall carbon nanotubes. We have conclusively established that the cobalt nanoparticles present in the SWNT materials do *not* contribute to observed hydrogen desorption. We have demonstrated that SWNTs in arc-generated carbon soots may be decapped by degassing in vacuum to 975 K. Once open the nanotubes are capable of adsorbing hydrogen at near ambient temperatures. This unusual stabilization is unique to SWNT material and is consistent with a nanocapillary filling

mechanism within the cavities of carbon nanotubes. The hydrogen storage capacities of our arc-generated materials may be increased by up to a factor of three by a low pressure oxidation in H₂O. The single-wall carbon nanotube caps are selectively removed by oxidation in water rather than in oxygen due to hydrogen termination of the opened nanotube dangling bonds in the presence of water. Finally, we have experimentally determined that the hydrogen storage capacity per nanotube is 10 wt%.

Methods for the cost effective production of aligned carbon nanotubes and the determination of their hydrogen storage capacities is a constant focus of our research. This year we correlated the optimization of hydrogen storage capacities with the production of SWNTs versus synthesis rate in the spark gap evaporator. These studies revealed that the nanotube inner diameters may change versus synthesis rate indicating that the range over which H₂ adsorption/desorption occurs may be regulated. We are now prepared to employ laser vaporization for the production of SWNTs as yields of ~50% have been reported with this approach (Guo et al. 1995). Finally, we have shown that SWNTs may be produced in NREL's unique High Flux Solar Furnace to form nanotubes by a new and potentially less expensive route.

Future Work

Unfortunately, the materials we have synthesized and researched thus far do not have high enough nanotube contents to allow the full promise of carbon nanotubes to be realized in hydrogen storage applications. In the next year we will focus on the production of high density aligned carbon nanotubes and on the evaluation of their hydrogen adsorption properties. As discussed previously, we will employ laser ablation or solar furnace techniques for the high-yield, cost effective production of carbon nanotubes. We will then investigate various methods for aligning these tubes. For example, large-diameter multi-walled nanotubes have been aligned by stretching of dispersions of nanotubes in polymer matrices (Ajayan 1995) or by the mechanical combining of randomly oriented nanotubes deposited on Delrin or Teflon. (de Heer et al. 1995). We will also explore methods for removing the heavy cobalt particles employed as catalysts in the synthesis. Possible methods may include acid extraction or vaporization in high vacuum. We may establish a collaboration with Hazen Research Laboratories in Golden, Colorado as cobalt separations have been an ongoing focus of Hazen's research efforts. Finally, we will optimize conditions for opening and filling these aligned nanotube ensembles.

Acknowledgments

The authors thank Tim Bekkedahl for synthesizing SWNT materials, Andrew Cahill for performing AFM measurements, John Webb for assistance with MIRIR measurements, and Jerry Fleming of Spectracorp, Ltd., for providing activated carbon samples.

Figures LN2 Cryostat Doser Electrical Feedthrough Leak Valve Sample Mechanical Pump Fump Fump Fump Fump Fump

Figure 1: Temperature programmed desorption (TPD) spectroscopy apparatus.

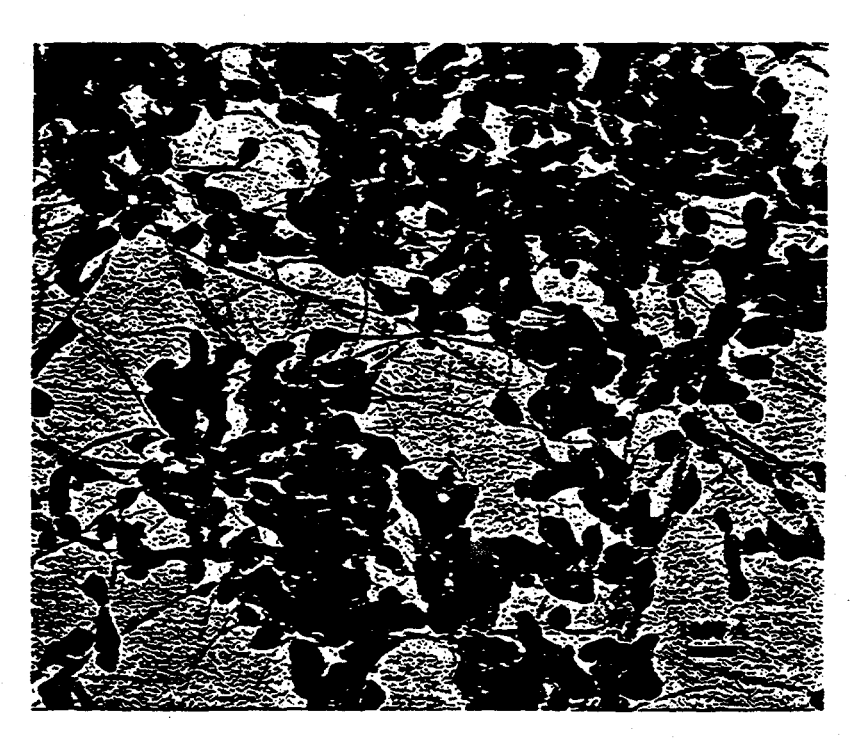


Figure 2: Single wall carbon nanotube material.



Figure 3: Activated carbon material M30 from Spectracorp, Ltd.

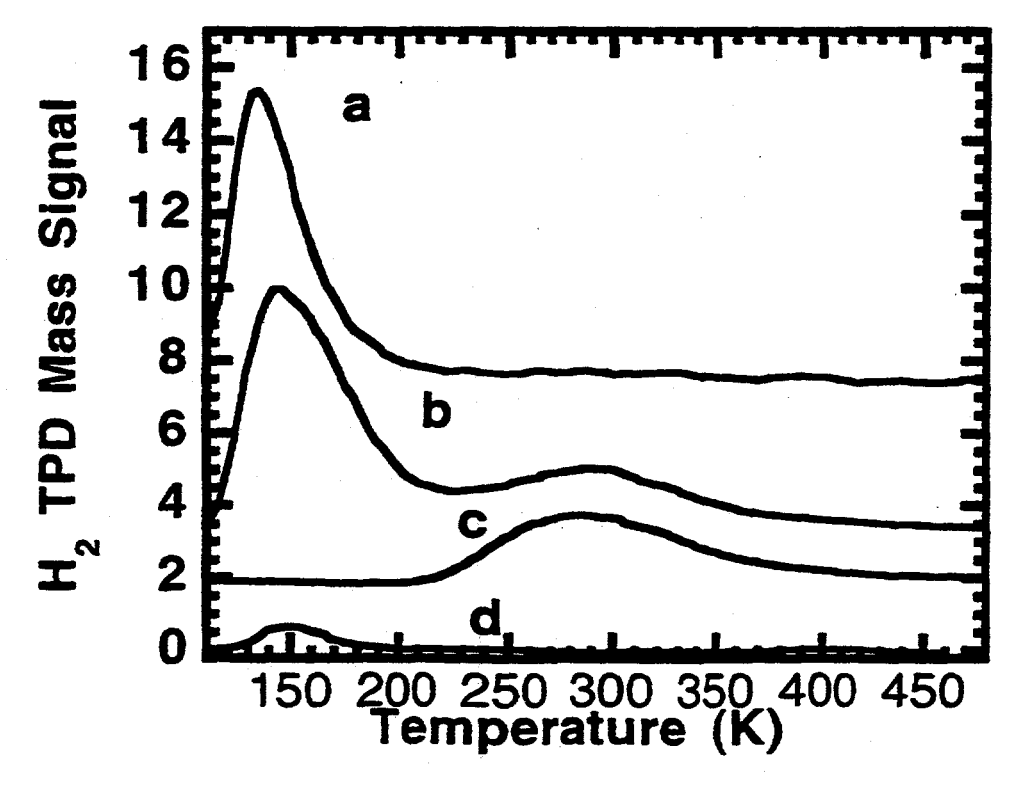


Figure 4: TPD spectroscopy of a) SWNT material after 133 K dose, b) SWNT after 273 K dose, c) same as (b) but with chamber evacuation at 223 K, and d) activated carbon with dose same as (b).

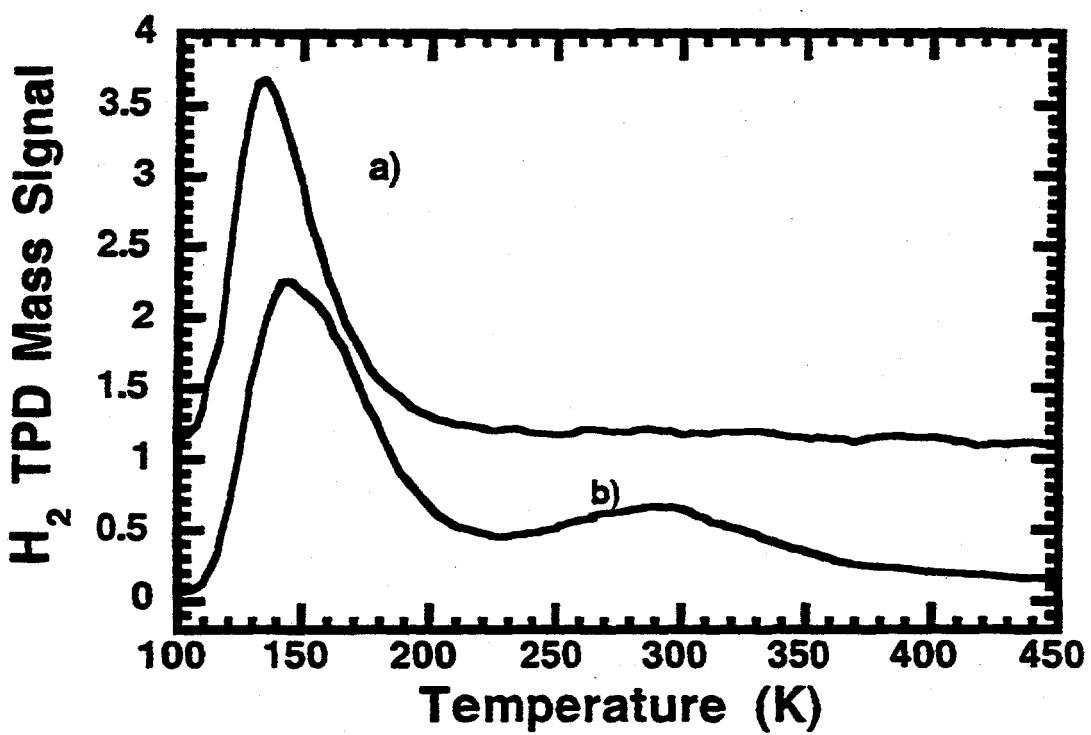


Figure 5: Hydrogen TPD spectra of a) as-prepared and b) degassed SWNT material.

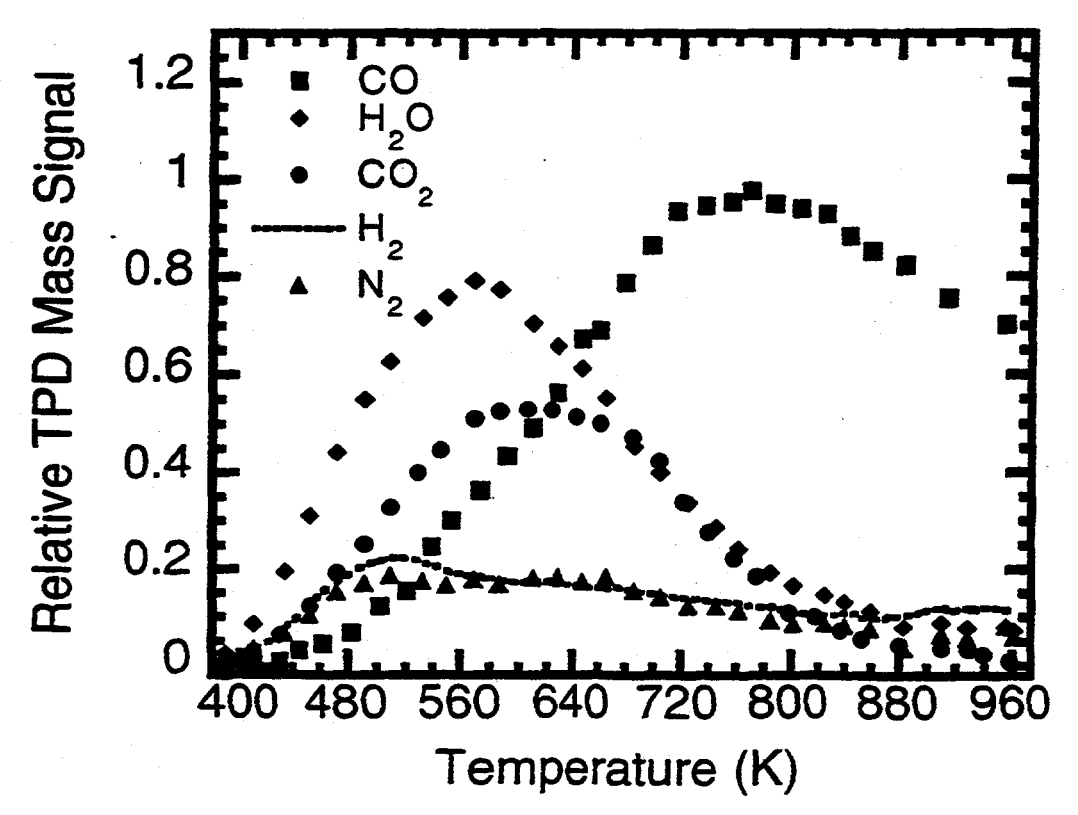


Figure 6: The evolution of CO, H₂O, CO₂, H₂ and N₂ during initial heating of SWNT material.

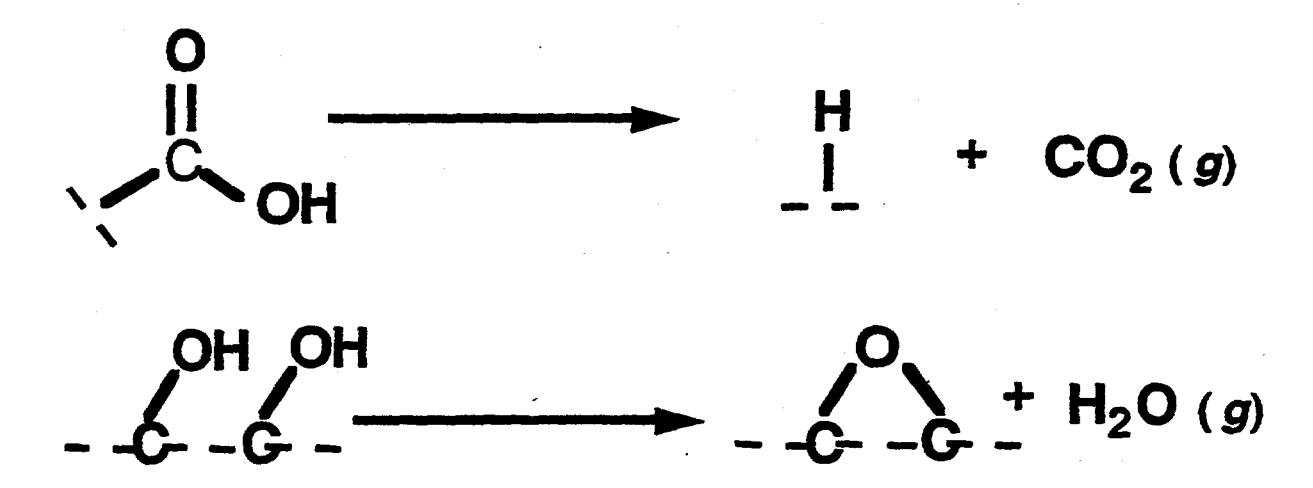


Figure 7: Mechanism for H₂O and CO₂ evolution during degassing

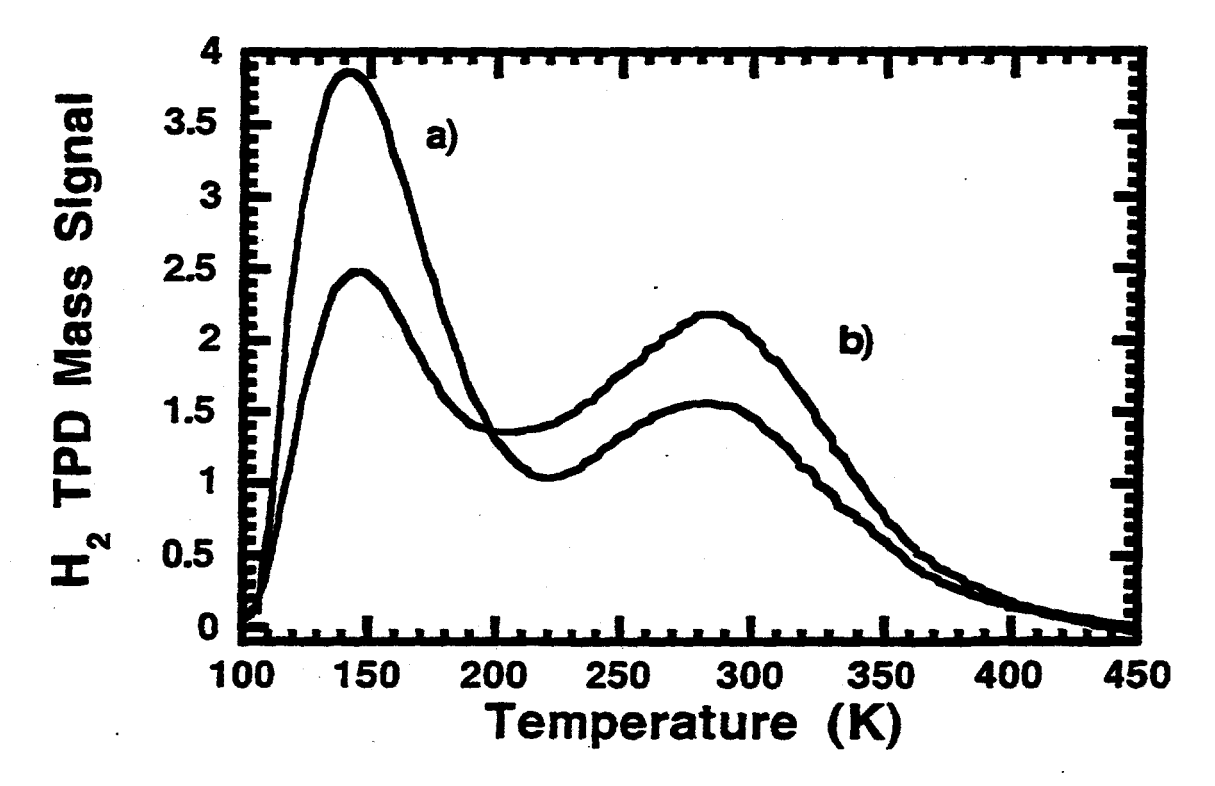


Figure 8: SWNT material following an H₂ exposure of 300 torr for 10 min at 273 K and 3 min at 133 K for: a) a degassed sample, b) a degassed sample oxidized in 1 torr H₂O between 325-975 K.

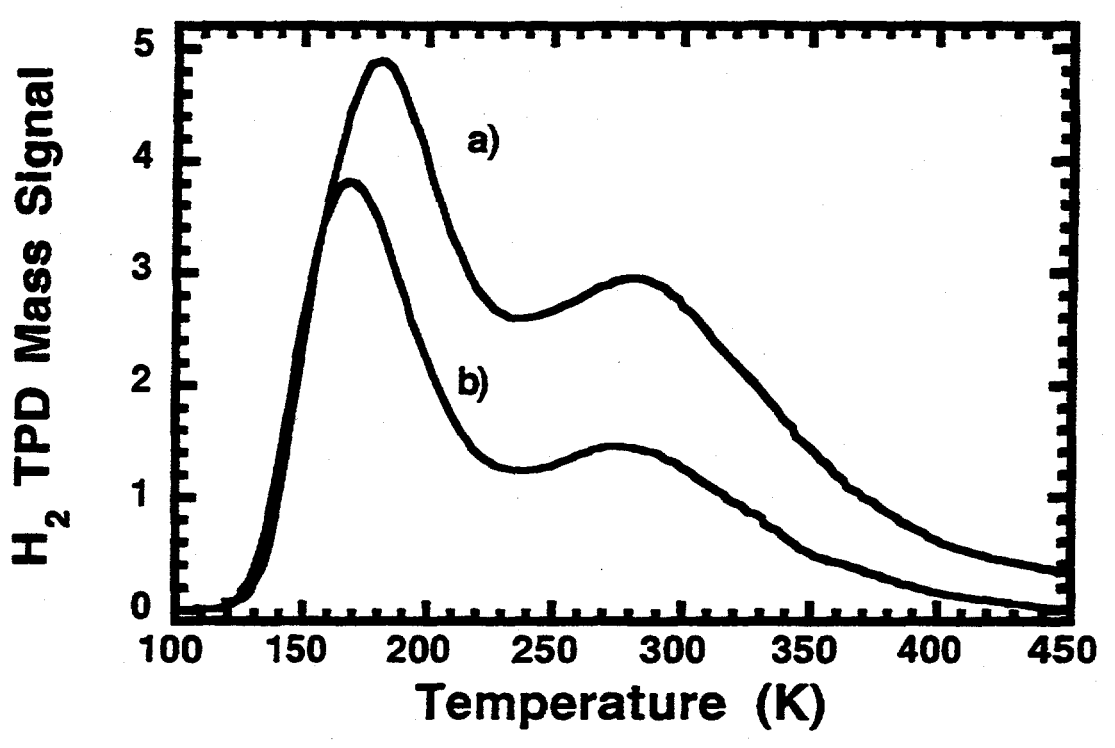


Figure 9: SWNT material following an H_2 exposure of 300 torr for 10 min at 273 K and 3 min at 133 K for: a) a degassed sample, b) a degassed sample oxidized in 1 x 10⁻⁵ torr H_2O at 825 K.

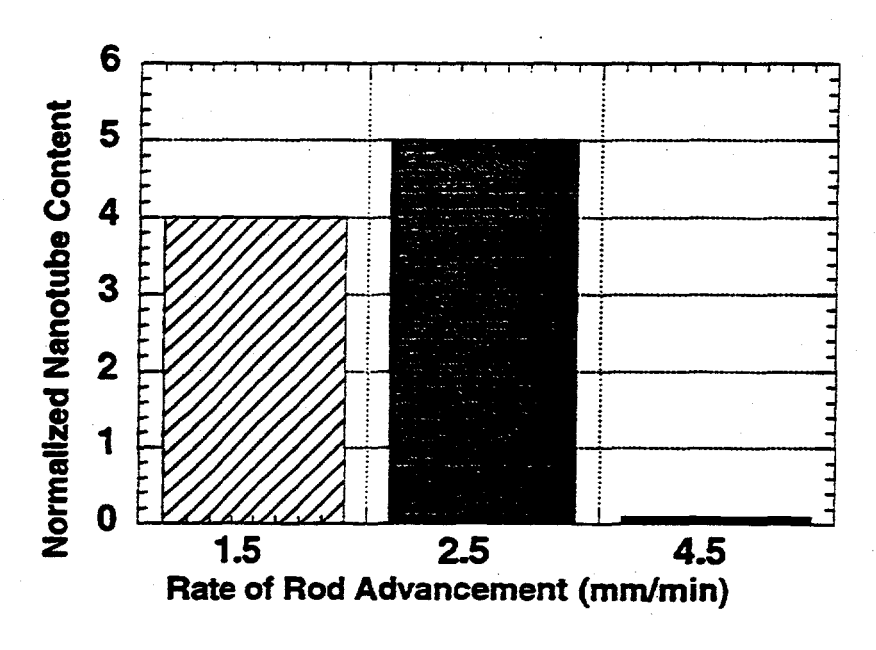


Figure 10: Relative SWNT contents generated with rod translation rates of 1.5, 2.5 and 4.5 mm/min.

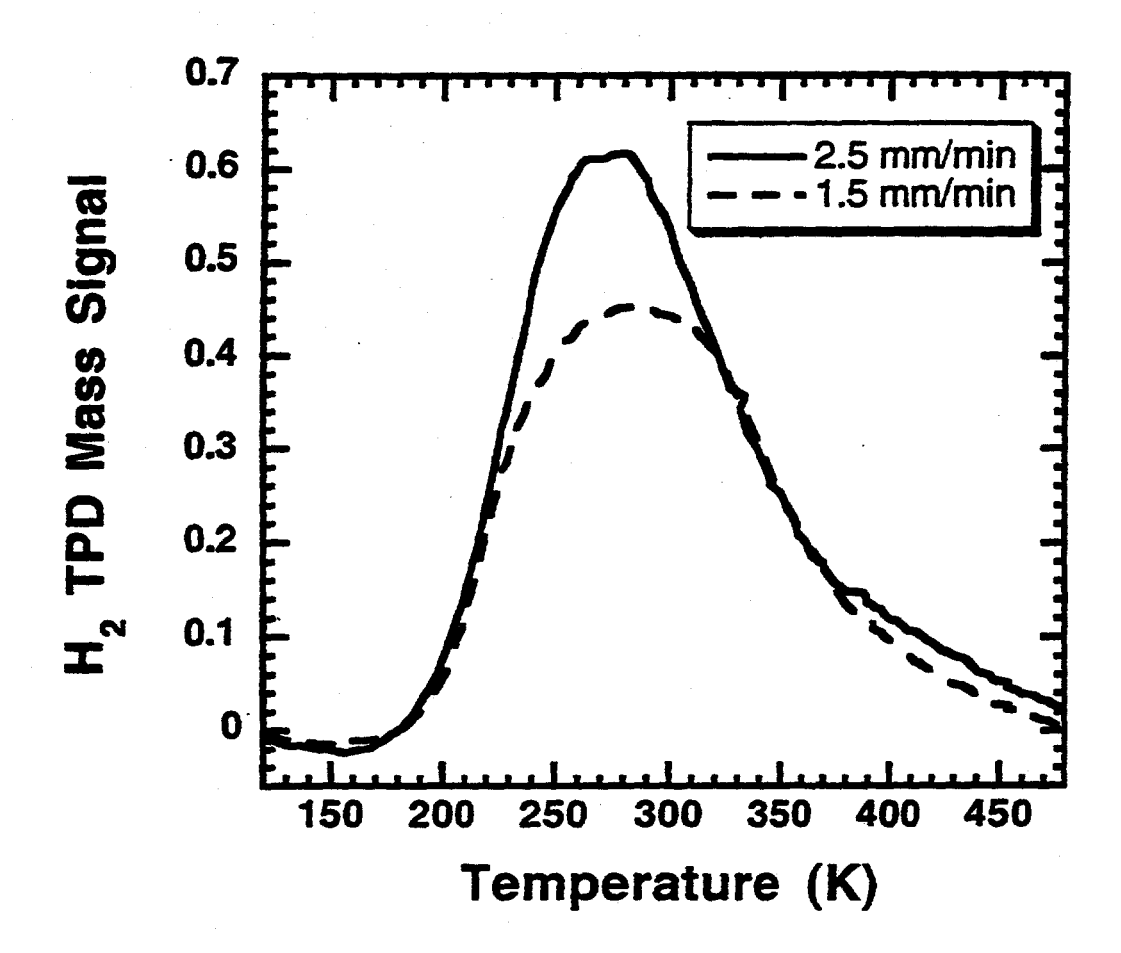


Figure 11: Hydrogen TPD spectra following exposures to 300 torr H₂ for 10 min at 273 K and 3 min at 223 K, followed by evacuation of the chamber with the sample at 223 K for carbon soots produced at 1.5 mm/min and 2.5 mm/min.

References

Ajayan, P. M. (1995). "Aligned Carbon Nanotubes in a Thin Polymer Film." Advanced Materials 7: 489.

Ajayan, P. M., T. W. Ebbesen, T. Ichihashi, S. Iijima, K. Tanigaki and H. Hiura (1993). "Opening carbon nanotubes with oxygen and implications for filling." *Nature* 362: 522.

Bethune, D. S., C.-H. Kiang, M. S. d. Vries, G. Gorman, R. Savoy, J. Vasquez and R. Beyers (1993). "Cobalt-catalyzed growth of carbon nanotubes with single-atomic-layer walls." *Nature* 363: 605.

Breck, D. W. (1974). Zeolite Molecular Sieves: Structure, Chemistry and Use. New York, Wiley.

Cabrera, A. L. (1993). "Studies of Hydrogen Desorption from Cobalt Surfaces." Journal of Vacuum Science and Technology A 11: 205.

Cannon, J. S. (1995). Harnessing Hydrogen. New York, INFORM, Inc.

Carpetis, C. and W. Peschka (1980). "A Study of Hydrogen Storage by Use of Cryoadsorbents." Int. J. Hydrogen Energy 5: 539-554.

Chelliah, H. K. (1996). Combustion and Flame 104: 81.

de Heer, W. A., W. S. Bacsa, T. Chatelain, R. Gerfin, R. Humphry-Baker, L. Forro and D. Ugarte (1995). "Aligned Carbon Nanotube Films: Production and Optical Electronic Properties." *Science* 268: 845.

Dillon, A. C., T. A. Bekkedahl, A. F. Cahill, K. M. Jones and M. J. Heben (1995). <u>Carbon Nanotube Materials for Hydrogen Storage</u>. Proceedings of the U.S. DOE Hydrogen Program Review, Coral Gables, FL.

Dillon, A. C., T. A. Bekkedahl, K. M. Jones and M. J. Heben (1996). <u>The Oxidative Opening and Filling by Hydrogen of Single Wall Carbon Nanotubes</u>. Recent Advances in the Physics and Chemistry of Fullerenes and Related Materials, Los Angeles, CA, Electrochemistry Society.

Dillon, A. C., K. M. Jones and M. J. Heben (in preparation):

Dillon, A. C., K. M. Jones, T. A. Bekkedahl, C. H. Kiang, D. S. Bethune and M. J. Heben "Evidence for Capillary Condensation of Hydrogen in Single-Shell Carbon Nanotubes." (Submitted to Nature).

Ernst, K. H., E. S. Schwarz and K. Christmann (1994). "The interaction of hydrogen with a Cobalt (1010) surface." J. Chem. Phys. 101: 5388.

Flavin, C. and N. Lessen (1994). Power Surge. New York, W.W. Norton & Co.

George, S. M. (1986). Journal of Vacuum Science and Technology A 4: 2394.

Gregg, S. J. and K. S. W. Sing (1982). Adsorption. Surface Area and Porosity. London, Academic Press.

Guo, T., P. Nikolaev, A. Thess, D. T. Colbert and R. E. Smalley (1995). "Catalytic growth of single-walled nanotubes by laser vaporization." Chemical Physics Letters 243: 49-54.

Heben, M. J. (1993). <u>Carbon Nanotubules for Hydrogen Storage</u>. Proceedings of the 1993 DOE/NREL Hydrogen Program Review, Cocoa Beach, FL.

Heben, M. J., T. A. Bekkedahl, D. L. Schulz, K. M. Jones, A. C. Dillon, C. J. Curtis, C. Bingham, J. R. Pitts, et al. (1996). <u>Production of Single-Wall Carbon Nanotubes using Concentrated Sunlight</u>. Recent Advances in the Physics and Chemistry of Fullerenes and Related Materials, Los Angeles, CA, Electrochemistry Society.

Iijima, S. and T. Ichihashi (1993). "Single Shell Carbon Nanotubes of 1 nm Diameter." Nature 363: 603.

Lisowski, W. (1989). "The Kinetics of the low-temperature hydrogen interaction with polycrystalline cobalt films." Applied Surface Science 37: 272.

N.E.S. (1991/1992). "National Energy Strategy."

Pace, E. L. and A. R. Siebert (1959). "Heat of adsorption of Parahydrogen and orthodeuterium on graphon." *Journal of Physical Chemistry* 63: 1398.

Pederson, M. R. and J. Q. Broughton (1992). "Nanocapillarity in Fullerene Tubules." Physical Review Letters 69: 2689.

Schwarz, J. A. (1). <u>Modification Assisted Cold Storage (MACS)</u>. contract report to Brookhaven National Laboratories, contract # 186193-S.

Schwarz, J. A. (1993). <u>Activated Carbon Based Storage System</u>. Proceedings of the 1993 DOE/NREL Hydrogen Program Review, Cocoa Beach, FL.

Hydrogen transport and storage in engineered microspheres*

Glenn Rambach
Lawrence Livermore National Laboratory
Livermore, CA 94550
and
Charles Hendricks
W.J. Schafer Associates
Livermore, CA 94550

Approach

This project is a collaboration between Lawrence Livermore National Laboratory (LLNL) and W.J. Schafer Associates (WJSA). We plan to experimentally verify the performance characteristics of engineered glass microspheres that are relevant to the storage and transport of hydrogen for energy applications. We will identify the specific advantages of hydrogen transport by microspheres, analyze the infrastructure implications and requirements, and experimentally measure their performance characteristics in realistic, bulk storage situations.

Past results

Our model analysis has previously shown that beds of glass microspheres of approximately 50 µm diameter can store pressurized hydrogen at 14% mass fraction and 10 kg_{HZ}/m³ storage densities when the spheres are pressurized to 24.82 MPa. At 62.05 MPa, a bed of glass microspheres can store hydrogen at 20 kg_{HZ}/m³, with a small reduction of mass fraction to about 10%. The geometry and dimensions for the microspheres anticipated in this project are shown in Figure 1. The microspheres can be filled by heating them to increase the glass permeability to hydrogen. Permeability is a strong function of temperature. For the spheres described above, the filling time constant can decrease from thousands of hours to tens of minutes as the temperature increases from 20C to 300C. The release of hydrogen occurs by reheating the spheres to again increase the permeability.

Current year results

Microsphere production:

W. J. Schafer Associates (WJSA) has designed and fabricated a two-stage microsphere production facility. The original LLNL process developed to produce advanced glass microspheres required several physical processes to occur serially in one vertical column. First, aqueous glass forming materials is ejected from a Rayleigh-Taylor droplet generator at several thousand droplets per second. The droplets in the resultant stream all contain the same total mass and mixture fraction of glass forming materials. The stream falls through a section of drying furnace where the water is rapidly evaporated. The resulting stream of sphere precursors then falls through a high temperature furnace section where the glass is formed. The gases that evolve during glass formation force a bubble to be

formed within the molten glass of each sphere. Following the bubble formation section, the spheres fall through a low temperature section, quenching the formation process at a high quality microsphere. Since all the identical droplets pass through identical time-temperature histories, all the microspheres produced have almost identical material and geometric properties.

In the two-stage process, two vertical towers are used. The first tower is dedicated to producing large quantities of droplets, each with the same mass and aqueous mix of glass forming materials. They are collected and frozen by dropping them into liquid nitrogen. The droplets are then vacuum dried to remove the water. The resulting microsphere precursors are then dropped into the second tower furnace and blown into microspheres.

At WJSA, dry precursor particles for glass microshells have been produced. They have also introduced some of the precursors into the high temperature (1500 C), vertical tube furnace and produced glass shells from the precursor particles. These preliminary test results substantiate their plans and calculations with regard to the production of glass microspheres from uniform-mass precursor particles of the glass forming components. It is anticipated that this method will be helpful in making milliliter size batches of microspheres for experimentation.

As the process becomes routine, a wide variety of glass microsphere compositions will be tested for hydrogen permeability, hoop-stress limits and crush pressure limits, shell surface and wall quality and freedom from micro-cracks.

Test facility:

A pressure-volume-temperature (P-V-T) system to control and measure the fill and release rates of small beds of microspheres has been designed (Figure 2.). Hydrogen will be provided at pressures up to 8500 psi into a temperature-controlled chamber. Temperatures can be controlled from 20C to 350C. Hydrogen will be provided from a prepressurized cylinder rated for 30,000 psi operation. A preheater volume and valve will permit the sequential process of heating the spheres in the absence of high pressure hydrogen, then exposing them to the preheated high pressure hydrogen. A programmable temperature controller will control heating rate and temperature. This will, for the first time, permit an accurate measurement of the hydrogen uptake rates by the spheres for a given temperature. The system will be operated at a location at LLNL which is rated for high pressure hydrogen operation.

The hardware for the system has been received, the safety review for the experiment is complete, and it is anticipated that the experimental setup will be complete during the fourth quarter of FY 1996.

Microsphere crush experiments:

During normal, future filling operations, microsphere bed loading will be accomplished by exposing heated microspheres to heated hydrogen. The increased permeability of the glass permits rapid loading of the spheres to the external pressure. When the temperature is

reduced to room temperature, the permeability decrease "traps" the hydrogen in the spheres. Since the spheres are thin shells, it is expected that the upper limit of external pressure to which they can be exposed is determined by the elastic buckling limit for thin shells¹:

$$P_b = \frac{8E}{(d/t)\sqrt{3(1-v^2)}}$$

Where P_b is the expected pressure limit for buckling failure, E is Young's modulus for the glass, v is Poisson's ratio for the glass, d is the sphere diameter and t is the sphere wall thickness. Failure from elastic buckling (crush) will occur at pressure differentials that are lower than for shell failures from reaching the compressive stress limit of the material.

The statistics of crush failure were measured for a batch of 45- μ m-diameter glass microspheres. 200 microspheres were divided into 20 samples. Each sample was exposed to an over pressure of nitrogen, successively increasing the pressure for each sample. The number of failed spheres was counted for each sample. The spheres had a wall thickness of about 0.9 μ m. With a Young's modulus expected at $9x10^6$ lb/in², and a Poisson's ratio expected to be 0.22, the maximum pressure for buckling failure of these spheres would be 17,000 psi.

Figure 3 shows fraction of failure for each sample. As shown, significant failures do not occur until 8,000 psi differential is applied to the samples, with an upper limit of approximately 16,000 psi. This is for room temperature over pressure. For the temperatures to be used in loading microspheres, E should only be reduced by 10 -15%. Hence, for the microspheres tested in this experiment, a constant differential over pressure of 6000 psi would not result in significant failure of spheres.

Plans for future work

The properties relevant to large-bed-transportation applications, of the best, currently producible, glass microspheres will be experimentally measured. While the crush statistics measurements were performed in a relatively simple pressure chamber using room temperature nitrogen, Performance related to hydrogen filling and discharging of microspheres requires the more complex, high temperature pressure chamber, rated for high temperature hydrogen use.

The measurements of hydrogen filling and discharging performance will be used to validate and enhance the density and kinetic model recently developed for microsphere hydrogen storage beds. We will then identify and implement the best possible material and process modifications to improve charge/discharge kinetics and minimize cycle energy requirements. Once the best material and process is identified, the methodology for scale up of the microsphere fabrication process for industrial and commercial use will be developed.

The batch handling characteristics of microspheres delivered by WJSA will be studied for

pour behavior and fracture resistance. We will measure the crush statistics of sphere bed sample and compare the measurements to the predicted values from sphere strength model. We will also evaluate durability of the spheres in a bed configuration and study surface-surface and point loading effects. The effects of handling, vibration, pouring, etc. on the survival of microspheres in protobeds will be part of this phase. The packing fraction for monodispersions will also be measured.

With the P-V-T cell we will study the property effects by comparison of microspheres made from 3 to 5 different glass formulations. Additionally, at least two different aspect ratios (diameter-to-membrane thickness) will be studied. The properties that will be measured will be: the charge/discharge kinetics vs temperature and materials, the storage density, the burst and crush statistics, and the strength vs. surface quality relationship.

We will perform a sensitivity analysis relating commercial and economic factors to microsphere physical properties. The loading temperature vs. time, and storage density and hydrogen mass fraction will be the metrics. Cost projection for tonnage quantities of glass microspheres will be done as part of an economic assessment for microsphere hydrogen transport.

An experimental safety study will be done to evaluate realistic issues such as: rapid decompression of a packed bed, flame propagation and flammability limits, pressure failure propagation, cycle life, safety factor, burst failure relationships, and the physical powder nature of normal and fractured microspheres associated with respiration.

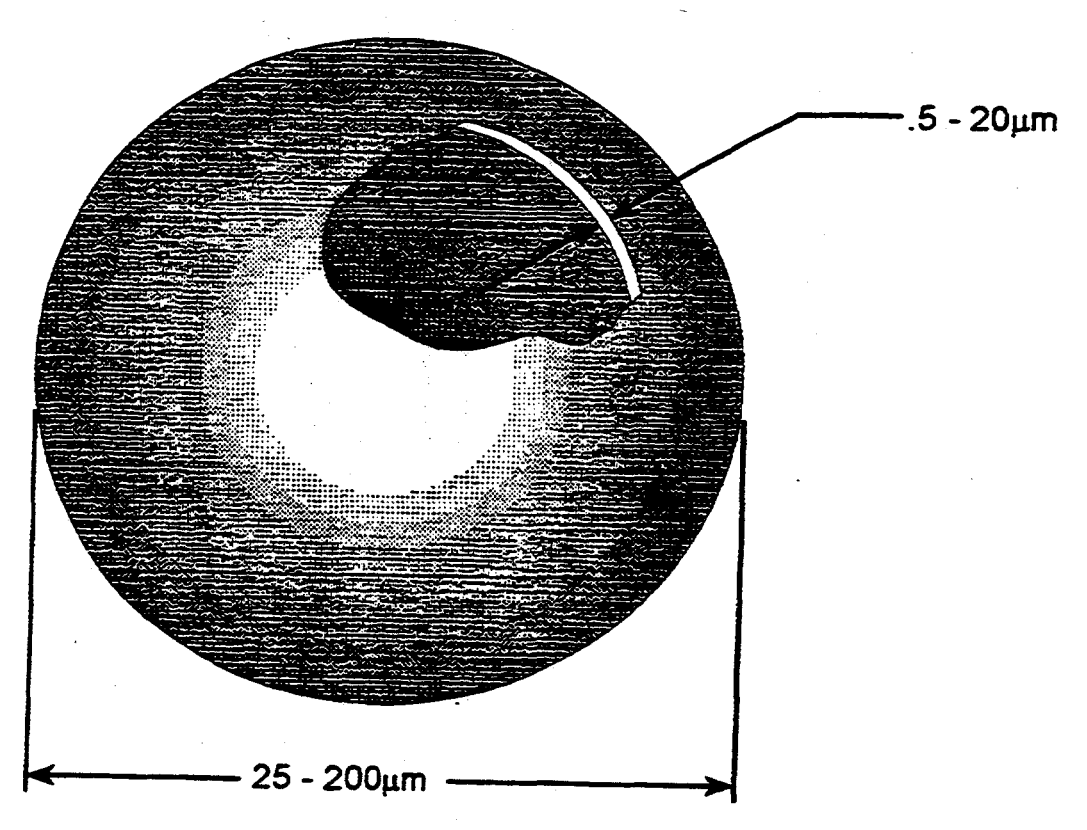
WJSA will then design and fabricate glass microsphere generator for high rate production, and produce several liters of best, current glass microspheres. Periodic quality checks will be done to assure uniformity.

1. Woerner, R. L., Weinstein, B. W., Moen, I. M., and Rittman, J. G. 1979. Working Strengths and D-T Fill Procedures for Glass Microsphere Laser Fusion Targets, Technical Report UCRL-82728, Lawrence National Laboratory, Livermore.

^{*}This work performed under the auspices of the U. S. Department of Energy by the Lawrence Livermore National Laboratory under contract No. W-7405-ENG-48.

Figures

- 1. The expected ranges of microsphere diameters and membrane thicknesses that will be tested in this experimental project.
- 2. The experimental setup that will be used to measure the charge and discharge rates and hydrogen storage densities for batches of glass microspheres.
- 3. Experimental crush pressure failure probability for a batch of glass microspheres. Each data point represents the fraction of glass microspheres that failed when the small batch was exposed to a specific external pressure.



 μm diameter glass spheres with 1 μm thick membrane walls can contain H_2 at 410 bar with a 1.5 factor of safety

Figure 1.

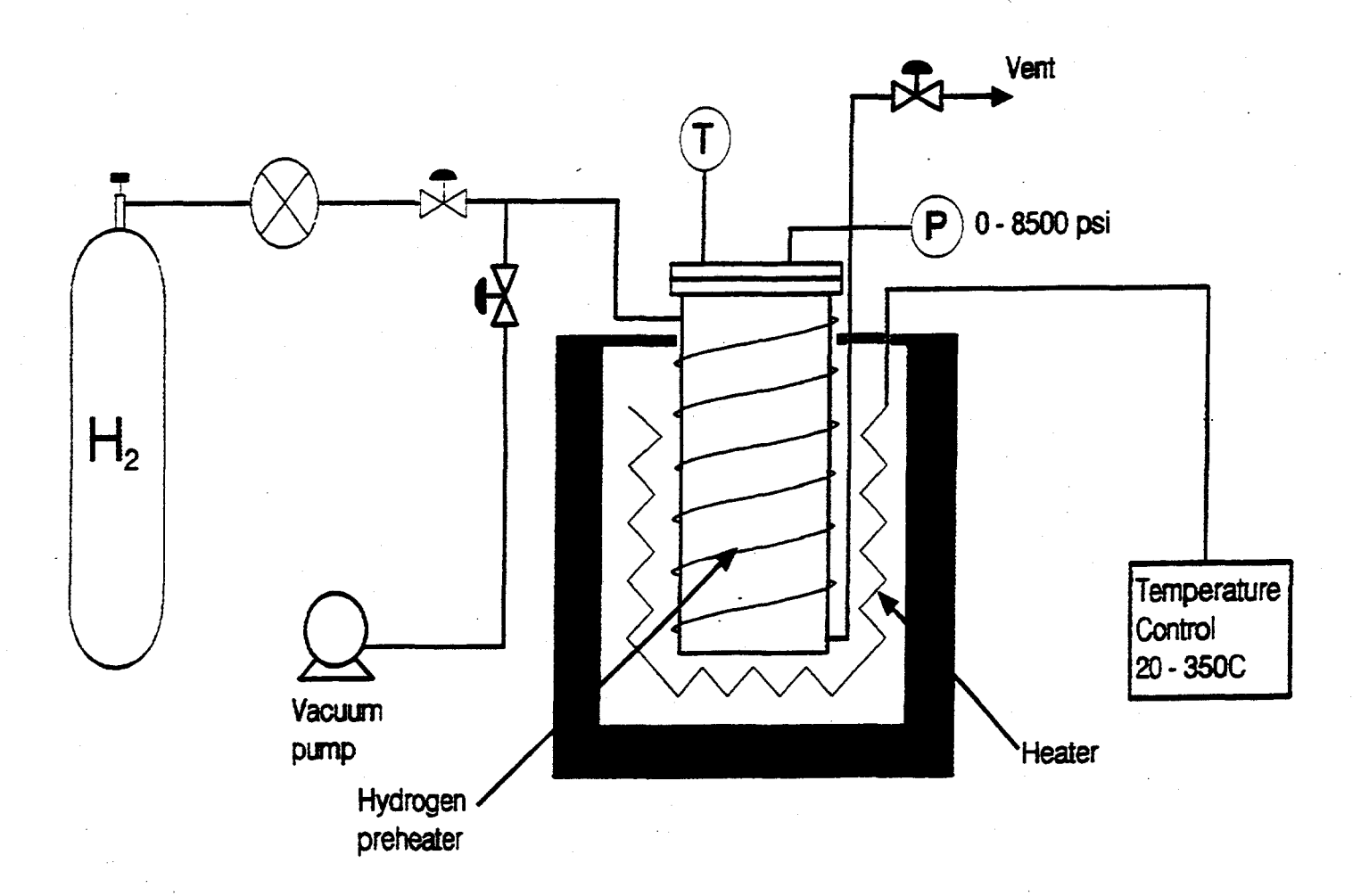


Figure 2.

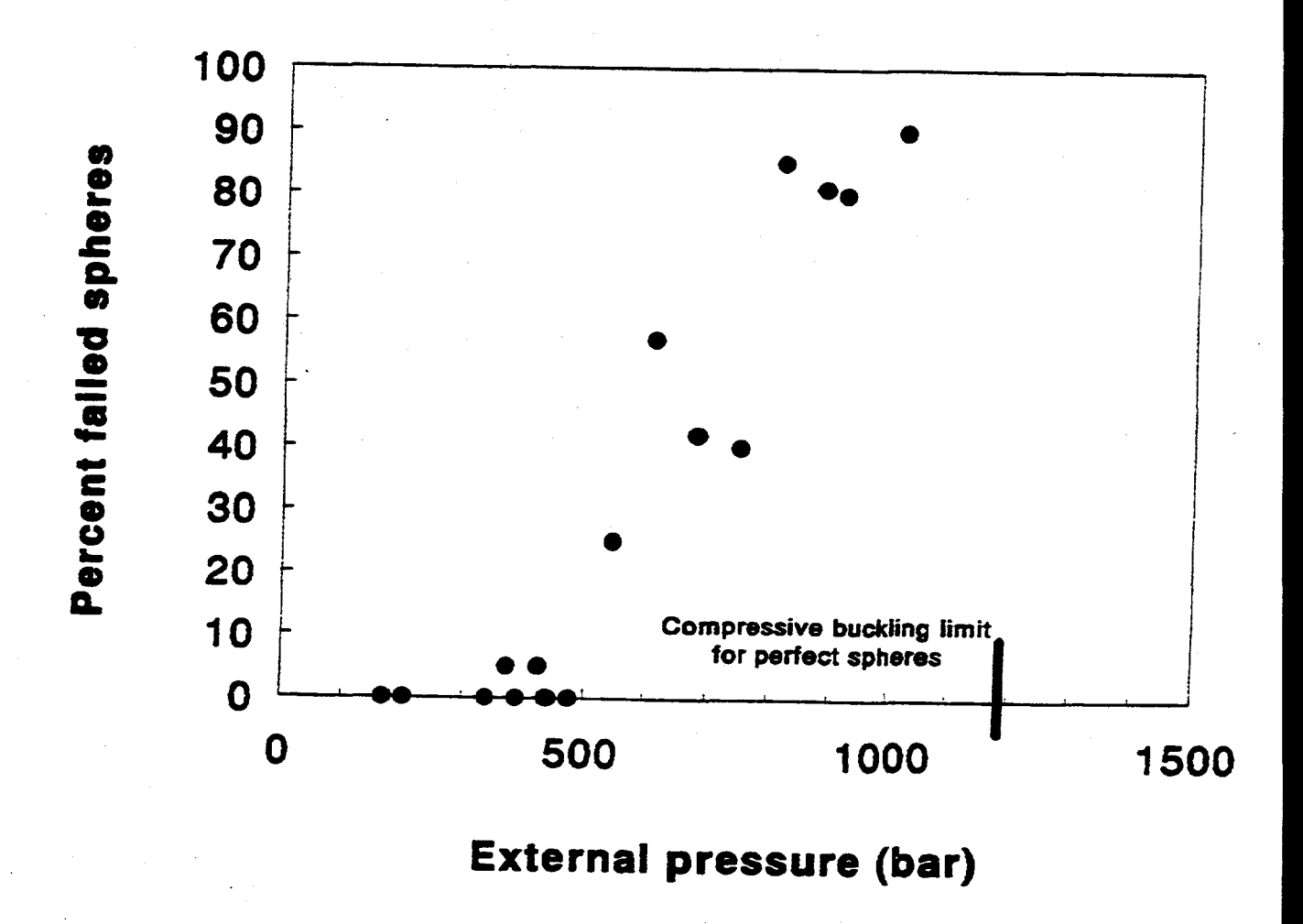


Figure 3.

HYDROGEN STORAGE AND DELIVERY SYSTEM DEVELOPMENT: FABRICATION

J. L. Handrock, M. E. Malinowski, and K. Wally Sandia National Laboratories Livermore, CA 94550

Abstract

Hydrogen storage and delivery is an important element in effective hydrogen utilization for energy applications and is an important part of the FY1994-1998 Hydrogen Program Implementation Plan. This project is part of the Field Work Proposal entitled Hydrogen Utilization in Internal Combustion Engines (ICE). The goal of the Hydrogen Storage and Delivery System Development Project is to expand the state-of-the-art of hydrogen storage and delivery system design and development. At the foundation of this activity is the development of both analytical and experimental evaluation platforms. These tools provide the basis for an integrated approach for coupling hydrogen storage and delivery technology to the operating characteristics of potential hydrogen energy use applications.

Analytical models have been developed for internal combustion engine (ICE) hybrid and fuel cell driven vehicles. The dependence of hydride storage system weight and energy use efficiency on engine brake efficiency and exhaust temperature for ICE hybrid vehicle applications is examined. Results show that while storage system weight decreases with increasing engine brake efficiency energy use efficiency remains relatively unchanged. The development, capability, and use of a newly developed fuel cell vehicle hydride storage system model will also be discussed. As an example of model use power distribution and control for a simulated driving cycle is presented. An experimental test facility, the Hydride Bed Testing Laboratory (HBTL) has been designed and fabricated. The development of this facility and its use in storage system development will be reviewed. These two capabilities (analytical and experimental) form the basis of an integrated approach to storage system design and development. The initial focus of these activities has been on hydride utilization for vehicular applications. A conceptual design for a hydride storage system for the Renewable Hydrogen Transportation System Project (Palm Desert) and continuing ICE storage system development work will be presented.

Introduction

Project Approach/Rationale

Hydrogen storage and delivery is an important element in effective hydrogen utilization for energy applications and is an important part of the FY1994-1998 Hydrogen Program Implementation Plan. This project is part of the Field Work Proposal entitled Hydrogen Utilization in Internal Combustion Engines (ICE). (See related DOE Hydrogen Program Review papers for additional programmatic activity discussions.) The goal of the Hydrogen Storage and Delivery System Development Project is to expand the state-of-the-art of hydrogen storage and delivery system design and development. At the foundation of this activity is the development of both analytical and experimental evaluation platforms. These tools provide the basis for an integrated approach for coupling hydrogen storage and delivery technology to the operating characteristics of potential hydrogen energy use applications.

In the previous programmatic year a steady state model was developed which integrated ICE and storage material characteristics into the design of light weight hydride storage and delivery systems (Handrock 1995). This activity was pursued in parallel with the light weight hydride material development work being conducted as part of the ICE Hydrogen Utilization program (Thomas 1995). An investigation was completed regarding future hydride material property improvements necessary to make light weight hydride utilization feasible in high efficiency leanburn ICE's.

In the current year modeling activities were expanded upon and an experimental test facility was built. In addition, hydrogen storage and delivery systems development activities were initiated/continued for two specific applications. In the first, low temperature hydride delivery systems are being developed for fuel cell vehicles as part of the Renewable Hydrogen Transportation System Program (Palm Desert). The Palm Desert program consists of a consortium headed by the Schatz Energy Research Center (SERC) whose goal is to develop a clean and sustainable transportation system for the city of Palm Desert. This program will demonstrate the practical utilization of hydrogen as a transportation fuel. Fuel cell powered public utility vehicles (PUV's) and neighborhood electric vehicles (NEV's) will be designed, built and tested. In the second application a light weight hydride delivery system is being developed for the Hydrogen Utilization in ICE's program. In this program hydrogen powered ICE's are integrated into a hybrid vehicle.

In summary, the four key parts of the Hydrogen Storage and Delivery System Development project are:

- 1. Analytical Evaluation Platform
- 2. Experimental Evaluation Platform
- 3. Fuel Cell Vehicle Delivery System
- 4. Internal Combustion Engine Vehicle Delivery System

These four separate, but related, goals provide the basis for an integrated approach for coupling hydrogen storage and delivery technology to the operating characteristics of potential hydrogen energy use applications. This integrated approach is crucial to the effective utilization of hydrogen in energy applications. The progress in these four areas will be discussed in the following section.

Discussion of Results

During the current program year the following key activities were completed.

- 1. ICE/hydride storage system parametric study.
- 2. Development of a fuel cell vehicle analytical model.
- 3. Design and fabrication of Hydride Bed Testing Laboratory (HBTL).
- 4. Initiated design of hydride storage system for fuel cell vehicle (PUV).
- 5. Investigation of hydride powder immobilization techniques.

These results will be discussed in relation to the four programmatic focus areas outlined in the Introduction section of this report.

1. Analytical Evaluation Platform

Hydrides have the potential for storing hydrogen in a safe, efficient, and economical manner for a variety of applications (Robinson 1994). The most commonly used hydrides are those which operate at or near room temperature (DeLuchi 1989). These materials have a relatively low heat of formation. Chemical bond characteristics of stable light weight hydrides (> 3 wt % hydrogen) are typically accompanied by elevated operating temperatures and large heats of reaction. These energy needs are in conflict with traditional operating characteristics of proposed high efficiency engines, requiring some form of supplemental heating (Hoffman 1976).

In the previous programmatic year a steady state model was developed which integrated engine and storage material characteristics in the design of light weight hydride (> 3 wt % hydrogen) storage and delivery systems (Handrock 1995). A schematic of the model is shown in Figure 1. The model includes individual modules representing the engine, startup and primary hydride beds, heat exchangers, and a burner. Energy and hydrogen mass flow balance were used as the means by which individual components in the model were linked together analytically. Modeling of the hydride material includes representation of such items as hydrogen/hydride weight fraction, reaction enthalpy, operating temperature, pressure-composition-temperature (PCT) hydrogen availability, packing density and specific heat. Material properties of the hydride container were also included to allow modeling of the hydride bed as an integral unit. In the current year this model was used to expand upon previously completed work regarding the effects of hydride operating temperature and heat of formation on system weight and energy use efficiency.

ICE Hybrid Vehicle Storage Studies

Hydrogen storage system weight and energy use efficiency were investigated for an internal combustion engine hybrid vehicle. The performance of several different hydride materials were examined over a range of engine brake efficiencies for two different engine exhaust temperatures. In each case the hybrid vehicle design performance consisted of 10k W average power and a 483 km (300 mile) range. In Figure 2 system weight is seen to decrease with increasing engine efficiency and exhaust temperature. For light weight hydrides (e.g., Mg based) the hydrogen storage system weight has the potential to be significantly less than that of low temperature hydride systems (e.g., FeTi). A 10% system weight reduction is exhibited by an

increase in exhaust temperature from 300 C to 400 C. A further 20% reduction in system weight results from an increase in brake efficiency from 32% to 42. (Engine operation of about 40% brake efficiency has been demonstrated (Van Blarigan 1996).)

Energy use efficiency is the ratio of hydrogen delivered to the engine versus total hydrogen energy availability. (Typically some hydrogen is needed for supplemental bed heating and is therefore lost.) As indicated in Figure 3 energy use efficiency is relatively insensitive to engine brake efficiency. As engine efficiency increases there is less waste heat available to drive hydrogen off the hydride bed, thereby increasing parasitic hydrogen use requirements. However, as engine efficiency increases there is also a reduction in overall hydrogen demand, thereby decreasing heat of formation energy requirements. These two factors tend to be selfcompensating. From an engineering design viewpoint this means that once a hydride alloy is selected hydrogen energy use efficiency will be relatively unaffected by changes in engine brake efficiency. This knowledge eases storage system sizing in the early stages of the design process. Figure 3 also shows that as exhaust temperature increases and hydride heat of formation decreases the hydrogen energy use efficiency increases. At an exhaust temperature of 400 C a system developed with Alloy SNL has a hydrogen energy use efficiency of unity over an engine brake efficiency range of 32% to 40%. (Alloy SNL is a Mg based Sandia developed alloy with a heat of formation and operating temperature less than that of traditional Mg2Ni (Handrock 1995, Thomas 1995).) Under these conditions available waste heat is sufficient to operate the hydride bed, eliminating the need for supplemental heating.

Fuel Cell Vehicle Storage System Models

The ICE hydride storage and delivery system model was expanded to provide a more generalized evaluation capability. Program coding was moved from a spreadsheet based platform to a compilable subroutine structure. This modification simplified the linking of modules and improved physical modeling capability, code documentation, and results presentation. Model components were represented via individual modules, which were linked together based upon energy/mass balance relationships. Upon assembling the necessary modules to form a desired system representation the user specifies drive power requirements as a function of time and component design characteristics (efficiencies, etc.). The model then calculates component and system operating characteristics, such as power distribution, fluid temperatures and mass flow rates, and operating duration.

The first application of this expanded modeling capability was a fuel cell vehicle model for the Palm Desert program. Figure 4 provides a schematic of the pressurized gas version of the model. Primary components include fuel cell, hydrogen pressure vessel, recirculation tank, circulation pump, heat exchangers, air blower, battery, parasitic loads, and power logic controller. These modules allow performance characteristics of the vehicle to be evaluated under a variety of operating conditions. For example, the power logic controller module controls the distribution of power between the fuel cell and battery based upon drive and parasitic power requirements. Figure 5 represents fuel cell and battery power response to a simulated vehicle drive cycle. Initially the fuel cell is able to meet total power requirements (drive power plus parasitic power (300 W) requirements). When the total power requirement exceeds the 4000 W capability of the fuel cell the battery acts a supplemental power supply. When the total power requirement drops below the fuel cell capability the fuel cell remains a full power until the battery has been recharged. Upon completion of battery recharging the fuel cell power output drops to that level necessary to meet current total power requirements.

This model was completed in collaboration with the Schatz Energy Research Center (SERC). SERC has provided Sandia with fuel cell heat generation data from both dynamometer and road test simulations for pressurized gas operation. This information is being used for initial model calibration. A sample of preliminary calibration results are given in Figure 6. Shown are fuel

cell fluid (water) inlet and exit temperatures at various fuel cell idle speeds, assumed fuel cell heat capacities, and ambient temperatures. As expected, fuel cell temperatures increase with fuel cell power, ambient temperature and decrease in fuel cell specific heat. Under the prescribed conditions the model predicts the general increases in temperature with fuel cell power and differences between inlet and exit temperatures, but under predicts absolute temperature values, especially at higher power levels. These results indicate further refinement is needed in the fuel cell heating and/or heat exchanger portions of the model. Sandia is working in collaboration with SERC to establish what additional test data are required to allow necessary refinement of individual model components. Development of a calibrated pressurized gas model will allow performance predictions of a fuel cell vehicle - hydride storage system to be made in support of the Palm Desert program. Figure 7 shows a schematic of the fuel cell vehicle - hydride storage system model. The pressurized gas vessel has been replaced with a hydride bed. An additional heat exchanger has been placed in the recirculation loop to allow maintenance of bed temperatures during gas delivery. The additional modules necessary for this model have already been developed.

2. Experimental Evaluation Platform

A Hydride Bed Testing Laboratory (HBTL) has been designed and constructed. A simplified schematic of the facility is shown in Figure 8. This facility will be used in conjunction with analytical modeling for the evaluation of hydrogen storage and delivery systems. Bed design and construction will be integrated with hydride material properties to reduce weight and volume, and therefore enhance system performance. The system will be used to simulate metal hydride bed operation, including delivery (dehydriding) and refueling (hydriding). Hydride properties, such as thermal conductivity and hydrogen kinetics, will be measured.

The HBTL consists of a medium pressure (1.72 MPa (250 psia) maximum) hydrogen manifold, with provisions for measuring input and output bed flows via a LabView® based data acquisition system. Instrumentation includes thermocouples, mass flow meters, pressure gauges and computer control. Leak checking of all system components is underway, and initial testing of the entire system has been started. Bed testing, using a 200 liter capacity, commercially available bed, will begin once system leak checking has been completed. Fuel cell hydrogen demand will be simulated by a programmable mass flow controller, allowing simulation of vehicle driving cycles. The entire system is interfaced with a vacuum system containing a residual gas analyzer, used for leak checking and real-time gas sampling.

The current system layout was configured to support the testing of metal hydride beds for the Palm Desert program. Being modular in nature, the HBTL can be easily modified to accommodate a variety of hydrogen storage systems. As such, direct coupling of experimental and modeling results can be accomplished to support advanced bed development activities.

3. Fuel Cell Vehicle Delivery System

A near term goal of this project is to design, develop, and fabricate a hydrogen storage and delivery system for the Palm Desert program. System interface and performance requirements have been established in collaboration with the Schatz Energy Research Center (SERC), who is responsible for program coordination and vehicle delivery.

A hydride bed system conceptual design has been completed. A pictorial representation of this design is shown in Figure 9. The bed system consists of nine individual modules, each of which contains commercially available C15 (GfE 1995) metal hydride alloy. The modular design will facilitate fabrication, testing and modification of the bed system. The system has been designed to fit in the space available in the Palm Desert PUV, utilizes existing bed construction technology, and delivers hydrogen to the fuel cell at the required rate (25 slm maximum) and pressure (2 psig minimum). The system will deliver a minimum of 190 grams of hydrogen

assuming a conservative one weight percent usable hydrogen storage capacity in the C15 alloy. The system is to operate between environmental temperatures of 5 C to 70 C and have a refueling time of less than five minutes. Current design activities include finalizing details of the bed control and "cold start" systems.

4. Internal Combustion Engine Vehicle Delivery System

A goal of the ICE Hydrogen Utilization Program is the demonstration of an internal combustion engine/storage/delivery subsystem. As part of the ICE program this project will provide a hydrogen storage and delivery system. However, most effort in this area has been redirected to support the more near-term goal of developing a hydride storage system for the Palm Desert program. One activity that has continued, though, is the investigation of utilizing emulsion derived foams as a means of mitigating the effects of hydride metal break-up.

Hydride beds consist of metal hydride particles located within a containment vessel. Repeated hydriding and dehydriding cycles can cause these particle to break-up into a range of particulate sizes. Under dynamic loading, such as vibration, these particles can segregate, with fine particles settling to the bottom of the vessel and coarse particles migrating to the top. Upon hydriding regions of small particle size (high density) can experience significant swelling and volumetric expansion, resulting in loads being transferred to the container walls. Such loads may be excessive, causing structural failure. Regions containing large (or no) particles will exhibit poor heat transfer conductivity, degrading the performance characteristics of the bed. Typically this problem of particle segregation is addressed by the use of mechanical separators such as wafers or plates. The use of emulsion derived foams eliminates the need for these mechanical separators. The foams can be formed in place from the liquid phase, are exceptionally light (<100 mg/cc) and reside in powder interstitials. As such, they add no significant weight or volume to the system. Such attributes simplify bed design and fabrication, thereby reducing product costs. Sample beds have been fabricated using representative materials from the AB2 and AB5 hydride families. Most notably, FeTi samples were investigated in support of hydride bed development for the Palm Desert program.

Plans for Future Work

Effort in the near term will be focused on the following areas:

- 1. Calibration of fuel cell analytical model. (Complete in collaboration with SERC.) Continue expansion of model.
- 2. Develop and test advanced bed materials and configurations in HBTL.
- 3. Design, develop and test hydride storage systems for the Palm Desert fuel cell vehicles (PUV, NEV).
- 4. Continue hydride immobilization studies.
- 5. Down-selection of storage system type for the ICE/hybrid vehicle demonstration.

These activities are described in more detail below in relation to the four main programmatic focus areas.

1. Analytical Evaluation Platform

Calibration of the fuel cell delivery system analytical model will be completed. The model will be used to assist in hardware design and development for the Palm Desert program. Sandia is working in collaboration with SERC to establish what additional test data are required to allow necessary refinement of individual model components. Development of a calibrated pressurized gas model will allow performance predictions of a fuel cell vehicle - hydride storage system to be made. The additional modules necessary for this model have already been developed.

The current modeling effort will be expanded to allow the performance characteristics of hydride storage systems to be compared against those of other storage systems (activated carbon, liquid, etc.). The structure of the current model was developed in a manner to support this more generalized modeling activity.

2. Experimental Evaluation Platform

Hydrogen operations in the HBTL will be initiated, with activities focused on the development of a hydride delivery system for the Palm Desert program. Medium pressure metal hydride beds will be tested to determine bed characteristics of hydrogen delivery to fuel cells. Hydride bed loading and hydrogen delivery performance will be experimentally determined and compared with theoretical fuel cell vehicle - hydride models. Advanced hydride materials and bed designs will also be investigated.

3. Fuel Cell Vehicle Delivery System

The Palm Desert program has as its near-term deliverable a metal hydride bed/fuel cell power system. Sandia will design, develop and test utility vehicle hydrogen storage and delivery systems to support this activity. The existing conceptual design will be refined, allowing fabrication of prototype hardware. Testing will be completed on the HBTL to establish component and system performance characteristics. A prototype bed will be delivered to SERC for integration into a fuel cell vehicle.

4. Internal Combustion Engine Vehicle Delivery System

A goal of the Hydrogen Utilization ICE program is the illustration of an internal combustion engine/storage/delivery subsystem. As part of this program, a hydrogen delivery system will be developed. The insights gained from the generalized storage system evaluation platform and the investigation of the utilization of light weight hydrides will guide the selection of the storage technology to be utilized. During the upcoming year the down-selection of the storage system type will occur, as will initial design and fabrication activities.

Hydride powder immobilization studies initiated in the previous year will continue. Activities will be directed at demonstrating particle immobilization concepts on full scale prototype hardware. Such a demonstration will lay the groundwork for utilizing the technology in field applications.

References

- DeLuchi, M. A. 1989. "Hydrogen Vehicles: An Evaluation of Fuel Storage, Performance, Safety, Environmental Impacts, and Cost." Int. J. of Hydrogen, Vol. 14, No. 2, pp. 81-130.
- GfE Gesellschaft Fur 1995. "Product Data," Elektrometallurgie MBH, Nurnberg, Germany.
- Handrock, J. L., Wally, K. and Raber, T. N. 1995. "Hydrogen Storage and Delivery System Development," In *Proceedings of DOE Hydrogen Program Review*, 477-491, Coral Gables, FL: Sandia National Laboratories.
- Hoffman, K. C., Reilly, J. J., Salzano, F. J., Waide, C. H., Wiswall, R. H., and Winsche, W. E. 1976. "Metal Hydride Storage for Mobile and Stationary Applications," In *Proceedings of the Society of Automotive Engineers, Fuels and Lubricants Meeting*, 760569. St. Louis, MO: Brookhaven National Laboratory.
- Robinson, S. L. and Handrock, J. L. 1994. Hydrogen Storage for Vehicular Applications: Technology Status and Key Development Areas, Sandia Report SAND94-8229, Livermore, CA: Sandia National Laboratories.
- Thomas, G. J. and Guthrie, S. E. 1995. "Lightweight Hydride Storage Materials," In *Proceedings of DOE Hydrogen Program Review*, 543-550, Coral Gables, FL: Sandia National Laboratories.
- Van Blarigan, P. 1996. "Hydrogen Engine Development: Experimental Program," To Be Published In *Proceedings of DOE Hydrogen Program Review*, Miami, FL: Sandia National Laboratories.

Figure Captions

- Figure 1. ICE Hydride storage model schematic.
- Figure 2. ICE hydride storage system weight versus engine brake efficiency.
- Figure 3. ICE hydrogen use efficiency versus engine brake efficiency.
- Figure 4. Fuel cell vehicle pressurized gas storage model schematic.
- Figure 5. Fuel cell vehicle driving cycle simulation.
- Figure 6. Steady state fuel cell temperatures at low loads.
- Figure 7. Fuel cell vehicle hydride storage model schematic.
- Figure 8. Hydride Bed Testing Laboratory simplified schematic.
- Figure 9. Fuel cell vehicle hydride bed conceptual design.

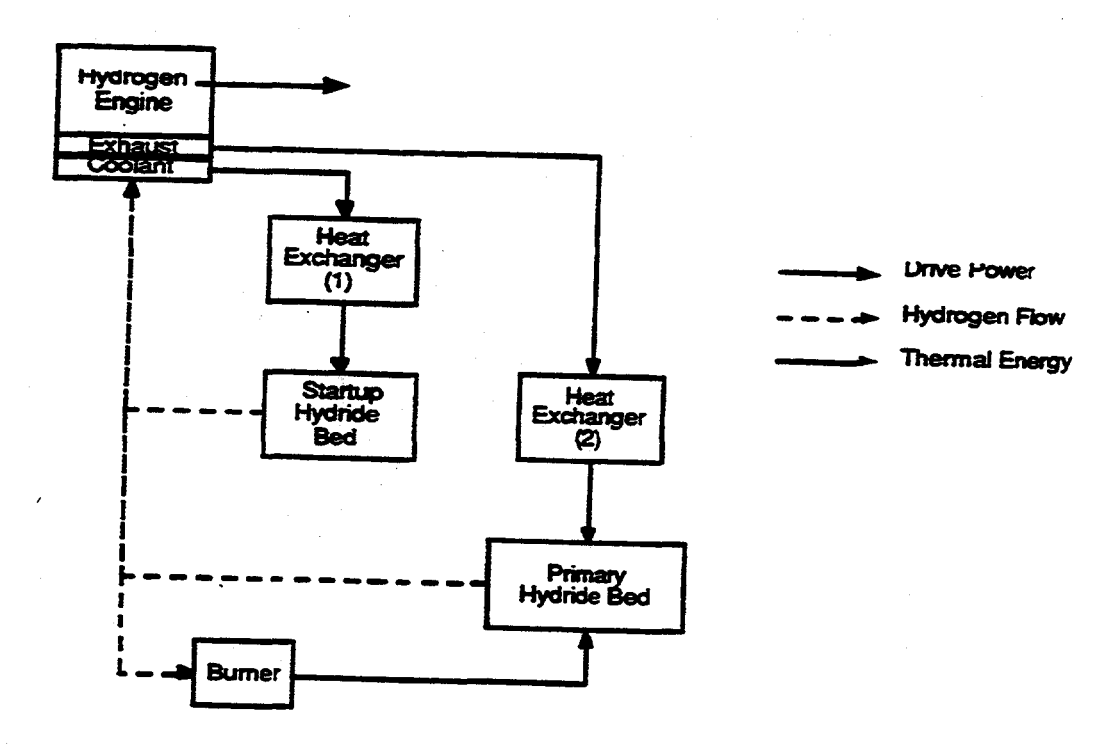


Figure 1. ICE Hydride storage model schematic.

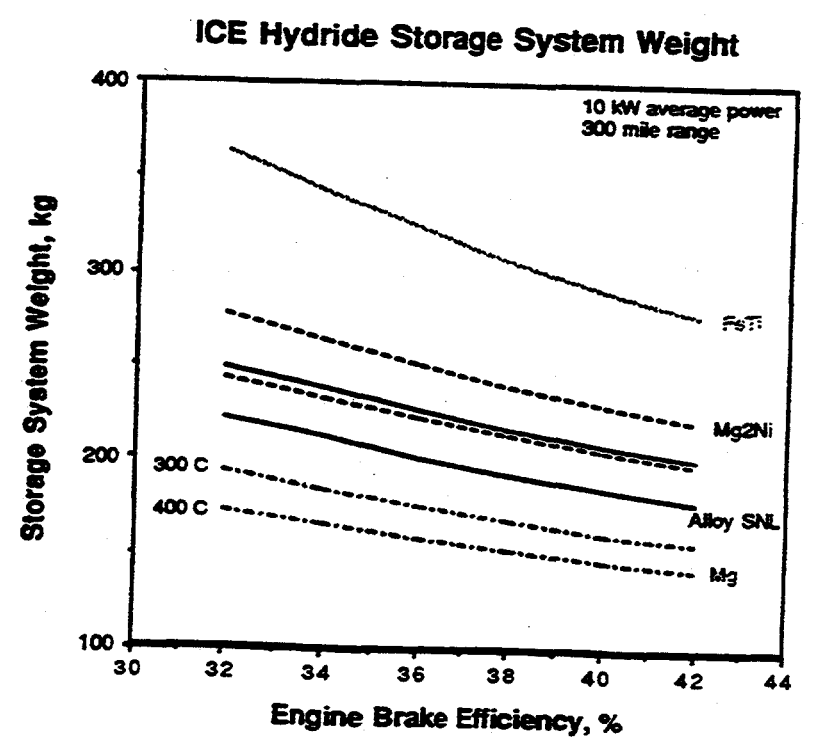


Figure 2. ICE hydride storage system weight versus engine brake efficiency.

ICE Hydrogen Use Efficiency

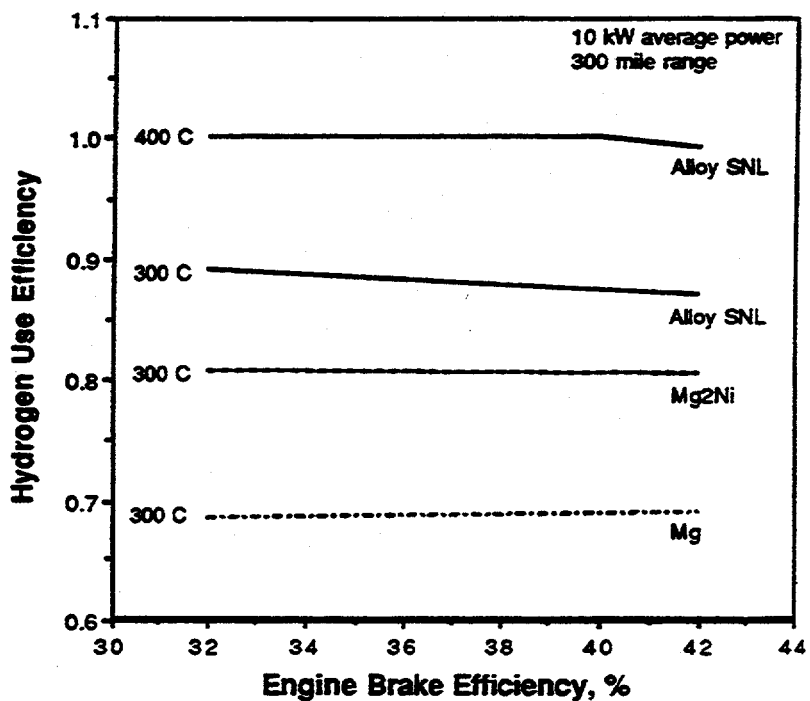


Figure 3. ICE hydrogen use efficiency versus engine brake efficiency.

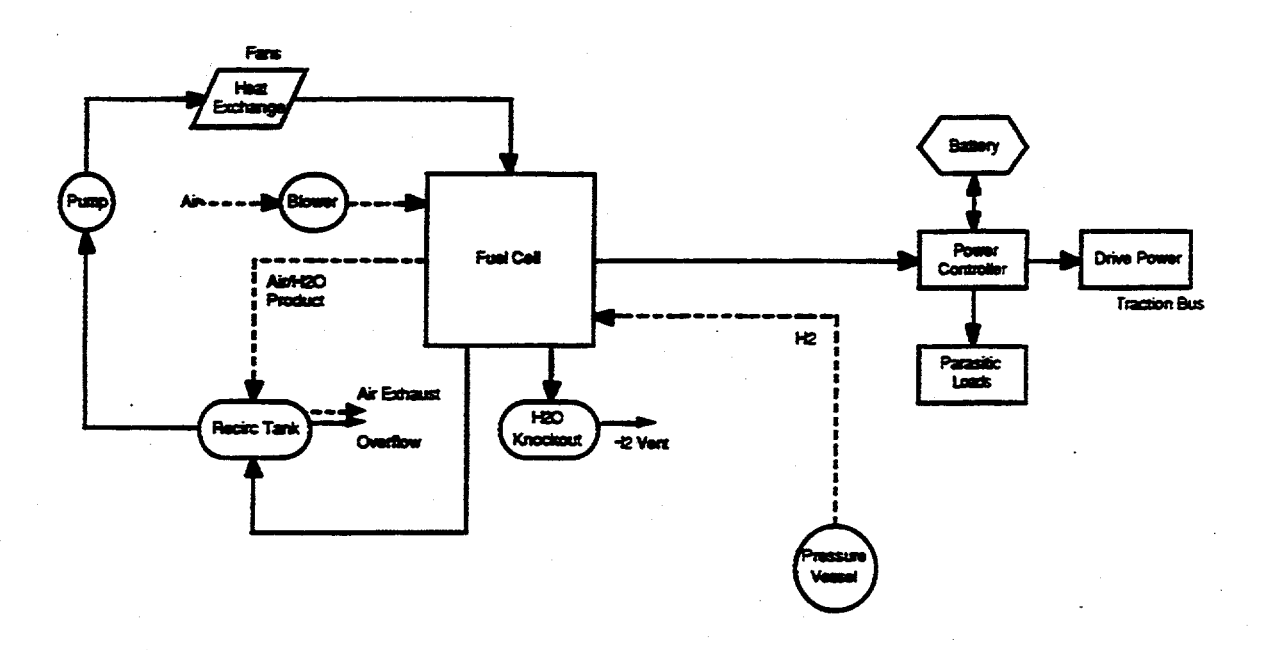


Figure 4. Fuel cell vehicle - pressurized gas storage model schematic.

Fuel Cell Vehicle Simulation Fuel Cell Power Fuel Cell Power Fuel Cell Power James Sec

Figure 5. Fuel cell vehicle driving cycle simulation.

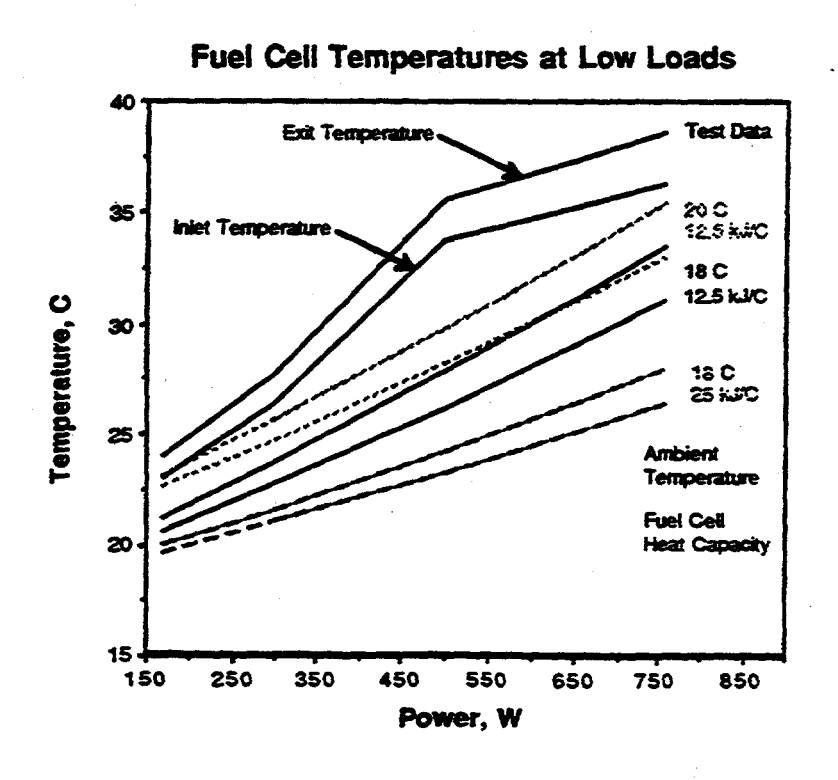


Figure 6. Steady state fuel cell temperatures at low loads.

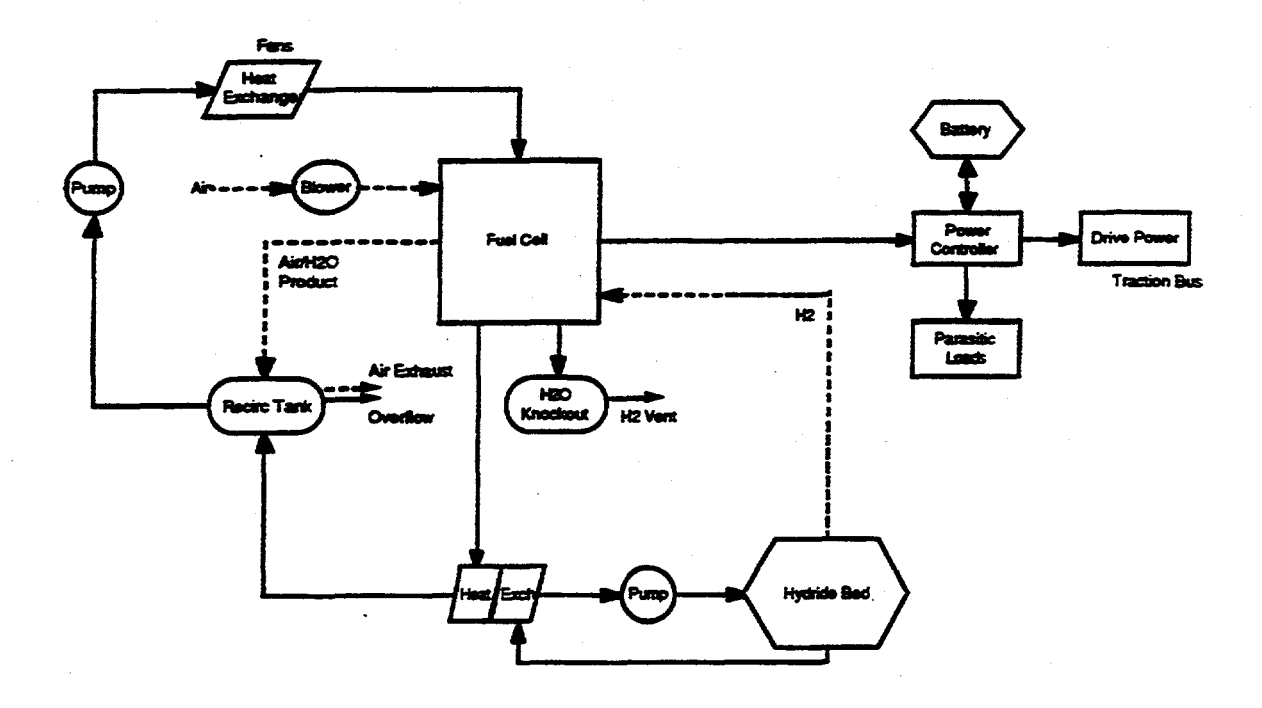


Figure 7. Fuel cell vehicle - hydride storage model schematic.

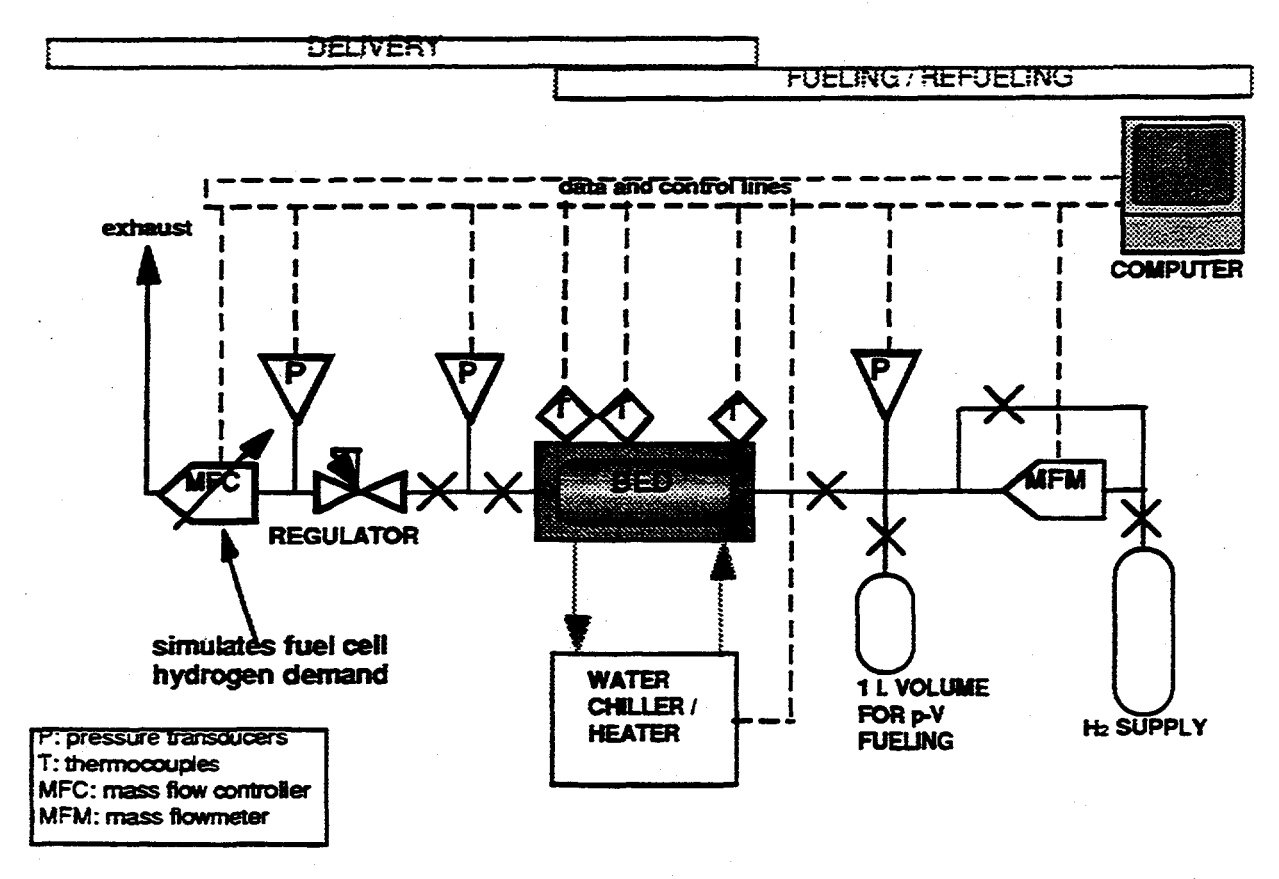


Figure 8. Hydride Bed Testing Laboratory - simplified schematic.

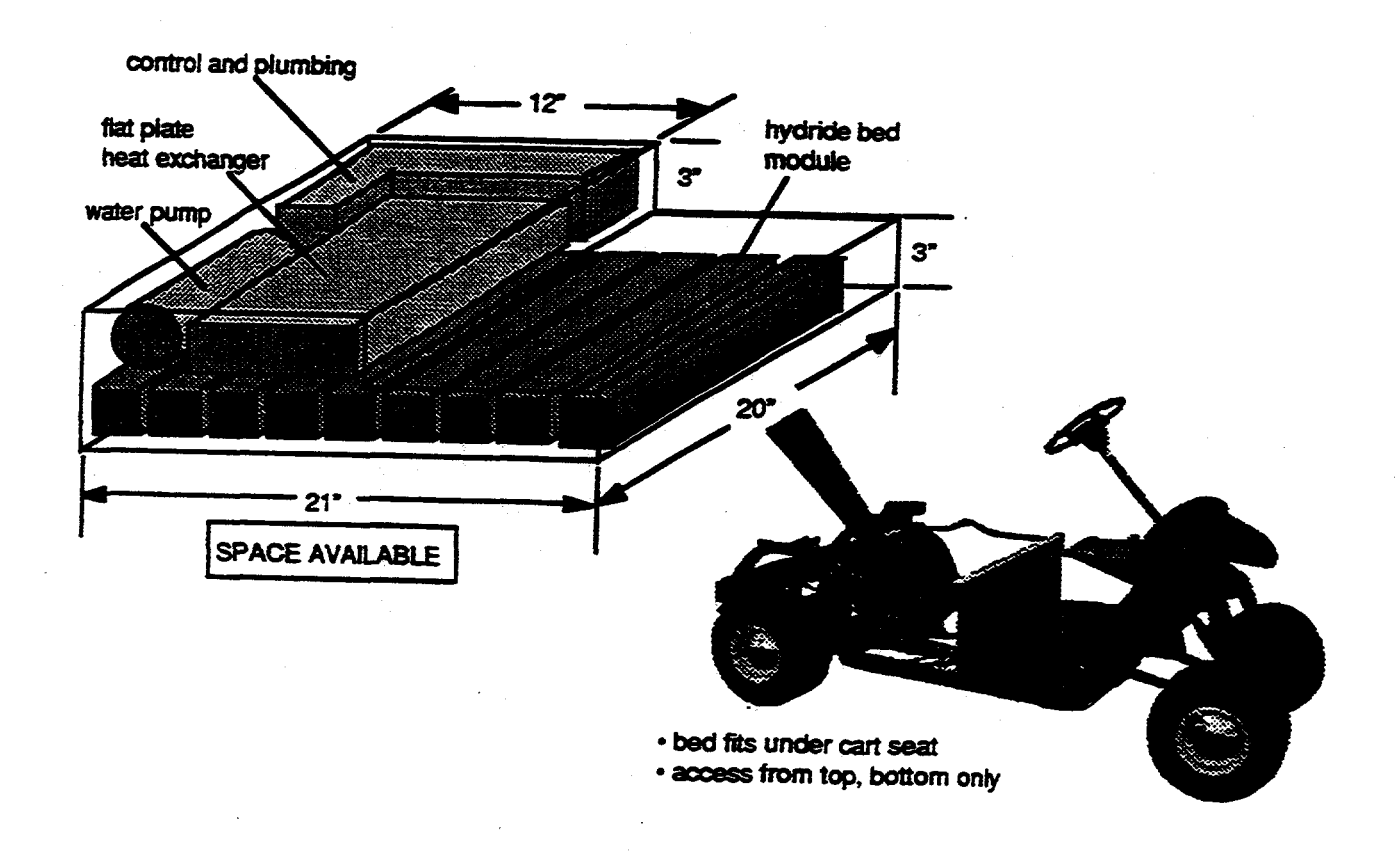


Figure 9. Fuel cell vehicle hydride bed conceptual design.

Hydrogen Storage via Polyhydride Complexes

Craig M. Jensen
Department of Chemistry
University of Hawaii
Honolulu. HI 96822

Abstract

Polyhydride metal complexes are being developed for application to hydrogen storage. Complexes have been found which catalyze the reversible hydrogenation of unsaturated hydrocarbons. This catalytic reaction could be the basis for a low temperature, hydrogen storage system with a available hydrogen density greater than 7 weight percent. The P-C-P pincer complexes, RhH2 { C6H3-2,6-(CH2PBu¹2)2 } and IrH2 { C6H3-2,6-(CH2PBu¹2)2 } have unprecedented, long term stability at elevated temperatures. The novel iridium complex catalyzes the transfer dehydrogenation of cyclooctane to cyclooctene at the rate of 716 turnovers/h which is 2 orders of magnitude greater than that found for previously reported catalytic systems which do not require the sacrificial hydrogenation of a large excess of hydrogen acceptor.

Introduction

A major concern in the development of hydrogen as a fuel is the problem of hydrogen storage. Solid hydrogen storage systems based on metal hydrides are safer and require

far less volume than either high pressure or cryogenic storage systems. However, hydrides of metals and alloys which reversibly release hydrogen at adequate rates contain too low of hydrogen weight percentages for the realization of hydrogen as an energy carrier. In our laboratory, we are developing nonclassical polyhydride metal complexes as hydrogen storage materials. We have demonstrated that nonclassical polyhydride metal complexes can be tailored to reversibly release hydrogen at virtually any rate and temperature. [1,2,3] As part of our effort to develop complexes of improved available hydrogen densities, hydride complexes containing unsaturated hydrocarbon ligands which reversibly bind hydrogen at both the metal center and the hydrocarbon ligands have been prepared. [4] While attempting to prepare one such complex, we made the serendipitous discovery that IrH₅(PPr¹₃)₃ and RhCl(PPh₃)₃ act as catalysts for the low temperature (≤150 °C), reversible dehydrogenation of cycloalkanes to aromatic hydrocarbons. We recognized this reversible, catalytic dehydrogen of alkanes by polyhydride complexes could be the basis for a low temperature, hydrogen storage system with a available hydrogen density greater than 7 weight percent. However, the utility of the initially identified catalysts were limited due to short lifetimes and low catalytic rates.

Dehydrogenation of methylcyclohexane to toluene in the presence of platinum group metals has been explored as a method of hydrogen storage. However, the dehydrogenation occurs only at temperatures in excess of 300 °C. This drastic energetic requirement has precluded such systems from consideration as practical methods for storing hydrogen as a fuel. Several soluble metal complexes catalyze the dehydrogenation of alkanes at moderate temperatures. [5-11] Systems have been reported that are driven by the hydrogen transfer from alkanes to hydrogen acceptors (transfer-dehydrogenation), [5-9] photoirradiation [9,10] and the thermal evolution of hydrogen. [11] However, the utility of these reactions is generally limited by very slow rates, low numbers of turnovers, and catalyst instability at the reaction conditions. [5-7,9-11] A system with significantly improved activity has been reported by Goldman but it requires the sacrificial hydrogenation of a 4-20 fold excess of an acceptor alkene in conjunction with the alkane dehydrogenation. [8]

Iridium and rhodium dihydrido complexes containing P-C-P pincer ligands have unusually high thermal stabilities. For example, IrH₂{Bu¹₂PC₂H₄)₂CH} is stable at 200 °C. [12] Dihydrido iridium bisphosphine complexes have been found to catalyze the transfer-dehydrogenation of alkanes. [5-7,9] We have therefore explored the reactivity of

rhodium and iridium P-C-P pincer complexes with alkanes in the presence of the hydrogen acceptor t-butylethylene (tbe).

Results

Syntheses of P-C-P Pincer Complexes

The complexes RhH₂{C₆H₃-2,6-(CH₂PBu^t₂)₂}, (1) and IrH₂{C₆H₃-2,6-(CH₂PBu^t₂)₂}, (2) were prepared in >85 % yield through treatment of the corresponding hydrido chloride complexes [13] with a THF solution of LiBEt₃H at 25 °C under an atmosphere of H₂ as shown in equation 1. Complex 1 was previously prepared in inferior yield by

M = Rh, Ir

the reaction of the hydrido chloride complex with KH. [14] The complexes were purified and isolated upon recrystallization from pentane. The 1 H and 31 P NMR spectra of 1 obtained through this procedure were identical to those previously reported. [14] The novel complex 2 was also characterized by NMR spectroscopy: 1 H NMR (400 MHz, toluene-d8), δ 7.43, m, 1H, para aromatic; 7.19, br s, 2H, meta aromatic; 3.36, vt, J_{P-H} = 3.7 Hz, 4H, CH₂; 1.24, vt, J_{P-H} = 6.7 Hz, 18H, CH₃; -9.01 J_{P-H} = 9.8 Hz Ir-H; 31 P{ 1 H} NMR (161.9 MHz, toluene-d8), δ 73.1. Satisfactory elemental analysis was also found for 2 (Calculated: C, 49.04; H, 7.72. Found: C, 49.12 H, 8.21).

Catalytic Dehydrogenation of Cycloalkanes by P-C-P Pincer Complexes

Solutions of cyclooctane (4.0 mL, 37.0 mmol) and the (0.2 mL, 1.6 mmol) were charged with 1 (10 mg, 0.019 mmol), in sealed tubes under argon, and fully immersed in an oil bath for the prescribed reaction times. The reaction mixtures did not darken or discolor

upon heating to 150 °C for periods as long as 1 week. The long term maintenance of catalyst integrity contrasts the short, c.a. 12 h half lives generally found for dehydrogenation catalysts at this temperature. The production of cyclooctene was quantified by temperature programmed (85 °C isothermal for 1 min; 5°/min to 200°C) gas chromatography analysis performed on a Hewlett Packard 5890 gas chromatography using a 250 µm x 25 m OV-1 capillary column. The rate of catalysis was determined to be 0.8 turnovers/h. The rate increases to 1.8 turnovers/h at 200 °C but significant decomposition of 1 is apparent after 24 h.

Strikingly higher activity is observed in solutions of cyclooctane (4.0 mL, 37.0 mmol), the (0.2 mL, 1.6 mmol), and the iridium complex 2 (3 mg, 0.0051 mmol). At 150 °C the catalytic reaction seen in equation 2 proceeds at the rate of 82 turnovers/h while a rate of

716 turnovers/h is observed at 200 °C. Appreciable activity (20.5 turnovers/h) is found even at 100 °C. The solutions containing 2 show no signs of catalyst decomposition up to 1 week of reaction time at all temperatures studied and remain active to the limit of complete hydrogenation of the hydrogen acceptor. The reaction is unaffected by the addition of metallic mercury to the mixture indicating that metallic iridium is not involved in the hydrogen transfer. [15] Comparable high levels of catalytic activity have previously been achieved only in systems catalyzed by RhCl(PMe₃)₂(CO) which require the sacrificial hydrogenation of 6-8 equivalents of norborene and 68 atm of H₂. [8] Our finding of far greater activity with 2 than 1 is in accordance with a recent theoretical study by Goddard et. al. which identified Ir⁺ as the most efficient transition metal for the dehydrogenation of methane. [16] The differences in the catalytic activities of 1 and 2 are possibly related to the ability of iridium to form stronger M-C and M-H bonds and the availability of the Ir(V) oxidation state.

At high concentration, both the and the hydrogenated product, t-butylethane (tha) acts as an inhibitor of the catalytic reaction. Diminished rates of catalysis are found in solutions

containing greater than a 300:1 ratio of the to catalyst. Thus, high turnover numbers can be achieved only in solutions containing a limited amount of the which must be periodically added to the reaction mixture. Pronounced inhibition of the catalytic system by the is observed after 1000 total turnovers. We have also found that the catalytic activity is strongly inhibited by N₂. In order to achieve the maximum catalytic rates, the solutions must be freeze-pump-thaw degassed prior to heating to remove any vestiges of N₂. Apparently, N₂ coordination is competitive with alkane coordination. This explanation is supported by the findings that 1 and Rh(H₂){HC(CH₂CH₂P(Bu¹)₂)₂} coordinate N₂ when placed under an atmosphere of N₂. [17]

In conclusion, 2 catalyzes the transfer-dehydrogenation of cyclooctane at rates which are 2 orders of magnitude greater than those of previously reported catalytic systems which do not require the sacrificial hydrogenation of a large excess of hydrogen acceptor [5-7,9] Furthermore, the P-C-P pincer complexes have unprecedented, long term stabilities under catalytic conditions.

Future Directions

The long term (>1 month) stability of the iridium catalyst 2, is presently under investigation. These experiments will also establish whether the catalytic dehydrogenation of cyclooctane proceeds beyond cyclooctane to cyclooctadiene and cyclooctatetrene. We plan to determine the activity and stability of 2 at 300 °C, where H₂ evolution is thermodynamically favorable and thus an organic hydrogen acceptor is unnecessary. The dehydrogenation of cycloalkanes to aromatic hydrocarbons is much more thermodynamically favorable than the dehydrogenation of cyclooctane. Therefore, we plan to investigate 2 as a catalyst for the dehydrogenation of cyclohexane to benzene and methylcyclohexane to toluene.

We estimate that a practical hydrogen storage system based on an iridium complex would require a catalyst which dehydrogenation of cycloalkanes at rates 1-2 orders of magnitude faster than 2. We plan to synthesize related P-C-P pincer complexes which are less sterically congested at the metal center (i.e. IrH₂{C₆H₃-2,6-(CH₂PCy₂)₂}, IrH₂{C₆H₃-2,6-(CH₂PBu¹₂)₂}, and IrH₂{C₆H₃-2,6-(CH₂PPh₂)₂}). We will then determine whether this reduction of steric congestion increases the catalytic activity of the complexes.

Alternatively, systems employing higher catalyst loadings would be practical if non-noble metal complexes could be developed as catalysts. Towards this end, we plan to explore the synthesis of cobalt P-C-P pincer complexes.

The simple apparatus we with which we have carried out the preliminary dehydrogenation reactions allow us to only roughly estimate the rates of the catalytic reactions. Accurate determination of the reaction kinetics are required for evaluation of the potential of these systems for hydrogen storage. Therefore, we plan to examine catalytic dehydrogenations/hydrogenations of cycloalkanes in a constant pressure system.

References

- 1. Mediati, M., G.N. Tachibana, and C.M. Jensen 1990 Inorg. Chem. 29:3.
- 2. Mediati, M., G.N. Tachibana, and C.M. Jensen 1992 Inorg. Chem. 31:1827.
- 3. Le-Husebo, T., and C.M. Jensen 1993 Inorg. Chem. 31:3.
- 4. Husebo, T. L., and C.M. Jensen 1995 Organometallics 14:1087.
- (a) Baudry, D; M. Ephritikhine, H. Felkin. 1983 J. Chem. Soc. Chem. Commun. 788.
 (b) Felkin, H., T. Fillebeen-Khan, R. Holmes-Smith, Y. Lin 1985 Tetrahedron Lett. 26:1999.
- 6. Felkin, H.; T. Fillebeen- Khan, R. Holmes-Smith, J. Zakrzewski. 1984 Tetrahedron Lett. 25:1279.
- 7. Aoki, T., R.H. Crabtree. 1993 Organometallics 12:294. (b) Belli, J., C.M. Jensen. 1996 Organometallics 15:1532.
- 8. (a) Maguire, J.A., A.S. Goldman. 1991 J. Am. Chem. Soc. 113:6706.
 - (b) Maguire, J.A., A. Petrillo, A.S. Goldman 1992 J. Am. Chem. Soc. 114:9492.
- (a) Burk, M. W., R.H. Crabtree, D.V. McGrath. 1985 J. Chem. Soc. Chem. Commun. 1829. (b) Burk, M.J., R.H. Crabtree 1987 J. Am. Chem. Soc. 109:8025.
- (a) Nomura, K., Y. Saito. 1988 J. Chem. Soc. Chem. Commun. 161. (b) Nomura, K.;
 Y. Saito. 1989 J. Mol. Catal. 54:57. (c) Sakakura, T., T. Sodeyama, M. Tanaka.
 1989 New J. Chem. 13:737. (d) Maguire, J.A., W.T. Boese, A.S. Goldman. 1989
 J. Am.. Chem. Soc. 111:7088. (e) Sakakura, T.; T. Sodeyama, F. Abe, M. Tanaka.
 1991 Chem. Lett. 297.
- (a) Fujii, T., Y. Satio. 1990 J. Chem. Soc. Chem. Commun. 757. (b) Fujii, T.,
 Y. Higashino, Y. Saito 1993 J.C.S. Dalton Trans. 517.

- 12. McLoughlin, M.A., R.J. Flesher, W.C. Kaska, H.A. Mayer. 1994 Organometallics 13:3816.
- 13. Moulton, C.J., B.L. Shaw. 1976 J. Chem. Soc. Dalton Trans. 1020.
- 14. Nemeh, S., C. Jensen, E. Binamira-Soriaga, W.C. Kaska. 1983 Organometallics 2:1442 and references therein.
- 15. Anton, D.R., R.H. Crabtree. 1982 Organometallics 2:855.
- 16. Perry, J.K., G. Ohanessian, W.A. Goddard. 1994 Organometallics 13:1870.
- 17. (a) Nemeh, S., W.C. Kaska. unpublished results. (b) Vigalok, A., Y. Ben-David, D. Milstein. 1996 Organometallics 15:1839.

Thermodynamic Characterization of Polyhydride Complexes

Ragaiy A. Zidan, Richard E. Rocheleau and Craig M. Jensen Hawaii Natural Energy Institute University of Hawaii at Manoa Honolulu, HI 96822

Abstract

We have investigated the interaction of hydrogen with solid IrXH₂(PPrⁱ₃)₂(H₂) (X=Cl, I). Gaseous hydrogen was found to react directly and reversibly with solid iridium chlorocomplex, IrClH₂(PPrⁱ₃)₂(H₂) under mild conditions of pressure and temperature. Equilibrium absorption and desorption isotherms were obtained at fixed temperatures ranging from 273° K to 323° K over the pressure range from 0.1 to 11 atmospheres. The rates of hydrogen uptake and release were found to be very rapid.

A Gaussian shaped thermal desorption spectrum showed that hydrogen desorption occurred over a wide range of temperatures from 200° K to 350° K. The TDS results and the absence of well defined plateaus in p-c isotherms indicated a disorder of the hydrogen arrangement in the iridium complex matrix. These observation were consistent with earlier findings from NMR and neutron diffraction measurements.

The enthalpy (ΔH) and the entropy (ΔS) of hydrogen desorption, from a van't Hoff's plot based on the hydrogen pressure at 50% of full loading of hydrogen at fixed temperatures, were -4.9 ± 0.3 kcal/mole of H_2 and 28.6 ± 2 cal/deg. mole of H_2 respectively.

Hydrogen desorption from IrIH₂(PPrⁱ₃)₂(H₂) was not observed at the above temperature and pressure ranges, indicating stronger hydrogen bond in iodo-complex compared to the chloro-complex.

Introduction

One of the major problems for utilizing hydrogen as a fuel is finding a practical and safe method for storage. Condensed phase materials (solid or liquid) that bond reversibly with hydrogen represent a simple and safe means for storing hydrogen. For many years, metal hydrides have been explored for use in hydrogen storage systems. Research in the area of metal hydrides has resulted in several intermetallic compounds that have shown potential for hydrogen storage (e.g. Mg2Ni, FeTi, LaNi5 etc.) (Reilly et. al. 1968,1974) and (Sandrock 1978). Unfortunately, metal hydrides that can store adequate quantities of hydrogen suffer from unfavorable kinetics and/or thermodynamics of the reversible release of hydrogen. On the other hand, metal hydrides that release hydrogen under mild conditions of temperature and pressure have low hydrogen storing capacity. In addition, many of the intermetallic alloys used for hydrogen storage suffer from disproportionation of elements in the alloy with repeated hydrogenation and dehydrogenation, resulting in a limited lifetime (Cohen et. al. 1981). Therefore, investigating unconventional materials is necessary and needed for any breakthrough to occur.

A new class of metal based materials, dihydrogen complexes, in which H-H bonding is preserved was first identified by (Kubas et. al. 1984). This discovery was followed by extensive work in the area of chemical synthesis in an effort to produce similar compounds and to investigate their properties.

The metal- hydrogen bond in these complex hydrides is relatively weak and hydrogen is reversibly released under mild conditions of temperature and pressure. Experimental studies have shown that the strength of the bond can be modulated by a slight change in the ligand environment. These excellent properties led us to believe that this class of polyhydrides have the potential of storing hydrogen on their own or as a composite system where the polyhydride is imbedded in a metal matrix.

Previous work (Jensen et. al. 1993) has shown that hydrogen reacts reversibly with Ircomplex in solution under mild conditions of temperature and pressure. However, a quantitative thermodynamic study of hydrogen reaction with the solid non-classical iridium polyhydride complex has not been conducted prior to this work and the material has not previously been characterized as a hydrogen storage media. Thermodynamic properties and kinetic behavior such as enthalpy, pressure temperature isotherms (PCT) and the rate of absorption/desorption are necessary factors in determining the practicability of these compounds as hydrogen storage media. These characterizations are also needed to guide the development of new materials or to modify existing ones in an effont to obtain compounds with higher hydrogen capacity and mild conditions of hydrogen release.

In order to achieve accurate measurements of the interaction of hydrogen with the solid phase of these compounds, we designed and built a computer controlled, high precision thermovolumeteric analyzer with a high speed data acquisition system. The system was designed so that it is capable of measuring different size samples over a wide range of temperatures and pressures with high accuracy.

Experiments

Apparatus:

The thermovolumeteric apparatus, used in the characterization of the samples (Fig. 1) consisted of two stainless steel high pressure vessels. One of the vessels was used to contain the sample and the other was used as a gas reservoir. The sample vessel contained a cylindrical aluminum insert which acted as a heat sink (or source) to minimize temperature fluctuation due to the reaction of the sample with hydrogen during isothermal measurements.

The insert had two cylindrical cavities, one was used as a sample cavity and the other was used as a reference cavity. The temperatures inside the cavities were measured, using two K-type thermocouples. Temperature inside the gas reservoir vessel was also measured using a K-type thermocouple. The gas pressures inside the vessels were measured using high precision pressure transducers. The temperature of the sample could be controlled and programmed to change linearly using a proportional integral differential controller that was connected to heating and cooling systems. In order to be able to measure different size samples, the volumes inside the vessels could be also changed by inserting different size aluminum cylinders into the cavities. The system was connected to pressure regulators and a pressure-vacuum manifold with shut-off diaphragm valves and micro-valves to control gas flows. All the readings from the thermocouples and the pressure measuring devices were recorded using a computer data acquisition system. The vessels were tested on regular basis for gas leaks using helium gas.

Experimental Methods:

The vessel volumes and the gas behavior in the absence of samples were carefully calibrated and found to closely obey the ideal gas law. Using this calibration, the amount of gas in either vessel could be calculated knowing the temperature and the pressures in the vessel. The amount of hydrogen transferred between the reservoir vessel and the sample vessel was quantified by measuring the pressure change in the reservoir. Thermodynamic and kinetic measurements of LaNi5 were conducted to check the system calibration. PCT isotherms agreed with those reported in the literature.

A series of pressure- composition isotherms (p-c isotherms) of hydrogen absorption and desorption at fixed temperature were obtained, for a 1.5 g of the iridium complex, IrH2Cl(PPrⁱ3)2(H2). The p-c isotherms of absorption were constructed by step-by-step admission of hydrogen from the reservoir vessel to the sample vessel through a micro-valve at fixed temperatures over a hydrogen pressure range from 0.1 to 11 atmospheres. The amount of hydrogen absorbed was calculated from the difference between the expected and the measured values of pressure in the vessels after establishing equilibrium. In a similar manner the p-c isotherms of desorption were obtained, except hydrogen was depleted from the sample vessel into the reservoir vessel at fixed temperatures over a pressure range from 11 to 0.1 atmospheres of hydrogen pressure above the sample.

In order to obtain the rate of hydrogen uptake by a fully dehydrogenated sample of Ircomplex, the hydrogen pressure was increased from vacuum to 10 atmospheres in about 1 second. The subsequent drop in pressure, due to hydrogen uptake by the sample was recorded as a function of time. The pressure above the sample vessel was kept constant by repressurizing the sample vessel back to 10 atmosphere every 0.3 atmospheres of pressure drop. Similarly, the rate of hydrogen release was determined by a sudden (1 second) lowering of hydrogen pressure above a fully hydrogenated sample from 11 to 0.1 atmospheres. The increase in pressure and the time it took the increase to occur were recorded. The pressure above the sample vessel was kept constant by evacuating the sample vessel back to 0.1 atmosphere every 0.3 atmosphere pressure rise.

To obtain a thermal desorption spectrum we started with a fully hydrogenated sample of Ircomplex, IrH2Cl(PPri3)2(H2). The sample was fully hydrogenated by keeping it under 11 atmospheres of hydrogen pressure overnight. The sample vessel was cooled to 196° K while maintaining 11 atmospheres of hydrogen pressure. The pressure in the sample vessel was then quickly lowered from 11 to 0.1 atmospheres. The sample vessel was left at 196° K to reach equilibrium. The hydrogen release at 196° K was recorded. The temperature was then linearly increased to 350° K at a rate of 1 degree per 5 minute. During the heating process the temperature and the rate of pressure increase, inside the sample vessel, were recorded. The pressure above the sample was kept constant, between 0.1 and 0.3 atmospheres by venting desorbed hydrogen.

Results and Discussion

The solid powder of chloro-iridium complex, IrClH2(PPr¹3)2(H2), was found to readily absorb and desorb hydrogen without activation; achieving, approximately, the full expected weight percent hydrogen uptake. On the other hand the iodo -iridium complex, IrIH2(PPr¹3)2(H2) was examined for hydrogen release over the temperature range of 196° K to 333° K and pressure range of 0.1 to 11 atmospheres. However, hydrogen desorption was not detected from the iodine iridium complex. This result is consistent with earlier finding that hydrogen has a stronger bond in the iodo iridium complex than the chloro iridium complex (Jensen et. al. 1993). This result also demonstrates that the strength of the hydrogen bond can be modulated by a slight change of the halide ligands in the complex. The weaker bond of the reversible hydrogen in the chloro-iridium complex, compared to the iodo -iridium complex, in the absence of a solution, could be attributed to the σ donation of the halide at the metal center of the complex.

Fig. 2 shows the pressure-composition isotherms of hydrogen absorption and desorption by the chloro-iridium complex over the temperature range from 273° K to 323° K. These isotherms (p-c-T) do not show well defined plateaus over the temperature range studied.

Fig 3. shows the thermal desorption spectrum (TDS) of hydrogen from the IrClH₂(PPr¹₃)₂(H₂). Hydrogen desorption occurred over a wide range of temperatures beginning at 200° K up to 350° K. The absence of plateaus in the isotherms and the Gaussian-like shape of the thermal desorption spectrum suggest a static or dynamic disorder in the local arrangement of hydrogen in the matrix of the IrClH₂(PPr¹₃)₂(H₂) complex. This observation is consistent with the earlier finding from NMR and neutron diffraction studies (Wisniewski et al. 1993). The neutron diffraction study of a single crystal of IrClH₂(PPr¹₃)₂(H₂) has ruled out the possibility of static disorder. This leads us to believe that the distribution function of the TDS does not represent a distribution of hydrogen occupation of different crystallographic sites but rather different energy levels of the occupied sites. The dihydrogen may be moving among different available energy states or exchanging with the hydride ligands in the complex. The Gaussian-like shape of the thermal desorption spectrum plot shows that dynamic fluctuation in the local hydrogen arrangement was occurring about some most probable energy configuration.

The isotherms of hydrogen absorption and desorption by and from the Ir-complex showed very small hysteresis if any, considering the uncertainty in the measurements. The reversible hydrogen content in the sample was found from the p-c isotherms to be about 0.34±0.02 weight percent. The result is consistent, within the uncertainty range, with one molecule of hydrogen reacting with one molecule of IrClH2(PPr¹3)2.

$$IrClH_2(PPr^i_3)_2(H_2) \leftrightarrow H_2 + IrClH_2(PPr^i_3)_2$$
 (1)

The enthalpy (ΔH) and the entropy (ΔS) of the reaction were obtained using van't Hoff relation, R lnPe= $\Delta H/T$ - ΔS , where Pe is the equilibrium pressure at temperature T. In the case of materials whose isotherms exhibit plateaus, the equilibrium pressure is normally taken as the pressure at the plateau. Since the p-c isotherms for the chloro-complex had no well defined plateaus, the characteristic pressures were taken to be the equilibrium pressure measured at 50% loading of hydrogen. Fig. 4. depicts a least-squares fit the logarithm of equilibrium pressures at 50% loading of hydrogen with reciprocal temperature which yields the following equation:

$$lnP = -2465/T + 14.38$$
 (2)

The data were used to calculate the enthalpy (ΔH) and the entropy (ΔS) for reaction 1. ΔH and ΔS were found to be -4.9 ± 0.3 kcal/mol of H_2 , and -28.6 ± 2 cal/deg.mol, respectively.

The reversible release of hydrogen from solid IrClH₂(PPr¹₃)₂(H₂) is characterized by a low enthalpy ΔH =-4.9 ± 0.3 kcal/mol H₂, in comparison to the enthalpy of the release of hydrogen from some popular metal and intermetallic hydrides. For example, ΔH (MgH₂)=-18.5 kcal/mol H₂, ΔH (Mg₂NiH₄)=-15.4 kcal/mol H₂, ΔH (LaNi₅)=-7.2 kcal/mol H₂ and ΔH (FeTi) \sim 6.7 kcal/mol H₂. The value of ΔH for the release of hydrogen from solid IrClH₂(PPr¹₃)₂(H₂) was found to be comparable to ΔH of the release of hydrogen from a similar compound, Ir(H)₂(H₂)Cl(PtBu₂Me)₂ reported by (Hauger et. al. 1994). The value of the enthalpy obtained by Hauger et. al. was 6.8 ± 0.2 kcal/mol H₂, however, it was measured in solution.

The rate of hydrogen uptake and release was found to be very fast over the range of the temperatures and pressures of the study. Fig. 5 shows the fraction of absorbed hydrogen verses time at constant overpressure of 10 atmospheres at different fixed temperatures ranging from 273° K to 323° K. Fig. 6 shows a plot of the fraction of desorbed hydrogen verses time at constant pressure of 0.1 atmospheres for fixed temperatures, ranging from 273°K to 323° K. More than 50% of the hydrogen was absorbed or desorbed within the first few seconds of the measurements and then a relatively slower rate of hydrogen uptake and release was observed. Fig. 5 and Fig. 6 show that in the slower regions the rate of both absorption and desorption increased with the increase of temperature, at constant pressure. The relatively slower rate could be a result of a slow diffusion of hydrogen through the Ircomplex and/or a poor heat conductivity through the powder. The fast regions of absorption and desorption suggest that the intrinsic kinetics of hydrogen reaction with IrIH2(PPr¹3)2(H2) are very rapid. Subsequent cycles of hydrogen uptake and release were reproducibly as fast.

In an effort to identify new polyhydride complexes that interact reversibly with hydrogen, similar to the Ir-complex, we are using the thermovolumeteric analyzer to investigate hydrogen reaction with other compounds. Our preliminary results have shown that a reversible hydrogen reaction can occur with triphenylphosphine copper complex. However, we have encountered inconsistency in the results of hydrogenation and dehydrogenation experiments when we tested different batches of the copper complex. We attributed this inconsistency to variation in the purity of the compound considering that the compound was purchased commercially and is reported to be only 90% pure.

Conclusion

We have shown that hydrogen can react with the solid chloro-iridium complex under mild conditions of temperature and pressure, as it did in solution. On the other hand, hydrogen release from iodo iridium complex did not occur. The inability to release of hydrogen from the iodo-iridium complex demonstrated that the strength of the hydrogen bond in these complexes can be modulated by a slight change of the halide ligands in the complex. The ability to modulate the strength of the hydrogen bond can be utilized to modify these complexes for the desired application. Although the reversible hydrogen content of the system studied was only 0.34 wt%, the reversibility of hydrogen reaction at practical temperatures and pressures and the rapid kinetics of hydrogen absorption and desorption confirm that these dihydrogen complexes represent a new class of hydrogen storing material that should be further investigated.

Future Work

Information obtained from the characterization experiments of the complexes will be utilized to synthesize new compounds that react reversibly with hydrogen under mild conditions and have a high hydrogen capacity. We will explore other Co-based, Ni- based, as well as magnesium based complexes that posses valence states expected to exhibit hydrogen uptake. If appropriate we will synthesize some of these complexes in our laboratory in order to control the purity of the material. In the case of hydrogen uptake and release by any of the tested compounds, a full thermodynamic characterization will be conducted to determine its applicability as a hydrogen storage medium. These compounds will also be combined with other metals, either physically or chemically, to examine the possibility of increasing the hydrogen capacity of the system by forming a composite matrix of the polyhydride and the metal. In these composite systems the polyhydride may modify the electronic properties of the metal, altering the hydrogen-metal bond but preserving the high capacity of the metal. Hydrogen interaction with metals which form metal hydrides, has been reported to improve when the metal is in contact with an organic or organo-metallic compound because of what is known as spill-over phenomena (Imamura and Tsuchiva 1983).

References

- Bryan E. Hauger, Dmitry Gusev, and Kenneth Caulton. 1994. J. Am. Chem. Soc. 116, 208
- G. J. Kubas, R. R. Ryan, B. I. Swanson, P.J. Vergamini and H. J. Wasserman. 1984. J. Am. Chem. Soc. 106, 451
- Sandrock, G.D. 1978. Development of Low Cost Nickel-Rare Earth Hydrides for Hydrogen Storage. Proc. 2nd World Hydrogen Energy Conf., Pargamon, Oxford, pp.1625-1656
- H. Imamura and S. Tsuchiya, 1983. Chem. Soc. Faraday Trans. 1, 79, 1461
- J. Eckart, C. M. Jensen T. F. Koeztel, T. L. Husebo, J. Nicole and P. Wu. 1995. Comm. J. Amer. Chem. Soc. 117, 7271
- J.J Reilly and R. H. Wiswall. 1974. J. Inorg. Chem., 13, 218
- J.J Reilly and R. H. Wiswall 1968. J. Inorg. Chem., 7, 2254
- L. L. Wisniewski, M. Mediati, C. M Jensen and K. W. Zilm 1993. Comm. J. Amer. Chem. Soc. 115, 7533
- R.L. Cohen, J.H. Wernick 198. Science 214, 1081
- T. Le-Husebo and C. M. Jensen 1993. J. Am. Chem. Soc. 32, 3797

Captions

Fig. 1 Components of the thermovolumeteric analyzer system

Fig. 2 Equilibrium pressure-composition isotherms (PCT) of hydrogen with IrClH₂(PPrⁱ₃)₂(H₂)

Fig. 3 Thermal desorption spectrum of hydrogen release from IrClH₂(PPrⁱ₃)₂(H₂)

Fig. 4 Van't Hoff plot based on equilibrium pressure at 50% of full loading $(\Delta H=-4.9 \text{ Kcal/mol and } \Delta S=-28.6 \text{ cal/deg.mol})$

Fig. 5 Rate of hydrogen uptake by IrClH₂(PPrⁱ₃)₂(H_{2)_X} at constant pressure of 10 atmospheres

Fig. 6 Rate of hydrogen release from $IrClH_2(PPr^i_3)_2(H_2)_X$ at constant pressure of 0.1 atmospheres (H2 loaded at 5 atm.)

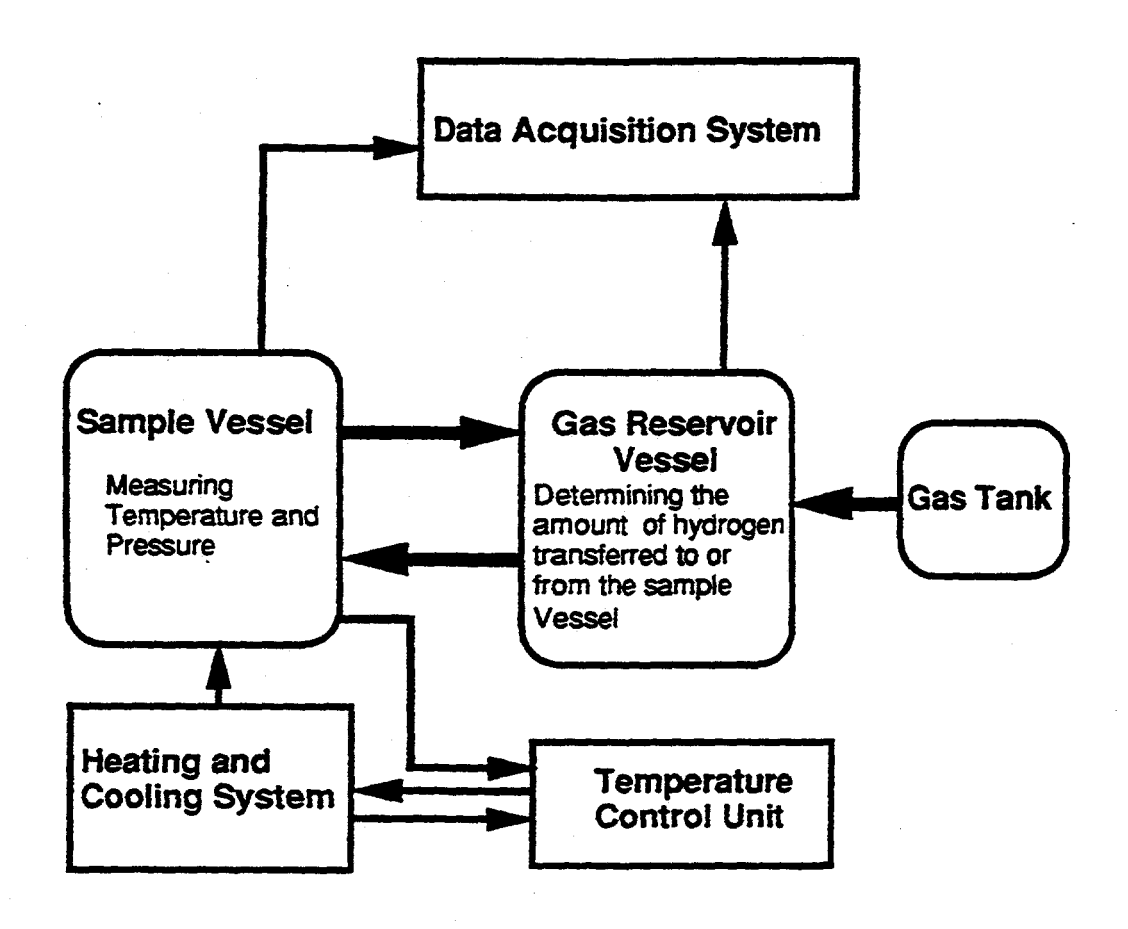


Fig. 1

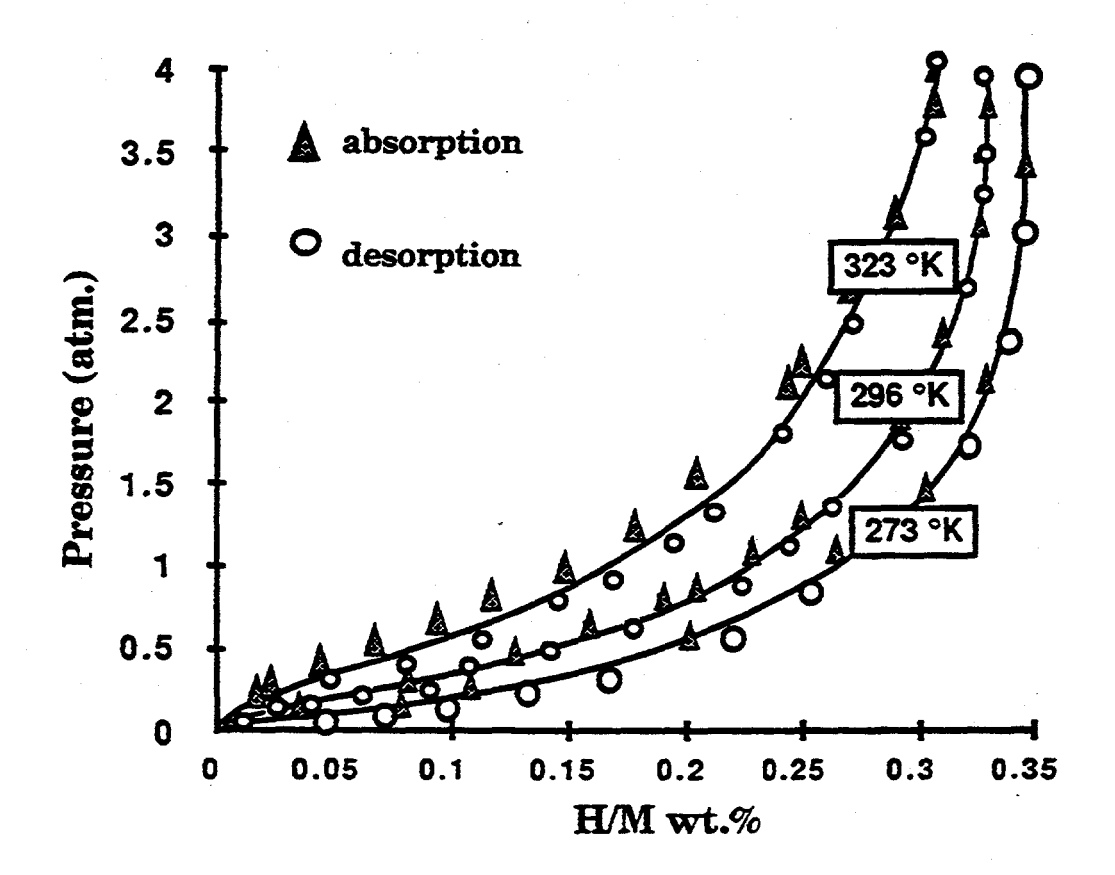


Fig. 2

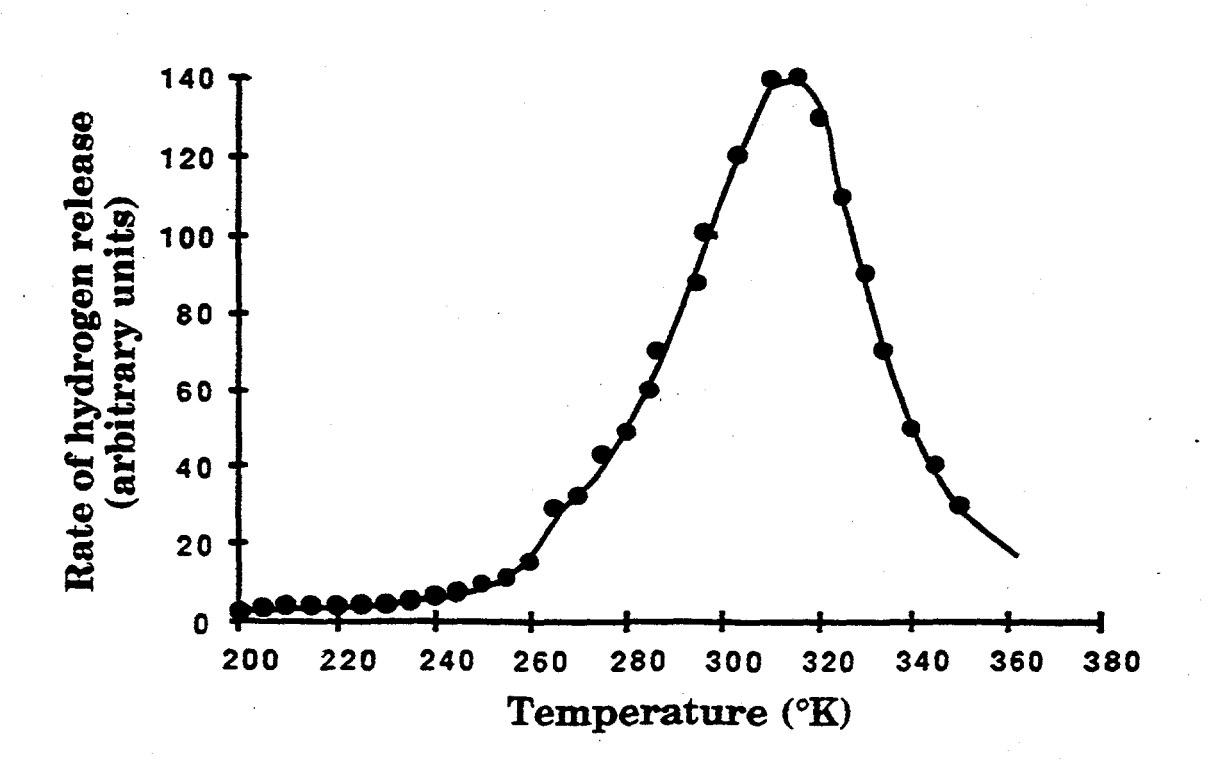


Fig 3

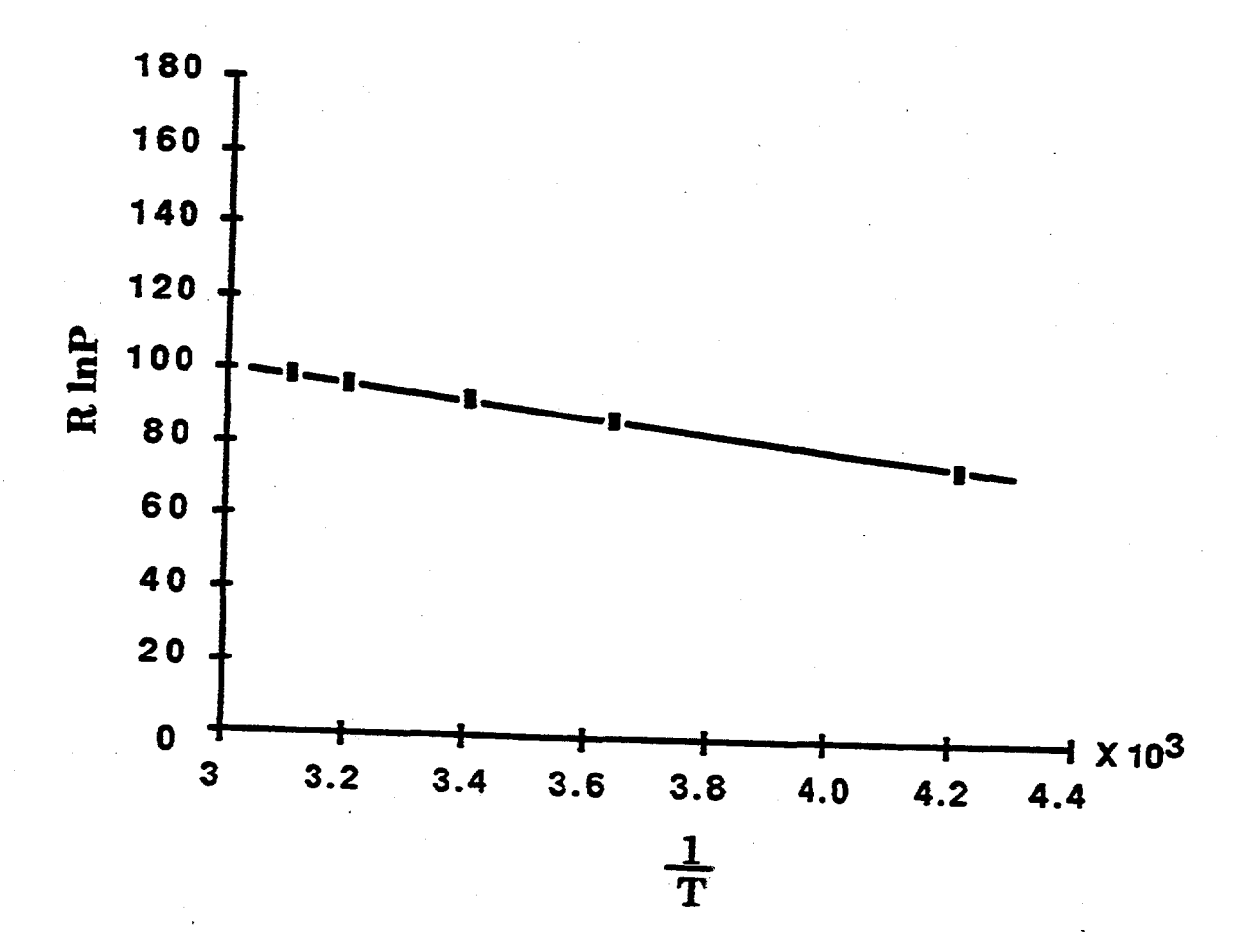


Fig. 4

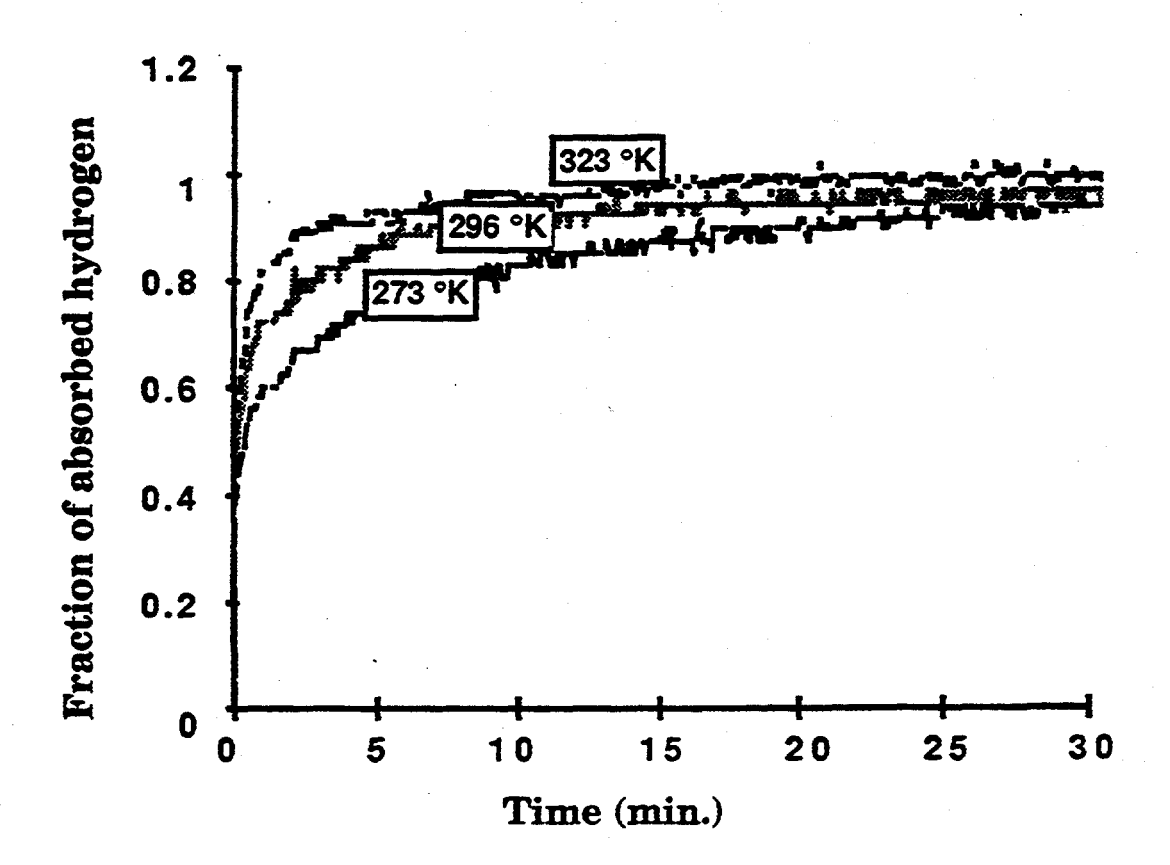


Fig. 5

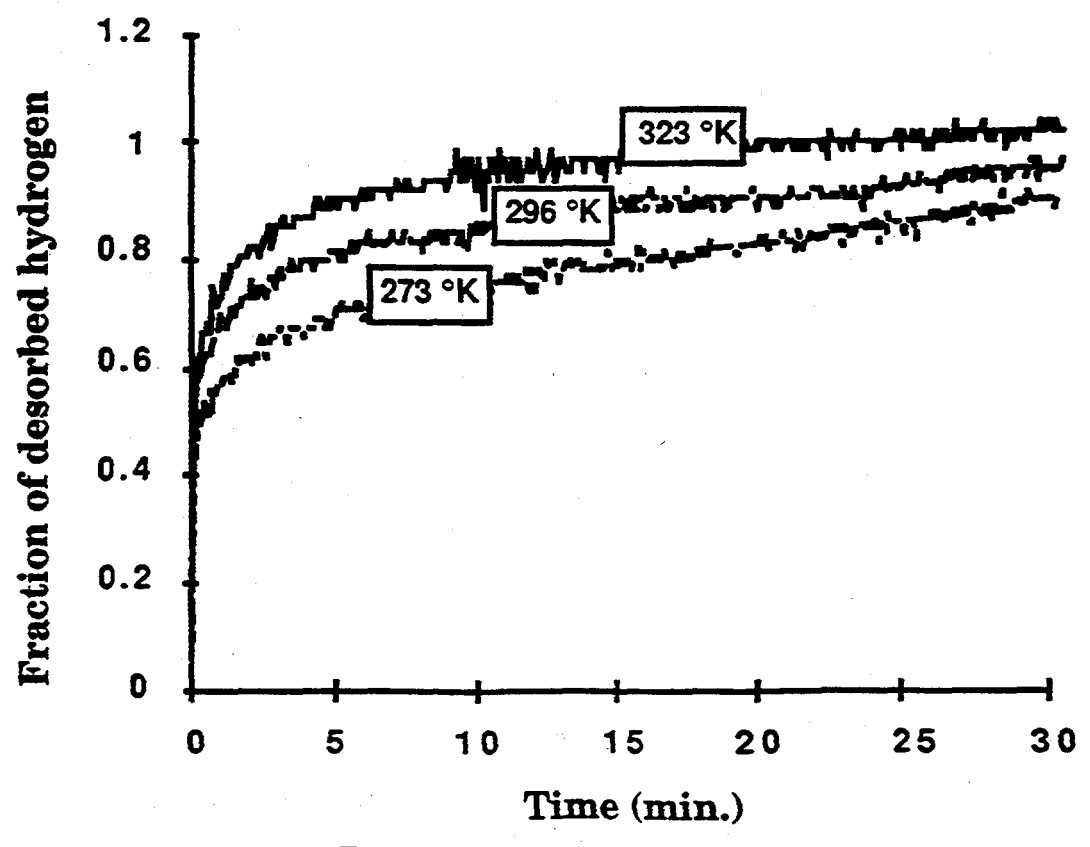


Fig. 6

Hydride Development for Hydrogen Storage

G.J. Thomas, S.E. Guthrie, W. Bauer and N.Y.C. Yang Sandia National Laboratories Livermore, CA 94550

> G. Sandrock SunaTech, Inc. Ringwood, NJ 07456

Abstract

The purpose of this project is to develop and demonstrate improved hydride materials for hydrogen storage. The work currently is organized into four tasks: hydride development, bed fabrication, materials support for engineering systems, and IEA Annex 12 activities. At the present time, hydride development is focused on Mg alloys. These materials generally have higher weight densities for storing hydrogen than rare earth or transition metal alloys, but suffer from high operating temperatures, slow kinetic behavior and material stability. Our approach is to study bulk alloy additions which increase equilibrium overpressure, in combination with stable surface alloy modification and particle size control to improve kinetic properties. This work attempts to build on the considerable previous research in this area, but examines specific alloy systems in greater detail, with attention to known phase properties and structures. We have found that specific phases can be produced which have significantly improved hydride properties compared to previous studies.

Project Approach/Rationale

The purpose of this project is to develop and demonstrate improved hydride materials for hydrogen storage. There are three main objectives:

- (1) develop improved light weight hydrides, particularly for vehicular applications.
- (2) develop improved and innovative hydride bed fabrication methods.
- (3) provide advanced materials to engineering and industrial collaborative programs.

Currently, the project is organized into the following four tasks:

Development of improved lightweight hydrides

At the present time, this work is focused on Mg alloy hydrides. These materials generally have higher weight densities for storing hydrogen than rare earth or transition metal alloys, but suffer from high operating temperatures, slow kinetic behavior and material stability. Our approach is to study bulk alloy additions which increase equilibrium overpressure, in combination with stable surface alloy modifications and particle size control to improve kinetic properties. This work attempts to build on the considerable previous work in this area, but examines specific alloy systems in greater detail, with particular attention to known phase properties and structures. Hydride pressure-composition-temperature measurements are correlated with detailed microstructural analyses in these studies. Various synthesis methods are employed, including melt-cast, rapid solidification and mechanical alloying.

In-situ Mg2Ni Hydride Bed Fabrication

In earlier work, we showed that single phase Mg2Ni could be synthesized by a vapor transport process. The resulting material had better kinetic properties and was more stable than conventionally produced alloys. This novel process will be employed, with an industrial collaborator, to demonstrate the fabrication of a storage bed using in-situ hydride synthesis.

Materials for Engineering Systems

This task is coupled with the Sandia activities in Hydrogen Storage and Delivery System Development. It includes material selection, procurement and processing, and measurements of pressure-temperature and kinetic behavior. The objectives are to optimize hydride properties for particular applications and also provide material properties data for engineering bed designs. Currently, this effort is concentrated on a hydride bed for the fuel cell powered PUV in the Palm Desert project, in collaboration with Humboldt State University.

IEA Activities in Hydrogen Storage

The IEA Annex 12 – Metal Hydrides program includes international collaboration in hydride synthesis, hydride characterization, data base development of material properties, and a review of current hydride technology. This work is focussed on two areas of hydride application: light weight hydrides for transportation and battery applications.

Discussion of Results

Improved lightweight hydrides

In our previous work, a promising new alloy hydride was found which has better pressure-temperature characteristics than any previous Mg alloy. A new fabrication process for existing Mg alloys was also developed and demonstrated. Work in these two areas have continued this year and, in addition, we have studied the effects of adding other elements to the Mg-Al system. Figure 1 is a van't Hoff plot summarizing the pressure-temperature properties for the two earlier alloys and shows some of the results obtained from the alloys studied this year.

As seen in the figure, two alloys have been found which have similar high equilibrium overpressures, a Mg-Al-Ni alloy reported last year and a Mg-Al-Cu alloy. Work has continued on the Ni-containing alloy with extensive microanalysis characterization and various fabrication methods. However, the synthesis yield on this alloy continues to be low. In contrast, the Cu-containing hydride has been successfully fabricated in larger quantities using a mechanical alloying process. This difference is believed to be due to the thermodynamic stabilities of the active hydride phases in each ternary system. Hydrogen release rates in the Mg-Al-Cu hydride have been found to be much slower than in the alloy with Ni, but we have not yet looked at the influence of particle size and surface properties on these rates.

We have also begun to examine Mg-Al-Zn alloys. The thermodynamic properties of this alloy system has been extensively studied and reviewed in the literature¹. A number of stable ternary phases have been identified. Our work has focused on the hydride properties of Mg-Al-Zn with Mg and Al contents similar to the binary alloys we reported earlier and which have been studied previously by others²³. Importantly, it was found that only minor additions of Zn (1-2 wt.%) to Mg-Al alloys produced stable phases which have higher equilibrium overpressures compared to the binary alloys. In some instances, improved kinetic behavior was also observed. Results on three alloys are shown in Figure 2, where the pressure-temperature properties of Mg-Al alloys are compared after small additions of Zn were made. The figure includes data from earlier investigations²³.

Microanalysis on these materials indicate that the Zn has also homogenized the microstructure. That is, the material is generally single phase, whereas Mg-Al alloys fabricated by melt-cast or rapid solidification typically show two-phase structures. Electron micrographs comparing the microstructures are shown in Figure 3. Based on these new results and our earlier Mg-Al-Ni work, a matrix of Mg-Al-Zn melt-cast alloys was defined and fabricated (Kaiser Industries). We are currently in the process of characterizing these materials prior to evaluating their PCT properties.

We also examined rare earth aditions to Mg and Mg alloys. It was found that an alloy phase of Mg-Mm (Mm indicates a rare earth mixture) enhanced the hydride kinetic

properties and also appeared to be more stable than Ni coatings. In earlier work, we found that Ni coated on pure Mg converted to Mg2Ni during hydride measurements and the resultant volume change caused discontinuous coatings and, in some cases, separation of the Mg2Ni from the Mg. Pressure-temperature plots shown in Figure 4 compare two Mg alloys with rare-earth additions. The data at lower temperatures indicate that desorption release rates were sufficiently fast to allow equilibrium measurements within equivalent time scales.

The microstructure of one of these samples is shown in Figure 5. The micrograph shows the Mg-Mm phase precipitated into thin layers which intersect the surfaces of the individual particles. The improved kinetic properties are believed to be due to this phase providing a surface for hydrogen dissociation and recombination to occur and a pathway for rapid diffusion of hydrogen, similar to the Mg-Ni case. Desorption rates currently measured with the rare earth phase are not as rapid as our vapor phase Mg2Ni material; however, the material processing has not yet been optimized.

In-situ Mg2Ni Hydride Bed Fabrication

Last year, it was shown that Mg2Ni could be formed directly from the reaction of vapor phase Mg with Ni particles. We have continued to investigate this process to determine its viability for synthesizing the alloy and also for fabicating Mg alloy hydride beds *in-situ*. Using PCT measurements and post-measurement microanalysis, we have now shown that the technique produces a hydride alloy with excellent properties starting with a variety of Ni and Mg particle sizes, and have examined the effects of processing temperature and different material and container configurations. We have also scaled up in size to produce 10-20 gram quantities of alloy. An industrial collaborator has been identified for demonstrating the fabrication of a Mg2Ni hydride bed and plans for the effort have been completed. The actual demonstration has been delayed until next fiscal year because of budget constraints.

Materials for Engineering Systems

In collaboration with Humboldt State University, Sandia will supply a hydride bed for use on a personal utility vehicle as part of the Palm Desert project. In support of this effort, commercially supplied low temperature hydrides were characterized (pressure-temperature, kinetics, particle size, etc.) for use in the bed. A material produced by GfE was selected and procured.

Initial results with a new approach to the fixation of hydride particles in a storage bed have been very promising. Isothermal measurements on an Fe-Ti hydride showed good loading and kinetic response following the treatment. If successful, the method should mitigate problems due to material decrepitation and result in reduced fabrication costs for hydride beds. This work is continuing to determine potential effects resulting from prolonged hydrogen exposure and hydride cycling.

IEA Activities in Hydrogen Storage

The IEA Annex 12 – Metal Hydrides program was finalized this year and activities begun in October 1995. At that time, Dr. G. Sandrock, SunaTech, Inc., joined the program. The first task was the generation of a comprehensive hydride data base. This data base contains information on specific alloy hydride compositions and includes pressure-temperature data, thermodynamic properties, loading ratio, plateau characteristics, hysteresis, crystal structure, metallurgy and synthesis, activation procedures, kinetics, cyclic stability, morphology and gas impurity effects. It also includes limited information on applications, suppliers and citations. Currently, there are 34 entries in the data base, with a target of about 100 entries for the completed project. It has been incorporated into an internet web-server site (http://hydpark.ca.sandia.gov) to allow for rapid and universal accessibility of the information.

A much less detailed, but comprehensive catalog of hydriding alloys has been nearly completed. This catalog is organized into the following alloy families: AB5, AB2, AB, A2B, intermetallic compounds, Mg alloys, solid solution alloys, multiphase alloys and composites, and amorphous alloys. There are currently over 600 entries in this catalog. In addition, it includes a reference list with 446 entries.

Plans for Future Work

Work on the Mg alloy hydrides will continue with the near-term goals of (a), studying the matrix of Mg-Al-Zn alloys fabricated this year in order to determine optimal alloy composition(s) for improved hydride properties, (b), improving the synthesis yield of the Mg-Al-Ni hydride, (c), examining particle size and surface properties for potential improvements in the hydrogen release kinetics of the Mg-Al-Cu hydride, and (d), further study the improved kinetic behavior of the Mg-Mm phase described above and attempt to use rare earth phases in other Mg-based alloy systems. Collaborative hydride studies will be continued and/or intitated with other laboratories within the DOE Hydrogen Program. At the present time, this includes ECD, ORNL and A.D. Little.

The Mg2Ni bed demonstration will be completed. Depending on results, a second, larger bed may be fabricated for use with an ICE in an integrated storage/engine test bed. Measurements on the effects of our particle fixation process on hydride performance will be completed within the next program year.

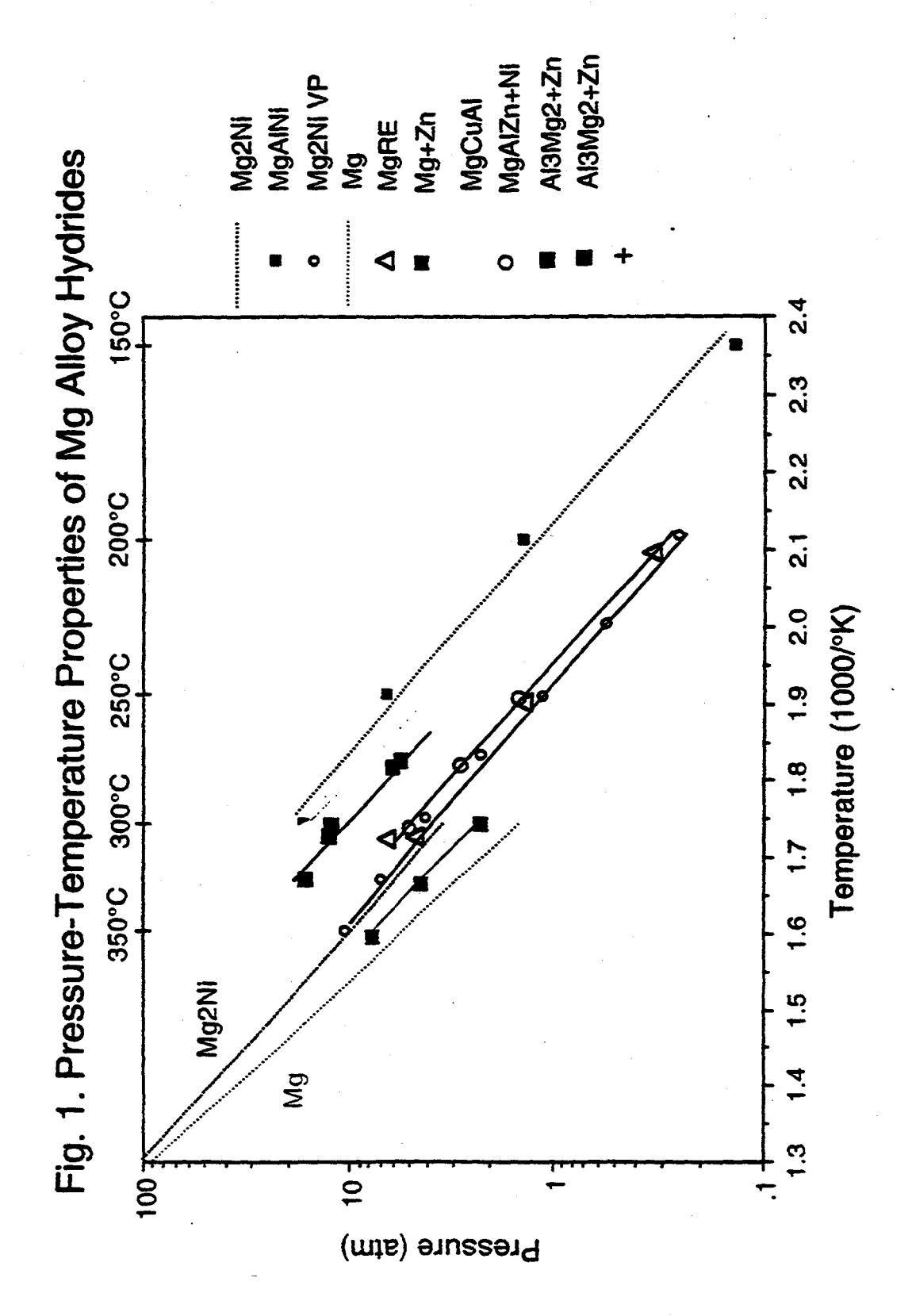
IEA Annex 12 activities will include mechanical alloying modifications to selected hydride alloys, preparation of Mg2Ni for characterization and measurements and PCT measurements on supplied hydrides. These experiments will be performed with international collaboration. Additions to the detailed on-line hydride data base will be completed, with the intent of reaching about 100 entries, and the comprehensive catalog of hydriding alloys will be completed.

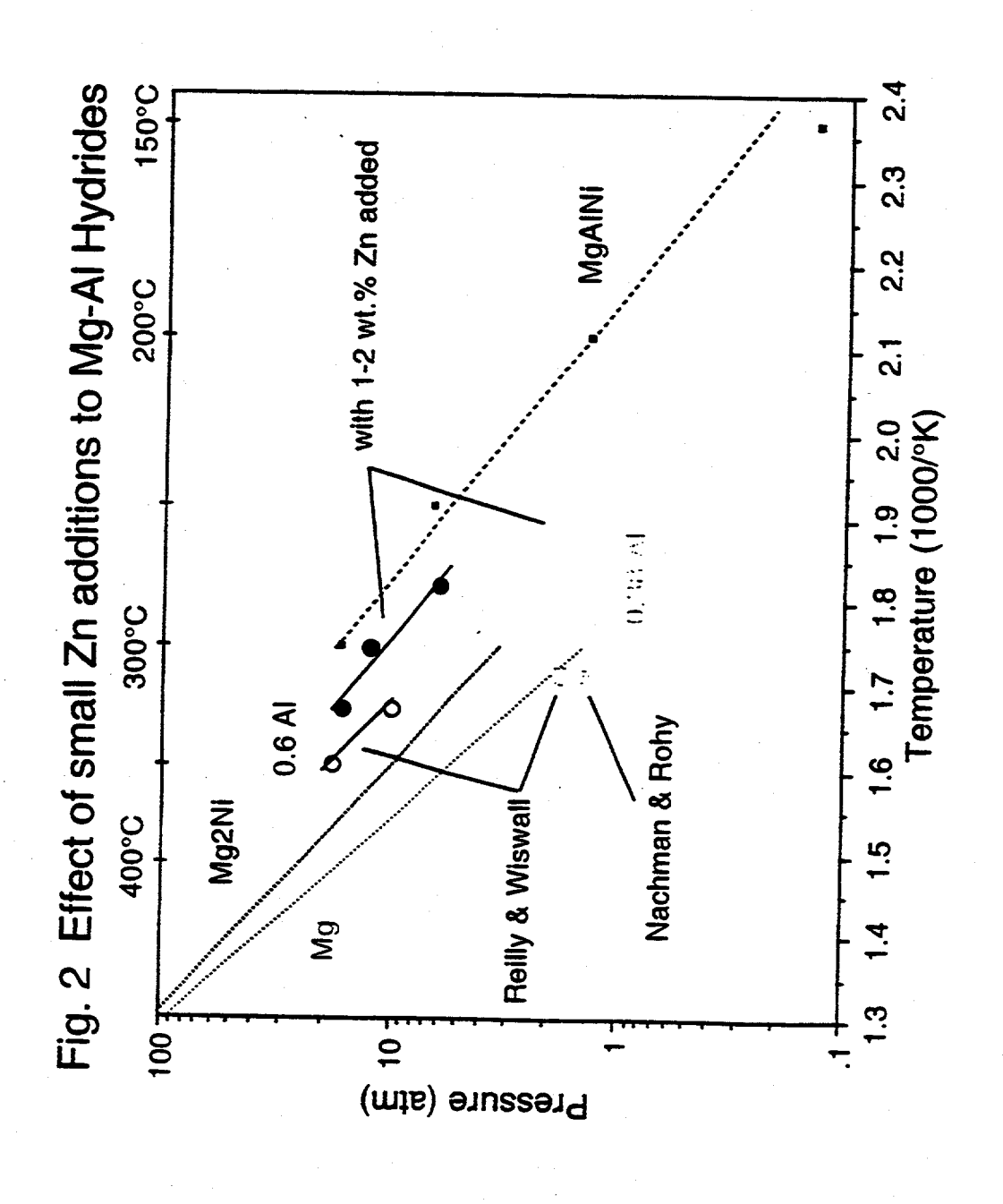
References

- 1. W. Guertler, M. Guertler and E. Anastasiadias: A Compendium of Constitutional Ternary Diagrams of Metallic Systems, WADC Technical Report 58-615 (translated from German), 1969.
- 2. J.J. Reilly and R.H. Wiswall, Jr.: BNL 19436, August 1, 1974.
- 3. J.F. Nachman and D.A. Rohy: DOE/CS0016-T1.

Figure Captions

- Figure 1. van't Hoff plot summarizing recent results. Included are pressure-temperature properties of Mg and Mg2Ni for comparison.
- Figure 2. van't Hoff plot showing the effects of small (1-2 wt.%) Zn additions to Mg-Al alloys.
- Figure 3. Electron micrographs of Mg alloys with and without Zn. Al-rich regions at the surface and in precipitates appear brighter than the matrix.
- Figure 4. van't Hoff plot showing differences obtained with samples containing a phase of rare-earth and Mg.
- Figure 5. Electron micrograph of sample containing a phase of rare-earth and Mg. The narrow phase can be seen extending throughout the particles and intersecting with the particle surfaces.





After Zn addition Figure 3. Single Phase Mg-Al-Zn Rapidly solidified Mg2Al3 Al rich precipitates and surface

Single phase

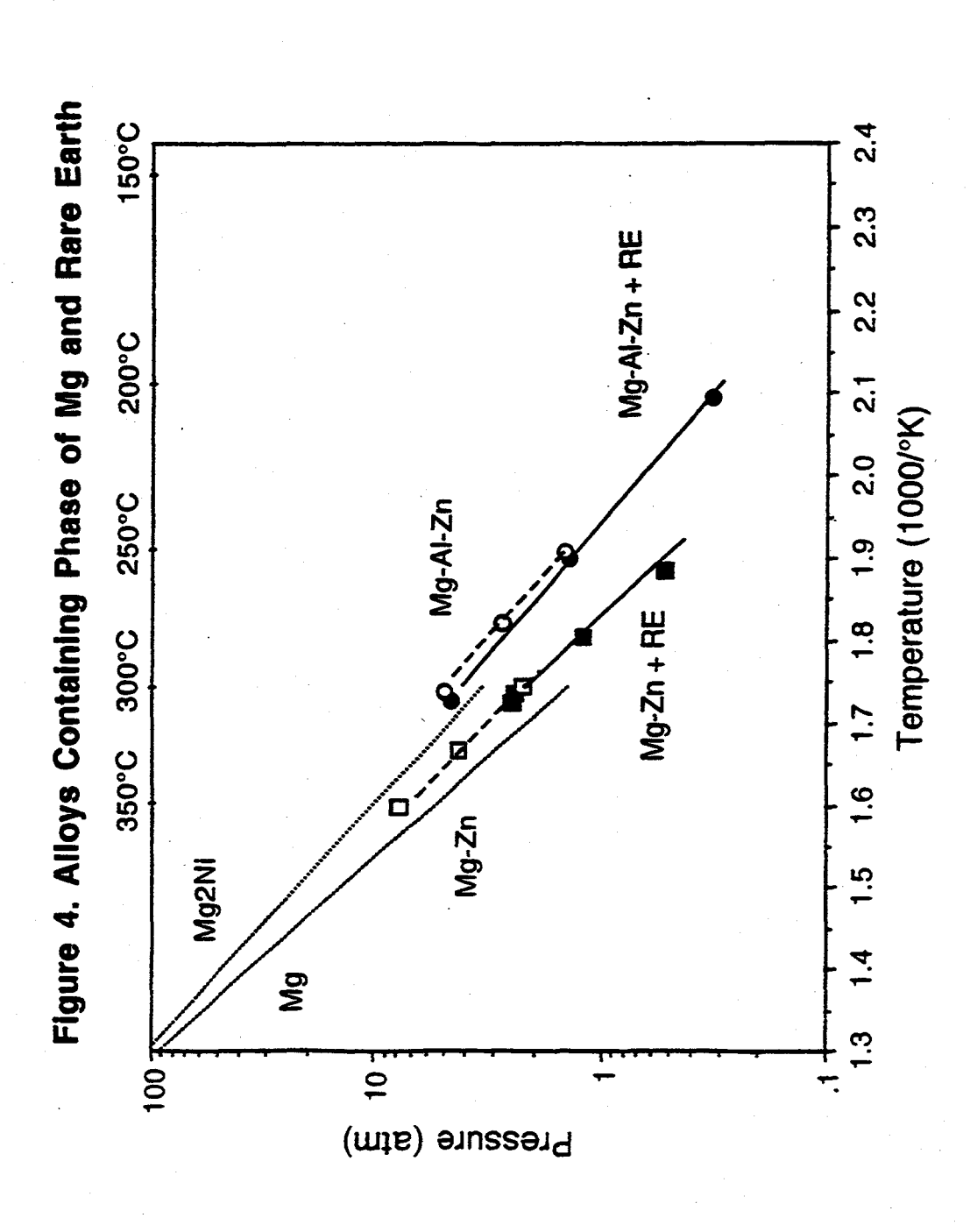


Figure 5. Rare earth phase in Mg alloy



THERMAL MANAGEMENT TECHNOLOGY FOR HYDROGEN STORAGE: FULLERENE OPTION

J. C. Wang, F. C. Chen, and R. W. Murphy Energy Division Oak Ridge National Laboratory Oak Ridge, Tennessee 37831

Abstract

Fullerenes are selected as our first option for investigating advanced thermal management technologies for hydrogen storage because of their potentially high volumetric and gravimetric densities. Experimental results indicate that about 6 wt% of hydrogen (corresponding to $C_{60}H_{48}$) can be added to and taken out of fullerenes. A model assuming thermally activated hydrogenation and dehydrogenation processes was developed to explain the experimental findings. The activation energies were estimated to be 100 and 160 kJ/mole (1.0 and 1.6 eV/H₂) for the hydrogenation and dehydrogenation processes, respectively. The difference is interpreted as the heat released during hydrogenation. There are indications that the activation energies and the heat of hydrogenation can be modified by the use of catalysts.

Preliminary hydrogen storage simulations for a conceptually simple device were performed. A 1-m long hollow metal cylinder with an inner diameter of 0.02 m was assumed to be filled with fullerene powders. The results indicate that the thermal diffusivity of the fullerenes controls the hydrogenation and dehydrogenation rates. The rates can be significantly modified by changing the thermal diffusivity of the material inside the cylinder, e.g., by incorporating a metal mesh. Results from the simulation suggest that thermal management is essential for efficient hydrogen storage devices using fullerenes.

While the preliminary models developed in this study explain some of the observations, more controlled experiments, rigorous model development, and physical property determinations are needed for the development of practical hydrogen storage devices. The use of catalysts to optimize the hydrogen storage characteristics of fullerenes also needs to be pursued. Future cooperative work between Oak Ridge National Laboratory (ORNL) and Material & Electrochemical Research Corporation (MER) is planned to address these needs.

Introduction

The present project is new. However, in a recent joint project under Cooperative Research And Development Agreement (CRADA) between ORNL and MER, initial work on hydrogen storage in fullerenes was performed. The work included sample preparation, thermal properties measurements, hydrogen absorption/desorption experiments, data analyses, and preliminary model development.

During FY96, the project has concentrated on explaining experimental results with physical models and conducting a first-order heat transfer analysis based on the initial thermal property measurements of various fullerenes. A model assuming both the absorption and desorption processes to be thermally-activated has been developed and found capable of explaining some of the observed data (Wang et al. 1995a,b). Thermal management simulations using analytical methods for a design with a simple geometry has paved the way for more realistic simulations of possible devices.

Rationale and Approach

Safe and cost-effective storage of hydrogen with high volumetric and gravimetric densities is one of the critical technologies needed in the National Hydrogen Program. Hydrogen stored in relatively non-reactive solids will be safer and thus a preferred storage method. ORNL is working jointly with MER to develop novel carbon materials such as fullerenes to offer new avenues for hydrogen storage. MER has been developing a continuous manufacturing process to increase production capacity of fullerenes. An inexpensive supply of fullerenes in the future appears to be feasible.

The overall goal of the present project is to investigate advanced thermal management technologies for hydrogen storage. The near-term objectives are to develop a heat generation/transfer model to describe hydrogen absorption in fullerenes, to characterize the thermomechanical behavior of the dynamic storage process, and to design practical configurations to thermally manage hydrogen absorption-desorption devices. The fullerenes are selected as our first option because of their potentially high gravimetric and volumetric hydrogen storage densities, and their projected low production costs.

Experimental results obtained by MER indicate that (1) up to about 6 wt% of hydrogen (corresponding to $C_{60}H_{48}$) can be absorbed by C_{60} fullerene, (2) the absorbed hydrogen can be released by heating, and (3) the rates of the absorption-desorption processes can be tailored by the use of various catalysts. Preliminary heat generation/transfer simulations at ORNL indicate that the characteristics of a hydrogen storage device can be significantly controlled by the heating and cooling rates in the device. The near-term approach adopted in the present project is to utilize the expertise at ORNL and MER in the areas of materials science, electrochemistry, solid state physics, and thermal management to (1) understand the mechanism of hydrogen storage in fullerenes, (2) optimize the hydrogen absorption/desorption properties of fullerene materials, (3) develop the thermal management technology needed for hydrogen storage in fullerenes, and (4) construct and demonstrate an experimental hydrogen storage device using fullerenes.

Results

Hydrogenation of Fullerenes

The hydrogenation rate of fullerenes observed at MER is very sensitive to temperature. For C_{60} powder samples under pressure, the amounts of H_2 absorbed in 30 min were 0.65, 1.40, and 2.50 wt% at 375, 400, and 425 °C, respectively. These results approximate a straight line on a ln (wt% H_2) vs. 1000/T graph (see Fig. 1). The straight-line graph suggests that the hydrogenation process is thermally activated. If this is

assumed, the slope of the graph gives an activation energy for hydrogenation of about 100 kJ/mole (1.0 eV/ H_2). The early-stage data at 30 min were used in the calculation because the hydrogenation rate can be slowed down by the amount of H_2 present in the samples.

Dehydrogenation of Fullerenes

As shown in Fig. 2, the dehydrogenation of a mixed fullerene powder sample was achieved by raising the temperature from 28 to 400 °C (assuming at a constant rate). Very little H₂ was released from the sample before the temperature approached 400 °C and the release became very rapid when this temperature was reached. This suggests that the dehydrogenation of fullerenes is also a thermally activated process.

To extract the activation energy for the dehydrogenation process, it was assumed that the escape rate of hydrogen from the powder sample can be written in a thermally activated form:

$$Rate = A \frac{c}{c_{\text{max}}} e^{-\frac{E}{kT}} , \qquad (1)$$

where c is the concentration of hydrogen in the fullerene and c_{max} is its maximum value, E the activation energy, and A the pre-exponential factor related to the attempt frequency of the *hydrogen atoms* to escape from the fullerenes. The dimensionless factor c/c_{max} is intended to capture the trend that at a given time, the hydrogen escape rate is proportional to the amount of hydrogen present in the sample. For a given set of parameter values, Eq. (1) was used to calculate the amount of hydrogen released and the result was compared with experimental data at various observation times. The parameter values were then changed and the calculations repeated until the best fit was obtained (using least-squares method). In the calculation, the temperature was assumed to change from 28 to 400 °C at a constant rate during the time period t and remained at 400 °C afterward. Using t, A, c_{max} , and E as adjustable parameters, the best-fit curve was obtained. The result together with the extracted parameter values is shown in Fig. 2.

Model for Hydrogenation and Dehydrogenation of Fullerenes

The results discussed above indicate that for a H₂ molecule to be absorbed by fullerene powders, it must overcome a potential barrier of about 100 kJ/mole (1.0 eV/H₂). For the absorbed hydrogen atoms to escape the fullerene powders to form H₂ molecules, they also need to overcome a potential barrier, which is about 160 kJ/mole (1.6 eV/H₂) (E in Fig. 2). This conceptual model for hydrogen absorption and desorption by fullerenes is schematically illustrated in Fig. 3. As can be seen from the figure, the activation energy for dehydrogenation is about 60 kJ/mole (0.6 eV/H₂) higher than that of hydrogenation. This difference is interpreted as the heat of hydrogenation h_h, i.e., when a H₂ molecule is absorbed as two hydrogen atoms in fullerene, this amount of heat is released. Calculated values of h_h for the reaction $C_{60}H_{2n} + H_2 - C_{60}H_{2(n+1)}$ in the gas phase have been reported in the literature (Guo and Scuseria 1992; Rathna and Chandrasekhar 1993; Yoshida 1992). They range from 150 kJ/mole (1.5 eV/H₂) for n=1 to some very small values for n>18. The magnitude of h_h in the gas phase can be qualitatively understood by considering the various chemical bond energies such as those of H-H, H-C, C-C, and C=C. No calculations of h, for the solid phase have been reported, but the values are expected to be similar to those for the gas phase because of the weak van der Waals interaction between fullerene molecules in the solid (Fischer et al. 1991). The value of 60 kJ/mole (0.6 eV/H₂) for h_h extracted from the present model for powder fullerene samples is within the range obtained for the gas phase calculations.

Thermal Management Simulations

The thermally activated processes discussed above are very sensitive to temperature. For example, a fully hydrogenated fullerene sample may be quite stable at room temperature, but can lose the absorbed hydrogen rapidly at 400 °C (see Fig. 2). On the other hand, because of the heat released (absorbed) during hydrogenation (dehydrogenation), the temperatures at various locations of a large sample may change at different rates during the processes. Therefore, several rates may be involved simultaneously and interactively. As a result, thermal management is very important for devices involving these processes.

To study the thermal management problems, a cylindrical-tube model was chosen to simulate the heat conduction, hydrogen absorption/release, and heat absorption/release processes. A 1-m long metal tube with an inner diameter of 0.02 m was assumed to be filled with fullerene powders. In the powder material, the transport rate of hydrogen from particle to particle was assumed to be negligibly small, while the transport within each particle was assumed to be fast. The temperature of the metal tube was used to control the processes. The heat conduction calculations were handled with a combination of analytical equations (Carslaw and Jaeger 1959) and numerical computation. Most values of the parameters used in the simulations are preliminary in nature. Refinements will be made as more experimental data become available.

The calculations were divided into small time steps, which were reduced until the results became stationary. For a given time step and temperature distribution, the temperature change due to heat conduction was first calculated. The hydrogen absorbed and/or released was calculated according to the rate equation, Eq. (1), at various points inside the cylinder using local temperature values. The heat release/absorption was then calculated and the temperature values modified accordingly using the specific heat of the material to obtain the new temperature distribution for the time step. The calculations were repeated for all time steps in each simulation.

A set of calculations for the fullerene-filled cylinder was made without the involvement of hydrogen, giving a base line for comparison. In the calculations, the temperature of the metal tube was raised from 28 to 400 $^{\circ}$ C in 10 min at a constant rate and was fixed at 400 $^{\circ}$ C afterward. For this case, the solutions given in Carslaw and Jaeger (1959) can be readily applied. The calculated distributions of temperature in the cylinder at various times are shown in Fig. 4. Notice that these results are equally applicable if there is hydrogen involvement but $h_h=0$.

The above calculations were repeated for the case in which the fullerene had been charged to a uniform hydrogen concentration of 400 std liter/kg sample (1 std liter = 1 liter under 1 atm at 273 K). The heat of hydrogenation, $h_h=60$ kJ/mole (0.6 eV/H₂), was taken into consideration during the simulation. As before, the temperature of the metal tube was raised from 28 to 400 °C in 10 min at a constant rate and maintained at 400 °C afterward. The calculated temperature distributions are also shown in Fig. 4. The increase of temperature inside the cylinder in this case became much slower because heat was needed and supplied from the metal tube through conduction. During the first few minutes, the results shown in the upper and lower parts of Fig. 4 are almost identical. This occurred because during that time period, the temperature was low and very little hydrogen was released. When the temperature became high enough, the release of hydrogen and the accompanying absorption of heat in the $h_h>0$ case caused a dip in the calculated temperature distribution (near the surface of the cylinder at time=10 min).

The distributions of hydrogen concentration at various times during the dehydrogenation simulation were also calculated. During the first few minutes, very little hydrogen was released because of the low temperature. The dehydrogenation proceeded from the metal tube toward the center of the cylinder

indicating the control of release by the heat conduction and supply from the metal tube. The total hydrogen released as a function of time is shown in Fig. 5. Also shown in the figure are the hydrogen release curves for the cases when the thermal diffusivity of the material inside the cylinder was increased. A comparison of the curves suggests that the performance of a device can be significantly altered by modifying the physical properties of the materials. One possible method of increasing the thermal diffusivity of the material inside the cylinder is to use a metal mesh.

Preliminary simulations for several hydrogenation cases were also performed. The hydrogen absorption and desorption rates can be significant at the same time and need to be treated simultaneously. More work will be performed when better software is developed or obtained. One conclusion from the preliminary results is that thermal management is very important in the hydrogenation process.

Expected Goals

The overall goal is to investigate advanced thermal management technologies for hydrogen storage. For a given hydrogen storage option we seek (1) to understand the storage mechanism and (2) to incorporate the understanding into simulation codes so that they can be used to facilitate material design and optimize the storage capabilities. For the fullerene option, specific goals are:

- (1) Understand the hydrogen storage mechanism in fullerenes and determine the values of essential parameters;
- (2) Develop physical models for explaining the experimental data;
- (3) Optimize material properties through the use of various catalysts and preparation methods;
- (4) Incorporate special properties of hydrogen and the fullerene materials into computer codes for thermal management simulations and device designs; and
- (5) Demonstrate hydrogen storage in fullerenes using experimental devices.

Plans for Future Work

Although the following plans are mainly for the fullerene option, the methodology developed and experience gained is readily applicable to other options:

- (1) Conduct further, systematic experiments to determine the values of essential parameters such as heat of hydrogenation, and activation energies for absorption, desorption, and hydrogen diffusion;
- (2) In collaboration with MER through CRADA, continue to test new catalysts and preparation methods to tailor the operating conditions such as temperature and pressure;
- (3) Develop an integrated model for the absorption and desorption processes;
- (4) Expand the thermal management simulations to more complicated and/or practical geometries using either analytical or numerical methods; and
- (5) Use the results from the above steps to evaluate possible engineering designs for their hydrogen storage performance and to use the most promising design to develop a demonstration hydrogen storage device using fullerenes.

Acknowledgment

This work was sponsored by the U.S. Department of Energy under contract No. DE-AC05-96OR22464 with Lockheed Martin Energy Research Corp. The authors wish to thank Drs. R. O. Johnson and J. D. Tauxe for their critical reading of the manuscript. Special appreciation is expressed to Drs. R. O. Loutfy and X. Lu of MER Corporation for their collaboration under the completed DOE ER-CRADA ORNL94-0277.

References

Carslaw, H.S., and J.C. Jaeger. 1959. Conduction of Heat in Solids, 2nd ed. New York: Oxford University Press.

Fischer, J.E. et al. 1991. "Compressibility of Solid C₆₀." Science 252: 1288-1290.

Guo, T., and G. E. Scuseria. 1992. "Ab Initio Calculations of Tetrahedral Hydrogenated Buckminsterfullerene." Chem. Phys. Lett. 191: 527-532.

Rathna, A, and J. Chandrasekhar. 1993. "Theoretical Study of Hydrogenated Buckminsterfullerene Derivatives with Benzenoid Rings, C₆₀H_{60-6n} (n=1-8)." Chem. Phys. Lett. 206: 217-224.

Wang, J.C., F.C. Chen, X. Lu, and R.O. Loutfy. 1995a. "Model for Hydrogenation and De-Hydrogenation of C₆₀/C₇₀ Fullerene." Presented at Symposium FF: Fullerenes, Buckytubes, and Related Materials - Science and Applications, Materials Research Society Fall Meeting. Boston, MA, November 27-December 1.

Wang, J.C., F.C. Chen, X. Lu, and R.O. Loutfy. 1995b. Analysis of Hydrogen Storage in Fullerenes. CRADA Final Report ORNL-94-0277. Oak Ridge, TN: Oak Ridge National Laboratory.

Yoshida, Z. 1992. "Investigation of Hydrogenation of C₆₀ using Theoretical Calculations." Chem. Phys. Lett. 201: 481-484.

Figure Captions

- Fig. 1. Absorption of hydrogen by C_{60} fullerene powders.
- Fig. 2. Release of hydrogen from mixed fullerene powders.
- Fig. 3. Conceptual model for hydrogen storage in fullerenes.
- Fig. 4. Temperature distributions during dehydrogenation calculated for h_h=0 and h_h=60 kJ/mole.
- Fig. 5. Total hydrogen released calculated for different thermal diffusivity values.

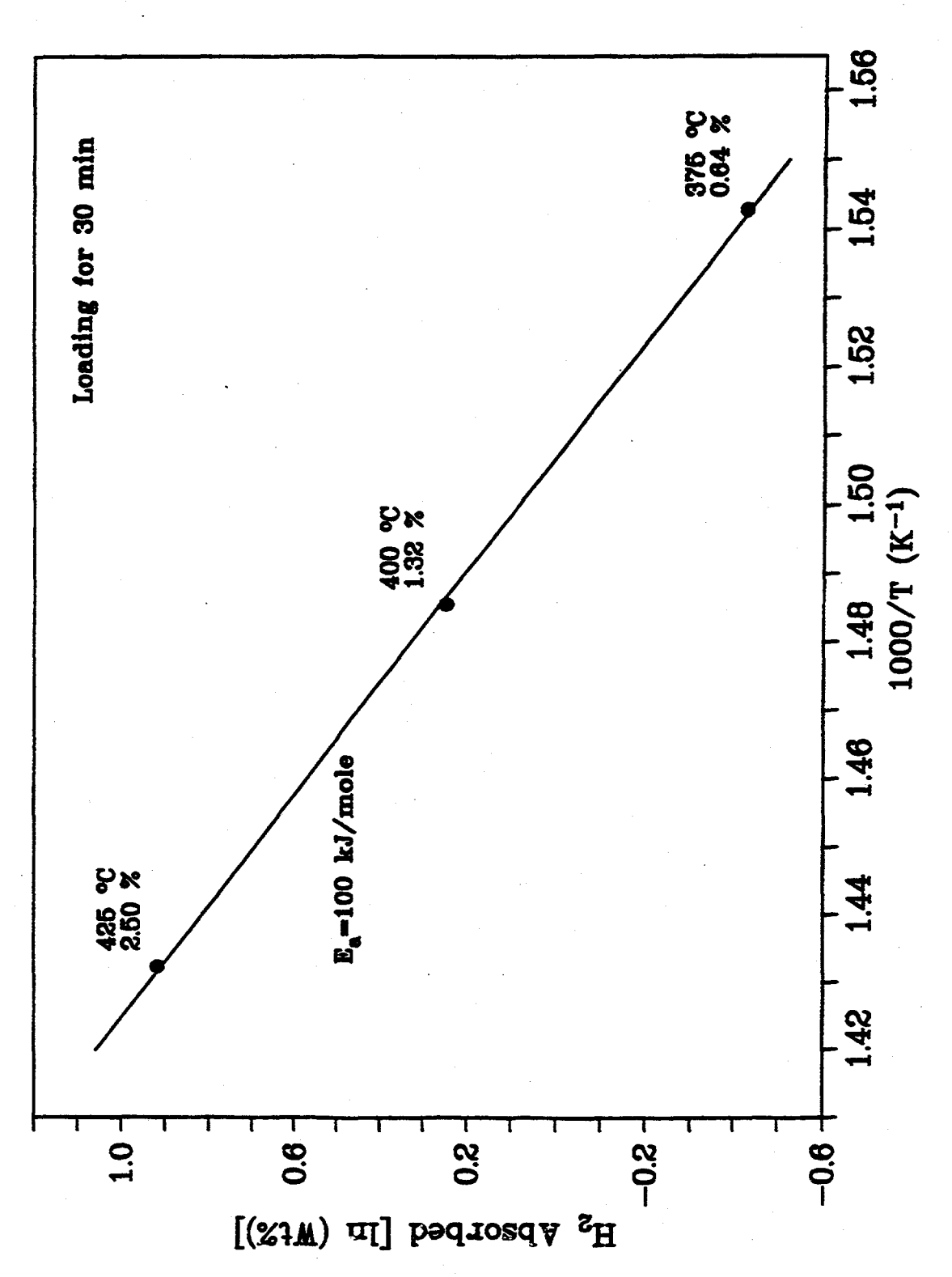


Fig. 1. Absorption of hydrogen by Cen fullerene powders.

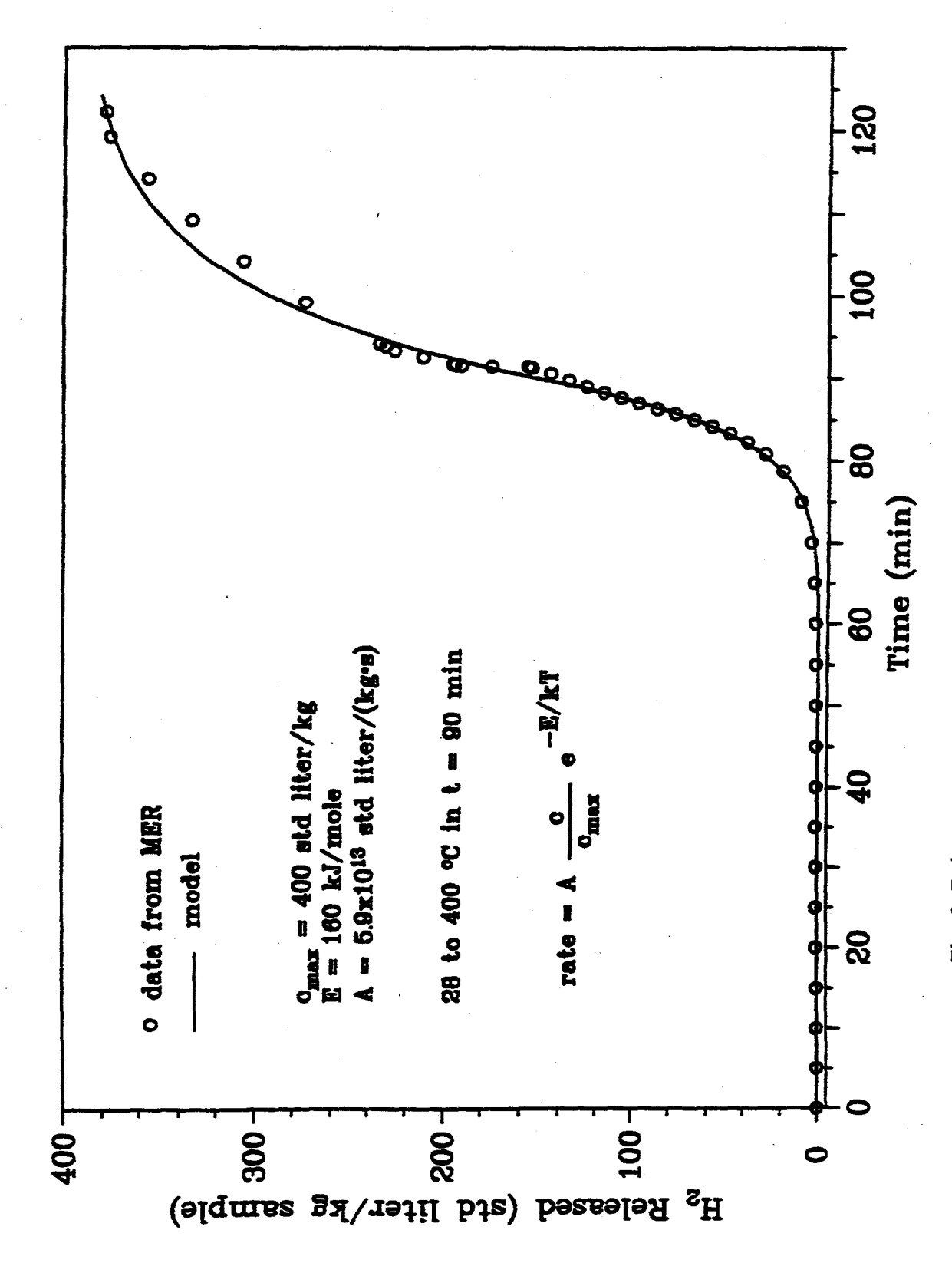


Fig. 2. Release of hydrogen from mixed fullerene powders.

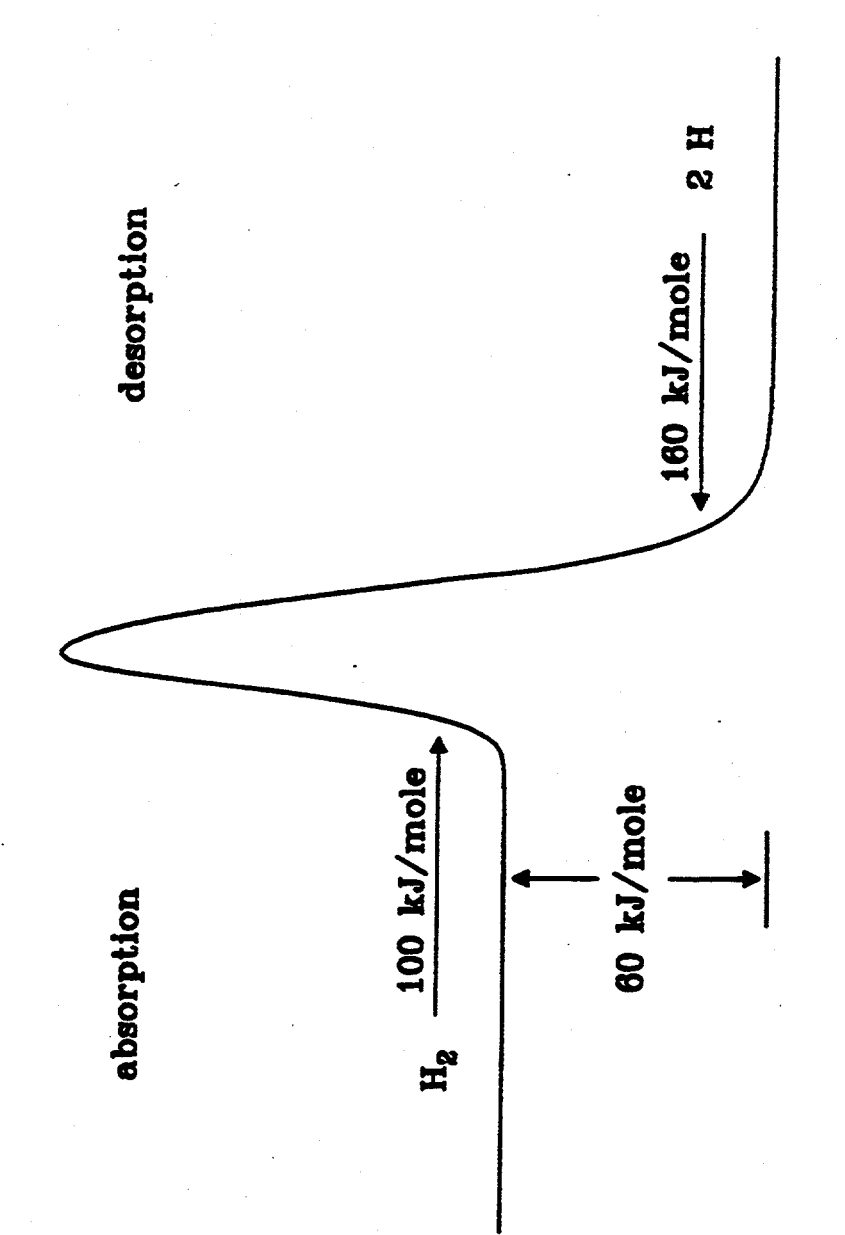


Fig. 3. Conceptual model for hydrogen storage in fullerenes.

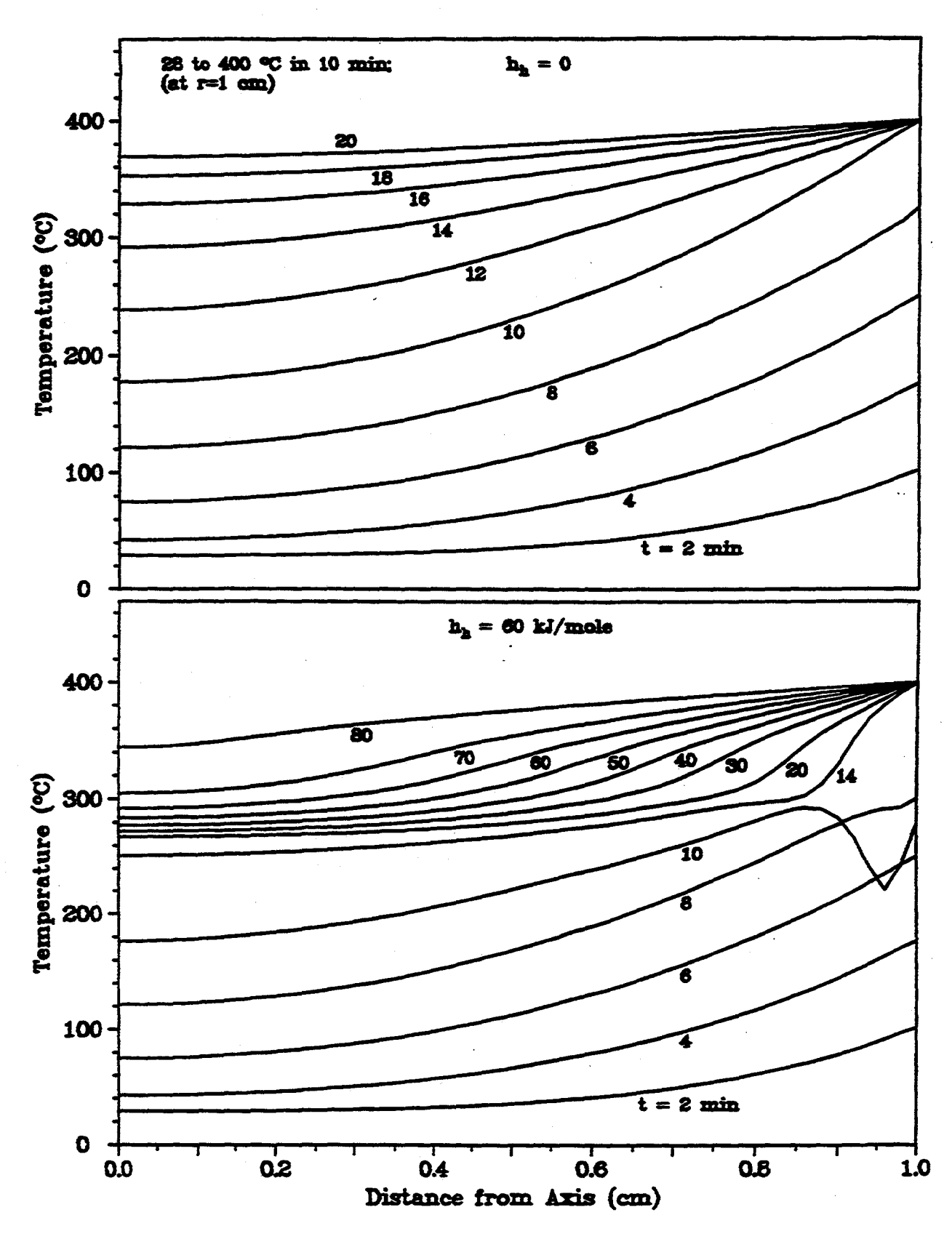


Fig. 4. Temperature distributions during dehydrogenation calculated for h_h =0 and h_h =60 kJ/mole.

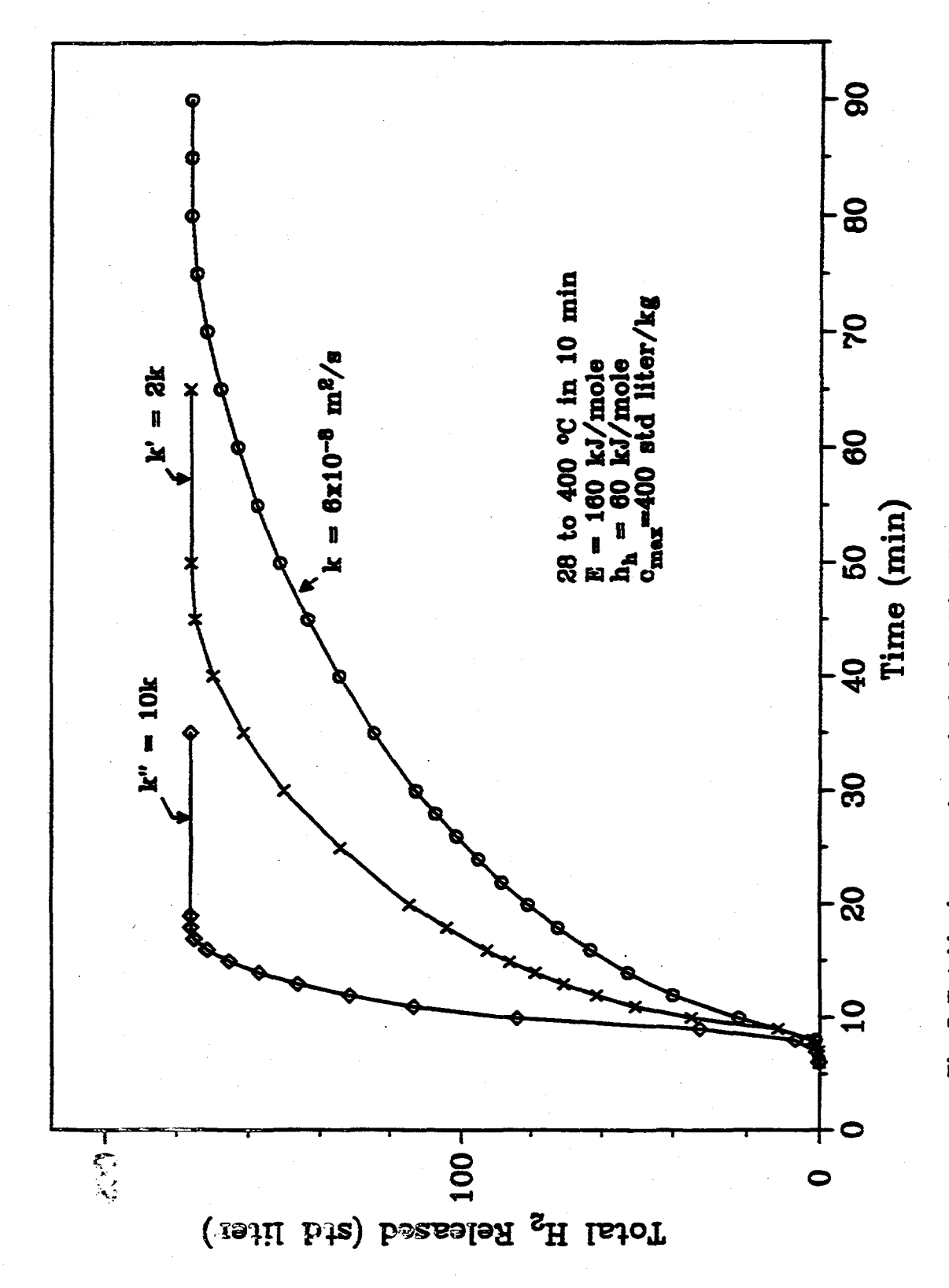


Fig. 5. Total hydrogen released calculated for different thermal diffusivity values.